COMPUTATIONAL ANALYSIS OF THE CATALYTIC AND FERROELECTRIC PROPERTIES OF POLYOXOMETALATES

Fei Wang

UNIVERSITAT ROVIRA i VIRGILI

Computational Analysis of the Catalytic and Ferroelectric Properties of Polyoxometalates

Fei Wang

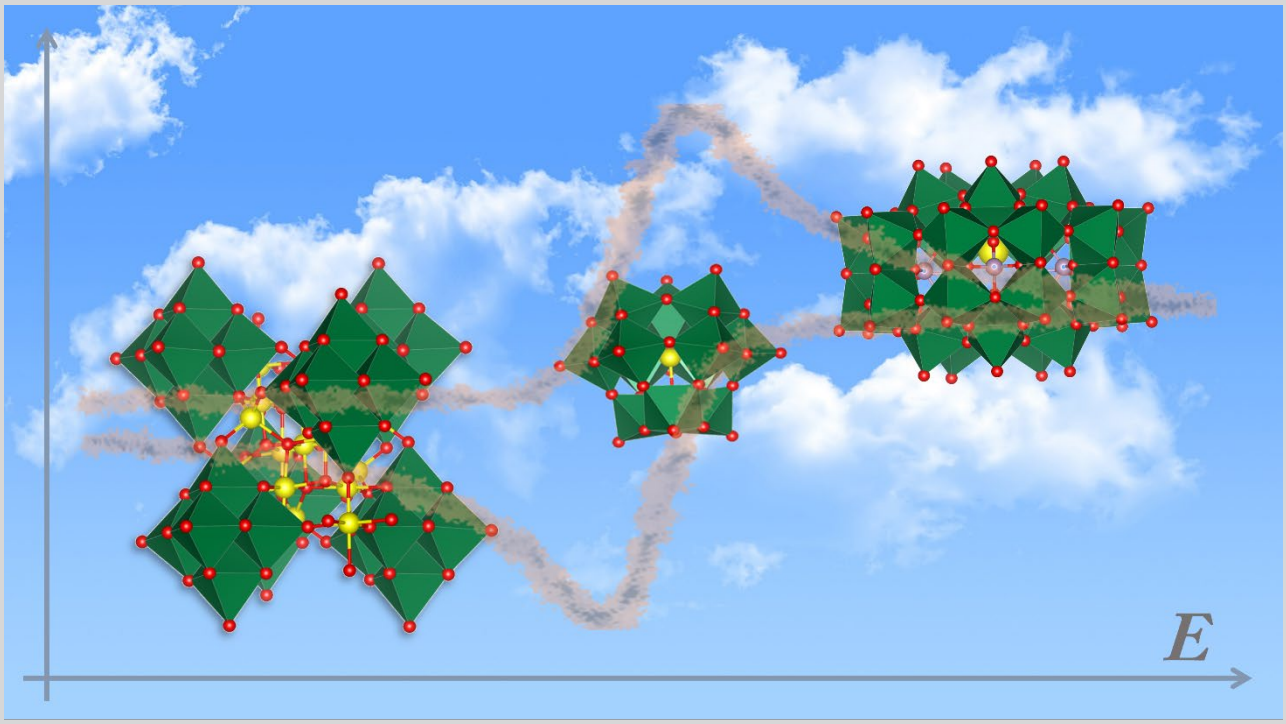

DOCTORAL THESIS

2022

UNIVERSITAT ROVIRA I VIRGILI
COMPUTATIONAL ANALYSIS OF THE CATALYTIC AND FERROELECTRIC PROPERTIES OF POLYOXOMETALATES
Fei Wang

Fei Wang

Computational Analysis of the Catalytic and Ferroelectric Properties of Polyoxometalates

DOCTORAL THESIS

Supervised by

Dr. Josep Maria Poblet Rius and Prof. Coen de Graaf

UNIVERSITAT ROVIRA i VIRGILI

Departament de Química Física i Inorgànica

Tarragona, 2022

UNIVERSITAT ROVIRA I VIRGILI
COMPUTATIONAL ANALYSIS OF THE CATALYTIC AND FERROELECTRIC PROPERTIES OF POLYOXOMETALATES
Fei Wang

UNIVERSITAT ROVIRA i VIRGILI

Josep Maria Poblet Rius, Professor of Physical Chemistry of Departament de Química Física i Inorgànica of Universitat Rovira i Virgili, and Coen de Graaf, ICREA Research Professor of Departament de Química Física i Inorgànica of Universitat Rovira i Virgili

We STATE that the present study, entitled

"**Computational Analysis of the Catalytic and Ferroelectric Properties of Polyoxometalates**",

presented by Fei Wang to receive the degree of Doctor, has been carried out under our supervision at the Departament de Química Física i Inorgànica of this university.

Tarragona, 06 June 2022

Doctoral Thesis Supervisors

Josep Maria Poblet Rius

Coen de Graaf

UNIVERSITAT ROVIRA I VIRGILI
COMPUTATIONAL ANALYSIS OF THE CATALYTIC AND FERROELECTRIC PROPERTIES OF POLYOXOMETALATES
Fei Wang

Table of Contents

UNIVERSITAT ROVIRA I VIRGILI
COMPUTATIONAL ANALYSIS OF THE CATALYTIC AND FERROELECTRIC PROPERTIES OF POLYOXOMETALATES
Fei Wang

List of Publications

Here is the list of publications achieved during the PhD.

Related to the thesis:

1. Dima Azaiza-Dabbah, Charlotte Vogt, Fei Wang, Albert Masip-Sánchez, Coen de Graaf, Josep M. Poblet, Eynat Haviv, Ronny Neumann. "**Molecular transition metal oxide electrocatalysts for the reversible carbon dioxide–carbon monoxide transformation**" *Angew. Chem. Int. Ed.* **2022**, 61, e202112915.
2. Fei Wang, Ronny Neumann, Coen de Graaf, and Josep M. Poblet. "**Photoreduction mechanism of CO_2 to CO catalyzed by a three-component hybrid construct with a bimetallic rhenium catalyst**" *ACS Catal.* **2021**, 11, 1495.
3. Guanyun Zhang, Mark Baranov, Fei Wang, Josep M. Poblet, Sebastian Kozuch, Nitai Leffler, Alexander I. Shames, Juan M. Clemente-Juan, Alevtina Neyman, and Ira A. Weinstock. "**Soluble complexes of cobalt oxide fragments bring the unique CO_2 photoreduction activity of a bulk material into the flexible domain of molecular science**" *J. Am. Chem. Soc.* **2021**, 143, 20769.
4. Fei Wang, Zhongling Lang, Likai Yan, Alessandro Stroppa, Josep M. Poblet, and Coen de Graaf. "**Density functional theory study of single-molecule ferroelectricity in Preyssler-type polyoxometalates**" *APL Mater.* **2021**, 9, 021109.
5. Fei Wang, Heng Gao, Coen de Graaf, Josep M. Poblet, Branton J. Campbell & Alessandro Stroppa. "**Switchable Rashba anisotropy in layered hybrid organic–inorganic perovskite by hybrid improper ferroelectricity**" *npj Comput Mater.* **2020**, 6, 183.
6. Fei Wang, Ronny Neumann, Coen de Graaf, and Josep M. Poblet. "**Electrochemical mechanism of CO_2 reduction versus CO oxidation using trimetallo-oxo POMs as alternative for rare-metal based catalysts**" (*In preparation*)
7. Guan-yun Zhang, Tal Tubul, Fei Wang, Josep M. Poblet, Mark Baranov, Nitai Leffler, Alevtina Neyman, Ira A. Weinstock. "**Molecular entrapment of a cubic-phase-like Nickel-oxide fragment for solar-light driven reduction of CO_2 by Water**" (*In preparation*)

8. Fei Wang, Coen de Graaf, Josep M. Poblet. "**Theoretical study of solution acidity (*p*Ka)-controlled products selectivity of the CO_2 electroreduction catalyzed by manganese bipyridine**" (*In preparation*)

Non-related to the thesis:

9. Saurav Bhattacharya, Uttara Basu, Mohamed Haouas, Pei Su, Michael Forrester Espenship, Fei Wang, Albert Solé-Daura, Dereje H. Taffa, Michael Wark, Josep M. Poblet, Julia Laskin, Emmanuel Cadot, Ulrich Kortz. "**Discovery and supramolecular interactions of neutral Palladium-oxo clusters Pd_{16} and Pd_{24}**" *Angew. Chem. Int. Ed.* **2021**, 60, 3632.

10. Ananthu Rajan, Mahmoud Elcheikh Mahmoud, Fei Wang, Josep M. Poblet, Saurav Bhattacharya, Ali S. Mougharbel, Xiang Ma, Anja B. Müller, Talha Nisar, Nikolai Kuhnert, Veit Wagner, and Ulrich Kortz, "**Synthesis, characterization and catalysis of a solution-stable trinuclear Platinum(II) complex, $Na_{10}[Pt_3(\mu_3\text{-}S)_2(SO_3)_6]\cdot 22H_2O$**" (*Submitted for publication*)

List of Abbreviations

	2D	two-dimensional
	3D	three-dimensional
	a_R	Rashba coefficient
A	ADF	Amsterdam Density Functional
	AFE	Anti-Ferroelectricity
	AFP	Anti-Ferroelectric Phase
	AFR	Anti-Ferrorotational
	AMP	4-Aminomethyl-Piperidinium
B	bipy	2,2'-Bipyridine
	BZ	Brillouin Zone
C	ca.	*circa* (approximately)
	CASSCF	Complete Active Space Self-Consistent Field
	CASPT2	Complete Active Space Second-order Perturbation Theory
	CBM	Conduction Band Minimum
	COSMO	Conductor-like Screening Model
	CPMD	Car–Parrinello molecular dynamics
	CV	Capacitance–Voltage
D	DFT	Density Functional Theory
	DMSO	Dimethyl sulfoxide
	DPE	Deprotonation Energy
	DPE	Deprotonation Energy
	DZP	Double–Zeta plus Polarization
F	FE	Ferroelectricity
	FMO	Frontier Molecular Orbital
	FP	Ferroelectric Phase
	FR	Ferrorotational
E	*E*	Electric Feld
	ECP	Effective Core Potential

	E_{ea}	Electron Affinity
	ΔE_{int}	Energy Interaction
	E_i	Ionization Energy
	ΔE	Relative Electronic Energy
	E_R	Rashba splitting energy
	et al.	*et alii (and others)*
	etc.	*et cetera*
G	g-CN	Graphitic Carbon Nitride
	GGA	Generalized Gradient Approximation
	ΔG_r	Relative Gibbs Energy
	$\Delta G_r^{\ddagger}$	Activation barrier
H	HF	Hartree-Fock
	HOIP	Hybrid Organic-inorganic Perovskite
	HOMO	Highest Occupied Molecular Orbital
	HPAs	Hetero-Polyanions
I	IEF-PCM	Integral Equation Formalism–Polarizable Continuum Model
	IPAs	Iso-Polyanions
K	k_R	momentum offset
L	LMCT	Ligand-to-Metal Electrons Transfer
	LUMO	Lowest Unoccupied Molecular Orbital
M	MA	Methylammonium
	MC	Monte Carlo
	MD	Molecular Dynamic
	MeCN	Acetonitrile
	MEDP	Maximum-Electron-Density Plane
	MEP	Molecular Electrostatic Potential
	mM	mMol L^{-1} (Millimoles per liter)
	MM	Molecular Mechanics
N	NHE	Normal Hydrogen Electrodes
	NPT	Isothermal–Isobaric ensemble (constant number of

		particles, pressure, and temperature)
	NVT	Canonical Ensemble (constant number of particles, volume and temperature)
P	PAW	Projector Saugmented Wave
	P_{cation}	Cationic Polarization
	P_{ele}	Electronic Polarization
	PF_6	Hexafluorophosphate
	P_{frame}	Framework Polarization
	P_{ion}	Ionic Polarization
	PME	Particle-particle Mesh Ewald PME
	POMs	Polyoxometalates
	POVs	Polyvanadates
	P_q	Polarization Quantum
	P_r	Remanent Polarization
	P_s	Spontaneous Polarization
	P_{total}	Total Polarization
	PVDF	Polyvinylidene Fluoride PVDF
	PZT	Lead Zirconate Titanate
Q	QM	Quantum Mechanics
R	RDF	Radial Distribution Functions
S	SME	Single-Molecule Electret
	SMM	Single-Molecule Magnet
	SOC	Spin-Orbit Coupling
	SOMO	Singly Occupied Molecular Orbital
T	TBA	Tetrabutylammonium
	T_C	Curie temperature
	TDDFT	Time-Dependent DFT
	TM	Transition Metal
	TMSPs	TM-substituted POMs
	TS	Transition State
	TZP	Triple–Zeta plus Polarization
U	UV-vis	Ultraviolet–visible

V	VASP	Vienna Ab initio Simulation Package
	VBM	Valence Band Maximum
	vs	*versus*
	v/v	volume per volume (volume concentration of a solution)
Z	ZORA	Zeroth-Order Regular Approximation

Overview

This initial chapter aims to give a brief description of the structure of the thesis so that readers can have a general outline of the primary content. As usual, the thesis starts with introducing the research background information of polyoxometalates (abbreviated as POMs), a class of polyanionic metal-oxygen clusters, shortly discussing their structures, properties, and applications. The focus is placed on presenting the studies in the field of classical catalysis and emerging ferroelectricity from both experimental and theoretical perspectives. This chapter ends with discussing two major challenges facing theoretical POM chemistry, where the common computational methods are summarized. Based on that, the goals of this thesis are proposed in *Chapter 2*. The following two chapters, *Chapters 3* and *4,* study the redox behaviors of POMs in the electro- and photo-catalytic carbon dioxide-carbon monoxide transformation reactions. The catalytic mechanisms are revealed in which the roles of the POMs are illustrated. Since ferroelectricity is an entirely new area for POM science and it is challenging to compute the ferroelectric polarization for a big, complex system, a simpler and common ferroelectric hybrid organic-inorganic perovskite (HOIP) is firstly studied to explore a rational method and gain experience in computing polarization in *Chapter 5*. The ferroelectricity of POMs is discussed in *Chapter 6*. The origin of polarization within POM clusters is analyzed by decomposing the ferroelectric effect into three contributions. All conclusions are summarized in the last *Chapter 7*.

Chapter 3 explores the electrochemical catalysis on the reversible CO_2-CO transformation of a series of trimetallic-oxo POMs that can be considered an alternative for rare-metal-based catalysts. A catalytic Tafel plot by experiments shows that the tri-Cu-substituted polyanion $[SiCu^{II}_3W_9]$ is highly reactive for CO_2 reduction with a 98% faradaic efficiency yielding a significant amount of CO. In contrast, the Fe-Ni compound, e.g. $[SiFe^{III}Ni^{II}_2W_9]$ prefers to catalyze CO oxidation to CO_2. To gain an in-depth insight into the different catalytic activities of the two POMs taking the nuclearities and configurations of the encapsulated *d*-block transition metal (TM) into account, molecular dynamic (MD) simulations and density functional theory (DFT) calculations are applied to model their redox behaviors in acetonitrile solution. MD simulations show that a double water shell is formed around the POM at the more basic M_3O_3 unit. DFT calculations reveal that the triprotonated, 2-electron reduced catalysts are the species active in CO_2 and CO fixation. For $H_3[SiFe^{II}Ni^{II}Ni^{I}W_9]$, CO_2

and CO are coordinated to the Ni^{I} center by forming strongly nonlinear C-O bonds with a small activation barrier. On the contrary, the only Cu^{I} center of the $H_3[SiCu^{II}_2Cu^{I}W_9]$ anion shows no binding interaction with CO_2, until the second electron is injected to generate two Cu^{I} ions. This species can bond CO_2 by forming a polyanion with an electronic configuration of $H_3[SiCu^{II}_2Cu^{0}W_9]$ through the electron transfer from one Cu^{I} to the other one during the CO_2 approaching. Since only one CO_2 molecule can bind to $H_3[SiCu^{II}_2Cu^{0}W_9]$, the formation of C_2 products often observed for Cu_x-based materials is prevented, leading to the selective formation of CO.

This chapter also analyzes the redox activity of $[SiCu^{II}Ga^{III}Fe^{III}W_9]$, which is reported the most reactive catalyst for CO_2 reduction in those trimetallic-oxo POM clusters. It is found that the inclusion of a Lewis acid center Ga^{3+} incorporates in one more coordinating site for CO_2. It can fix CO_2 through a double-bonding model, Ga-O-C-O(Cu) with a ΔE of -25.4 kcal mol^{-1} after an exothermic process with a ΔG of -12.3 kcal mol^{-1}. Notably, this cluster is capable of coordinating CO_2 before any reduction, leading to a potential for reducing Cu^{II} that is lower than for Fe^{III}. Those computational results illustrate the influence of the nuclearities and configurations of the substituted *d*-block TMs on the coordination of CO_2 where the synergy effect between multiple TMs may exist, which should be taken into account when designing the electrocatalysts. Our findings described here also provide a better understanding on the interaction of POMs with small molecules and further the design of new POM-based CO_2 reduction catalysts.

Chapter 4 discusses the photochemical CO_2 reduction processes catalyzed by multi-components systems, which involves two kinds of POM clusters, the pure and coordinated POMs, respectively. The pure POM with a typical structure of Keggin, $[PW_{12}O_{40}]^{3-}$, is combined with graphitic carbon nitride (g-CN) and bimetallic Re(I) compounds, ($[Re^{1}(bipyNNH_2)(CO)_3Cl–Re^{2}(bipy)(CO)_3Cl]$, bipy = 2,2'-bipyridine), forming a three-component hybrid construct. A combination method of DFT and CASSCF/CASPT2 calculations is adopted to explore the catalytic mechanism involving in proton-coupled electron transfer within CO_2 reduction coupled to hydrocarbon dehydrogenation reaction catalyzed by this hybrid catalyst. After absorbing visible blue light, the photosensitizer graphitic carbon nitride (g-CN) transfers electrons to the POM, which is driven by the energy difference of the LUMO levels of the two species. Then, the hydrocarbon substrate (cyclohexene or cyclohexadiene) is dehydrogenated due to the hole formation effect during the

photoexcitation of g-CN. This process is accompanied by the electrons transfer to the oxidized g-CN and protons to the reduced POM cluster. Under red light irradiation, the reduced and proton-rich POM releases two electrons and two protons to a bimetallic Re(I) compound ($[Re^1(bipyNNH_2)(CO)_3Cl–Re^2(bipy)(CO)_3Cl]$, bipy = 2,2'-bipyridine) to activate it to catalyze CO_2 reduction to CO. At the same time, the co-product, H_2O, is generated. Acting as an electron/proton shuttle, the POM cluster promotes hydrocarbon dehydrogenation by increasing the electron/hole separation upon photoactivation of g-CN and facilitates the transfer of electrons and protons to the Re catalyst for CO_2 reduction. The first electron released to the Re-complex is initially located on the $bipyNNH_2$ ligand and then transferred to the Re-5dz^2 orbital, which activates the coordination of CO_2. The combination of a strong interaction between the nearly degenerate d-π^* orbitals of the Re center and the $bipyNNH_2$ ligand, the low reduction potential of -0.77 eV and a shallow free energy barrier of +2.4 kcal mol^{-1} for CO_2 fixation makes the bimetallic Re compound one of the most promising catalysts for transforming CO_2 to CO.

Moreover, we also study the photoexcited behaviors of two novel coordinated clusters $[(Co_{13}O_8)(Nb_6O_{19})_6]^{31-}$ and $[Ni_{30}(OH)_{24}(Nb_6O_{19})_{10}]^{44-}$. By sharing the common oxygen ligands, two different types of metal-oxide clusters are bonded together where the core $[Co_{13}O_8]$ or $[Ni_{30}O_{32}]$ fragment is encapsulated by several peripheral $[Nb_6O_{19}]^{8-}$ fragments. To illustrate the electron tranfer mechanism during the process of reducing CO_2 coupled to oxidizing H_2O, the electronic structures of the two cooordinated clusters are examined with focusing on the orbital interaction between the core and peripherial parts. DFT calculations demonstrate that the core $[Co_{13}O_8]$ fragment is relatively independent to the $[Nb_6O_{19}]$ fragment due to the big gap between the MOs contributed by the two metals, respectively. Both HOMO and LUMO are located at the core $[Co_{13}O_8]$ fragment, which thereby is the catalysis center of the CO_2 reduction and the H_2O oxidisation. On the contrary, the core $[Ni_{30}O_{24}]$ fragment has considerable interaction with the $[Nb_6O_{19}]$ cluster, where the HOMO is mainly contributed by the $[Ni_{30}O_{24}]$ part while the LUMO is located at the orbital of Nb. The Ni empty orbitalis is slightly higher, implying the potential electron transfer from the Ni to the Nb cluster after irradiation. As a result, the CO_2 can be reduced by receiving excited electrons from the peripheral Nb cluster, although the possiblity where CO_2 is immediately reduced by the Ni centers can not be completely excluded. The H_2O is predicted to be oxidized by receiving the holes from the core Ni centers. Having revealed the interactions between the two reactive fragments provides in-

depth understanding on stabilizing coordinated metal-oxide clusters within molecular complexes, which points out that complexation of small metal oxide clusters whose structural motifs closely match those of solid-state crystalline analogues can bring the unique reactivities of the bulk materials into the flexible realm of molecular science.

The research in *Chapters 5* and *6* deal with ferroelectricity. *Chapter 5* presents how to approach the calculation of the ferroelectric polarization. Therefore, this chapter performs a detailed theoretical analysis on a common ferroelectric hybrid organic-inorganic perovskite (HOIP), (AMP)PbI_4 (AMP = 4-aminomethyl-piperidinium) to explain the coexistence phenomenon of ferroelectricity and spin-orbit interactions in HOIP materials, which may introduce new directions in the photovoltaic materials landscape. The calculated polarization and Rashba parameter are in excellent agreement with experimental values. A considerably large Rashba anisotropy that can be tunable by ferroelectric polarization is reported. Specifically, as polarization is reversed, not only the spin texture chirality is inverted, but also the major and minor axes of the Rashba anisotropy ellipse in *k*-space are interchanged – a pseudo rotation. A $k \cdot p$ model Hamiltonian and symmetry-mode analysis reveal a quadrilinear coupling between the cation-rotation modes responsible for the Rashba ellipse pseudo-rotation, the framework rotation, and the polarization. These findings could provide new avenues for spin-optoelectronic devices like spin valves or spin-field effect transistors (FET).

In *Chapter 6*, with the gained experience of computing polarization, the single-molecule ferroelectric property within the Preyssler-type POMs $[M^{3+}P_5W_{30}O_{110}]^{12-}$ (M = La, Gd and Lu) is explored by DFT calculations. Linked to one H_2O molecule, the cation (M^{3+}) encapsulated in the Preyssler framework cavity is off-centered, generating a permanent dipole essential for a ferroelectric ground state. Accompanied by a 180° rotation of H_2O, the switching of the M^{3+} ion between two isoenergetic sites on both sides of the cavity results in the inversion of the electric polarization with a calculated barrier of 1.15 eV for Gd^{3+}. The height of the barrier is in good agreement with the experimentally measured barrier for the Tb^{3+} ion, whose ionic radius is similar to Gd^{3+}. The total polarization value of the crystal is calculated to be 4.7 μC/cm² by the modern theory of polarization, which is close to the experimental value. Considering that the order of contributions to the polarization is M^{3+}-H_2O > counter cations (K^+) > $[P_5W_{30}O_{110}]^{15-}$ framework, the interconversion of M^{3+}-H_2O between the two isoenergetic sites with a contribution of 3.4 μC/cm² is predicted to be the primary origin of the ferroelectricity. The contributions of K^+ counter-cations with an amount

of 1.2 μC/cm^2 cannot be disregarded, whereas the framework appears to contribute negligibly to the total ferroelectric effect. Our study suggests that a suitable choice of the M^{3+}-H_2O could be used to tune the single-molecule ferroelectricity in Preyssler-type POMs. Finally, all main conclusions are summarized in *Chapter 7*.

UNIVERSITAT ROVIRA I VIRGILI
COMPUTATIONAL ANALYSIS OF THE CATALYTIC AND FERROELECTRIC PROPERTIES OF POLYOXOMETALATES
Fei Wang

Chapter 1. Polyoxometalates: Structures, Properties and Applications

UNIVERSITAT ROVIRA I VIRGILI
COMPUTATIONAL ANALYSIS OF THE CATALYTIC AND FERROELECTRIC PROPERTIES OF POLYOXOMETALATES
Fei Wang

CHAPTER 1

Polyoxometalates: Structures, Properties and Applications

This chapter is written for general audiences without specialized knowledge about polyoxometalates (POMs) chemistry and computational science. Here the basic background information about POMs, including structures, properties, and applications, especially in those fields related to the purpose of this thesis, will be explained. Moreover, the current research progresses on catalysis and ferroelectricity of POMs will be addressed. Mainly, focus shall be put on those studies performed through computations.

1.1 Introduction to polyoxometalates

Polyoxometalates (POMs) are molecular systems that belong to the class of medium-to-large-sized metal-oxide clusters ($[M_xO_y]^{q-}$) of *d*-block transition metals, like W, Mo, V, Nb, and Ta.[1] The first POM ($PMo_{12}O_{40}^{3-}$ anion) was reported by Berzelius in 1826 without declaring a well-defined structure.[2] Then the molecular composition of the POM cluster was proposed by Pauling[3] in 1929, and later Keggin resolved the X-ray structure of 12-phosphotungstic acid in 1933 for the first time.[4] However, systematic investigation on POM compounds did not start until the 1960s, which was further promoted by a review paper published by Baker and Glick in 1998.[5] Up to now, various examples with diversified structures, sizes and properties have been reported.[6] Notably, thanks to their overwhelmingly versatile nature in terms of charge distribution, electronic activity, and photochemistry, POM compounds possess numerous and remarkable properties, such as acid strength, redox reactivity, and bioactivity. These capabilities enable developing materials with specific properties in a controlled manner and use them in different research areas, for example, catalysis,[7] material science,[8] biomedicine,[9] *etc*. What is more, their physicochemical features can be purposefully modified by combining the POM with versatile blocks during synthesis processes, i.e. that, POMs can act as a well-defined platform to assimilate a variety of molecules for developing multifunctional materials.[10] In short, this class of compounds has attracted wide and long-lasting attention over the decades.

1.1.1 Structures and classifications

It is challenging to present all reported structures of this enormous POM family. Here we introduce their main structures and classifications by covering the basic building units, hetero-(or iso-)polyanions, the five classical structures and their isomers, as well as some common "lacunary" structures.

Building units: POMs, usually anions, can be described as aggregates of oxo species of early-transition metals with several bridging and terminal oxygen atoms. The basic building block of POM frameworks is the MO_n unit, as shown in Figure 1.1. Although MO_n units with n=4, 5,or 7 are present in some POMs, most structures are built by corner-sharing and/or edge-sharing MO_6 units.[11] Only in the rarest cases can also be constructed by face-sharing MO_6 units.[12] That is basically because he Coulomb repulsion between the addenda metal ions is weaker in the first two connection modes due to the much larger distance between them compared to the face-sharing mode. In the complete polyanions, the terminal O^{2-} ligands are doubly bonded to the addenda metals on account of $p\pi$–$d\pi$ interactions allowing electrons to transfer from the filly-occupied *p*-orbitals of oxygens to the unoccupied *d*-orbitals of transition metals, which are of great significance to stabilise of metal-oxide clusters.

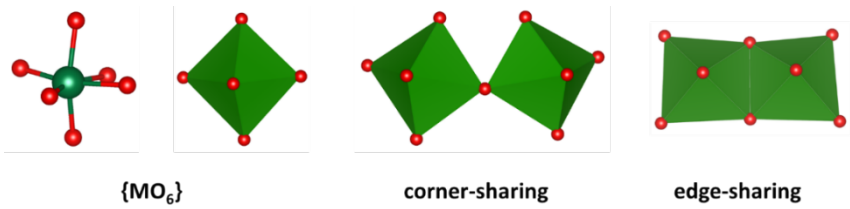

Figure 1.1. Ball-and-stick and polyhedral representation of the typical building $[MO_6]$ unit as well as two common coordination patterns. Color code: red for O and green for M.

Isopolyanions (IPAs) and heteropolyanions (HPAs): Although it has been almost two centuries since the first POM example was reported,[2] the structure and properties of numerous POM clusters were not determined until recent years when those work has received tremendous impetus from the significant advances of spectroscopic techniques and single-crystal X-ray diffraction. Since then, POM compounds have rapidly developed into an immense family. In a broad sense, they can be classified into two main types: those that contain a heteroatom X, hetero-polyanions (HPAs) with general formula $[X_aM_bO_c]^{q-}$ typically a < b < c, and those that do not, iso-polyanions (IPAs) with general formula $(M_aO_b]^{q-}$. The M atoms, usually

possessing a high positive charge, are called (peripheral) addenda atoms, whose coordination number with oxygens can alter from 4 to 6 by polymerisation in an acidic solution.[13] The X element is called the (central) heteroatom, which is either a main group element, such as Si, P, S, Ge, As, Se, B, Al, Ga and so forth, or also a transition metal, like Co, Ge, *etc*.[14] Properties of POMs can be remarkably affected by them. In principle, the selection of X atom is not limited. In contrast, the M atom is limited to certain metals, which are supposed to have a favourable charge/radius ratio and empty *d*-orbitals to bind with oxygen atoms. Therefore, only a few M elements are typically found constructing POMs, such as W, Mo, V, Nb with the d^0 or d^1 electronic configurations in their high oxidation states. In general, Mo- and W-based clusters with the octahedral $[MO_6]$ building units are more common as large aggregations.[15] By contrast, the vanadium metal centres with a wide variety of building units ranging from tetrahedral $[VO_4]$ to square pyramidal $[VO_5]$ and octahedral $[VO_6]$ units are more common in small- to medium-sized clusters, typically with between 4 and 30 vanadium centres.[16] In some cases, those addenda metals can be partly substituted by others, including Al, Ti, Cr, Mn, Fe, Co, Zn, Ni, Cu, Zr, Ru, Ln, *etc*.[17] resulting in POMs with more than one M addenda-type which are known as mixed-addenda clusters.[18]

IPAs are synthesised by Brønsted acid-base condensation–addition reactions in a solution containing the addenda metal oxo anions, e. g. VO_3^-, MoO_4^{2-} or WO_4^{2-}. HPAs can be acquired using the similar method but with the existence of a X atom in the form of oxo anions such as SO_4^{2-}, PO_4^{3-} or SiO_4^{4-}.[7a] The general formation reaction of POMs can be written as

$$x\mathrm{MO}_4^{2-} + y\mathrm{XO}_4^{\mathrm{n}-} + 2z\mathrm{H}^+ \rightarrow \mathrm{X}_y\mathrm{M}_x\mathrm{O}_{4x+4y-z}^{(2x+yn-2z)-} + z\mathrm{H}_2\mathrm{O} \qquad \text{(i.)}$$

in which MO_4^{2-} is an oxyanion, and $\mathrm{X}_y\mathrm{M}_x\mathrm{O}_{4x+4y-z}^{(2x+yn-2z)-}$ is an IPA when $y = 0$, or HPA when $y \neq 0$. Compared with IPAs, HPAs are usually more stable and amenable to chemical variation of the central template X, leading to a large structural variety. Therefore, HPAs in principle possess more potential applications ranging from catalysis to biological fields, which have already stimulated researchers' lots of interest in recent years, which will be explained in more detail in the following sections.

Five "classical" structures and isomers: During recent decades, a significant number of structures of POMs have been discovered, among which there are five classical types the most appealing to chemists and have been extensively studied. They are Lindqvist $[M_6O_{19}]^{q-}$, Anderson-Evans $[XM_6O_{24}]^{q-}$, Keggin $[XM_{12}O_{40}]^{q-}$, Wells-

Dawson $[X_2M_{18}O_{62}]^{q-}$ and Preyssler $[P_5W_{30}O_{110}]^{15-}$ (Figure. 1.2), entitled by the names of the scientists who deduced and resolved the structures.[19] They can also be described as clathrate-like molecular or supramolecular systems in which an external fragment encapsulates an internal fragment.[20] A molecular formulation for molecules satisfying the a clathrate-like arrangement was introduced in the manner of I@E, where I and E are the internal and the external units, respectively. Therefore, those classical structures can also be formulated as $[O]^{2-}@M_6O_{18}$ for Lindqvist, $[XO_4]^{q-}@M_{12}O_{36}$ for Keggin, $[XO_4]_2^{q-}@M_{18}O_{54,}$ for Wells-Dawson and $[PO_4]_5^{15-}@M_{30}O_{90}$ for Preyssler. This formulation indicates that the external M_xO_y core is formally neutral when the POM is completely oxidised. This viewpoint is beneficial in explaining some complex phenomena, like isomerism.[21]

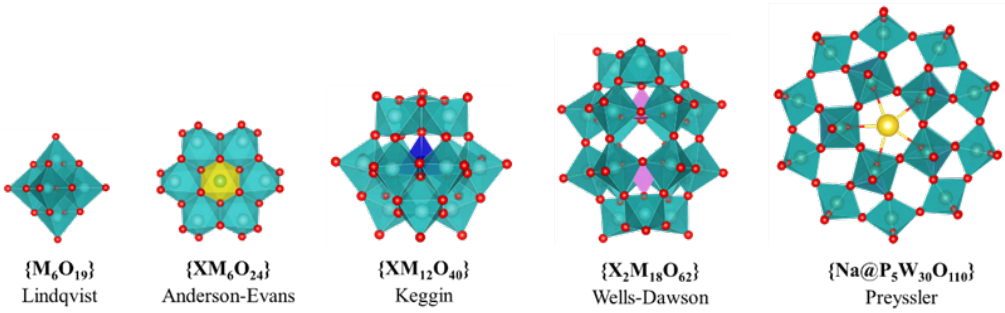

Fig. 1.2. Polyhedral representations of the five classical structures of POMs.

Speaking of isomerism, here only the isomers of the Keggin and Wells–Dawson types of POMs are discussed, the most basic and extensively studied clusters. Keggin archetypes with the formulation of $[XM_{12}O_{40}]^{q-}$ with a sole tetrahedral unit $[XO_4]^{q-}$ encapsulated in the centre of the cage $[M_{12}O_{36}]$ possesses the symmetry elements of the T_d symmetry point group. Then by stepwise rotating each of the four $[M_3O_{12}]$ triads, this structure can isomerise, generating α-, β-, γ-, δ-, ε-Keggin isomers, as shown in Figure 1.3.[22] Since the rotation of a triad shortens the distance of M-M increasing the Coulomb repulsion between them, the stability of the structure decreases with the number of rotated triads, being the alpha and beta isomers the most common isomers. The beta isomer is only slightly less stable than the alpha form. However, when it comes to the reduced forms, the rationalisation of the relative stability becomes more complicated and cannot be summarised in this simple way. With a topology of $[X_2M_{18}O_{62}]^{q-}$ and being described as the bonding of two Keggin-like XM_9 fragments, Wells–Dawson POMs display a combination of geometric and configurational isomerism.[23] Within it, there are two distinctive metal sites generally called the belt and

the cap sites, where two belts (M_6) constitute an M_{12} array by alternative corner- and edge-sharing MO_6 units near the equator place and two caps (M_3) in the polar areas are formed by three edge-sharing MO_6 octahedra.[24] Therefore, there are 8 distinct oxygen sites within the structure, showing differences on the basis of symmetry. By the rotating the caps (i) with eclipsed belts or (ii) with staggered belts one after the other, six isomers of Wells–Dawson POMs can be obtained (Figure 1.3).[25]

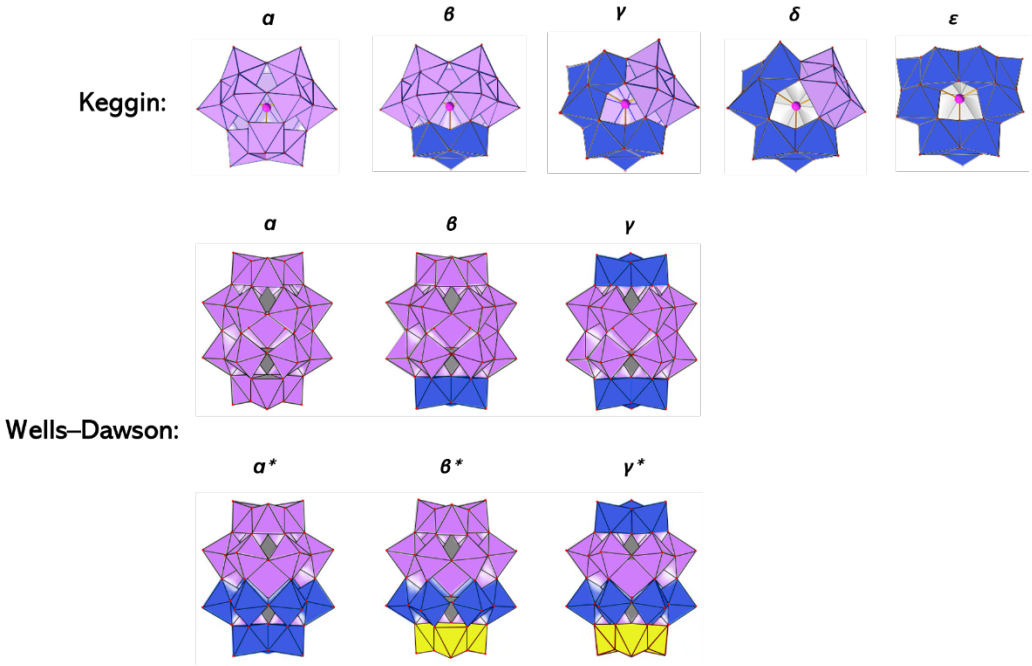

Figure 1.3. Polyhedral representations of the isomers of the Keggin and Wells-Dawson anions with highlighting the rotating units.

"Lacunary" structures: By removing one or more [MO_x] fragments from the complete (parent) POMs, so called "lacunary" structures can be formed, which are common precursors of functional POMs.[17b] While the complete POM clusters can exist stably in a solvent with pH ranging from neutral or slightly basic to strongly acidic, the lacunary systems remain stable only in a specific pH range.[26] By empirically adjusting the pH, temperature, reagent concentration and mixing ratio within solvents, a great amount of lacunary POMs have been constructed up to now.[27] Generally, lacunary structures derived from polyoxotungstates are more common than those of polyoxomolybdates and polyoxovanadates.[28] This is because the complete Keggin $[XW_{12}O_{40}]^{q-}$ and Wells–Dawson $[X_2W_{18}O_{62}]^{q-}$ clusters could be partly decomposed

through adding a weak base without destroying the parent topologies, and thereby form lacunary species, such as $[XW_9O_{34}]^{q-}$, $[XW_{10}O_{36}]^{q-}$, $[X_2W_{15}O_{56}]^{q-}$, and $[X_2W_{12}O_{48}]^{q-}$ (X = Si, P, Ge, As, *etc.*). With high negative charges and vacancies that act as coordination sites with different geometrical orientation, lacunary systems are incredibly reactive to a broad range of nucleophiles, including cationic or organometallic groups.[29] As a result, they can be used as rigid multidentate inorganic ligands to restore the corresponding parent structures or to build larger metal oxo clusters and hybrid materials, in which novel properties can be expected.[30] Two related examples are shown in Scheme 1.1, where the lacunary $[A\text{-}\alpha\text{-}PMo_9O_{34}]^{9-}$ cluster is used to restore a series of parent structures (1a) or to construct a larger POM-organic hybrid structure (1b) via a di-vacant lacunary $[\gamma\text{-}PMo_{10}O_{36}]^{7-}$ anion which is obtained by selectively transforming the pyridine-coordinated $[A\text{-}\alpha\text{-}PMo_9O_{34}]^{9-}$ in the organic solvent using a new ligand-directed method, proposed by Li and co-workers.[31] However, sometimes these lacunary POMs containing reactions might be accompanied by undesired condensation reactions due to their high reactivity caused by their low stability which increases the difficulty in controlling the product's selectivity, and somehow limits their application.[32] More details about the lacunary POMs will be discussed in Chapter 3.

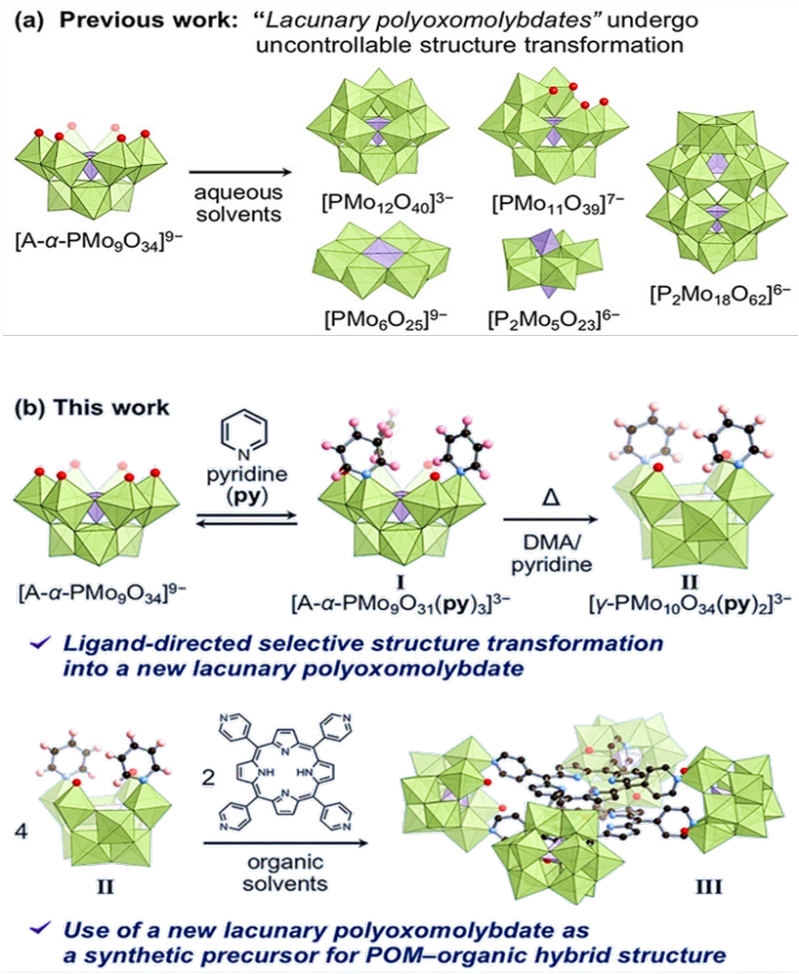

Scheme 1.1. Examples for restoring the related parent structures (**a**) and constructing a larger POM-organic hybrid structure (**b**) using the lacunary Keggin-POM as the building block. Taken from ref. 31.

1.1.2 General characteristics

POM species, including IPAs, HPAs and giant POMs,[33] have excellent acidic, electronic, catalytic, bioactive characteristics, and so forth. All these properties are relatively easily tuned in a controlled manner. As a result, they are being used and show significant potential to further increase their applicability in wide-ranging fields, like catalysis (homogeneous and heterogeneous catalysis, electrocatalysis and photocatalysis), material science, medicine, *etc*.

Acid strength: The majority of POMs are soluble showing the strong acidity in an aqueous solution, while their solubility degree in the organic solvent depends on media polarity.[34] Some acid-base equilibria in liquid media involving POMs as polyacids have been reported.[35] In most cases, their p*K*a is less than 0, indicating firm acidity, although they can be further protonated in a very acidic solution. Although experimental information is scarce, calculations have established that the basicity of the different oxygen sites is not identical, and hence, the (de)protonation capacity varies accordingly.[36] Thus, (de)protonation capacity also varies accordingly. Alternatively, the deprotonation energy (DPE), a theoretical metric available for solid acids, was proposed by Neurock and co-workers to reflect the ability of donating protons and thus the strength of Brønsted acids.[37] DPE was described as the energy for removing a H^+ from a neutral species to generate an anionic conjugate base ($AH \rightarrow A^- + H^+$). Thus, lower DPE numbers indicate stronger acidity. The more acidic a POM cluster is, the faster the deprotonation reaction is predicted to happen. Recently, Deshlahra *al. et* compared DPE values for different types of acids, including POM acids (W-POM and Mo-POM), mineral acids, and superacids, as seen in Figure. 1.4.[36] The DPE values of POM acids are lower than those of mineral acids and comparable to those of superacids, which fully demonstrates the strong acidity of the POM clusters. These calculational results are in line with the discovery of Kulikov and Khozhevnikov *et al.* that $H_3PW_{12}O_{40}$ showed a higher Hammett acidity constant (Ho) than that of $HClO_4$ or H_2SO_4.[38] The firm Bronsted acidity makes POM compounds better catalysts than mineral acids (such as, H_2SO_4, H_3PO_4) in some homogeneous catalytic reactions where proton transfer occurs. The corresponding kinetics and reactions mechanisms have been partly revealed by computational work regarding the basic steps, where the transition states are also taken into account.[39] The theoretical study on ether and alkanol cleavage reactions using POM clusters as Brønsted acid catalysts suggests that the energies of cationic transition states and intermediates are up to proton affinity of reactants, deprotonation enthalpy of the POM clusters and stabilisation energy of the ion-pairs in transition states or intermediates. Moreover, the stabilisation energy and the accompanying charge density and distribution in the anion rather than the DPE determine the kinetic tolerance of donors and the selectivity of reactions where POM clusters serve as catalysts.[39a]

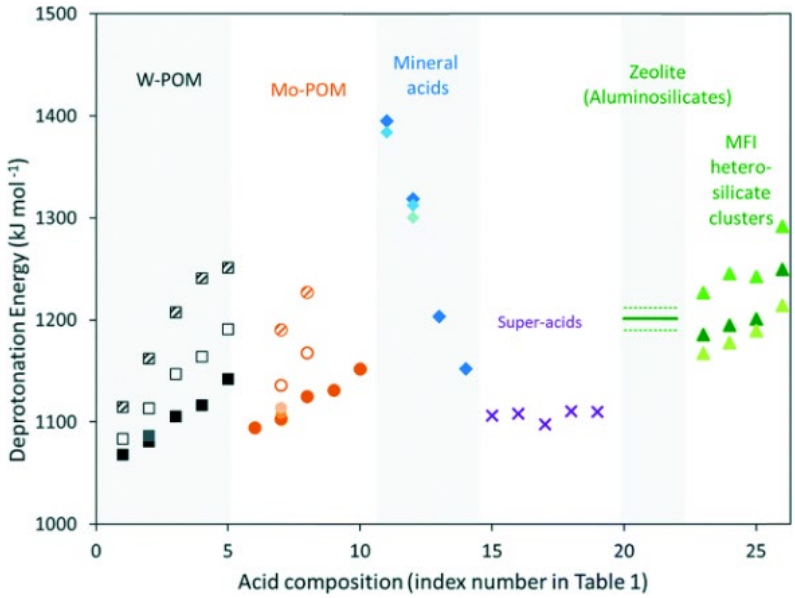

Figure 1.4. The calculated deprotonation energy (DPE) values for different types of Bronsted acids. Reproduced from ref. 36.

Catalytic activity: Relying on the ability to undergo reversible multi-electron redox processes and forming mix-valence species, the catalytic performance is considered one of the most powerful features of the POM family. They are able to catalyse a wide range of photo/electro-oxidation/reduction reactions, and many systems involving POMs as catalysts have been reported. As catalysts, they possess numerous advantages, the most prominent of which are the following: (i) strong Bronsted acidity approaching the superacid region; (ii) multiple protonation sites due to the abundant accessible oxygen atoms on the skeleton of the POMs; (iii) rapidly reversible multielectron transformations; (iv) high stability under harsh electrochemistry conditions or high photoactivity in the UV and near-visible region; (v) facile separation when using as heterogeneous catalysts. This property will be explained detailedly in the next section.

Biological activity: The potential use of POMs in medicine, such as anti-viral, anti-tumoral and anti-bacterial characteristics, has been demonstrated in recent years.[40] As one of the efficient inorganic medicines with low toxicity, POMs have drawn considerable interest in biomedicine science. The biological activity of POM was first discovered in 1970 when Chermann *et al.* reported that silicotungstic acid could act as a potent inhibitor of murine leukaemia and sarcoma viruses.[41] This finding

stimulated broad interest among scientists in exploring the antiviral effect of POMs. So far, their significant roles in inhibiting certain enzymes,[42] like α-glucosidase, tyrosinase, protein kinase or exonuclease, have been revealed, although the working mechanism at the molecular level is still unclear.[43] Apart from enzymes, POMs also have some inhibitory effects on the activities of nucleotidase, phosphatase, sulfate transferase, and others.[9]

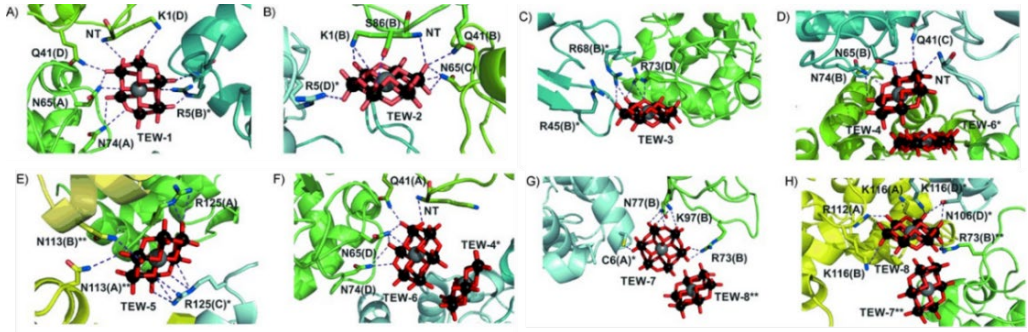

Figure 1.5. (A–H) Binding modes of all TEW ($Na_6[TeW_6O_{24}]\cdot 22H_2O$) molecules with protein side chains, binding sites. Adapted from the ref. 44.

Moreover, by being associated with some natural biomolecules, including proteins, peptides, and amino acids, hybrid POMs can take advantage of both moieties' features and thereby have improved bio-properties. Notably, almost all characteristics affecting the interplay between POM species with target biomacromolecules can be adjusted for improving favourable behaviours. However, it is challenging to determine those interactions because the structural complexities of both POMs and biomolecules inevitably result in highly complex interplays between them. For example, by using the X-ray structure determination, Bijelic *et al.* revealed numerous contact sites between TEW molecules ($Na_6[TeW_6O_{24}]\bullet 22H_2O$, an Anderson–Evans-type POM) and the egg-white lysozyme, as shown in Figure 1.5.[44] They interact by specific binding models through electrostatic interactions and hydrogen bonds. The TEW polyoxotungstate with negative charges are bonded to sites by a positive electrostatic potential between two (or more) symmetrical protein chains, which boots the formation of protein-protein interfaces of otherwise repulsive surfaces, hence realising a stabilizing crystal lattice. Currently, the research on those interactions has achieved remarkable progress through the joint efforts of experiments and computations. As summarised, it is found that redox potential, polarity, shape, surface charge distribution, and acidity are a set of fundamental features governing the interaction between target biomolecules and drugs in the medical or

biological/chemical fields. Hence, chemists can skilfully alter these features of POMs to suit the identification rules for medical applications. A comprehensive collection of the knowledge introducing POMs applications in the field of medicine is presented in these review publications.[45]

Other properties: As more novel POM structures are discovered, new properties and applications are also demonstrated. For instance, some POMs exhibit luminescent properties,[46] whereas other cases, such as the spherical keplerate (Mo_{132}), the cyclic (P_8W_{48}), the dimeric ($X^{III}_2W_{18}$) (X = As, Sb), and dimeric fused (Si_2W_{18}) types are reported to have unusual magnetic properties. The presence of 3*d* transition metal paramagnetic centers open the possibility for single molecule magnet behaviour, which can be possibly used in nano-computer storage devices.[47] Thus, they can be possibly used in some nano-computer storage devices, like single-molecule magnets (SMM);[48] A few potential green applications of POMs are also presented, such as a non-chlorine based, wood pulp bleaching process and a method of decontaminating water.[49]

1.1.3 Functionalization

In recent years, nanocomposite materials' design, fabrication, and functionalisation have received much attention. The combination of being highly charged, showing a tunable architecture, and being formed by self-assembly indicates that POM frameworks own great potential to develop nanocomposite materials with multiple length scales.[50] In addition, various reactive multidentate lacunary POM species generated by the selective removal of addenda atoms through hydrolysis offers limitless synthetic modifications prospects.[51] As reported, POM frameworks are able to contain inorganic, organic as well as organometallic groups, producing hybrid materials with improved properties.[10a, 46] The synthesis of such hybrid materials requires several processing steps. Different synthetic strategies have been developed to deposit POM onto scaffold materials. The three common and straightforward fabrication methods are chemisorption to a surface, , layer-by-layer self-assembly and immobilisation in a polymer matrix. The details about those three methods are beyond the scope of this computational thesis are not explained here. If readers are eager to acquire more knowledge about them, this review work is recommended where the advantages and disadvantages of these three methods are discussed.[52]

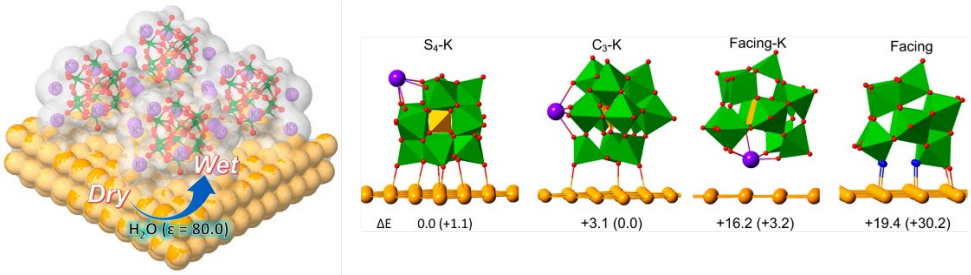

Figure 1.6. The structural representations for the PW_{11} cluster deposited on the Au(100) surface. Taken from ref. 54.

Not only countless experiments have been performed to investigate the POM-hybridisation, but theoretical chemists have also made great efforts in this field. Computational simulations are a powerful tool to gain insight into the interactions between POMs and associated substrates or scaffold materials, especially when the result is not intuitive or even counterintuitive.[53] For example, based on DFT calculations, Lang *et al.* found some results exactly contrary to expectations when studying the absorption of a lacunary $[PW_{11}O_{39}]^{7-}$ (PW_{11}) cluster with high charges onto the gold (or silver) surfaces.[54] According to the calculated interaction energies of the different absorption modes shown in Figure 1.6, the more nucleophilic mono-defect face of the PW_{11} cluster is not the favourable side to interact with the gold surface but the side featuring terminal oxygen ligands with less negative charges, with an orientation similar to that found in the non-defective Keggin anion $[SiW_{12}O_{40}]^{4-}$. The authors speculated that it is caused by the strong anion–cation interactions from the same and neighbouring units. Later, Muñiz summarized those computational work on the solid-state systems based on POMs grafted on carbon substrates and reviewed different types of interactions, including the covalent bonding between the PMo_{12} cluster and cristobalite, the non-covalent attraction of the electrostatic-type at the interface POM/graphene, and the inverse charge transfer in system PMo_{12} adsorbed on a CNT in the presence of $(C_4H_9)_4N^+$.[53] In a general sense, the POM-based-hybrid systems can be separated into two main types according to the driving force of construction: i) a weak nonbonding interaction between the two parts, like electrostatic, hydrogen bonds, and van der Waals interactions; ii) a more vital bonding interaction (covalent or mixed-ionic-covalent) takes place, including the organic ligands permitting a direct substitution of oxo group of the POM clusters, like alkoxides, carboxylates, organosylil derivatives, and so forth.

However, we have to point out that there are still some problems within this field

that require our full attention to improve our understanding and finally resolve these long-standing issues. From the experimental point of view, one major challenge is to develop general methods or hybrid sample-preparation techniques to construct nanoscale functional architectures based upon these versatile building blocks. The difficulty is that several factors have to be considered simultaneously, including the constituents, sample preparation, environment, *etc*.[55] The problems for theoretical studies include accurately modelling the interactions for those nanoscale systems and describing the solvent effects that may appear in aqueous media. In fact, these two problems widely exist in theoretical simulations, which we will explain in detail in Section 1.4.

1.2 The classical catalytic performance of POMs

The ease of modifying the multi-electron redox characteristics, their acid-base properties and the tremendous amount of tunable topologies at the molecular level explains the pivotal status of POMs in the field of catalysis.[56] Their plentiful catalytic activities have been extensively investigated for many years, although interest in their properties in medicine, magnetism, and luminescence are also increasing.[57] The rapidly growing number of published articles involving POMs as catalysts per year in the past three decades is summarized in Figure 1.7.

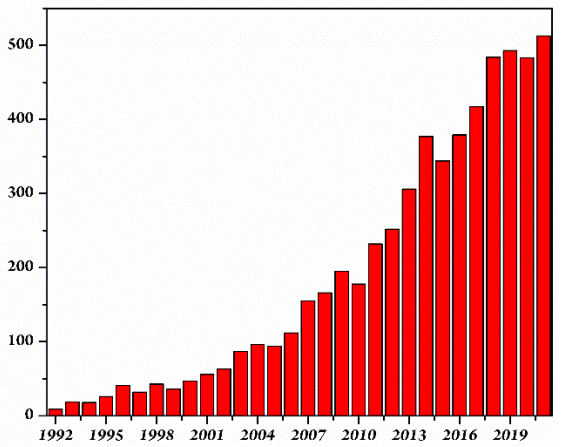

Figure 1.7. The number of published articles involving POMs as the catalysts in sorts of chemical reactions per year over the past three decades. Data is from "Web of Science" by simply entering "polyoxometalate*" and "cataly*" in the search box.

The catalytic activity of the POMs is (at least in part) explained by their outstanding redox properties, as the capacity to provide electrons is one of the most critical factors influencing the efficiency of catalysts. Actually, certain POMs can accept and release such a large amount of electrons that they are considered to work as electron sponges.[58] The redox behavior of the POMs is mainly originated from two factors. On the one hand, there are many oxygen atoms on the surface which are capable of donating electrons. Therefore, POMs can act as Lewis's bases. On the other hand, numerous transition metals in the highest state within the structure, typically in the electronic configurations of d^0 or d^1, have empty orbitals to accept electrons, making POMs can also be recognized as Lewis's acids.[1b] They can afford different oxidation states without decomposing or changing their structural arrangements,

showing high stability under harsh working conditions. In general, POMs can be used as redox-active materials for all sorts of chemical reactions,[7a, 59] in which their catalytic performance depends on (i) the type and number of transition metals in the framework, (ii) the basicity of the first reduced species; (iii) the size of the cluster, (iv) the overall negative charge, and (v) the size of the central heteroatom.[21b] Compared to common organometallic complexes, they are oxidatively, thermally, and (over wide and adjustable pH ranges) hydrolytically stable.[60] Therefore, POMs have already been considered as one of the most promising catalysts for a number of acid and redox reactions, and some POM-catalyzed processes involving organic substrates have been commercialized.[61]

1.2.1 Applications in photo-catalyzed reactions

It is well known that there are plenty of photochemical activities in POM compounds due to their excellent UV-light-responsiveness. The powerful photoinduced charge-transfer properties and acid-base activities allow them to catalyze a variety of reactions in which incoming sunlight is transformed into useful chemical energy. As a result, POMs are often described as eco-friendly photoactive materials and a hopeful way to mitigate the energy crisis.[8b, 62]

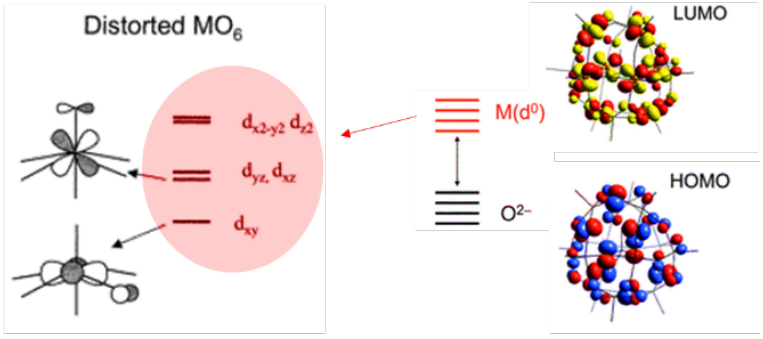

Figure 1.8. Molecular orbitals scheme of a α-Keggin anion. Adapted from ref. 65a.

Photochemistry: Over the past decades, many concepts illustrating the unique catalytic behaviors within POM compounds in the photo-redox reactions have been proposed.[59, 63] In photocatalysis, optical band gaps and band edge positions are of significance to the selectivity and efficiency of a particular photo-redox reaction.[64] Because of ideal redox potentials and multi active sites, POM compounds demonstrate exceptional photocatalytic characteristics. As shown in Figure 1.8, the optical absorption process of a typical POM anion primarily corresponds to the transitions

from the occupied O-2*p* band to the unoccupied M-*d* band. Characteristic wave lengths for these band-gap transitions fall in the 200-500 nm range for many POMs, having a good overlap with the solar spectrum.[65] The ligand-to-metal electrons transfer (LMCT) generates a CT excited state that nominally comprises a reduced metal center and a cation radical at the oxygen donor.[66] Hence, the photoexcited species is highly reactive and can serve as better oxidizing agents with a higher electron affinity E_{ea} and better reducing agents with a lower ionization energy E_i than the ground state species.[7b]

Single-component system: Although the first research on the photocatalytic activity of POM clusters was reported more than 100 years ago, the comprehensive work on their photochemistry began in the early 1970s when Yamase *et al.* observed the H_2 formation accompanied with photoreduction of molybdates in aqueous solution[67] and similarly, Savino and co-workers demonstrated H_2 evolution in the presence of $SiW_2O_{40}^{6-}$.[68] Later, Papaconstantinou's group examined these processes in detail and reported the reduction rates of several POM clusters by a variety of radicals produced by ^{60}Co-γ-radiation.[69] In 1985, Hill *et al.* provided the first overview of the vast scope of POM-catalyzed photooxidation of organic compounds. By emphasizing the underestimated photophysical and chemical phenomena within these highly complex redox processes,[70] this work played a crucial role in promoting the development of the POMs photochemistry. Inspired by the predecessors' work, a large number of POMs-based photocatalysts have been synthesized, from which many photocatalytic systems have been constructed in the past few decades.[71] Traditional photocatalytic systems are single-component systems where both light absorption and target molecule catalysis are performed by the sole POM cluster. In multi-component photocatalytic systems these processes take place at different moieties and will be discussed in the next section. Especially, with the growing importance and urgency of developing sustainable clean energy to restrict carbon emissions, POMs have been used in a range of photo-redox reactions with direct environmental influences, such as H_2 evolution (water oxidation or O_2 evolution),[72] CO_2 reduction,[73] and organic pollutants degradation.[74] With the rapid development and broad application of POM-type photocatalysts in experiments, numerous theoretical studies have been carried out to reveal the photocatalytic mechanisms.[75] Theoretical chemists study photo-redox reactions in detail by decomposing the entire redox process into several individual steps, which generally includes: (i) activating the POM by irradiation generating excited electrons or holes; (ii) fixing the target molecule onto the excited

POM cluster; (iii) electrons transfer, sometimes coupled with protons transfer; (iv) forming and dissociating products and (v) recovering the POM.[76]

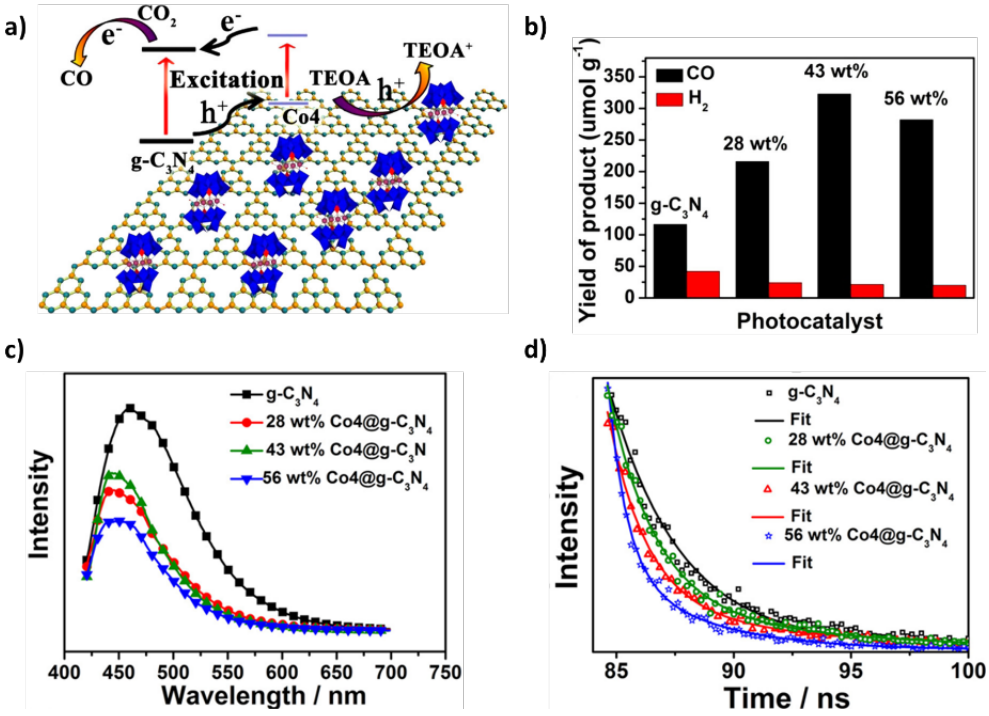

Figure 1.9. a) Schematic illustration of the transfer process of electron-hole pairs; **b)** photocatalysts of pure g-C_3N_4 and composites with different Co_4 content; **c)** Steady-state PL spectra; **d)** Transient PL decay for pure g-C_3N_4 and composites. Adapted from the ref. 81.

Hybrid-construct system: Recently, due to the weak visible spectral absorbance and poor overlap with the solar spectrum of some POM compounds, especially the polymolybdates, the idea of linking POMs with efficient photosensitizers is proposed. The hybrid systems are generally formed by covalent bonds or electrostatic couplings, in which absorbing light and catalyzing a reaction are assigned to different moieties to enhance the light-harvesting.[77] The relative energies of the bands of the two moieties, with lower energy levels at the catalysts, facilitates the photosensitizer to transfer photogenerated charges to the redox-active POM cluster.[50, 78] Then, the reduced POMs acts as "electrons shuttle" and releases electrons to the target molecule.[79] Therefore, this mode of "division and cooperation" substantially improves the overall catalytic efficiency by increasing both the light absorption and electron transfer processes. Since carbon nitride (g-C_3N_4) is a common photosensitive material,[80] Zhou *et al.* first combined it with a noble-metal-free POM (Co_4) with the oxidative ability for

obtaining inexpensive hybrid materials (Co_4@g-C_3N_4), as shown in Figure 1.9a.[81] By optimizing the Co_4 content, the hybrid samples showed a superior performance for CO_2 reduction and higher selectivity for CO production than the bare g-C_3N_4 (seen in Figure b). The mechanistic studies based on steady-state and transient photoluminescence spectra (Figures c and d) reveal that the charge transfer between the Co_4 cluster and the g-C_3N_4 is enhanced, and thereby the surface catalytic oxidation ability is promoted. The complex kinetic process of the direct photochemical electron transfer from the photosensitizer to the POM cluster in a hybrid-construct system is also studied. What has been found is that the whole process is ultrafast (occurring at the femtosecond level), regardless of the transfer process is intramolecular or intermolecular.[82] For instance, Hill *et al.* observed that optical excitation resulted in an instantaneous (<50 fs) electron transfer from the Re^I center to the POM ligand, as shown in Figures 1.10a and b evidenced by the almost immediate appearance of a Re^I-to-POM charge transfer (MPCT) band.[83] To understand the electron transfer mechanisms of the organic-functionalized POMs, Gao and co-workers examined the pyrene-grafted POM hybrid by combining experimental and theoretical methods. After the strong electronic absorption in the visible region attributed to the optically allowed π–π* transitions of the pyreneimido component (S_0 to S_2 transition), the excited electron would transfer to the POM species within ~700 fs, attributed to the fast internal conversion of singlet excited states from S_2 state to S_1 state (Figure 1.10c).[84] These kinetic studies could offer a new route for designing POMs-based hybrid construct systems involving the electrons transfer process and crucial guidance for future optical and electrical device applications.

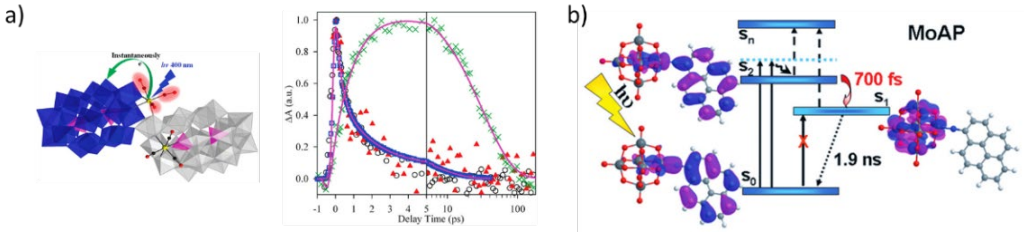

Figure 1.10. a) the structural representation (left) and transient kinetics and the delay time (right) of $[P_4W_{35}O_{124}(Re(CO)_3)_2]^{16-}$. Adapted from ref. 83. **b)** Schematic illustration of the charge transfer pathway within the pyrene-$[Mo_8O_{26}]$ hybrid. Reproduced from the ref. 84.

Challenges: The development of the POMs-based photocatalysts is always accompanied by various challenges. One major challenge is to close the photocatalytic cycle efficiently, particularly the recovery of the POM cluster, which could be rate-

determining in some cases.[85] Some researchers proposed to use excess O_2 as the re-oxidant to restore the POM catalyst under ambient conditions.[86] However, this process is usually demonstrated kinetically slow or thermodynamically unfavorable within some original POMs systems.[87] As reported, protons can also be used to recover the POM anion with yielding H_2 without the presence of oxygen.[88] Moreover, the addition of photosensitizers and/or sacrificial agents for maintaining the catalytic reaction cycle could cause the heteromerization of POM clusters when they are crystallized.[59] This is also a big challenge for the practical application and product separation and needs to be significantly improved in the future.

1.2.2 Applications in electro-catalyzed reactions

With the increasing popularity of POM clusters in the field of electrochemistry, many efforts have been made to optimize their electrocatalytic performance, especially to improve the conversion efficiency from electric energy to useful chemical reactivity.[89] Several reviews on the use of POMs in the electrochemical process are published,[7a, 73b] in which strengths of POMs as electrocatalysts are summarized: (i) the multiple active sites within their crystal structures; (ii) the excellent redox capability being able to reversibly store multiple electrons without structural deformation; (ii) abundant and inexpensively available materials.[19, 89a, 74b] Therefore, in 2020, Li et al. concluded that POMs would be very appealing and promising electrocatalysts for various chemical reactions.[59]

Active sites: Multiple active sites within POM-based catalysts contain protons, oxygen atoms, and metals, which make them able to catalyze varied reactions, like C-C cleavage,[90] hydrogen peroxide activation,[91] and so on. Protons can improve acid-catalyzed responses acting as Brønsted acids .[92] Abundant oxygen atoms on POM skeletons, particularly those on the exposed sites of the highly negatived lacunary POM structures, are basic enough to react with protons, even to extract protons from organic complexes. Hence, these surface oxygens is considered as the active sites in base-catalyzed reactions. Nevertheless, the most majority of interest is put on the metals of POMs frameworks.[57a, 88b] The energy levels of LUMOs of those metals used to accommodate extra electrons are directly related to redox potentials, which is one of the most vital factors that has to be considered when designing or selecting the catalyst for an electrochemical process. As shown in Figure 1.11,[73b, 93] the structural diversity of POM compounds gives rise to a wide range of LUMO levels resulting in the various

redox potentials. This advantage not only enables them to catalyze a large number of electrochemical processes but also facilitate their synergy with other electroactive species for higher efficiencies.[94]

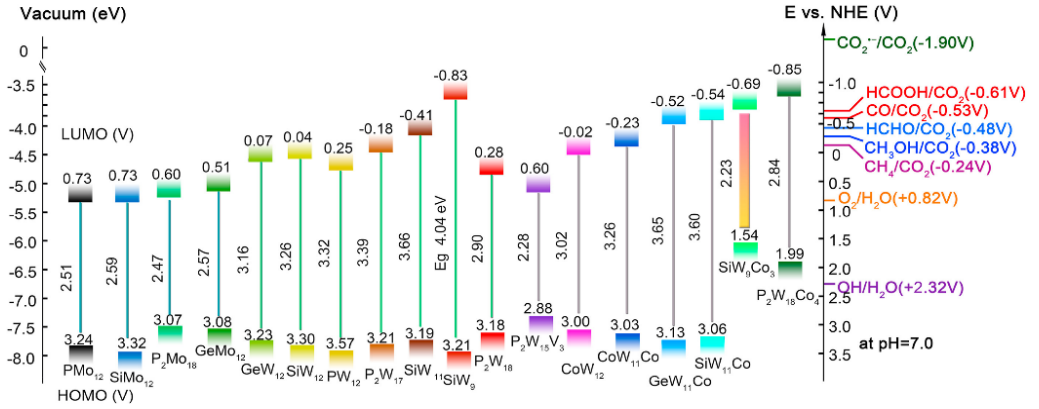

Figure 1.11. The schematic illustration of calculated energy levels of HOMO and LUMO and the corresponding gap of a series of POM clusters in eV. The redox potentials versus normal hydrogen electrodes (NHE) are presented here. Taken from ref. 73b.

Redox potentials: Although the redox potential can be determined experimentally in a relatively simple manner, uncovering relationship with composition and electronic structure needs in-depth theoretical analysis. It is a complex and challenging topic due to the quantification of potentials, which will be explained more in Section 1.4. Computational researchers working on POM-electrochemistry have devoted themselves to revealing the connection between redox potentials with charges (q), masses (m), volumes (v), electronic structures *etc.*, hoping to capture the most crucial factors. In 2006, Lopez and his colleagues studied the redox properties of a series of POMs using DFT to summarize the possible parameters influencing potentials.[20] They found a linear dependence between the difference in LUMO energies within the neutral and charged clusters and the q/m ratio by calculating the electronic structures and reduction energies. In the following year, the same group identified the effect of the encapsulated X^{q+} cation (X = Na^+, Ca^{2+}, Y^{3+}, La^{3+}, Ce^{3+}, and Th^{4+}) inside the Preyssler frameworks $[X^{q+}P_5W_{30}O_{110}]^{(15-q)-}$ on the redox behaviors.[95] A linear relationship between the first one-electron reduction energies and the encapsulated X^{q+} charge with a slope of 48 mV per unit charge was reported by them. They pointed out that more positive values for the reduction potential were obtained when the POMs were protonated. These computing results were in good agreement with the experimental observations on the one-electron reduction of

Keggin-type POMs, $[XV^{V}M_{11}O_{40}]^{4-}$ (X = P, As; M = Mo, W) in acetonitrile with the techniques of voltammetric and EPR studies by Nambu *et al.*[96] All voltammetric and spectroscopic data indicated that the V^{V} and V^{IV} redox chemistry were coupled to the protonation reactions, concluding that the reduced V^{IV} state is much more basic than the V^{V} one. So far, it has been generally known that the reduction process of POM anions is usually accompanied by the protonation of the produced anions because the reduction raises the negative charge density at the POM clusters as well as the basicity. Therefore, the potentials of the reversible redox pairs of POM clusters are considerably influenced by the pH (or protonation degree). Moreover, both Sartorel's and Niemiec's groups agree that the heteroatoms within the POM frameworks could also affect the redox potentials. Sartorel's group observed that the different heteroatom of in the clusters of $Ru(DMSO)PW_{11}$ and $Ru(DMSO)SiW_{11}$ lead to the different cyclic voltammograms curves and thus the corresponding redox favorable path (Figure 1.12).[97] Apart from that conclusion, Niemiec *et al.* also proposed that a total energy interaction (ΔE_{int}), calculated between the internal tetrahedron (XO_4^{n-}), and the rest of the Kegging anion skeleton, could be a proper theoretical parameter to reflect the oxidizing ability of the Keggin-typed tungsten and molybdenum systems modified in the central ion position by investigating their electronic structures through the DFT calculations.[98]

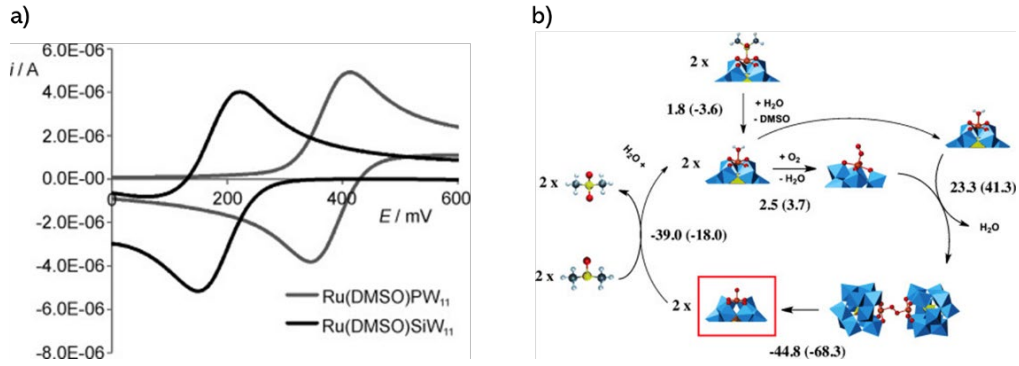

Figure 1.12. a) cyclic voltammograms of $Ru(DMSO)PW_{11}$ and $Ru(DMSO)SiW_{11}$; **b)** calculated the favourable path for reducing NO to N_2. Taken from ref. 97.

Performance enhancement: Except that the potentials and catalytic behaviours of pure POM-molecular clusters are evaluated, those of hybrid materials obtained by combining POMs with other functional groups or supramolecules constructed by POM clusters self-assembly are also considered.[99] The research on those constructs is very topical in synthetic chemistry and material science.

Hybrid materials are commonly recognised to benefit from the characteristics of each component and thereby gain enhanced performance. For example, combining POMs with organic ingredients can feature both inorganic frameworks (strength, thermal stability, and chemical resistance) and organic groups (lightness, flexibility, and versatility). The enhanced properties cannot directly be extrapolated from the chemical nature of each individual constituent, but strongly depends on the synergism between these, as reported by Wang and co-workers.[100] They designed a series of POM-metalloporphyrin organic frameworks by integrating $[\varepsilon\text{-}PMo_8VMo_4^{VI}O_{40}Zn_4]$ cluster with metalloporphyrin (Figure 1.13) and observed that these hybrid systems have excellent electron collecting, donating, and migration properties that greatly facilitate the CO_2 reduction reaction. The calculated mechanism reflected that those frameworks could catalytically reduce CO_2 with a lower energy barrier than the pure POM cluster. This molecular-level combination provides one of the latest directions in materials science, pointing to the possibility of developing multifunctional materials based on performance tuning.

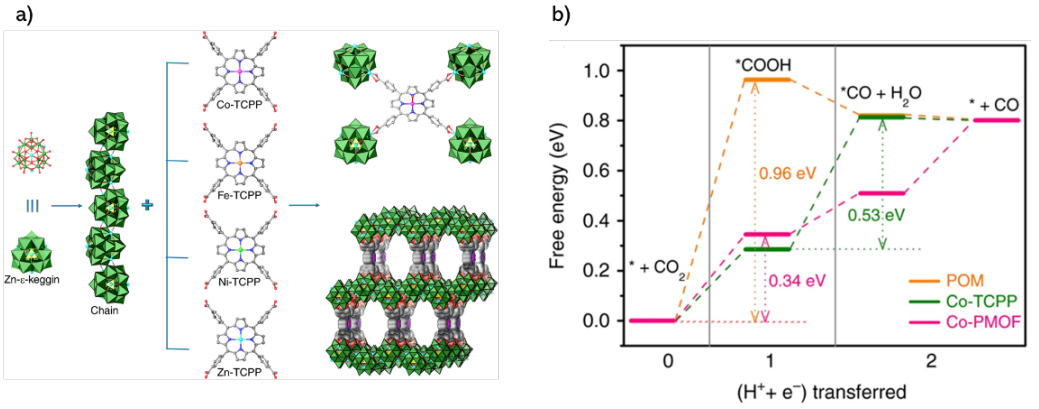

Figure 1.13. Schematic illustration of the M-PMOFs structures. (**a**) and corresponding CO_2 reduction mechanism (**b**) by the hybrid compounds proposed by DFT calculations. Adapted from ref. 100.

POM-based supramolecules also with characteristical structures and unique features, drawing growing interest in the decade. Figure 1.14 is an example of a supramolecular assembly formed by a Wells–Dawson hybrid molecule $H_6[P_2W_{17}O_{57}(H_{27}C_{17}O_4PS)_2]\bullet 3C_4H_9NO$, in which the electrochemical states of the conjugate and the individual molecules are compared.[99b, 101] In water, the hybrid forms regular micellar assemblies which exhibit reversible redox chemistry (Figure 1.14b and c) although addition of DMF leads to the disruption of the supramolecular species.

This transformation from the molecular to the supramolecular/nano materials with enhanced physical properties provides a chance to develop new environmentally friendly species in the field of catalysis. However, due to their large size, quantum calculations are far from trivial, so an in-depth understanding is still needed.

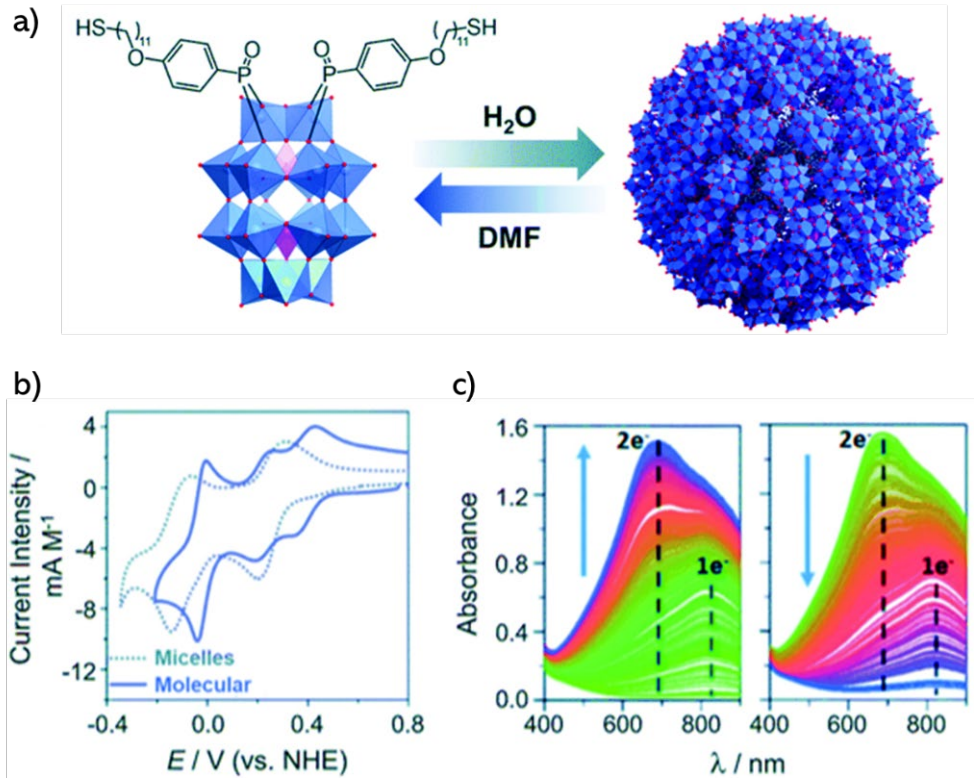

Figure 1.14. a) Structure of the molecular POM cluster species and the hybrid micelles; **b)** cyclic voltammograms; **c)** spectro-electrochemical analysis showing reduction and reoxidation. Taken from ref. 99b.

Challenges: Although both experimental and theoretical work has made outstanding achievements on POM electrochemistry, some problems are also reported when applying POMs as the catalysts, which can be summarized as follows: i) limited structural stability under the electrocatalytic conditions, including aggregation, precipitation, loss of activity and difficult separation when used in homogeneous catalysis;[102] ii) poor catalytic performance due to impoverished mechanical and electrical connection between POMs and electrodes resulting in leakage during operation and high electrical resistance;[103] iii) poor electronic conductivity (most of POM assemblies are insulating); iv) the large crystal size of them requiring grinding to

prepare electrodes; v) one major challenge existing in the hybrid catalysts is to develop the general functionalization routes for stable, long-lived materials.[104] The future electrochemistry study on POM compounds should focus on solving these issues.

1.3 The emerging ferroelectric property in POMs

Hitherto, most studies have focused on the (electro)catalytic capabilities, bioactivities and frameworks extension for functionalization of the POM species. However, recently, Nishihara and co-workers reported the first example of POM clusters exhibiting single-molecule electric polarization switching that could operate above room temperature, called a single-molecule electret (SME).[105] As shown in Figure 1.15, the Preyssler cluster $[Ln^{3+}@P_5W_{30}O^{110}]^{12-}$ (Ln = Tb or Er) studied by Nishihara and co-workers displayed all the characteristics of ferroelectricity but without long-range dipole ordering. It was assumed that the SME affords bi-stability as a result of the two potential positions of localization of a Tb^{3+} ion trapped in the POM, leading to prolonged relaxation of the polarization and electric hysteresis with high spontaneous polarization and coercive electric fields. The report of ferroelectricity in the POM compound implies that the wide range of promising properties of single-molecule Preyssler-type POMs can be explored to develop quantum devices and computers operating at room temperature.

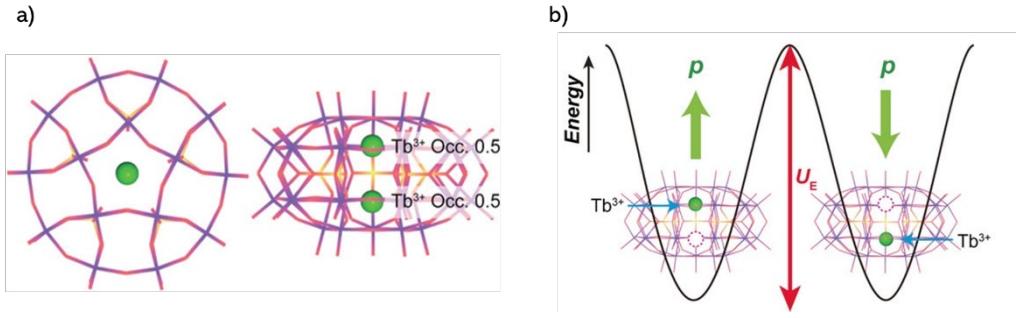

Figure 1.15. a) Top and side views of the structure of the Preyssler cluster $[Tb^{3+}@P_5W_{30}O^{110}]^{12-}$; **b)** schematic representation of the double-well potential structure of the dipole moment with an energy barrier. Adapted from ref. 105a.

While experimental studies have detected the ferroelectric phenomenon of Preyssler systems, some points still need further clarification for a complete description of the origin of FE in the Preyssler-type POM clusters. For example, several published experimental works claimed that $[M^{n+}@P_5W_{30}]^{(15-n)-}$ (M = Na, Ca, Y, Ag and Bi) were observed in the presence of a water molecule inside the cavity linked to the M^{n+} ion by X-ray and EXAFS studies.[106] However, it is not clear whether there is a water molecule bound to the Ln^{3+} cation inside the central cave of those ferroelectric POM clusters, which certainly influences the cation's interconversion between the two

isoenergetic sites. Moreover, on account of the relatively high charge of the Preyssler anion, quite a few counter-cations are supposed to present in the crystal, which is closely associated with the redistribution of charges and may play a role in the polarization switching. Therefore, attributed to the complexity of the Preyssler-POM systems, in-depth analysis on the microscopic mechanism at the origin of this "single-molecule" ferroelectricity is lacking and necessary for unravelling the mysteries that haunt the ferroelectricity of POM compounds. Since ferroelectricity is a brand new and uncharted area for POM chemistry, the basic knowledge includes the definition, nature, origin of ferroelectricity, the common ferroelectrics, and the modern ferroelectricity theory used for computing the polarization will be presented here.

1.3.1 What is ferroelectricity?

Ferroelectricity is a characteristic usually existing in insulator materials. It can be described as the spontaneous polarization (P_s, defined as the separation of the center of positive and negative electric charge, making one side of the crystal positive and the opposite side negative) that can be reversed by inverting the direction of the applied electric field (E).[107] The reversal of polarity can be retained even after switching-off the electric field, which is called remanent polarization (P_r). Since it is the macroscopic manifestation of the microscopic P_s, it is often measured in experiments to represent the P_s, although it should in principle be slightly less than P_r. The other two terms closely related to ferroelectricity are the Curie temperature and paraelectric phase. The Curie temperature (T_C) is defined as the temperature at which a phase transition occurs from the ferroelectric phase with non-zero P_s to a paraelectric phase where the P_s is lost.[108] All concepts mentioned above are illustrated in Scheme 1.2, where P_r is also approximately equal to P_s. Typical ferroelectrics with switchable P_r display exciting features such as the long-range ordered domain structure and unique hysteretic behavior,[109] which is also explained in Scheme 1.2.[110] In 1921, J. Valasek recognized the ferroelectric property in the Rochelle salt for the first time,[111] no more ferroelectric materials were found until G. Busch, and P. Scherrer in 1935 observed the ferroelectric behavior in Potassium dihydrogen phosphate (KDP, KH_2PO_4) below 122 K.[112] Since then, research on ferroelectric phenomena, including the physical and chemical origins, switching kinetics, as well as applications, are rapidly developed and flourished, as summarized in recent reviews.[113] Up to now, many good examples of ferroelectrics have been demonstrated, like $BaTiO_3$,[114] lead zirconate titanate (PZT),[115] polyvinylidene fluoride (PVDF)[116] *etc.* Those materials can provide outstanding

dielectric, piezoelectric, and ferroelectric properties.[117] By coupling with optical, electronic, magnetic, and mechanical characteristics, they have been proven to be one of the most promising candidates in the field of optoelectronics,[118] spintronics,[119] information storage[120] and sensing.[121]

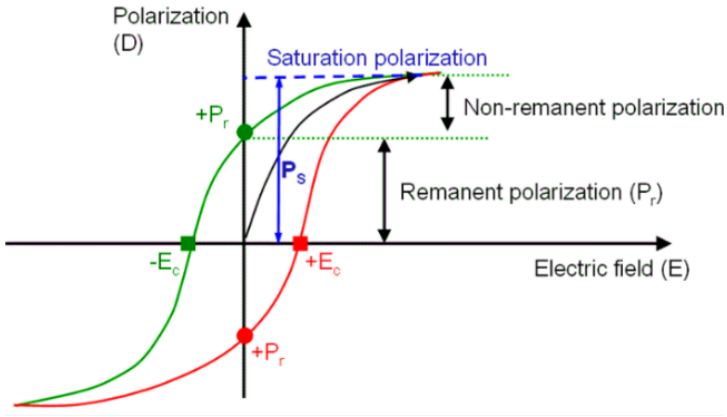

Scheme 1.2. A typical hysteresis loop as well as the corresponding structural characters. Adapted from ref. 110.

1.3.2 Common ferroelectrics — Perovskite

Traditional pure perovskite: Perovskites are popular ferroelectrics and have attracted enormous attention owing to their excellent ferroelectric performance.[122] Perovskites are crystals with a structural formula ABX_3, where A and B are metal cations of different sizes and X is an anion coordinated to B, such as $PbTiO_3$ and $BaTiO_3$.[123] Figure 1.16 describes the generic crystal structures of the cubic phase of a perovskite. The commonly accepted mechanism for the origin of ferroelectricity within perovskite materials is the atomic displacement, also called displacive type transition, signifying that the P_s results from ions collectively displaced from their equilibrium position. In general, this type of P_s decreases the stabilities of the crystal structure, leading the material into a polar state dominated by lattice deformation.[124] With extensive and in-depth analysis on the multitudinous robust performances of perovskites, they are found to hold great potential in the various fields of non-volatile memory,[125] thermistors,[126] oscillators,[127] capacitors,[128] filters[129] and so on.[122c, 130] However, every coin has two sides. There are also some drawbacks to their applications. Two major points often mentioned are that the processing of perovskites-based ferroelectrics usually requires high temperatures, and many of these

materials contain expensive and rare-earth metal elements, causing additional environmental and cost issues.[131] Hence, exploring novel ferroelectric materials with excellent properties but relatively simple processing is of great significance for a new generation of ferroelectric devices.

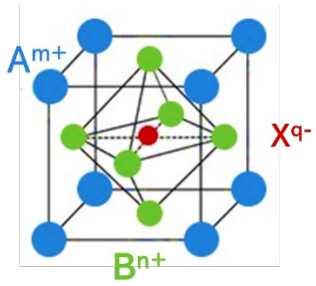

Figure 1.16. The unit cells of perovskites' cubic phase.

Hybrid organic-inorganic perovskites (HOIPs): By replacing the inorganic cation on the A site of the traditional perovskites with an organic counterpart, such as methylamine ($CH_3NH_3^+$), a hybrid material can be obtained,[132] which are known as hybrid organic-inorganic perovskites (HOIPs). The chemical bonding in HOIPs was described by Walsh taking $CH_3NH_3^+PbI_3$ as an example. He proposed that the bonding can be separated into three distinct components: i) the heteropolar bonding within the BX_3–anionic framework (PbI_3^- here), which arises from the mixed ionic/covalent interactions between Pb^{2+} and I^-; ii) the intermolecular interactions between $CH_3NH_3^+$ cations in neighboring cages of ~6 Å apart. The 18-electron closed shell electronic configuration can generate a large permanent electric dipole and thereby give rise to a nonnegligible electrostatic point dipole-dipole interaction energy; and iii) the molecule–framework interplays, which are dominated by the electrostatic bonding between the positive molecule (A site) and the negative framework.[133] The author pointed out the crucial role of the organic component, that is, the orientational freedom of the dipolar organic group results in the temperature-dependent dielectric screening and the possibility of forming the polar (ferroelectric) domains.

The story of HOIPs started in the 20th century. Notably, in 1978, Weber reported a series of hybrid perovskites with structures of $MAPbX_3$ (MA = methylammonium and X = Cl, Br or I), arousing great enthusiasm among scientists for research on this class of the compounds.[134] Compared with the traditional purely inorganic perovskites, the inclusion of organic components in the structure of HOIPs increases the structural flexibility, which can bring in a few additional functionalities.

Diverse structural compositions, including halides,[135] azides,[136] formates,[137] *etc.*, combined with their chemical variability, provide HOIPs with substantial opportunities for simple chemical modifications and thereby tune and modulate their chemical and physical properties. Moreover, HOIPs-based ferroelectric materials usually possess high T_c and P_r, as well as other features, like the ease of synthesis and lightweight. Solution-processability under room temperature further makes them a promising alternative to the traditional oxide ferroelectrics.[138] Importantly, the breakthrough in many energy-related applications in recent years makes HOIPs emerge as powerful semiconducting materials,[139] which attract considerable attention in the field of solar energy conversion, like photovoltaics,[140] solid-state lighting technology,[141] photodetection,[142] and so forth.

The ferroelectric performance of HOIPs can be optimized by tuning the band gap, which can take a wide range of values due to the structural flexibility of these compounds. In theory, bandgap and ferroelectricity are inherently contradictory because leakage currents caused by the increased amount of the thermally excited carriers in a narrow bandgap might deteriorate ferroelectricity.[143] Many efforts have been made to shed light on the relationship between the structural properties and bandgaps of HOIP ferroelectrics. To understand the role of the organic group on the bandgap and ferroelectricity, Cao and colleagues designed three one-dimensional hybrid perovskites with a formula of $[Me_3PCH_2X][PbBr_3]$ (X=H, F, and Cl, respectively, seen in Figure 1.17a) through precise molecular modifications.[144] The authors discovered that the presence of heavier halogen atoms (F or Cl) in the organic group increased the potential energy barrier required for the tumble motion of the cation. Hence, the phase transition temperature also increased from low degrees (192 K) to room degrees (285 K) and high degrees (402K), as seen in Figure b. DFT calculations revealed that the structural distortion by the halogen-substituted cation within the inorganic $PbBr_6$ octahedron is responsible for band gaps (Figure c). Very recently, some effective designing strategies and synthesis methods for designing HOIP ferroelectrics with suitable band gaps have been obtained and summarized by Yao et al., as "quasi-spherical theory," "H/F substitution," and "hydrogen bonding design." However, applying these strategies often requires rather specific conditions, so they are still not extensively suitable for all molecular ferroelectric systems.[124] Therefore, explaining the structure-property relationship in hybrid perovskites, especially when ferroelectricity and other properties both exist, shall still be necessary and meaningful to broaden the application of hybrid perovskite materials.

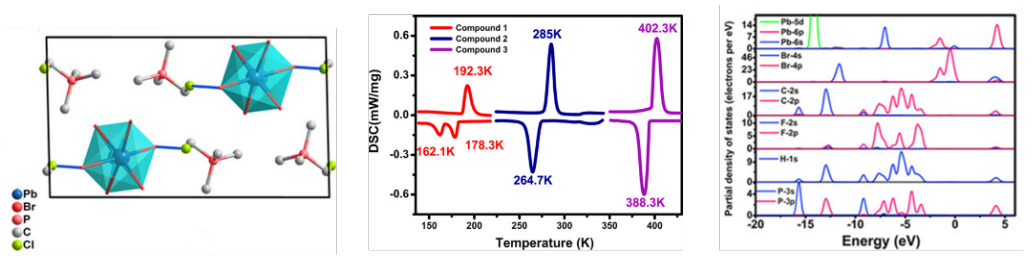

(a) (b) (c)

Figure 1.17. a) the unit cell packing diagram of $[Me_3PCH_2Cl][PbBr_3]$; **b)** differential scanning calorimetry measurements for confirming the phase transition temperature; c) calculated partial density of states. Adapted from the ref. 144.

1.3.3 Modern (computational) theory of polarization

The theoretical basis of the polarization computation is the *Modern Theory of Polarization*, which explains its definition in a periodic solid and provides a route for its quantitative computation.[145] Several critical understandings about polarization are contained within this theory, even though sometimes they are counterintuitive: (i) it is not a well-defined quantity, but multi-valued; (ii) the changes of polarization are equivalent and have physical meaning, so they are the quantities measured in experiments; (iii) it is usually described in the form of a Berry phase;[146] (iv) it is a quantum phenomenon and cannot be treated with a classical model.[147] Those perceptions together establish a strong and powerful basis for studying the polarization-related characteristics of ferroelectric materials using modern computational methods. Based on that, most commonly used commercial software developed for calculating bulk electronic structures are capable of computing polarization, like vasp.[148] Here, the principle of the theory is briefly described, presenting the detailed procedures for calculating polarization.

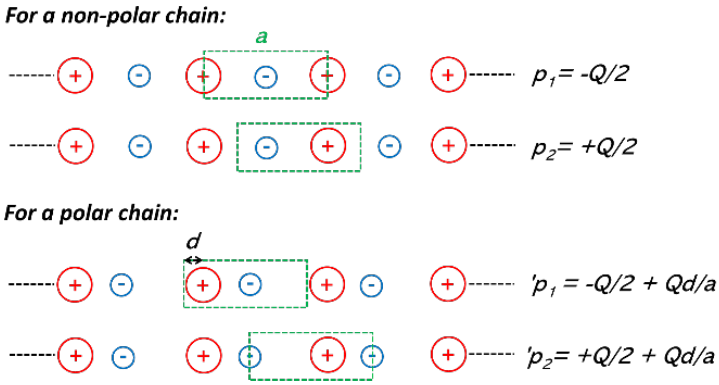

Figure. 1.18. An illustration of the calculated results' dependence by the polarization's definition on the unit cell selection, where *a* is the lattice constant.

The polarization of a dielectric medium is defined as the electric dipole per unit volume. However, when computing the polarization of a non-polar one-dimensional chain, it can be found that the value of the polarization (supposed to be zero) is non-zero and worse, is dependent on the choice of the unit cell as illustrated in Figure 1.18. The same problem also occurs with a polar phase. However, if using the p_1 minus 'p_1 and p_2 minus 'p_2 in the above figure, the differences are equivalent between the non- and polar phases,

$$\Delta p = \frac{Qd}{a} \qquad \text{(ii.)}$$

The polarization change is well-defined and single-valued no matter in which unit cell, so it is chosen to represent the polarization value both experimentally and computationally.

The periodic boundary conditions of the infinite lattice bring in a new problem. According to the definition, a charge of -1 moving a distance *a* would lead to the dipole moment changing by -*a* and thereby the polarization by -1, which is expected to be unchangeable. The polarization's changing value due to the displacement is called the *Polarization Quantum*, P_q. In one dimension, it is equal to the lattice constant divided by the length of the unit cell, which is 1 here, as seen in the right panel of Figure 1.19. Therefore, to avoid the pseudo P_q, the polarization is defined to be the polarization difference on the *Same Branch* of the lattice (the same "n" in the figure) between the polarized and unpolarized states.[145] If extending the one-dimension chain to the three-dimension solid, the P_q for each direction can be written as

$$P_{q,i} = \frac{i}{\Omega} eR_i \qquad \text{(iii.)}$$

where Ω is the unit cell volume, e is the electronic charge and R_i is the length of the ith primitive basis vector.

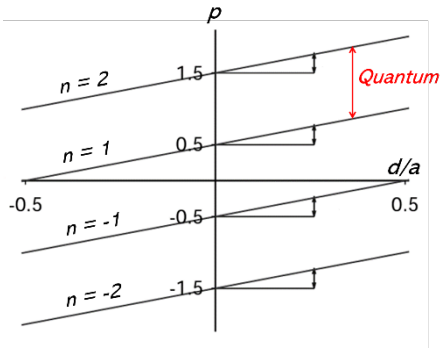

Figure. 1.19. Polarization as a function of the relative displacement (d/a). The polarization lattice is zero-centered where the branches are separated by the polarization quantum.

The full polarization effect can be divided into electronic polarization (P_{ele}) and ionic polarization (P_{ion}). The electron cloud of an atom is displaced relative to the heavy nucleus in the presence of an external electric field. This is called electronic polarization. As the name implies, ionic polarization is caused by the displacement of the positive and negative ions to the point where ionic bonding force stops this displacement. In consequence, dipoles are induced. This type of polarization only occurs in some ionic crystals. If we want to quantify the two-part polarization effects, we need to express the electron density of the periodic system in localized orbitals, which can be done by Wannier functions.[149] The formal mathematical expression for computing the P_{ele} with Wannier functions is given by the following formula:

$$P_{ele} = -\frac{2e}{\Omega} \sum_n \int r|w_n|^2 \, dr \qquad \text{(iv.)}$$

Or in the form of the Berry phase:

$$P_{ele} = -\frac{2ie}{(2\pi)^3} \sum_n \int \left\langle u_{nk} \middle| \frac{\partial u_{nk}}{\partial k} \right\rangle e^{-ikR} d^3k \qquad \text{(v.)}$$

where u_{nk} is the part of the Bloch function that belongs to the unit cell under consideration; $R = \Sigma_i n_i R_i$ is any lattice vector with R_i the length of the ith primitive basis vector. The matrix elements are calculated by integrating along strings of k-points, which is implemented within the DFT approximation in most of the commonly used

software packages. As for the calculation of P_{ion}, it can be simply achieved by the formula of

$$P_{ion} = \frac{1}{\Omega}\Sigma_i Q_i r_i \qquad \text{(vi.)}$$

After explaining the definition of polarization with providing the practical solutions for the intrinsical problems, as well as introducing the calculation methods for both P_{ele} and P_{ion}, it is time to summarize. In short, the *Modern Theory of Polarization* not only provides essential prescriptions for computing the polarization from a physical perspective of view, but also explains the relationship between polarization and Berry phase of the Bloch wavefunctions as the wavevector traverses the Brillouin zone from a mathematical viewpoint. Based on this, the thesis is capable of performing the calculation of polarization.

1.4 Challenges on computational POM chemistry

Rapid advances in computation applied to POM chemistry enable us to understand better their properties over the past decades, including the electronic structures,[33a, 65a, 150] redox behaviors, reactivities,[151] magnetism[152] and so on. However, there are still many important challenges within this field, including the deposition of POMs on metal surfaces, the study of nucleation mechanisms, the rationalization of the cation exchange in POMs with pores, *etc*.[153] Apart from them, two more major challenges related to the scope of the present thesis are: solvent modelling and the accurate estimation of redox potentials.

1.4.1 Solvent modelling

Most chemical activity involving POM anions actually takes place in solution.[154] Because of their high negative charges and abundant oxygen atoms on the surface, it is easy for POM clusters to interact with the solvent environment. For instance, POM anions could be multi-protonated in aqueous solutions or even some organic solvents that may contain traces of water in the experimental conditions, making a big difference in the calculated redox potential values.[155] Further, the interplays between the POMs charges and the solvent polarity, counter-cation size, and hydrophilicity are reported to have significance for their agglomeration phenomena.[156] Figure 1.20 shows the substantial agglomeration dependence on the solvent media of a series of polyvanadates (POVs). It demonstrates that only the highest-charged POV can form agglomerates, and the lowest-charged POV tend to agglomerate into a microphase in water. In contrast, agglomeration is more pronounced for intermediate-charged POVs in acetonitrile.[156a] The complexity of those interactions is like “confusing fog on a lake”, obscuring the actual state of a POM cluster in a solvent environment. As a result, it is challenging for the computation to create a realistic model of those POM anions. This work becomes even more complicated when some addenda (peripheral) metals of the POM frameworks are substituted by other unsaturated metals to improve reactivity, which increases the possibility of interacting with solvent molecules and other active particles in the media.[157] Thus, one major challenge for the computing of POMs is to build appropriate solvent models as close as possible to the realistic experimental conditions for accurately simulating the POM states as well as their solution behaviors within a reasonable computational cost.

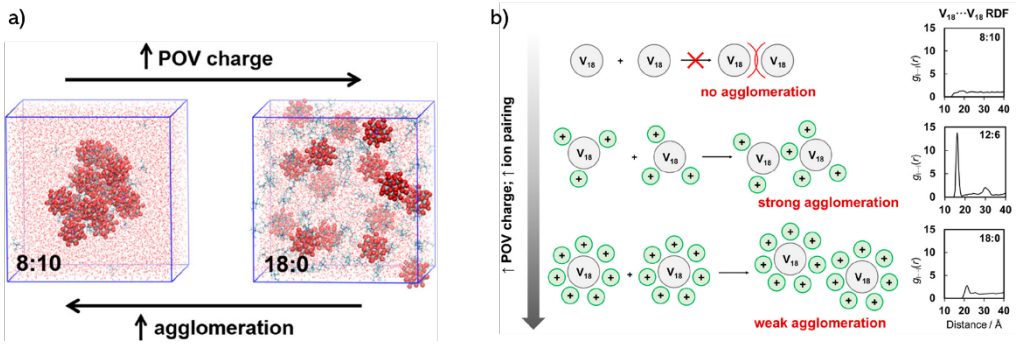

Figure 1.20. a) Snapshot of the periodic simulation in water; **b)** Relationship between the POV and ion-pairing and agglomeration in pure MeCN. Adapted from the ref. 156a.

Two main types of solvent models have been developed and successfully applied to various commercial computing codes to deal with those complex solvent effects: explicit and implicit models. As its name would suggest, the explicit solvent model treats the central solute molecule and its surrounding solvent molecules as a combined system and calculates the free energy of solvation by simulating solute-solvent interactions. The molecular detail of each single solvent unit is considered.[158] As a result, this model could better reflect the natural solvent environment. The fidelity of this kind of model is generally positively related to the number of solvent molecules included, where quite an extensive calculation can be expected to ensure reliability. On the contrary, the implicit model ignores solvent molecules' structure and distribution, but considers them abstractedly and infinitely extending continuum medium with a fixed dielectric constant surrounding the cavities occupied by the solute molecule.[159] In this model, the free energy of solvation is given by

$$\Delta G_{solv} = \Delta G_{cav} + \Delta G_{disp} + \Delta G_{elec} (+ \Delta G_{hb}) \qquad \text{(vii.)}$$

where ΔG_{cav} is required to form the solute cavity. Hence, it is the sum of the entropic penalty of reorganization of the solvent molecules around the solute and the work done in creating the cavity; ΔG_{disp} is the Van der Waals interaction between the solute and solvent molecules; ΔG_{elec} denotes the electrostatic component resulting from the polarization induced by the charge redistribution between the solute and solvent parts; ΔG_{hb} can be used to include the hydrogen bonding term. Compared with the explicit solvent model, this model effectively reduces the number of nuclei and electrons in the simulating system, thus cutting down the computing costs. As a consequence, it can be applied to study not only small and medium-sized systems but is also capable of estimating the free energy of solute-solvent interactions in large biological systems,

such as folding or conformational transitions of proteins, transport of drugs across biological membranes, and so on.[160]

Each model can be further subdivided based on the level of theory. In general, the explicit models apply classical molecular mechanics (MM)[161] and dynamics (MD)[162] or Monte Carlo (MC)[163] simulations to describe (part of) the solvent, although sometimes it can also be included in quantum chemical calculations. MD simulations taking advantage of MM force fields with empirical, parametrized functions can efficiently calculate the properties and motions of a large portion of the whole system by studying the time evolution of a chemical system in discrete time intervals. The implicit model is widely used in both force field methods and quantum chemical situations, covering Hartree-Fock (HF),[164] DFT[165] and Post-HF.[166] The accuracy can be roughly recognized in the following order: classical MM < semi-empirical quantum mechanics < DFT < post-HF. The selection of the computational method is determined by the size and the desired level of accuracy of the target system. For instance, it is not possible to apply explicit solvent models to study the association of biological macromolecules with ligands. The implicit model is not an excellent choice to deal with systems where the solvent participates in the reaction or systems with strong interactions (such as hydrogen bonds) between the solute and the solvent.

Since both solvent models have unavoidable defects, in order to make full use of their advantages, a combined model of the two models is put forward in which only the first (and in some cases a second) solvation sphere is included explicitly. The rest of the solvent molecules are treated in an implicit way. In this case, a mixed QM/MM (quantum mechanics/molecular mechanics) scheme can be considered. A core containing the solute and a small number of explicit solvent molecules is treated by QM, while the second layer could then be comprised of MM solvent molecules with a final third layer of implicit solvent representing the bulk. Therefore, the combined model can simulate the experimental environment more accurately keeping the computational expense at an acceptable level. Figure 1.21a is a typical example of the integrated model where the solvent molecules are included in the first solvation shell explicitly, and long-range bulk effects and counter-ions are represented with a set of point charges.[167] As reported, this model can strongly stabilize the electronic structure of the POM anion, which is reflected by the decreased frontier molecular orbital levels (Figure b). This model calculates the total solvation energy by dividing it into three terms so that the effects of solvent and counterions can be evaluated. However, this model still has some drawbacks, such as insufficient sampling with only one solvent

configuration being considered and failing to explicitly include additional electrolytes used in experiments to fix ionic forces. In 2014, our group adopted a combination method of static DFT calculations, classical MD and Car–Parrinello molecular dynamics (CPMD) simulations to study the nature of Zr-monosubstituted monomeric and dimeric POMs in water at different pHs. Both DFT and CPMD methods indicate that the Zr center could bind up to three water molecules. Classical MD simulations show that H_3O^+ mainly interacts with the hydroxo ligand while OH^- anions prefer the protons of the H_2O ligands. An observed rise of the acidity favoring the generation of Zr-aqua species explains the fact that a low pH can promote dimer dissociation.

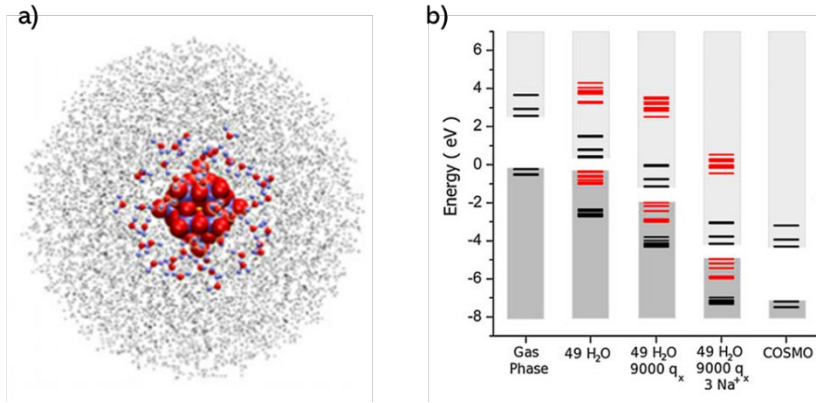

Figure 1.21. The mixed solvent model in the left panel. Calculated energy levels of the HOMOs and LUMOs based on different POM–water models (the right panel). Reproduced from ref. 167.

1.4.2 Redox potentials

The other big problem within the scope of this thesis is how to accurately calculate the redox potential of the POM clusters in solution. Here, the primary strategies developed for correctly estimating redox potentials are discussed. As mentioned above, creating a proper model for taking the solvent effect into account is essential. Without including the solvent effect treatment in computation, the calculated redox potentials are not comparable and usually much higher than the experimental values since orbital energy levels of those anion clusters are overestimated.[153] The initial computational work that calculated the POMs potentials only took the structure of the POMs into account and simulated the electrolyte environment on the DFT level with an implicitly polarizable continuum model due to

the medium-to-big sizes of the POM clusters.[168] Falbo and Penfold used several distinct methods with the use of the implicit and explicit solvent models, respectively, to study the potentials of $[SiW_{12}O_{40}]^{4-}$ (SiW_{12}) and $[PV_{14}O_{42}]^{9-}$ (PV_{14}).[169] First thermodynamic cycle approach in combination with quantum method and implicit solvation were adopted to calculate the potentials. Later, MD was applied to promote an explicit description of the solvent environment. They pointed out that deviations between the calculated and experimental values increase since the highly charged nature of these species can cause a strong interplay with the surrounding solvent. The accuracy of simulations can be significantly improved by explicitly treating the solvent environment.

Since the redox potential is dependent on the LUMO energy level, the accuracy and reliability of its evaluation can also be significantly improved by selecting suitable theoretical methods to analyze the electronic structure. With the Hohenberg-Kohn and Kohn-Sham theorems as the foundation, DFT has been proved a successful theory to give a quantitative understanding of the electronic structure of atoms, molecules, and solids.[170] It is also broadly applied for examining the electronic structure in POM chemistry and has achieved remarkable results.[65a, 171] Different functionals of DFT were considered by Kremleva *et al.*, including counter cations surrounding around the POM up to a neutral system.[172] The computational potentials were consistent with the experimental values very well but were somewhat dependent on the DFT functional used. Later, our group evaluated the capability of DFT methods to accurately simulate potentials and describe electron (de) localization within POM systems by examining the electronic structures of the completely oxidized $[P_2W_{18}O_{62}]^{6-}$ and α_1/α_2-$[P_2MW_{17}O_{62}]^{n-}$ (M = V, Mo) clusters and their corresponding one-electron reduced species with DFT.[173] It was found that hybrid functionals such as B3LYP or M05 can localize electrons at the right site. In contrast, pure GGA functionals cannot properly describe the additional electron due to their well-known tendency to overestimate the delocalization of the unpaired electron density. All strategies mentioned above shall give inspiration to the present work to overcome these challenges and improve the estimation quality.

References

1. (a) Pope, M. T., *Heteropoly and Isopoly Oxometalates*. Springer: New York, 1983; (b) Gumerova, N. I.; Rompel, A., *Nat. Rev. Chem.* **2018,** *2* (2), 0112.

2. Berzelius, J. J., *Ann Phys* **1826,** *82* (4), 369-392.

3. Pauling, L., *J. Am. Chem. Soc.* **1929,** *51* (10), 2868-2880.

4. Keggin, J. F.; Bragg, W. L., Proceedings of the Royal Society of London. Series A, Containing Papers of a Mathematical and Physical Character **1934,** 144 (851), 75-100.

5. Baker, L. C. W.; Glick, D. C., *Chem. Rev.* **1998,** *98* (1), 3-50.

6. Long, D.-L.; Burkholder, E.; Cronin, L., *Chem. Soc. Rev.* **2007,** *36* (1), 105-121.

7. (a) Horn, M. R.; Singh, A.; Alomari, S.; Goberna-Ferrón, S.; Benages-Vilau, R.; Chodankar, N.; Motta, N.; Ostrikov, K.; MacLeod, J.; Sonar, P.; Gomez-Romero, P.; Dubal, D., *Energy Environ. Sci.* **2021,** *14* (4), 1652-1700; (b) Streb, C.; Kastner, K.; Tucher, J., *Phys. Sci. Rev.* **2019,** *4* (6).

8. (a) Song, Y.-F.; Tsunashima, R., *Chem. Soc. Rev.* **2012,** *41* (22), 7384-7402; (b) Chen, L.; Chen, W.-L.; Wang, X.-L.; Li, Y.-G.; Su, Z.-M.; Wang, E.-B., *Chem. Soc. Rev.* **2019,** *48* (1), 260-284.

9. Čolović, B. M.; Lacković, M.; Lalatović, J.; Mougharbel, S. A.; Kortz, U.; Krstić, Z. D., *Curr. Med. Chem.* **2020,** *27* (3), 362-379.

10. (a) Liu, J.-X.; Zhang, X.-B.; Li, Y.-L.; Huang, S.-L.; Yang, G.-Y., *Coord. Chem. Rev.* **2020,** *414*, 213260; (b) Müller, A.; Gouzerh, P., *Chem. Soc. Rev.* **2012,** *41* (22), 7431-7463.

11. Mazeaud, A.; Ammari, N.; Robert, F.; Thouvenot, R., *Angew. Chem., Int. Ed. Engl.* **1996,** *35* (17), 1961-1964.

12. Osada, H.; Ishikawa, A.; Saku, Y.; Sakai, Y.; Matsuki, Y.; Matsunaga, S.; Nomiya, K., *Polyhedron* **2013,** *52*, 389-397.

13. Bridgeman, A. J.; Cavigliasso, G., *Inorg. Chem.* **2002,** *41* (7), 1761-1770.

14. Mizuno, N.; Misono, M., *J. Mol. Catal.* **1994,** *86* (1), 319-342.

15. (a) Müller, A.; Beckmann, E.; Bögge, H.; Schmidtmann, M.; Dress, A., *Angew. Chem. Int. Ed.* **2002,** *41* (7), 1162-1167; (b) Zhan, C. H.; Winter, R. S.; Zheng, Q.; Yan, J.; Cameron, J. M.; Long, D. L.; Cronin, L., *Angew. Chem.* **2015,** *127* (48), 14516-14520.

16. (a) Suber, L.; Bonamico, M.; Fares, V., *Inorg. Chem.* **1997,** *36* (10), 2030-2033; (b) Mizuno, N.; Kamata, K., *Coord. Chem. Rev.* **2011,** *255* (19-20), 2358-2370.

17. (a) Zheng, S.-T.; Yang, G.-Y., *Chem. Soc. Rev.* **2012,** *41* (22), 7623-7646; (b) Patel, A.; Narkhede, N.; Singh, S.; Pathan, S., *Catal. Rev.* **2016,** *58* (3), 337-370; (c) Han, Q.; Ding, Y., *Dalton Trans* **2018,** *47* (25), 8180-8188.

18. (a) Pratt III, H. D.; Anderson, T. M., *Dalton Trans* **2013,** *42* (44), 15650-15655; (b) Simms, C.; Kondinski, A.; Parac-Vogt, T. N., *Eur. J. Inorg. Chem.* **2020,** *2020* (27), 2559-2572.

19. Anyushin, A. V.; Kondinski, A.; Parac-Vogt, T. N., *Chem. Soc. Rev.* **2020,** *49* (2), 382-432.

20. Lopez, X.; Fernandez, J. A.; Poblet, J. M., *Dalton Trans* **2006,** (9), 1162-7.

21. (a) Thouvenot, R.; Fournier, M.; Franck, R.; Rocchiccioli-Deltcheff, C., *Inorg. Chem.* **1984,** *23* (5), 598-605; (b) López, X., *Phys. Sci. Rev.* **2017,** *2* (11).

22. Li, D.; Ma, P.; Niu, J.; Wang, J., *Coord. Chem. Rev.* **2019,** *392*, 49-80.

23. Baker, L. C. W.; Figgis, J. S., *J. Am. Chem. Soc.* **1970,** *92* (12), 3794-3797.

24. (a) Crans, D. C.; Sánchez-Lombardo, I.; McLauchlan, C. C., *Front. Chem* **2019,** *7*; (b) López, X.; Carbó, J. J.; Bo, C.; Poblet, J. M., *Chem. Soc. Rev.* **2012,** *41* (22), 7537-7571.

25. Aparicio Sánchez, P. A. *Electronic Effects Governing the Redox Properties of Polyoxometalates*. Doctoroal, Universitat Rovira i Virgili, 2014.

26. (a) Yang, H.; Gao, S.; Lü, J.; Xu, B.; Lin, J.; Cao, R., *Inorg. Chem.* **2010,** *49* (2), 736-744; (b) Gumerova, N. I.; Rompel, A., *Chem. Soc. Rev.* **2020,** *49* (21), 7568-7601.

27. (a) Hayashi, Y., *Coord. Chem. Rev.* **2011,** *255* (19), 2270-2280; (b) Cai, J.; Ye, R.; Jia, K.; Qiao, X.; Zhao, L.; Liu, J.; Sun, W., *Inorg. Chem. Commun.* **2020,** *112*, 107694.

28. Rong, C.; Pope, M. T., *J. Am. Chem. Soc.* **1992,** *114* (8), 2932-2938.

29. Li, C.; Mizuno, N.; Yamaguchi, K.; Suzuki, K., *J. Am. Chem. Soc.* **2019,** *141* (19), 7687-7692.

30. Yu, T.; Ma, H.; Zhang, C.; Pang, H.; Li, S.; Liu, H., *Dalton Trans* **2013,** *42* (46), 16328-16333.

31. Li, C.; Yamaguchi, K.; Suzuki, K., *Angew. Chem. Int. Ed.* **2021,** *60* (13), 6960-6964.

32. Minato, T.; Suzuki, K.; Yamaguchi, K.; Mizuno, N., *Chem. Eur. J.* **2017,** *23 57*, 14213-14220.

33. (a) Bo, C.; Miró, P., *Dalton Trans* **2012,** *41* (33), 9984-9988; (b) Li, Z.; Lin, L. D.; Yu, H.; Li, X. X.; Zheng, S. T., *Angew. Chem.* **2018,** *130* (48), 16003-16007.

34. Cronin, L.; Müller, A., *Chem. Soc. Rev.* **2012,** *41* (22), 7333-7334.

35. Middleton, A. R., *J. Chem. Educ.* **1933,** *10* (12), 726.

36. Deshlahra, P.; Iglesia, E., *Chem. Commun.* **2020,** *56* (54), 7371-7398.

37. Macht, J.; Janik, M. J.; Neurock, M.; Iglesia, E., *Angew. Chem. Int. Ed.* **2007,** *46* (41), 7864-7868.

38. Kozhevnikov, I. V.; Khankhasaeva, S. T.; Kulikov, S. M., *Kinet. Katal.* **1988,** *29* (1), 76-80.

39. (a) Macht, J.; Janik, M. J.; Neurock, M.; Iglesia, E., *J. Am. Chem. Soc.* **2008,** *130* (31), 10369-10379; (b) Janik, M. J.; Macht, J.; Iglesia, E.; Neurock, M., *J. Phys. Chem. C.* **2009,** *113* (5), 1872-1885.

40. (a) Rhule, J. T.; Hill, C. L.; Judd, D. A.; Schinazi, R. F., *Chem. Rev.* **1998,** *98* (1), 327-358; (b) Arefian, M.; Mirzaei, M.; Eshtiagh-Hosseini, H.; Frontera, A., *Dalton Trans* **2017,** *46* (21), 6812-6829.

41. Chermann, J. C.; Raynaud, M.; Jasmin, C.; MathÉ, G., *Nature* **1970,** *227* (5254), 173-174.

42. Stephan, H.; Kubeil, M.; Emmerling, F.; Müller, C. E., *Eur. J. Inorg. Chem.* **2013,** *2013* (10 - 11), 1585-1594.

43. Zhao, M.; Chen, X.; Chi, G.; Shuai, D.; Wang, L.; Chen, B.; Li, J., *Inorg. Chem. Front* **2020,** *7* (22), 4320-4332.

44. Bijelic, A.; Molitor, C.; Mauracher, S. G.; Al-Oweini, R.; Kortz, U.; Rompel, A., *ChemBioChem* **2015,** *16* (2), 233-241.

45. (a) Hasenknopf, B., *Front. Biosci* **2005,** *10* (275), 10.2741; (b) Van Rompuy, L. S.; Parac-Vogt, T. N., *Curr. Opin. Biotechnol.* **2019,** *58*, 92-99; (c) Yamase, T., *Biomedical inorganic polymers* **2013**, 65-116.

46. (a) Wang, H.; Li, J.; Sun, J.; Wang, Y.; Liang, Z.; Ma, P.; Zhang, D.; Wang, J.; Niu, J., *Sci. Rep.* **2017,** *7* (1), 10653; (b) Wu, H.; Yan, B.; Li, H.; Singh, V.; Ma, P.; Niu, J.; Wang, J., *Inorg. Chem.* **2018,** *57* (13), 7665-7675.

47. (a) Müller, A.; Peters, F.; Pope, M. T.; Gatteschi, D., *Chem. Rev.* **1998,** *98* (1), 239-272; (b) Duan, Y.; Clemente-Juan, J. M.; Giménez-Saiz, C.; Coronado, E., *Front. Chem* **2018,** *6*.

48. Omwoma, S.; Gore, C. T.; Ji, Y.; Hu, C.; Song, Y.-F., *Coord. Chem. Rev.* **2015,** *286*, 17-29.

49. Bujanovic, B.; Ralph, S.; Reiner, R.; Hirth, K.; Atalla, R., *Materials* **2010,** *3* (3), 1888-1903.

50. Long, D. L.; Tsunashima, R.; Cronin, L., *Angew. Chem. Int. Ed.* **2010,** *49* (10), 1736-1758.

51. (a) Dolbecq, A.; Dumas, E.; Mayer, C. R.; Mialane, P., *Chem. Rev.* **2010,** *110* (10), 6009-6048; (b) Miras, H. N.; Yan, J.; Long, D.-L.; Cronin, L., *Chem. Soc. Rev.* **2012,** *41* (22), 7403-7430.

52. Genovese, M.; Lian, K., *Curr. Opin. Solid State Mater. Sci.* **2015,** *19* (2), 126-137.

53. Muniz, J., *MOJ Biorg Inorg Chem* **2017,** *1* (3).

54. Lang, Z.; Aparicio-Anglès, X.; Weinstock, I.; Clotet, A.; Poblet, J. M., *Inorg. Chem.* **2017,** *56* (7), 3961-3969.

55. He, T.; Yao, J., *Prog. Mater Sci.* **2006,** *51* (6), 810-879.

56. (a) Zhou, Y.; Chen, G.; Long, Z.; Wang, J., *RSC Adv.* **2014,** *4* (79), 42092-42113; (b) Zhang, S.; Ou, F.; Ning, S.; Cheng, P., *Inorg. Chem. Front* **2021,** *8* (7), 1865-1899.

57. (a) Wang, S.-S.; Yang, G.-Y., *Chem. Rev.* **2015,** *115* (11), 4893-4962; (b) Lu, M.; Zhang, M.; Liu, J.; Yu, T.-Y.; Chang, J.-N.; Shang, L.-J.; Li, S.-L.; Lan, Y.-Q., *J. Am. Chem. Soc.* **2022,** *144* (4), 1861-1871.

58. Liu, R.; Zhang, G.; Cao, H.; Zhang, S.; Xie, Y.; Haider, A.; Kortz, U.; Chen, B.; Dalal, N. S.; Zhao, Y.; Zhi, L.; Wu, C.-X.; Yan, L.-K.; Su, Z.; Keita, B., *Energy Environ. Sci.* **2016,** *9* (3), 1012-1023.

59. Li, N.; Liu, J.; Dong, B. X.; Lan, Y. Q., *Angewandte Chemie* **2020**.

60. Sumliner, J. M.; Lv, H.; Fielden, J.; Geletii, Y. V.; Hill, C. L., *Eur. J. Inorg. Chem.* **2014,** *2014* (4), 635-644.

61. Sullivan, K. P.; Yin, Q.; Collins-Wildman, D. L.; Tao, M.; Geletii, Y. V.; Musaev, D. G.; Lian, T.; Hill, C. L., *Front. Chem* **2018,** *6*, 365-365.

62. Zhang, Y.; Liu, J.; Li, S.-L.; Su, Z.-M.; Lan, Y.-Q., *EnergyChem* **2019,** *1* (3), 100021.

63. Streb, C., *Dalton Trans* **2012,** *41* (6), 1651-1659.

64. Ashwin Kishore, M. R.; Ravindran, P., *J. Phys. Chem. C.* **2017,** *121* (40), 22216-22224.

65. (a) Poblet, J. M.; López, X.; Bo, C., *Chem. Soc. Rev.* **2003,** *32* (5), 297-308; (b) Walsh, J. J.; Bond, A. M.; Forster, R. J.; Keyes, T. E., *Coord. Chem. Rev.* **2016,** *306*, 217-234.

66. Cameron, J. M.; Wales, D. J.; Newton, G. N., *Dalton Trans* **2018,** *47* (15), 5120-5136.

67. Toshihiro, Y.; Tsuneo, I.; Hiroshi, K.; Eiichi, I., *Chem. Lett.* **1973,** *2* (6), 615-616.

68. E. N. Savinov, S. S. S., V. N. Parmon and K. I. Zamaraev, Doklady, *Phys. Chem. SSSR,* **1983,** *272* (741).

69. Papaconstantinou, E., *Anal. Chem.* **1975,** *47* (9), 1592-1595.

70. Hill, C. L.; Bouchard, D. A., *J. Am. Chem. Soc.* **1985,** *107* (18), 5148-5157.

71. (a) Troupis, A.; Hiskia, A.; Papaconstantinou, E., *Angew. Chem. Int. Ed.* **2002,** *41* (11), 1911-1914; (b) Antonaraki, S.; Triantis, T. M.; Papaconstantinou, E.; Hiskia, A., *Catal. Today* **2010,** *151* (1), 119-124; (c) Tucher, J.; Schlicht, S.; Kollhoff, F.; Streb, C., *Dalton Trans* **2014,** *43* (45), 17029-17033.

72. (a) Ding, Y.-S.; Wang, H.-Y.; Ding, Y., *Dalton Trans* **2020,** *49* (11), 3457-3462; (b) von Allmen, K.; Moré, R.; Müller, R.; Soriano‐López, J.; Linden, A.; Patzke, G. R., *ChemPlusChem* **2015,** *80* (9), 1389-1398; (c) Papaconstantinou, E.; Ioannidis, A.; Hiskia, A.; Argitis, P.; Dimotikali, D.; Korres, S., *Photocatalytic processes by polyoxometalates. Splitting of water. The role of dioxygen*. Springer: 1994; pp 327-335.

73. (a) Cao, Y.; Chen, Q.; Shen, C.; He, L., *Molecules* **2019,** *24* (11), 2069; (b) Gu, J.; Chen, W.; Shan, G. G.; Li, G.; Sun, C.; Wang, X. L.; Su, Z., *Mater. Today Energy* **2021,** *21*, 100760.

74. Lan, J.; Wang, Y.; Huang, B.; Xiao, Z.; Wu, P., *Nanoscale Adv.* **2021,** *3* (16), 4646-4658.

75. (a) Zhang, B.; Sun, G.; Ding, S.; Asakura, H.; Zhang, J.; Sautet, P.; Yan, N., *J. Am. Chem. Soc.* **2019,** *141* (20), 8185-8197; (b) Zhang, L.-H.; Wang, Y.; Ma, F.; Liu, C.-G., *J. Organomet. Chem.* **2012,** *716*, 245-251; (c) Su, X.-F.; Zhu, B.; Wu, C.-X.; Yan, L.-K.; Su, Z.-M., *J. Theor. Comput. Chem.* **2017,** *16* (06), 1750054.

76. (a) Xie, S.-L.; Liu, J.; Dong, L.-Z.; Li, S.-L.; Lan, Y.-Q.; Su, Z.-M., *Chem. Sci.* **2019,** *10* (1), 185-190; (b) Huang, Q.; Liu, J.; Feng, L.; Wang, Q.; Guan, W.; Dong, L.-Z.; Zhang, L.; Yan, L.-K.; Lan, Y.-Q.; Zhou, H.-C., *Natl. Sci. Rev.* **2019,** *7* (1), 53-63.

77. (a) Zhang, Z.-M.; Zhang, T.; Wang, C.; Lin, Z.; Long, L.-S.; Lin, W., *J. Am. Chem. Soc.* **2015,** *137* (9), 3197-3200; (b) Schönweiz, S.; Rommel, S. A.; Kübel, J.; Micheel,

M.; Dietzek, B.; Rau, S.; Streb, C., *Chem. Eur. J.* **2016,** *22* (34), 12002-12005; (c) Qin, L.; Zhao, C.; Yao, L.-Y.; Dou, H.; Zhang, M.; Xie, J.; Weng, T.-C.; Lv, H.; Yang, G.-Y., *CCS Chemistry* **2022,** *4* (1), 259-271.

78. Luo, Y.; Maloul, S.; Endres, P.; Schönweiz, S.; Ritchie, C.; Wächtler, M.; Winter, A.; Schubert, U. S.; Streb, C.; Dietzek, B., *Sustain. Energy Fuels.* **2020,** *4* (9), 4688-4693.

79. (a) Amthor, S.; Knoll, S.; Heiland, M.; Zedler, L.; Li, C.; Nauroozi, D.; Tobaschus, W.; Mengele, A. K.; Anjass, M.; Schubert, U. S.; Dietzek-Ivanšić, B.; Rau, S.; Streb, C., *Nat. Chem.* **2022**; (b) Winter, A.; Endres, P.; Schröter, E.; Jäger, M.; Görls, H.; Neumann, C.; Turchanin, A.; Schubert, U. S., *Molecules* **2019,** *24* (24), 4446.

80. (a) Yu, H.; Haviv, E.; Neumann, R., *Angew. Chem. Int. Ed.* **2020,** *59* (15), 6219-6223; (b) Zhao, S.; Zhao, X.; Ouyang, S.; Zhu, Y., *Catal. Sci. Technol.* **2018,** *8* (6), 1686-1695.

81. Zhou, J.; Chen, W.; Sun, C.; Han, L.; Qin, C.; Chen, M.; Wang, X.; Wang, E.; Su, Z., *ACS Appl. Mater. Interfaces* **2017,** *9* (13), 11689-11695.

82. (a) Madonia, A.; Martin-Sabi, M.; Sciortino, A.; Agnello, S.; Cannas, M.; Ammar, S.; Messina, F.; Schaming, D., *J. Phys. Chem. Lett.* **2020,** *11* (11), 4379-4384; (b) Xiang, X.; Fielden, J.; Rodríguez-Córdoba, W.; Huang, Z.; Zhang, N.; Luo, Z.; Musaev, D. G.; Lian, T.; Hill, C. L., *J. Phys. Chem. C.* **2013,** *117* (2), 918-926; (c) Harriman, A.; Elliott, K. J.; Alamiry, M. A. H.; Pleux, L. L.; Séverac, M.; Pellegrin, Y.; Blart, E.; Fosse, C.; Cannizzo, C.; Mayer, C. R.; Odobel, F., *J. Phys. Chem. C.* **2009,** *113* (14), 5834-5842.

83. Zhao, C.; Huang, Z.; Rodríguez-Córdoba, W.; Kambara, C. S.; O'Halloran, K. P.; Hardcastle, K. I.; Musaev, D. G.; Lian, T.; Hill, C. L., *J. Am. Chem. Soc.* **2011,** *133* (50), 20134-20137.

84. Gao, J.; Liu, X.; Liu, Y.; Yu, L.; Feng, Y.; Chen, H.; Li, Y.; Rakesh, G.; Huan, C. H. A.; Sum, T. C.; Zhao, Y.; Zhang, Q., *Dalton Trans* **2012,** *41* (39), 12185-12191.

85. (a) Liu, R.; Streb, C., *Adv. Energy Mater.* **2021,** *11* (25), 2101120; (b) Kim, M.; Chamack, M.; Geletii, Y. V.; Hill, C. L., *Inorg. Chem.* **2018,** *57* (1), 311-318.

86. Lechner, M.; Güttel, R.; Streb, C., *Dalton Trans* **2016,** *45* (42), 16716-16726.

87. Hardin, B. E.; Snaith, H. J.; McGehee, M. D., *Nat. Photonics* **2012,** *6* (3), 162-169.

88. (a) Rüther, T.; Hultgren, V. M.; Timko, B. P.; Bond, A. M.; Jackson, W. R.; Wedd, A. G., *J. Am. Chem. Soc.* **2003,** *125* (33), 10133-10143; (b) Ueda, T., *ChemElectroChem* **2020,** *7* (13), 2888-2888.

89. (a) Wang, X.-L.; Tian, Y.; Chang, Z.-H.; Lin, H., *ACS Sustain. Chem. Eng.* **2020,** *8* (41), 15696-15702; (b) Abdelkader-Fernández, V. K.; Fernandes, D. M.; Balula, S. S.; Cunha-Silva, L.; Freire, C., *ACS Appl. Energy Mater* **2020,** *3* (3), 2925-2934.

90. (a) Sarma, B. B.; Neumann, R., *Nat. Commun.* **2014,** *5* (1), 4621; (b) Rubinstein, A.; Jiménez-Lozanao, P.; Carbó, J. J.; Poblet, J. M.; Neumann, R., *J. Am. Chem. Soc.* **2014,** *136* (31), 10941-10948.

91. Kholdeeva, O. A., *Eur. J. Inorg. Chem.* **2013,** *2013* (10-11), 1595-1605.

92. Lang, Z.; Miao, J.; Lan, Y.; Cheng, J.; Xu, X.; Cheng, C., *APL Mater.* **2020,** *8* (12), 120702.

93. Li, J.-S.; Sang, X.-J.; Chen, W.-L.; Zhang, L.-C.; Zhu, Z.-M.; Ma, T.-Y.; Su, Z.-M.; Wang, E.-B., *ACS Appl. Mater. Interfaces* **2015,** *7* (24), 13714-13721.

94. (a) Ren, Y.; Wang, M.; Chen, X.; Yue, B.; He, H., *Materials* **2015,** *8* (4), 1545-1567; (b) Lotfian, N.; Heravi, M. M.; Mirzaei, M.; Heidari, B., *Appl. Organomet. Chem.* **2019,** *33* (4), e4808.

95. Fernández, J. A.; López, X.; Bo, C.; de Graaf, C.; Baerend, E. J.; Poblet, J. M., *J. Am. Chem. Soc.* **2007,** *129* (40), 12244-12254.

96. Nambu, J.-i.; Ueda, T.; Guo, S.-X.; Boas, J. F.; Bond, A. M., *Dalton Trans* **2010,** *39* (31), 7364-7373.

97. Sartorel, A.; Miró, P.; Carraro, M.; Berardi, S.; Bortolini, O.; Bagno, A.; Bo , C.; Bonchio, M., *Chem. Eur. J.* **2014,** *20* (35), 10932-10943.

98. Niemiec, P.; Tokarz-Sobieraj, R.; Witko, M., *Molecules* **2022,** *27* (1), 187.

99. (a) Stuckart, M.; Monakhov, K. Y., *Chem. Sci.* **2019,** *10* (16), 4364-4376; (b) Cameron, J. M.; Guillemot, G.; Galambos, T.; Amin, S. S.; Hampson, E.; Mall Haidaraly, K.; Newton, G. N.; Izzet, G., *Chem. Soc. Rev.* **2022,** *51* (1), 293-328.

100. Wang, Y.-R.; Huang, Q.; He, C.-T.; Chen, Y.; Liu, J.; Shen, F.-C.; Lan, Y.-Q., *Nat. Commun.* **2018,** *9* (1), 4466.

101. Kastner, K.; Kibler, A. J.; Karjalainen, E.; Fernandes, J. A.; Sans, V.; Newton, G. N., *J. Mater. Chem. A* **2017,** *5* (23), 11577-11581.

102. Cherevan, A. S.; Nandan, S. P.; Roger, I.; Liu, R.; Streb, C.; Eder, D., *Adv. Sci.* **2020,** *7* (8), 1903511.

103. Liu, R.; Cao, K.; Clark, A. H.; Lu, P.; Anjass, M.; Biskupek, J.; Kaiser, U.; Zhang, G.; Streb, C., *Chem. Sci.* **2020,** *11* (4), 1043-1051.

104. Ji, Y.; Huang, L.; Hu, J.; Streb, C.; Song, Y.-F., *Energy Environ. Sci.* **2015,** *8* (3), 776-789.

105. (a) Kato, C.; Machida, R.; Maruyama, R.; Tsunashima, R.; Ren, X. M.; Kurmoo, M.; Inoue, K.; Nishihara, S., *Angew. Chem.* **2018,** *57* (41), 13429-13432; (b) Nishihara, S., *Nat. Nanotechnol* **2020,** *15* (12), 966-967.

106. (a) Kim, K. C.; Pope, M. T.; Gama, G. J.; Dickman, M. H., *J. Am. Chem. Soc.* **1999,** *121* (48), 11164-11171; (b) Du, J.; Cao, M. D.; Feng, S. L.; Su, F.; Sang, X. J.; Zhang, L. C.; You, W. S.; Yang, M.; Zhu, Z. M., *Chem. Eur. J.* **2017,** *23* (58), 14614-14622; (c) Hayashi, A.; Haioka, T.; Takahashi, K.; Bassil, B. S.; Kortz, U.; Sano, T.; Sadakane, M., *Z. Anorg. Allg. Chem.* **2015,** *641* (15), 2670-2676.

107. (a) Lines, M. E.; Glass, A. M., Principles and Applications of Ferroelectrics and Related Materials. OUP Oxford: 2001; (b) T., M., Ferroelectrics and Antiferroelectrics. In: Warlimont H., Martienssen W. (eds) Springer Handbook of Materials Data. Springer Handbooks., Springer, Cham: 2018.

108. (a) Abrahams, S. C.; Kurtz, S. K.; Jamieson, P. B., *Phys. Rev.* **1968,** *172* (2), 551-553; (b) Song, X.-J.; Zhang, T.; Gu, Z.-X.; Zhang, Z.-X.; Fu, D.-W.; Chen, X.-G.; Zhang, H.-Y.; Xiong, R.-G., *J. Am. Chem. Soc.* **2021,** *143* (13), 5091-5098.

109. Ahn, C. H.; Rabe, K. M.; Triscone, J.-M., *Science* **2004,** *303* (5657), 488-491.

110. Liao, Y., *Practical Electron Microscopy and Database*, **2006**, https://www.globalsino.com/EM/.

111. Valasek, J., *Phys. Rev.* **1921,** *17* (4), 475-481.

112. Busch, G.; Scherrer, P., *Naturwissenschaften* **1935,** *23* (43), 737-737.

113. (a) Scott, J. F., *Ferroelectrics* **2016,** *503* (1), 117-132; (b) Li, L.; Xie, L.; Pan, X., *Rep. Prog. Phys.* **2019,** *82* (12), 126502.

114. (a) Zhang, Q.; Cagin, T.; Goddard, W. A., *Proc. Natl. Acad. Sci. U.S.A.* **2006,** *103* (40), 14695-14700; (b) Zhou, C.; Ke, X.; Yao, Y.; Yang, S.; Ji, Y.; Liu, W.; Yang, Y.; Zhang, L.; Hao, Y.; Ren, S.; Zhang, L.; Ren, X., *Appl. Phys. Lett.* **2018,** *112* (18), 182903.

115. Hinterstein, M.; Rouquette, J.; Haines, J.; Papet, P.; Glaum, J.; Knapp, M.; Eckert, J.; Hoffman, M., *Phys. Rev. B* **2014,** *90* (9), 094113.

116. (a) Fukada, E.; Furukawa, T., *Ultrasonics* **1981,** *19* (1), 31-39; (b) Li, M.; Wondergem, H. J.; Spijkman, M.-J.; Asadi, K.; Katsouras, I.; Blom, P. W. M.; de Leeuw, D. M., *Nat. Mater.* **2013,** *12* (5), 433-438.

117. (a) Li, F.; Jin, L.; Xu, Z.; Zhang, S., *Appl. Phys. Rev.* **2014,** *1* (1), 011103; (b) Wu, F.; Lin, W.; Wang, J.; Zhang, C.; Fan, J., *Integr. Ferroelectr.* **2018,** *190* (1), 85-90.

118. (a) Asadi, K.; Li, M.; Blom, P. W. M.; Kemerink, M.; de Leeuw, D. M., *Mater. Today* **2011,** *14* (12), 592-599; (b) Xue, F.; He, X.; Liu, W.; Periyanagounder, D.; Zhang, C.; Chen, M.; Lin, C.-H.; Luo, L.; Yengel, E.; Tung, V.; Anthopoulos, T. D.; Li, L.-J.; He, J.-H.; Zhang, X., *Adv. Funct. Mater.* **2020,** *30* (52), 2004206.

119. (a) Ramesh, R., *Nat. Mater.* **2010,** *9* (5), 380-381; (b) Li, X.; Liu, H.; Chen, Z.; Wu, Q.; Yu, Z.; Yang, M.; Wang, X.; Cheng, Z.; Fu, Z.; Lu, Y., *Nat. Commun.* **2019,** *10* (1), 1409.

120. (a) Pulvari, C., *IRE Transactions on Component Parts* **1956,** *3* (1), 3-11; (b) Lee, D. H.; Lee, Y.; Yang, K.; Park, J. Y.; Kim, S. H.; Reddy, P. R. S.; Materano, M.; Mulaosmanovic, H.; Mikolajick, T.; Jones, J. L.; Schroeder, U.; Park, M. H., *Appl. Phys. Rev.* **2021,** *8* (2), 021312.

121. (a) Pan, H.; Zhang, J.; Jia, X.; Xing, H.; He, J.; Wang, J.; Wen, F., *Ceram. Int.* **2018,** *44* (5), 5785-5789; (b) Li, J.; Long, Y.; Yang, F.; Wei, H.; Zhang, Z.; Wang, Y.; Wang, J.; Li, C.; Carlos, C.; Dong, Y.; Wu, Y.; Cai, W.; Wang, X., *Adv. Funct. Mater.* **2020,** *30* (39), 2002868.

122. (a) Cohen, R. E., *Nature* **1992,** *358* (6382), 136-138; (b) Picozzi, S.; Yamauchi, K.; Sergienko, I. A.; Sen, C.; Sanyal, B.; Dagotto, E., *J. Phys.: Condens. Matter* **2008,** *20* (43), 434208; (c) Gao, W.; Zhu, Y.; Wang, Y.; Yuan, G.; Liu, J.-M., *J. Materiomics* **2020,** *6* (1), 1-16.

123. Thomson, S., Book of Observing Phase Transitions in a Halide Perovskite Using Temperature Dependent Photoluminescence Spectroscopy. **2018**.

124. Yao, J.; Pan, Q.; Feng, Z.-J.; Xiong, Y.-A.; Sha, T.-T.; Ji, H.-R.; Gu, Z.-X.; You, Y.-M., *APL Mater.* **2021,** *9* (4), 040901.

125. Liu, D.; Lin, Q.; Zang, Z.; Wang, M.; Wangyang, P.; Tang, X.; Zhou, M.; Hu, W., *ACS Appl. Mater. Interfaces* **2017,** *9* (7), 6171-6176.

126. Maria Joseph Raj, N. P.; Alluri, N. R.; Chandrasekhar, A.; Khandelwal, G.; Kim, S.-J., *Nano Energy* **2019,** *62*, 329-337.

127. Wu, J.; Su, R.; Fieramosca, A.; Ghosh, S.; Zhao, J.; Liew, T. C.; Xiong, Q., *Advanced Photonics* **2021,** *3* (5), 055003.

128. Liu, F.; Fina, I.; Sauthier, G.; Sánchez, F.; Rappe, A. M.; Fontcuberta, J., *ACS Appl. Mater. Interfaces* **2018,** *10* (28), 23968-23975.

129. Rassay, S.; Hakim, F.; Ramezani, M.; Tabrizian, R., 18-22 Jan. 2020; 2020; pp 1254-1257.

130. Nuraje, N.; Su, K., *Nanoscale* **2013,** *5* (19), 8752-8780.

131. Yang, D.; Luo, L.; Gao, Y.; Chen, S.; Zeng, X. C., *Mater. Horiz.* **2019,** *6* (7), 1463-1473.

132. He, R.; Ren, S.; Chen, C.; Yi, Z.; Luo, Y.; Lai, H.; Wang, W.; Zeng, G.; Hao, X.; Wang, Y.; Zhang, J.; Wang, C.; Wu, L.; Fu, F.; Zhao, D., *Energy Environ. Sci.* **2021,** *14* (11), 5723-5759.

133. Walsh, A., *J. Phys. Chem. C.* **2015,** *119* (11), 5755-5760.

134. (a) Weber, D., *Z Naturforsch B* **1978,** *33* (12), 1443-1445; (b) Wei, L.; Stroppa, A.; Wang, Z.-M.; Gao, S., *Hybrid organic-inorganic perovskites*. John Wiley & Sons: 2020.

135. (a) Kepenekian, M.; Even, J., *J. Phys. Chem. Lett.* **2017,** *8* (14), 3362-3370; (b) García-Fernández, A.; Juarez-Perez, E. J.; Bermúdez-García, J. M.; Llamas-Saiz, A. L.; Artiaga, R.; López-Beceiro, J. J.; Señarís-Rodríguez, M. A.; Sánchez-Andújar, M.; Castro-García, S., *J. Mater. Chem. C* **2019,** *7* (32), 10008-10018.

136. Zhao, X.-H.; Huang, X.-C.; Zhang, S.-L.; Shao, D.; Wei, H.-Y.; Wang, X.-Y., *J. Am. Chem. Soc.* **2013,** *135* (43), 16006-16009.

137. (a) Jain, P.; Ramachandran, V.; Clark, R. J.; Zhou, H. D.; Toby, B. H.; Dalal, N. S.; Kroto, H. W.; Cheetham, A. K., *J. Am. Chem. Soc.* **2009,** *131* (38), 13625-13627; (b) Abhyankar, N.; Kweon, J. J.; Orio, M.; Bertaina, S.; Lee, M.; Choi, E. S.; Fu, R.; Dalal, N. S., *J. Phys. Chem. C.* **2017,** *121* (11), 6314-6322.

138. (a) Rong, Y.; Hu, Y.; Mei, A.; Tan, H.; Saidaminov, M. I.; Seok, S. I.; McGehee, M. D.; Sargent, E. H.; Han, H., *Science* **2018,** *361* (6408), eaat8235; (b) Hei, X.; Li, J., *Chem. Sci.* **2021,** *12* (11), 3805-3817.

139. Xu, W.-J.; Kopyl, S.; Kholkin, A.; Rocha, J., *Coord. Chem. Rev.* **2019,** *387*, 398-414.

140. Grancini, G.; Nazeeruddin, M. K., *Nat. Rev. Mater.* **2019,** *4* (1), 4-22.

141. (a) Dohner, E. R.; Jaffe, A.; Bradshaw, L. R.; Karunadasa, H. I., *J. Am. Chem. Soc.* **2014,** *136* (38), 13154-13157; (b) Zhou, G.; Li, M.; Zhao, J.; Molokeev, M. S.; Xia, Z., *Adv. Opt. Mater.* **2019,** *7* (24), 1901335.

142. (a) Yang, T.; Li, Y.; Han, S.; Liu, Y.; Xu, Z.; Li, M.; Wang, J.; Ma, Y.; Luo, J.; Sun, Z., *J. Mater. Chem. C* **2020,** *8* (37), 12848-12853; (b) Tang, L.; Chen, H.; Ma, Y.; Liu, Y.; Hua, L.; Lu, L.; Wang, B.; Han, S.; Sun, Z.; Luo, J., *Inorg. Chem. Front* **2022**.

143. Zhang, H. Y.; Wei, Z.; Li, P. F.; Tang, Y. Y.; Liao, W. Q.; Ye, H. Y.; Cai, H.; Xiong, R. G., *Angew. Chem.* **2018,** *130* (2), 535-539.

144. Cao, Y.-J.; Zhou, L.; He, L.; Shi, P.-P.; Ye, Q.; Fu, D.-W., *Chem. Eur. J.* **2020,** *26* (62), 14124-14129.

145. Spaldin, N. A., *J. Solid State Chem.* **2012,** *195*, 2-10.

146. D., R., *Berry's Phase*. Springer, Berlin, Heidelberg: 2009.

147. (a) Resta, R., *Rev. Mod. Phys.* **1994,** *66* (3), 899-915; (b) Resta, R., *Europhys. Lett. (EPL)* **1993,** *22* (2), 133-138; (c) King-Smith, R. D. V., V, *Phys. Rev. B* **1993,** *47* (3), 4.

148. (a) Kresse, G.; Hafner, J., *Phys. Rev. B* **1993,** *47* (1), 558-561; (b) Kresse, G.; Furthmüller, J., *Computational Materials Science* **1996,** *6* (1), 15-50; (c) Kresse, G.; Furthmüller, J., *Phys. Rev. B* **1996,** *54* (16), 11169-11186.

149. (a) Wannier, G. H., *Phys. Rev.* **1937,** *52* (3), 191-197; (b) Wannier, G. H., *Rev. Mod. Phys.* **1962,** *34* (4), 645-655.

150. Gao, Y.; Guan, W.; Yan, L.-K.; Su, Z.-M., *J. Mater. Chem. C* **2020,** *8* (1), 219-227.

151. (a) Rohmer, M.-M.; Bénard, M.; Blaudeau, J.-P.; Maestre, J.-M.; Poblet, J.-M., *Coord. Chem. Rev.* **1998,** *178*, 1019-1049; (b) Bjorklund, J. L.; Bennett, J. W.; Forbes, T. Z.; Mason, S. E., *Cryst. Growth Des.* **2019,** *19* (5), 2820-2829.

152. Clemente-Juan, J. M.; Coronado, E.; Gaita-Ariño, A., *Chem. Soc. Rev.* **2012,** *41* (22), 7464-7478.

153. López, X.; Miró, P.; Carbó, J. J.; Rodríguez-Fortea, A.; Bo, C.; Poblet, J. M., *Theor. Chem. Acc.* **2011,** *128* (4), 393-404.

154. Jimenez-Lozano, P.; Carbo, J. J.; Chaumont, A.; Poblet, J. M.; Rodriguez-Fortea, A.; Wipff, G., *Inorg. Chem.* **2014,** *53* (2), 778-786.

155. (a) Long, D.-L.; Streb, C.; Song, Y.-F.; Mitchell, S.; Cronin, L., *J. Am. Chem. Soc.* **2008,** *130* (6), 1830-1832; (b) Ueda, T.; Yamashita, K.; Onda, A., *Appl. Catal. A: Gen.* **2014,** *485*, 181-187.

156. (a) Solé-Daura, A.; Notario-Estévez, A.; Carbó, J. J.; Poblet, J. M.; de Graaf, C.; Monakhov, K. Y.; López, X., *Inorg. Chem.* **2019,** *58* (6), 3881-3894; (b) Serapian, S. A.; Bo, C. *J. Phys. Chem. B* **2016**, 120 (50), 12959−12971; (c) Chaumont, A.; Wipff, G., *J. Phys. Chem. C* **2009**, 113 (42), 18233−18243.

157. (a) Xiao, W.; Li, S.; Zhao, Y.; Ma, Y.; Li, N.; Zhang, J.; Chen, X., *Dalton Trans* **2021,** *50* (25), 8690-8695; (b) Benseghir, Y.; Solé-Daura, A.; Mialane, P.; Marrot, J.;

Dalecky, L.; Béchu, S.; Frégnaux, M.; Gomez-Mingot, M.; Fontecave, M.; Mellot-Draznieks, C.; Dolbecq, A., *ACS Catal.* **2022,** *12* (1), 453-464.

158. Del Buono, G. S.; Figueirido, F. E.; Levy, R. M., *Proteins: Struct. Funct. Genet.* **1994,** *20* (1), 85-97.

159. (a) Cramer, C. J.; Truhlar, D. G., *Chem. Rev.* **1999,** *99* (8), 2161-2200; (b) Corrigan, R. A.; Qi, G.; Thiel, A. C.; Lynn, J. R.; Walker, B. D.; Casavant, T. L.; Lagardere, L.; Piquemal, J.-P.; Ponder, J. W.; Ren, P.; Schnieders, M. J., *J. Chem. Theory Comput.* **2021,** *17* (4), 2323-2341.

160. (a) Feig, M.; Brooks III, C. L., *Curr. Opin. Struct. Biol.* **2004,** *14* (2), 217-224; (b) Kleinjung, J.; Fraternali, F., *Curr. Opin. Struct. Biol.* **2014,** *25*, 126-134.

161. (a) Engler, E. M.; Andose, J. D.; Schleyer, P. V., *J. Am. Chem. Soc.* **1973,** *95* (24), 8005-8025; (b) Allinger, N. L.; Zhou, X.; Bergsma, J., *J. Mol. Struct. THEOCHEM* **1994,** *312* (1), 69-83.

162. (a) Hansson, T.; Oostenbrink, C.; van Gunsteren, W., *Curr. Opin. Struct. Biol.* **2002,** *12* (2), 190-196; (b) Hollingsworth, S. A.; Dror, R. O., *Neuron* **2018,** *99* (6), 1129-1143.

163. (a) Swendsen, R. H.; Wang, J.-S., *Phys. Rev. Lett.* **1987,** *58* (2), 86; (b) Fichthorn, K. A.; Weinberg, W. H., *J. Chem. Phys.* **1991,** *95* (2), 1090-1096.

164. Lieb, E. H.; Simon, B., *Commun. Math. Phys.* **1977,** *53* (3), 185-194.

165. (a) Parr, R. G., *Annu. Rev. Phys. Chem.* **1983,** *34* (1), 631-656; (b) Cohen, A. J.; Mori-Sánchez, P.; Yang, W., *Chem. Rev.* **2012,** *112* (1), 289-320.

166. Johnson, E. R.; Becke, A. D., *J. Chem. Phys.* **2005,** *123* (2), 024101.

167. Miró, P.; Poblet, J. M. P. M.; Ávalos, J. B. B.; Bo, C., *Can. J. Chem.* **2009,** *87* (10), 1296-1301.

168. (a) Klamt, A.; Schüürmann, G., *J. Chem. Soc. Perkin Trans. II* **1993,** (5), 799-805; (b) Barone, V.; Cossi, M., *J. Phys. Chem. A* **1998,** *102* (11), 1995-2001.

169. Falbo, E.; Penfold, T. J., *J. Phys. Chem. C.* **2020,** *124* (28), 15045-15056.

170. Kohn, W.; Becke, A. D.; Parr, R. G., *J. Phys. Chem.* **1996,** *100* (31), 12974-12980.

171. Zhang, G.; Baranov, M.; Wang, F.; Poblet, J. M.; Kozuch, S.; Leffler, N.; Shames, A. I.; Clemente-Juan, J. M.; Neyman, A.; Weinstock, I. A., *J. Am. Chem. Soc.* **2021,** *143* (49), 20769-20778.

172. Kremleva, A.; Aparicio, P. A.; Genest, A.; Rösch, N., *Electrochim. Acta* **2017,** *231*, 659-669.

173. Aparicio, P. A.; López, X.; Poblet, J. M., *J. Mol. Eng. Mater.* **2014,** *2* (01), 1440004.

UNIVERSITAT ROVIRA I VIRGILI
COMPUTATIONAL ANALYSIS OF THE CATALYTIC AND FERROELECTRIC PROPERTIES OF POLYOXOMETALATES
Fei Wang

Chapter 2. Goals of the Thesis

UNIVERSITAT ROVIRA I VIRGILI
COMPUTATIONAL ANALYSIS OF THE CATALYTIC AND FERROELECTRIC PROPERTIES OF POLYOXOMETALATES
Fei Wang

CHAPTER 2

Goals of the Thesis

This chapter presents the goals of the thesis, which are proposed after summarizing the current research achievements and major challenges in the field of catalysis and ferroelectricity of polyoxometalates in the previous chapter. The two primary goals are to give an in-depth understanding of the reaction mechanism in the catalytic reduction of CO_2 and the determination of the origin of ferroelectricity within the polyoxometalates salts.

■ The reaction mechanism in the catalytic reduction of CO_2:

Although the TM-substituted POM clusters are able to catalyze a large number of reactions, here, the present thesis only analyze their catalytic behavior on the CO_2 reduction. The electro- and photo-processes are considered in *Chapters 3* and *4*, respectively.

Chapter 3: Electrochemical Catalysis of the CO Oxidation and CO_2 Reduction Using Trimetallo-oxo POMs as Alternatives for Rare-metal Based Catalysts

The electrochemical catalysis of a series of trimetallic-POM clusters on the reversible CO_2-CO transformation is explored. With similar structures, the catalytic properties have considerable differences, where $[SiCu_3W_9]$ prefers to reduce CO_2 to CO whereas $[SiFeNi_2W_9]$ is highly reactive to transform CO to CO_2. In addition, $[SiCuGaFeW_9]$ shows the highest efficiency to reduce CO_2 to CO. To shed light on the differences in the catalytic activities of those trimetallic-POM clusters, MD simulations and DFT calculations are applied for the following specific goals:

- Explore the possible paths for activating those catalysts.
- Describe the interaction of POMs with small molecules by analyzing CO_2 and CO coordination models.
- Reveal the potential synergy effect between multiple substituted *d*-block TMs.
- Acquire an understanding of the highest efficiency of $[SiCuGaFeW_9]$.

Chapter 4: The Photocatalytic Behaviors of the Pure and Coordinated POM Clusters within the Multi-components Systems Reducing CO_2 to CO

A pure POM cluster ($[PW_{12}O_{40}]^{3-}$) connecting with a photosensitizer and a Re-based catalyst, and two coordinated clusters obtained by combining two types of metal-oxo fragments are studied. Their photocatalytic activities on CO_2 reduction are investigated by a combination method of DFT and CASSCF/CASPT2 calculations, in which several goals are contained:

For the three-components hybrid construct:

- Close the catalytic cycle by illustrating the essential intermediates
- Explore the proton-coupled multiple-electrons transfer among the three components.
- Clarify the role of the different components, especially the POM anion.
- Explain the important factors affecting the catalytic efficiency.

For the two coordinated clusters:

- Describe the interaction and reveal its influence on the electronic structure between the core and peripheral fragments.

■ The determination of the origin of ferroelectricity:

The other primary goal of the thesis is to analyze the ferroelectric properties of the Preyssler-POM clusters, especially to clarify several unclear but important points by computational methods.

Chapter 5: Density Functional Theory Analysis of Single-molecule Ferroelectricity in Preyssler-type Polyoxometalates

Considering the structural complexity of the Preyssler clusters and the fact that ferroelectricity is a fully uncharted area for the POM chemistry, it is essential to explore the methods for computing ferroelectric polarization in a relatively simple but common ferroelectric system. Therefore, a HOIP, $(AMP)PbI_4$ (AMP = 4-aminomethyl-piperidinium) is selected as the first object to work on in *Chapter 5*, where the goals can be summarized as:

- Explore the computing method of the ferroelectric polarization.
- Calculate the Rashba parameters related to the spin-orbit interactions.
- Explain the coexistence phenomenon of ferroelectricity and the Rashba effect.

Chapter 6: Density Functional Theory Analysis of Single-molecule Ferroelectricity in Preyssler-type Polyoxometalates

Based on the validated polarization-computing method in the previous work, *Chapter 6* is aimed to provide an in-depth analysis on the single-molecule ferroelectricity of the Preyssler-type POMs $[M^{3+}P_5W_{30}O_{110}]^{12-}$ (M = La, Gd and Lu) by DFT calculations, in which there are a number of goals:

- Ascertain the possible presence a water molecule linked to the cation (M^{3+}) encapsulated in the cavity of the Preyssler framework.
- Illustrate the complete path for the switching of the M^{3+} ion between two isoenergetic sites on both sides of the cavity, including calculating the barrier.
- Compute the polarization.
- Identify the origin of the ferroelectric feature within the POM cluster by determining the contributions of the different parts: the framework, the encapsulated M^{3+} center, and the counter-cations.

UNIVERSITAT ROVIRA I VIRGILI
COMPUTATIONAL ANALYSIS OF THE CATALYTIC AND FERROELECTRIC PROPERTIES OF POLYOXOMETALATES
Fei Wang

Chapter 3. Electrochemical Catalysis of the CO Oxidation and CO_2 Reduction Using Trimetallo-oxo POMs

UNIVERSITAT ROVIRA I VIRGILI
COMPUTATIONAL ANALYSIS OF THE CATALYTIC AND FERROELECTRIC PROPERTIES OF POLYOXOMETALATES
Fei Wang

CHAPTER 3

Electrochemical Catalysis of the CO Oxidation and CO_2 Reduction Using Trimetallo-oxo POMs

This chapter explores the electrochemical catalysis of the reversible CO_2-CO transformation of a series of trimetallic-oxo POMs that can be considered an alternative for rare-metal-based catalysts. To gain an in-depth insight into the different catalytic activities of two POM clusters, where $[SiCu^{II}_3W_9]$ prefers to reduce CO_2 whereas $[SiFe^{III}Ni^{II}_2W_9]$ is favorable in oxidizing CO, MD simulations and DFT calculations are applied to model their redox behaviors in an acetonitrile solution containing a small amount of water. Taking the nuclearities and configurations of the substituted d-block TM into account, this present work focuses on the activation of the catalysts by considering several possible pathways which involves multiple steps of protonation and reduction. To provide a better understanding on the interaction of POMs with small molecules instead of revealing the catalytic cycle of CO_2 reduction to CO that has been widely studied, the coordination of CO_2 and CO to the catalysts are examined in which the synergy effect between multiple TMs is elucidated. Moreover, this chapter also analyzes the redox activity of $[SiCu^{II}Ga^{III}Fe^{III}W_9]$, which is reported as the most reactive catalyst for CO_2 reduction in the trimetallic-oxo POM clusters. The special roles of the Ga^{III} center working as a Lewis acid site, as well as the unusual redox potentials of this cluster where the potential required to reduce Cu^{II} is lower than Fe^{III}, are both illustrated by presenting an unusual double-bonding model of CO_2 coordination, which greatly enhances its ability to fix CO_2.

This work is done in collaboration with the experimental group of Prof. Ronny Neumann (Weizmann Institute of Science, Israel), and part of it has been published with the title of "Molecular Transition Metal Oxide Electrocatalysts for the Reversible Carbon Dioxide–Carbon Monoxide Transformation" (https://doi.org/10.1002/anie.202112915)

3.1 Background

The dwindling fossil fuels, and their non-renewability underscore the importance of the conversion of CO_2 into fuels and other chemicals by using renewable energy.[1] Fixing and transforming CO_2 through an electrochemical process is regarded as a

promising strategies.[2] Operated at mild conditions, electrochemical processes can be selectively tuned towards products and allow modular design, providing opportunities to integrate renewable electricity with CO_2 reduction for industrial-scale mass production.[3] The remarkable advances have been achieved in developing highly efficient and selective catalysts for electrochemical CO_2 reduction in recent years.[4]

The lacunary POMs generated by the loss of one or more MO_6 polyhedra of the saturated Keggin-/Dawson-type clusters[5] are highly active to all kinds of TM ions. They can serve as good multidentate oxo ligands to induce TM ions to form high-nuclear clusters, giving rise to a class of TM-substituted POMs (TMSPs) with significantly improved properties.[6] In recent years, driven by their catalytic and magnetic properties as well as structural aesthetic appreciation, the chemistry of TMSPs has attracted much attention. A lot of unique POM examples with a higher number of TMs have been designed and synthesized, which are reported to own fascinating electronic properties and many useful applications.[7] The incorporation of the TM cations that can fix or bind CO_2 where the site for CO_2 reduction resides at the metal center makes TMSPs can be considered as the potential CO_2 electrocatalysts, which allow a myriad of possibilities to direct catalytic activity and selectivity, simply by the choice of the active metal(s). Since Yamase observed the CO_2 reduction to CH_4 in water catalyzed by a di-Ti-substituted Keggin ion $[PTi_2W_{10}O_{40}]^{7-}$ in 1990,[8] TMSPs have been used for the reduction of CO_2 in the past decades.[9] Ronny's group demonstrated that $[RuSiW_{11}O_{39}]^{5-}$ could promote the CO_2 reduction to CO in toluene,[10] and Girardi *et. al.* reported $[CoSiW_{11}O_{39}]^{6-}$ to be an electrocatalyst for the CO_2 reduction to CO in the presence of acid yielding formaldehyde.[11] What is more, the Rh^{III} was also incorporated in the form of $[Cp^*(bpy)Cl]^+$ (Cp^* = pentamethyl-cyclopentadienyl anion; bpy = 2,2′-bipyridine) to generate the catalyst $[\alpha\text{-}H_2PW_{11}O_{39}[Rh^{III}Cp^*(OH_2)]]^{3-}$ which is capable of catalyzing the CO_2 reduction.[12] Those reports demonstrate the feasibility of TMSPs being used as the electrocatalysts of CO_2 although there are some problems. On the one hand, those results were limited where the vast majority of molecular electrocatalysts are restricted to single site TM compounds. On the other hand, the introduction of TMs may produce unprecedented nanocluster cores, change the oxidation states, particularly of transition and rare earth metal ions, and also affect the shell functionalities by increasing/decreasing the vacant positions in POMs and thus result in the formation of new basic building blocks by the serendipitous molecular assembly. Therefore, rational tailoring of their structural

features of TMSPs remains a challenge which can be improved by exploring the conformation and property relationships through theoretical calculations.

Very recently, Ronny's group synthesized a novel, modular catalyst framework which involves the use of tri-TM substituted POMs $[SiM_3W_9]$. M_3 can be Cu_3, Fe_3, Ni_3, $CuFe_2$, Cu_2Ni, $CuNi_2$, Fe_2Ni and $FeNi_2$, or be a combination of transition and main metals, Cu_2Ga, $CuGaFe$ and Cu_2Al. Figure 3.1 shows the structural representation of $[SiM_3W_9]$. A catalytic Tafel plot by experiments shows that the tri-Cu-substituted polyanion $[SiCu_3W_9]$ is highly reactive for CO_2 reduction with a 98% faradaic efficiency yielding a significant amount of CO. In contrast, the Fe-Ni compound, e.g. $[SiFeNi_2W_9]$, prefers to catalyze CO oxidation to CO_2. Given the fact that although the lacunary POMs can almost encapsulate all TMs, including the same kind of metal ion with different valances, the paramagnetic 3*d* metals Mn, Fe, Co, Ni, and Cu with rich electronic and magnetic properties are of special interest, and therefore POMs incorporating those TMs represent the five most intensely studied subclasses of TMSPs.[13] It is significant to gain an in-depth understanding into the different catalytic activities under the electrocatalytic conditions of the two tri-TM substituted clusters, $[SiCu_3W_9]$ and $[SiFeNi_2W_9]$ from a theoretical view. Moreover, the redox activity of $[SiCuGaFeW_9]$ is also worthy of further exploration, which is observed to be the most reactive catalyst for CO_2 reduction in those trimetallic-oxo POM clusters. Especially, the role of the Ga^{III} needs to be clarified for a better understanding of its highest efficiency as the electrocatalyst of CO_2 reduction to CO.

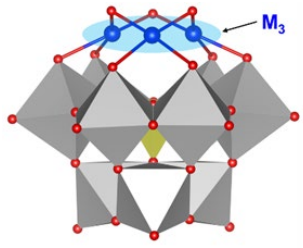

Figure 3.1. Combined polyhedral and balls-and-stick representation of the trimetallo(M_3)-substituted POM. Color code: bule (metal, M); red (O); gray polyhedral ($[W_9]$)

Hence, we apply MD simulations and DFT calculations to model their redox behaviors, especially explore the possible paths for activating the catalysts in acetonitrile solution. The nuclearities and configurations of the encapsulated *d*-block TM are considered, especially the synergy effect between multiple TMs on the

coordination of CO_2 and CO. Whereas the Ni(I) center of the Fe-Ni derivative can easily react with CO and CO_2, only one Cu(I) center of the tri-Cu_3 catalyst does not react with CO_2 unless two electrons have been injected to form two Cu(I) centers, which cooperates to reach an active Cu(0) center during CO_2 approaching. As a Lewis acid site, the Ga(III) center brings in one more coordinating site for CO_2, making it possible to form a double-bonding model Ga-O-C-O(Cu) between CO_2 and the cluster, which greatly enhances its ability to fix CO_2. As a result, this cluster is capable of coordinating CO_2 before any reduction and leading to a decreased potential for reducing Cu^{II} even lower than Fe^{III}. Our calculations lead to an understanding of binding reactions and possible relevant reaction intermediates, providing a characterization of the ability of M_3O_3-POM catalysts to react with CO_2 and CO in electrolytical conditions.

3.2 Computational Details

Molecular Dynamics: Atomistic MD simulation was performed to determine the cation distribution around the M_3-POMs in different solvents using the GROMACS 5.1.2 code[14] and the AMBER 99 Force Field,[15] which has been satisfactorily employed to study the aggregation of POMs in different environments.[16] POM force-field parameters were obtained following the procedure by Bonet-Ávalos *et al.*[17] CHelpG atomic charges were obtained with the Gaussian16 package[18] at the same level of density functional theory was used. For the MD trajectory, a cubic box of ca. 9.4 nm side was calculated in 3D-periodic boundary conditions, containing one M_3-POM anion, 60 TBA, 50 PF_6, 278 water molecules and the embedding MeCN for ca. 2 mM POM concentration and 1% v/v water concentration. The TIP3P water model[19] was used to represent H_2O molecules, and MeCN was described by the full-atom model provided by van der Spoel *et al.*[20] For 1-4 van der Waals interactions we applied an atom cutoff of 14 Å, and for Coulombic interactions of 10 Å corrected for long-range electrostatics by using the particle-particle mesh Ewald (PME) summation method. Production trajectory was performed within a canonical (NVT) ensemble during 20 ns, collecting data from every 1 ps. Simulation was carried out at 298 K, controlling the temperature by coupling the system to a thermal bath using the velocity-rescaling algorithm. Before production run, the system was equilibrated by a successive NVT fixed solute–NPT–NVT relaxed solute 500 ps simulations.

DFT calculations: All DFT calculations were performed by employing the Gaussian16 A.03 program package.[18] The geometries optimizations and vibrational frequency calculations were carried out using the hybrid B3LYP exchange-correlation functional. The WB97XD function was also used for a comparison, by which we obtained very similar results with B3LYP. The LanL2DZ effective core potential (ECP) basis set was applied for Fe, Ni, Cu, Ga and W atoms while the 6-31+G* basis set was used for the remaining H, C, O, and Si atoms. The implicit solvation model IEF-PCM was adopted to include the solvent effect of MeCN. Since MD calculations show that the water molecules form a shell around the POM, inside the shell of acetonitrile molecules, the water effect was also consid by using IEF-PCM. All reported reduction potentials are referenced to the Fc/Fc^+ couple. The value of 4.99 V reported by Namazian *et al.*[21] is used as the absolute potential of Fc/Fc^+ in acetonitrile. Other estimates of the absolute value of this potential reported in the literature[22] range from -4.88 to -5.17 V, with a median of 5.00 V.

3.3 Results and Discussion

3.3.1 The protonation degree of the M_3-POMs catalysts

The first point to consider is the effect of the presence of small amounts of water in the medium, because water is probably the proton source needed for CO_2 reduction to CO. Small amounts of water can help to stabilize the system and the catalytic activity of the complex is not affected by adding up to 1% extra water, whereas larger amounts reduce the hydrolytic stability of the POMs under the reducing conditions. It suggests that the experiments were done in slightly humid acetonitrile. To analyze whether the water molecules are preferentially located around the POM anion and are involved in the catalytic cycle, classical MD simulations were carried out on $[SiFe^{II}Ni^{II}_2W_9]$. The calculations showed that the initially randomly distributed water molecules with a low concentration of 1% rapidly form a double shell around the POM cluster within 20 ns, expelling all solvent acetonitrile molecules and quaternary ammonium cations from this region, see Figure 3.2a-c. As expected from the molecular electrostatic potential (MEP) distribution, Figure 3.2d, the $Fe^{III}Ni^{II}_2O_3$ unit is more basic and attracts more water molecules.

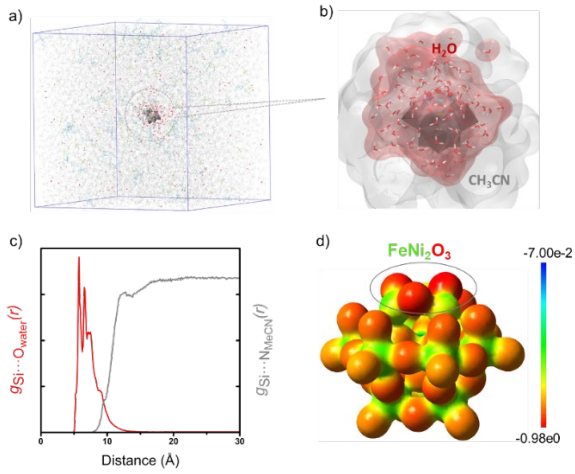

Figure 3.2. a) and **b**) Representation of the water and acetonitrile shells around the $[SiFe^{II}Ni^{II}_2W_9]$ anion obtained from a 20 ns classical MD simulation snapshot. **c**) POM···water and POM···MeCN radial distribution functions (RDFs) computed from MD simulations, taking as reference the internal Si atom of the POM. The gSi···Owater(r) and gSi···NMecN(r) RDFs are in red and gray, respectively. **d**) Computed molecular electrostatic potential (MEP) distribution for $[SiFe^{III}Ni^{II}_2W_9]$.

3.3.2 Pathways for activating the catalysts

To prove that the presence of water is essential to stabilize the POM anion under the reaction conditions, we have determined the degree of protonation of $[SiFe^{III}Ni_2W_9]$ as a result of reduction upon application of potential. Scheme 3.1 shows the conceivable pathways to activate the catalyst $[SiFe^{III}Ni^{II}_2W_9]$ after applying a potential. In absence of any protonation, the Fe^{III} center is first reduced at -2.8 V vs Fc/Fc^+.[22b] It is worth mentioning that the simple presence of water in contact with the POM permits its protonation, as emphasized by the large exergonic values computed for the first and second protonation without electron reduction of the POM. These values were computed from the reaction POM + $H_2O \rightarrow HPOM^+ + OH^-$ in acetonitrile. This means, for example, that if the M_3O_3 unit is protonated twice, the reduction potential of the Fe^{III} ion decreases by 1.7 V. However, the second electron reduction, which involves one of the two Ni centers, still requires -3.6 V (-3.2 V in water). However, given that the protonation free energy of $[SiFe^{II}Ni^{II}_2W_9]$ is still very exergonic, -25.2 kcal mol^{-1} (-19.9 kcal mol^{-1} in pure water), it is reasonable to assume that the active species reacting with CO_2 or CO is the three-fold protonated form of the catalyst, $H_3[SiFe^{II}Ni^{I}Ni^{II}W_9]$. The reduction potentials computed for this species

are -3.2 V in pure acetonitrile, similar to the optimal potential in the CV measurement (-3.0 V vs Fc/Fc^+) and -2.9 V in pure water. Probably, the real value is in between these values, and would agree with potentials used in the experiments. A similar analysis was performed on the $[SiCu^{II}_3W_9]$ derivative.

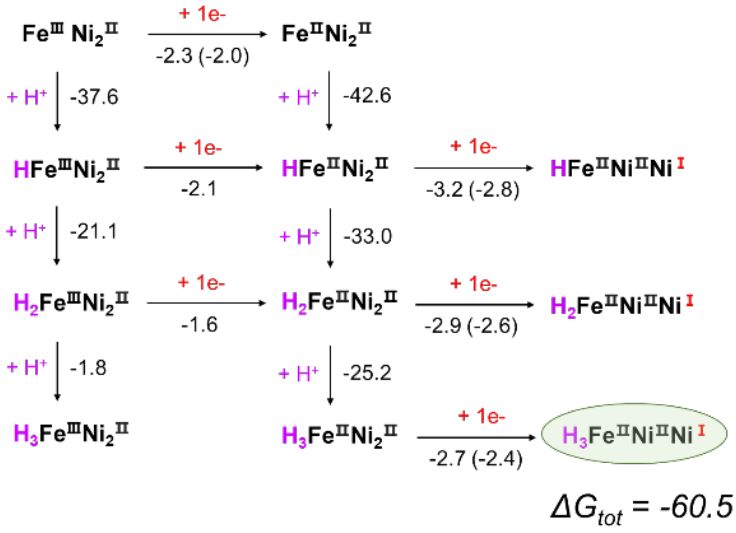

Scheme 3.1. Multiple steps of reduction and protonation of $[SiFe^{III}Ni^{II}_2W_9]$. The computed potential values in acetonitrile and in water (in parenthesis) are in V vs Fc/Fc^+. The reaction free energies for the protonation steps are in kcal mol^{-1}.

The possible pathways for activating the catalyst were also considered and summarized in Scheme 3.2. In the absence of any electron reduction, $[SiCu^{II}_3W_9]^{10-}$ is somewhat easier to tri-protonate (ΔG = -77.0 kcal mol^{-1}) than $[SiFe^{III}Ni^{II}_2W_9]^{9-}$ (ΔG = -60.5 kcal mol^{-1}). Therefore, we have assumed that the tri-cupper derivative is also triply protonated. For $[SiH_3Cu^{II}_3W_9]^{7-}$, the first electron reduction potential was computed to be only -1.9 V, much lower than the potential used in the experiments (-2.5 V), suggesting that it is possible to incorporate one more electron into the catalyst below of the applied potential. Indeed, the potential for the second electron was found to be -2.4 V, still lower than -2.5 V.

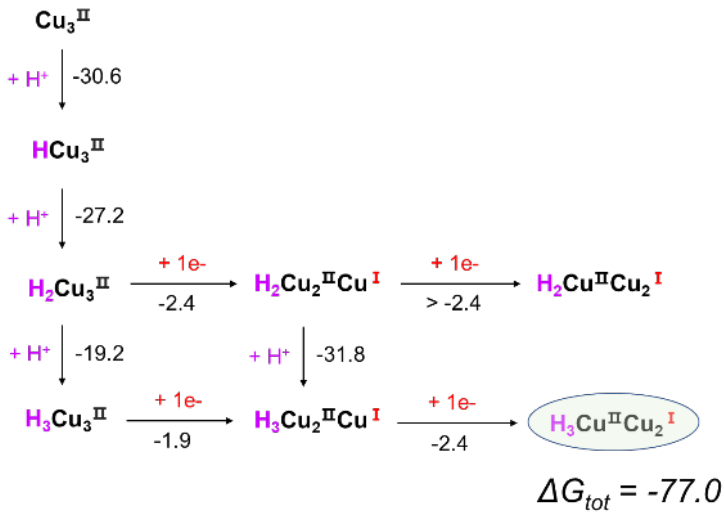

Scheme 3.2. Multiple steps of reduction and protonation of $[SiCu^{II}_3W_9]$. The computed potential values in acetonitrile and in water (in parenthesis) are in V vs Fc/Fc^+. The reaction free energies for the protonation steps are in kcal mol^{-1}.

The structural changes and the atomic spin densities distributions related to the M_3O_3 motif during the two-electron reduction of the $H_3[SiFeNi_2W_9]$ and $H_3[SiCu_3W_9]$ clusters are presented in Figure 3.3. For $H_3[SiFeNi_2W_9]$, the coordination bond lengths with five O ligands to each Ni and Fe center are all about 2.0 Å, giving spin densities of the Ni of 1.70e and the Fe of 4.20e. They are in line with the formal electronic configurations of d^8 for the Ni^{II} and d^5 for the Fe^{III} ions. The first injected electron localizes at the Fe center, decreasing the spin density to 3.77e, corresponding to the electronic structure d^6 of the high-spin Fe^{II}. As expected, the second electron enters one of the Ni centers forming a d^9 species with a spin density of 0.90e, which is a highly reactive species. Within $H_3[SiCu_3W_9]$, the Mulliken spin density computed for the Cu^{II} with d^9 electrons is 0.63e. Then the first extra electron locates on one of the Cu centers, decreasing the spin density to almost 0 (0.02e), in full agreement with the electronic structure of d^{10} for Cu^I, while the spin densities on the other two Cu^{II} ions remain 0.62e. One of coordination bond lengths of the O ligands of the Cu^I extends from 2.042 to 3.040 Å, which can be considered as the loss of that O ligand. Thereby, the coordination field of Cu^I with d^{10} electrons deforms to be trigonal-bipyramidal-like with an upwards doubly occupied dz^2 orbital, which will be beneficial to coordinate a CO_2 molecule. With the second electron injected, one more Cu^{II} is reduced whose spin density decreases to 0.01e. Hence, there are two Cu^I in the two-electrons reduced Cu_3-POM anion.

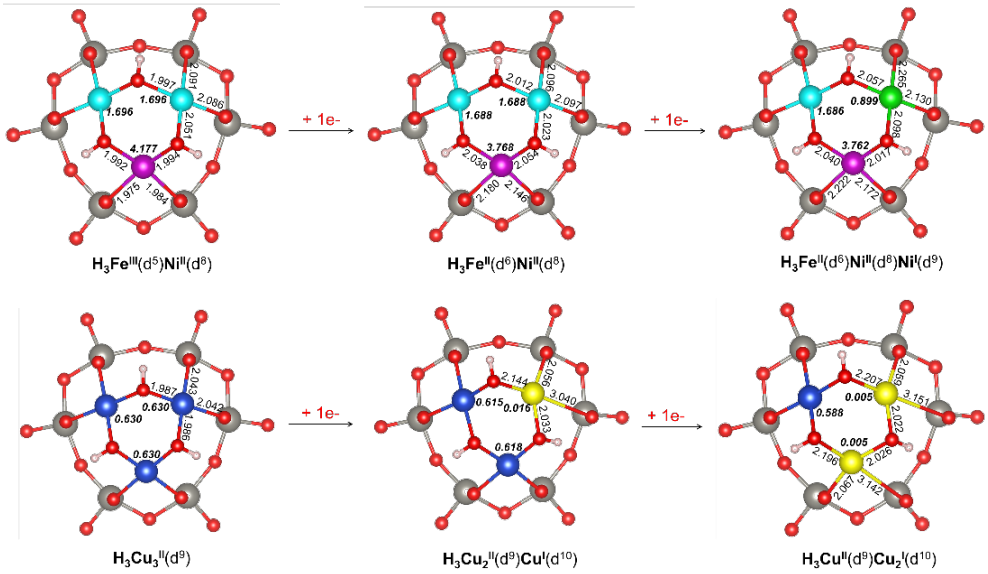

Figure 3.3. The structural representation of the H_3FeNi_2- and H_3Cu_3-POM as well as the corresponding reduced states. The main distances (in angstroms) are shown in black numbers and the spin densities are highlighted in yellow. Color code: cyan (Ni^{II}), green (Ni^{I}), blue (Cu^{II}), yellow (Cu^{I}), purple (Fe), red (O), pink (H) and gray (W). POM clusters are hidden for clarity.

3.3.3 The single-bonding coordination of CO and CO_2

The CO_2 and CO coordination models are discussed in this section where the electronic structures of the polyanions are examined before and after coordination. It is difficult to track the extra electrons when there are multiple reactive metal centers with numerous unpaired electrons in the $Fe^{III}_2Ni^{II}$- and Cu^{II}_3-derivatives. Hence, we firstly decrease the amount of the reactive sites by replacing two Fe^{III} and Cu^{II} ions with Zn^{II} ions with the d^{10} closed shell, forming two simplified models, $H_3[SiZn_2NiW_9]$ and $H_3[SiZn_2CuW_9]$, respectively. A ball-and-stick representation including main bond lengths, atomic spin densities and charges of the M_3O_3 unit within the steps of one-electron reduction and CO_2 coordination can be seen in Figure 3.4. After being activated by one electron, the distance between the Ni^{I} center and CO_2 is 2.191 Å where the O=C=O fragment bends up to 137.4°. The relative electronic energy (ΔE) is rather exothermic, -10.8 kcal mol^{-1} which demonstrates that a moderate bond can be formed between Ni^{I} and CO_2. On the contrary, the distance between CO_2 and the Cu^{I} ion generated after one electron injecting the $H_3[SiZn_2CuW_9]$ cluster is 3.579 Å, much

longer than other works reported about the distance of C-Cu (only about 2.0 Å).[23] The O=C=O molecule is almost linear with an angle of 175°. These structural facts together with the lack of electron transfer from the Zn_2CuO_3 fragment to the CO_2, clearly suggest that a POM with only one Cu^I ion is not capable of forming a bonding interaction.

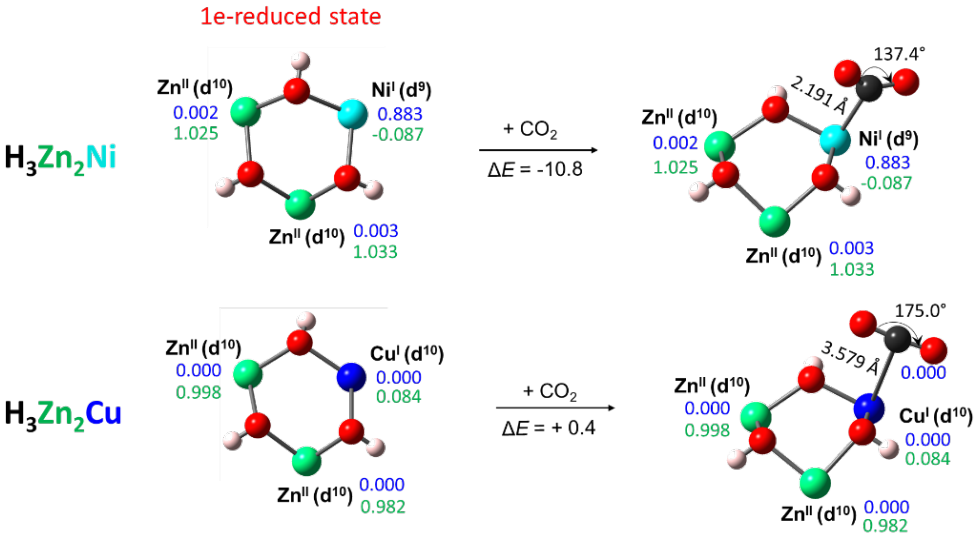

Figure 3.4. The structural representation of the M_3O_3 motifs of the $[H_3Zn_2Cu]$ and $[H_3Zn_2Ni]$ clusters associated with the 1e-reduction and CO_2 coordination steps. The Milliken charges and spin densities are shown in green and blue numbers, respectively. Color code: blue (Cu), green (Zn), cyan (Ni), red (O), pink (H), and black (C).

Bearing the preliminary conclusions obtained on the simplified models in mind, the attention is turned to the $[SiFeNi_2W_9]$ and $[SiCu_3W_9]$ clusters. The optimized structures associated with the steps of CO_2 and CO coordination for $H_3[SiFe^{II}Ni^{I}Ni^{II}W_9]$ are shown in Figure 3.5. The reaction energies of CO_2 and CO binding to Ni^I were found to be -11.2 and -12.4 kcal mol^{-1}, respectively. The Ni-C bond lengths of 2.192 Å (CO_2) and 1.962 Å (CO) seen in Table 1, as well as the acute O=C=O angle of 137.5° for CO_2 complexation, are in line with the rather strong interaction between both molecules and $H_3[SiFe^{II}Ni^{II}Ni^{I}W_9]$. The free energies are less favorable due to the entropic contribution, but still negative for the diprotonated anion (-1.7 kcal mol^{-1}) and slightly positive for the triprotonated form (+0.3 kcal mol^{-1}). The associated free energy barriers are very low, less than 4 kcal mol^{-1}. The reaction of $H_3[SiFe^{II}Ni^{I}Ni^{II}W_9]$ with CO is slightly preferred to that with CO_2, which would be in line with the experiments. These values clearly provide evidence that the reduced

Ni^{I} center is prone to react with both CO_2 and CO. Moreover, the similarity of the computational results of the $FeNi_2$-and Zn_2Ni-derivatives illustrates that the active Ni(I) center is independent from the other metal centers (Ni^{II} and Fe^{II}) and can bond small molecules on its own.

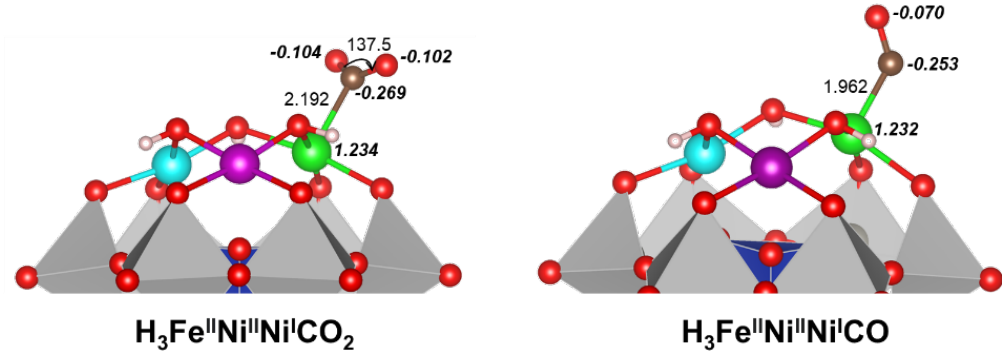

Figure 3.5. The structural representation of $H_3[SiFe^{II}Ni^{I}Ni^{II}W_9]$ (**a**) and models for CO_2 and CO coordination (**b** and **c**). The angles (in degrees) and main distances (in angstroms) are shown in black numbers and the spin density is in italic and bold. Color code: Cyan (Ni^{II}), green (Ni^{I}), purple (Fe^{II}), red (O), pink (H) and gray (W).

Table 1. Electronic and free energies computed for the coordination of CO_2 and CO to $H_x[SiFe^{II}Ni^{I}Ni^{II}W_9]$.[(a)]

	CO_2			CO		
	ΔE_r	ΔG_r	$\Delta G^{\#}$	ΔE_r	ΔG_r	$\Delta G^{\#}$
$HFe^{II}Ni^{I}Ni^{II}$	-13.3	-3.3	+1.2	-11.6	-1.3	+1.6
$H_2Fe^{II}Ni^{I}Ni^{II}$	-14.5	-1.7	+2.7	-14.6	-4.3	+0.5
$H_3Fe^{II}Ni^{I}Ni^{II}$	-11.2	+0.3	+3.6	-12.4	-1.2	+1.8

a) ΔE_r and ΔG_r represent the electronic and free energies, respectively, whereas $\Delta G^{\ddagger}$ values represent the free energy barriers. All energies are in kcal mol^{-1}.

Figure 3.6 shows the coordination of CO_2 to the Cu_3O_3 fragment for the 1e- and 2e-reduced anions, respectively. For the 1e-reduced state, the similar results as the $[SiZnCu_2W_9]$ are obtained, where the optimized distance between Cu^{I} and CO_2 is 3.578 Å and the O=C=O is almost linear with an angle of 175.0°. These calculated results validate that–an isolated Cu^{I} ion cannot bind a CO_2 molecule, which is consistent with the experimental observation that a simple mono-copper substituted

POM, $[SiCu^{II}W_{11}O_{39}]^{6-}$ was inactive to CO_2/CO, proving the conjecture that at least two Cu cations are required for catalysis. The situation radically changes when a second electron is incorporated to the Cu_3O_3 motif, and a second Cu^I is generated. The distance between C and Cu is 2.086 Å and the O=C=O is bent to 130.9°. Combining with a spin density transfer of 0.43e from the Cu center to the CO_2 molecule, it shows that the 2e-reduced state is able to coordinate CO_2 after an endothermic reaction of +7.8 kcal mol^{-1}. The reason why the Cu_3 derivative requires two electrons to activate is clarified in the following section.

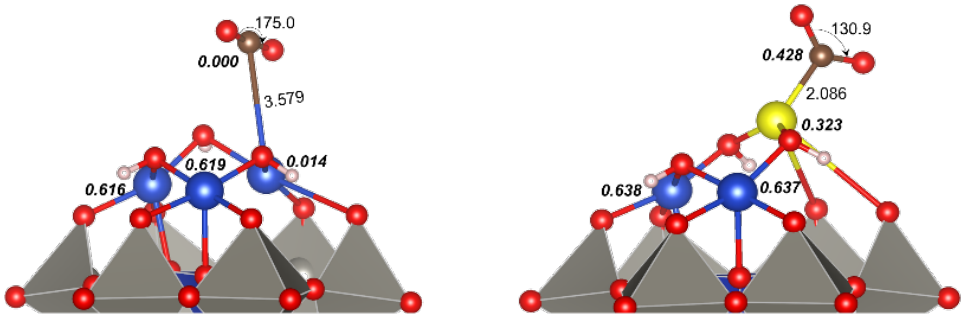

Figure 3.6. The structural representation of the $[SiCu^{II}_3W_9]$ catalyst in the oxidized and reduced states (the upper panel) and the ball-stick models of CO_2 and CO coordination (the lower panel). The angles (in degrees) and main distances (in angstroms) are shown in black numbers and the spin density are highlighted in green. Color code: blue (Cu^{II}), yellow (Cu^I), red (O), pink (H) and gray (W). POM clusters are hidden for clarity.

To analyze the different abilities in coordinating CO_2, the electronic structures of $Ni^{II}_2Fe^{II}$ and Cu^{II}_3 derivates associated to the electron reduction and CO_2 coordination steps are examined. The spin density distribution on the metal centers is further decomposed here according to the orbital quantum number. As shown in Scheme 3.3, the spin population on the *d* orbitals of the Ni^I center before and after CO_2 coordination is 1.02e and 1.46e, respectively, which demonstrates that the d^9 species can bind CO_2 by sharing one beta electron. Therefore, formally the oxidation state would in between Ni^I and Ni^{II}. However, the Cu_3-POM requires to be doubly reduced to form two Cu^I centers, to reach a Cu^0 oxidation state through one electron transferring from one Cu^I to the other one during CO_2 approaching. Then the open-shell Cu^0 with an electronic configuration of $d^{10}s^1$ is the active center to form a bond with CO_2, which also involves a partial electron transfer from Cu^0 to CO_2, thus the

oxidation of the metal center would be in between Cu^0 and Cu^I. Since only one Cu^0 can be formed able to coordinate one CO_2 molecule at a time, the formation of C_2 products often observed for Cu_x-based materials is prevented, leading to selective formation of CO. Generally, for both the $H_3[SiCu^{II}Cu^{I}_2W_9]$ and $H_3[SiFe^{II}Ni^{I}Ni^{II}W_9]$ compounds, there is a metal to ligand transfer of ~0.5e upon coordination to CO_2. Those computational results illustrate the influence of the nuclearities and configurations of the substituted *d*-block TMs of POMs on the interaction with small molecules where the synergy effect might exist, which should be taken into account when designing the electrocatalysts.

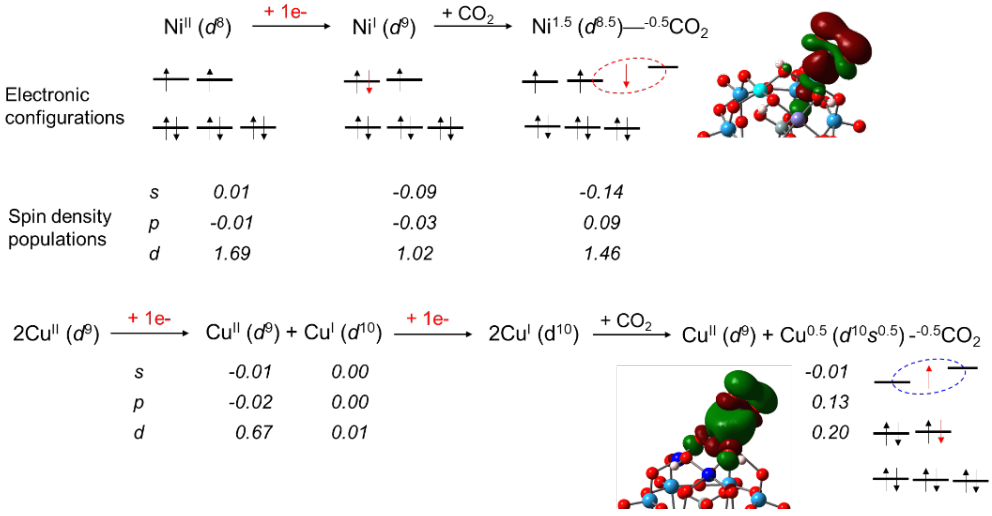

Scheme 3.3. Schematic representation of the electronic structures of $Ni^{II}_2Fe^{II}$ and Cu^{II}_3 derivates associated to the electron reduction and CO_2 coordination steps.

3.3.4 The double-bonding coordination of CO and CO_2

A double-bonding coordination mode is more favorable when a Ga^{III} is introduced to the M_3O_3 motif of the POM cluster, where the other two metals are Cu^{II} and Fe^{III}. As shown in Figure 3.7, one of the O atoms of CO_2 is bonded to the Ga^{III} with a short distance of 2.006 Å where the Ga^{III} is considered working as a Lewis acid site. The C atom is bonded to the O atom between the Ga and Cu ions, written as $O(Cu^{II})$, with a distance of 1.335 Å. Hence there are two bonds between the M_3O_3 unit with the CO_2 molecule. This double-bonding mode, Ga-O-C-O(Cu), is so strong with a ΔE of -41.8 kcal mol^{-1} and a ΔG of -28.3 kcal mol^{-1} that it can fix CO_2 before any

reduction reaction. The first and second potentials computed for the species bonded with CO_2 are -1.66 and -2.23 V, which corresponds to the reduction of the Cu^{II} and Fe^{III} ions. The results are in line with the experimental observation. According to the experiments, the capacitance–voltage (CV) measurement on the GaFeCu-POM shows two potential regions within this complex, less negative peak at -1.5 V and more negative at -2.5 V, which are assigned to the contribution of the reduction of the Cu^{II} and Fe^{III}, respectively. However, the first potential required for the tri-Cu derivative is about 1 V more negative than here. The reason for the low potential of Cu^{II} is probably because the formation of the double-bonding model with CO_2 that can diffuse the electron densities on the O(Cu^{II}) atom as well as the adjacent Cu^{II} ion by those empty orbitals within CO_2, making it easier for the Cu^{II} center to accept an extra electron. Therefore, the double-bonding model of CO_2 can be considered as one of the reasons why this cluster shows the best catalytic performance at reducing CO_2 as well as the low potential required.

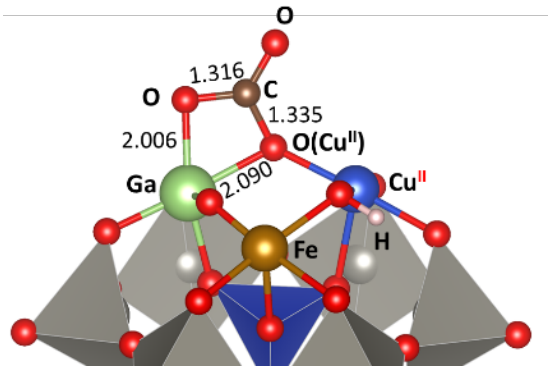

Figure 3.7. The structural representation of the CO_2 coordination to the [$SiCuGaFeW_9$] catalyst before any reduction reaction. The angles (in degrees) and main distances (in angstroms) are shown in black numbers.

3.4 Concluding Remarks

To summarize, the present analysis has provided a characterization of the ability of M_3O_3-POM catalysts to react with CO_2 ad CO in electrolytical conditions. Classical MD simulations showed that 1% water randomly dissolved in an acetonitrile solution of [$SiFe^{II}Ni^{II}_2W_9$] migrates within 20 ns to the surface of [$SiFe^{II}Ni^{II}_2W_9$] to form a double shell of water around the polyanion, preferentially at the more basic $Fe^{II}Ni^{II}_2O_3$ unit. A further analysis of the degree of protonation by static DFT calculations showed

that the triprotonated, 2-electron reduced species, $H_3[SiFe^{II}Ni^{II}Ni^{I}W_9]$ and $H_3[SiCu^{II}Cu^{I}_2W_9]$, are those active in CO_2 and CO binding and activation. For $H_3[SiFe^{II}Ni^{II}Ni^{I}W_9]$, binding of CO_2 and CO occurs at the Ni(I) center with true bonding interactions as evidenced by the Ni@C bond lengths commensurate with coordination and the formation of strongly nonlinear C@O bonds. The binding reactions are found to be exergonic for both CO and CO_2 coordination with small activation barriers, ΔG^*, indicating that substrate binding is not rate determining.

In contrast, only one Cu(I) ion is not able to bond with CO_2 unless two Cu(I) ions are formed after receiving two electrons, which can generate a species with a $H_3[SiCu^{II}_2Cu^{0}W_9]$ electronic configuration during the CO_2 approaching. Eventually, CO_2 is bound to the Cu^0 atom. This reaction appears to be endergonic indicating that it may be involved in the reaction's rate-determining step. Generally, for both the $H_3[SiCu^{II}Cu^{I}_2W_9]$ and $H_3[SiFe^{II}Ni^{I}Ni^{II}W_9]$ compounds, there is a metal to ligand transfer of ~0.5e upon coordination to CO_2. The presence of a Lewis acid center Ga^{III} in $[SiCuGaFeW_9]$ brings one more site to coordinate CO_2 which enables this cluster to coordinate a CO_2 molecule by a double-bonds mode before any reduction step. As a result, the potential required to reduce the Cu^{II} after CO_2 coordination decreases by 1 eV, even lower than that of Fe^{III}. Those computational results illustrate the influence of the nuclearities and configurations of the encapsulated *d*-block TMs on the coordination of CO_2 where the synergy effect between multiple TMs could exist. Our findings described here will contribute to understand the interaction of POMs with small molecules and also further the design of new POM based CO_2 reduction catalysts.

UNIVERSITAT ROVIRA I VIRGILI
COMPUTATIONAL ANALYSIS OF THE CATALYTIC AND FERROELECTRIC PROPERTIES OF POLYOXOMETALATES
Fei Wang

References

1. Chu, S.; Cui, Y.; Liu, N., *Nat. Mater.* **2017,** *16* (1), 16-22.

2. Nitopi, S.; Bertheussen, E.; Scott, S. B.; Liu, X.; Engstfeld, A. K.; Horch, S.; Seger, B.; Stephens, I. E.; Chan, K.; Hahn, C., *Chem. Rev.* **2019,** *119* (12), 7610-7672.

3. Verma, S.; Lu, S.; Kenis, P. J., *Nature Energy* **2019,** *4* (6), 466-474.

4. (a) Jin, S.; Hao, Z.; Zhang, K.; Yan, Z.; Chen, J., *Angew. Chem. Int. Ed.* **2021,** *60* (38), 20627-20648; (b) Overa, S.; Ko, B. H.; Zhao, Y.; Jiao, F., *Acc. Chem. Res.* **2022,** 748-755.

5. (a) Patel, A.; Narkhede, N.; Singh, S.; Pathan, S., *Catal. Rev.* **2016,** *58* (3), 337-370; (b) Sakai, Y.; Shinohara, A.; Hayashi, K.; Nomiya, K., Wiley Online Library: 2006.

6. (a) Neumann, R.; Khenkin, A. M., *Inorg. Chem.* **1995,** *34* (23), 5753-5760; (b) Sadasivan, R.; Patel, A.; Patel, A., *Polyhedron* **2021,** *193*, 114896; (c) Izarova, N. V.; Maksimovskaya, R. I.; Willbold, S.; Ko¨gerler, P., *Inorg. Chem.* **2014,** *53* (21), 11778-11784.

7. (a) Huang, L.; Wang, S.-S.; Zhao, J.-W.; Cheng, L.; Yang, G.-Y., *J. Am. Chem. Soc.* **2014,** *136* (21), 7637-7642; (b) Singh, V.; Chen, Z.; Ma, P.; Zhang, D.; Drew, M. G. B.; Niu, J.; Wang, J., *Chem. Eur. J.* **2016,** *22* (31), 10983-10989.

8. Yamase, T.; Sugeta, M., *Inorg. Chim. Acta* **1990,** *172* (2), 131-134.

9. (a) Wang, M.-Y.; Song, Q.-W.; Ma, R.; Xie, J.-N.; He, L.-N., *Green Chemistry* **2016,** *18* (1), 282-287; (b) Yu, X.; Zhao, C.-C.; Gu, J.-X.; Sun, C.-Y.; Zheng, H.-Y.; Yan, L.-K.; Sun, M.; Wang, X.-L.; Su, Z.-M., *Inorg. Chem.* **2021,** *60* (10), 7364-7371.

10. Khenkin, A. M.; Efremenko, I.; Weiner, L.; Martin, J. M. L.; Neumann, R., *Chem. Eur. J.* **2010,** *16* (4), 1356-1364.

11. Girardi, M.; Blanchard, S.; Griveau, S.; Simon, P.; Fontecave, M.; Bedioui, F.; Proust, A., *Eur. J. Inorg. Chem.* **2015,** *2015* (22), 3642-3648.

12. Girardi, M.; Platzer, D.; Griveau, S.; Bedioui, F.; Alves, S.; Proust, A.; Blanchard, S., *Eur. J. Inorg. Chem.* **2019,** *2019* (3-4), 387-393.

13. Zheng, S.-T.; Yang, G.-Y., *Chem. Soc. Rev.* **2012,** *41* (22), 7623-7646.

14. (a) Van Der Spoel, D.; Lindahl, E.; Hess, B.; Groenhof, G.; Mark, A. E.; Berendsen, H. J. C., *J. Comput. Chem.* **2005,** *26* (16), 1701-1718; (b) Hess, B.; Kutzner, C.; van der Spoel, D.; Lindahl, E., *J. Chem. Theory Comput.* **2008,** *4* (3), 435-447.

15. Wang, J.; Cieplak, P.; Kollman, P. A., *J. Comput. Chem.* **2000,** *21* (12), 1049-1074.

16. Chaumont, A.; Wipff, G., *Phys. Chem. Chem. Phys.* **2008,** *10* (46), 6940-6953.

17. López, X.; Nieto-Draghi, C.; Bo, C.; Avalos, J. B.; Poblet, J. M., *J. Phys. Chem. A* **2005,** *109* (6), 1216-1222.

18. Frisch, M. J.; Trucks, G. W.; Schlegel, H. B.; Scuseria, G. E.; Robb, M. A.; Cheeseman, J. R.; Scalmani, G.; Barone, V.; Petersson, G. A.; Nakatsuji, H.; Li, X.; Caricato, M.; Marenich, A. V.; Bloino, J.; Janesko, B. G.; Gomperts, R.; Mennucci, B.; Hratchian, H. P.; Ortiz, J. V.; Izmaylov, A. F.; Sonnenberg, J. L.; Williams; Ding, F.; Lipparini, F.; Egidi, F.; Goings, J.; Peng, B.; Petrone, A.; Henderson, T.; Ranasinghe, D.; Zakrzewski, V. G.; Gao, J.; Rega, N.; Zheng, G.; Liang, W.; Hada, M.; Ehara, M.; Toyota, K.; Fukuda, R.; Hasegawa, J.; Ishida, M.; Nakajima, T.; Honda, Y.; Kitao, O.; Nakai, H.; Vreven, T.; Throssell, K.; Montgomery Jr., J. A.; Peralta, J. E.; Ogliaro, F.; Bearpark, M. J.; Heyd, J. J.; Brothers, E. N.; Kudin, K. N.; Staroverov, V. N.; Keith, T. A.; Kobayashi, R.; Normand, J.; Raghavachari, K.; Rendell, A. P.; Burant, J. C.; Iyengar, S. S.; Tomasi, J.; Cossi, M.; Millam, J. M.; Klene, M.; Adamo, C.; Cammi, R.; Ochterski, J. W.; Martin, R. L.; Morokuma, K.; Farkas, O.; Foresman, J. B.; Fox, D. J. Wallingford, CT, 2016.

19. Jorgensen, W. L.; Chandrasekhar, J.; Madura, J. D.; Impey, R. W.; Klein, M. L., *J. Chem. Phys.* **1983,** *79* (2), 926-935.

20. Caleman, C.; van Maaren, P. J.; Hong, M.; Hub, J. S.; Costa, L. T.; van der Spoel, D., *J. Chem. Theory Comput.* **2012,** *8* (1), 61-74.

21. Namazian, M.; Lin, C. Y.; Coote, M. L., *J. Chem. Theory Comput.* **2010,** *6* (9), 2721-2725.

22. (a) Kelly, C. P.; Cramer, C. J.; Truhlar, D. G., *The Journal of Physical Chemistry B* **2007,** *111* (2), 408-422; (b) Pavlishchuk, V. V.; Addison, A. W., *Inorg. Chim. Acta* **2000,** *298* (1), 97-102.

23. (a) Liu, C.; Cundari, T. R.; Wilson, A. K., *J. Phys. Chem. C.* **2012,** *116* (9), 5681-5688; (b) Zhao, H.; Lin, Z.; Marder, T. B., *J. Am. Chem. Soc.* **2006,** *128* (49), 15637-15643.

Chapter 4. The Photocatalytic Behaviors of Reducing CO_2 to CO of the Pure and Coordinated POM Clusters within Multi-Components Systems

UNIVERSITAT ROVIRA I VIRGILI
COMPUTATIONAL ANALYSIS OF THE CATALYTIC AND FERROELECTRIC PROPERTIES OF POLYOXOMETALATES
Fei Wang

CHAPTER 4

The Photocatalytic Behaviors of Reducing CO_2 to CO of the Pure and Coordinated POM Clusters within Multi-Components Systems

The photochemical CO_2 reduction processes catalyzed by multi-components systems are discussed in this chapter, which involve two kinds of POM clusters, the pure and coordinated POMs, respectively. The pure POM with a typical structure of Keggin, $[PW_{12}O_{40}]^{3-}$ is combined with g-CN and bimetallic Re(I) compounds, ($[Re^1(bipyNNH_2)(CO)_3Cl–Re^2(bipy)(CO)_3Cl]$, bipy = 2,2'-bipyridine), forming a three-component hybrid construct. The proton-coupled electron transfer mechanism within CO_2 reduction coupled to hydrocarbon dehydrogenation reaction catalyzed by this hybrid catalyst are revealed by DFT and CASSCF/CASPT2 calculations. The roles of the three components are analyzed separately with an emphasis on the POM cluster. By comparing with other catalytic system containing bimetallic Re(I), the unique advantages of this hybrid construct are revealed. This work has been published with the title of "Photoreduction Mechanism of CO_2 to CO Catalyzed by a Three-Component Hybrid Construct with a Bimetallic Rhenium Catalyst" (https://doi.org/10.1021/acscatal.0c04366)

Moreover, we also study the photoexcited behaviors of two novel coordinated clusters in collaboration with the experimental group of Prof. Ira A. Weinstock (Ben-Gurion University of the Negev, Israel). By sharing the common oxygen ligands, two different types of metal-oxide clusters are bonded together where the core $[Co_{13}O_8]$ or $[Ni_{30}O_{32}]$ cluster is encapsulated by several peripheral $[Nb_6O_{19}]^{8-}$ clusters, generating the coordinated clusters $[(Co_{13}O_8)(Nb_6O_{19})_6]^{31-}$ or $[Ni_{30}O(Nb_6O_{19})_{10}]^{68-}$, respectively. The electronic structures of the two cooordinated clusters are examined with focusing on the orbital interaction between the core and peripherial parts, which illustrates the electron tranfer mechniasm of the process of reducing CO_2 coupled to oxidizing H_2O. The work related to $[(Co_{13}O_8)(Nb_6O_{19})_6]^{31-}$ can be found as "Soluble Complexes of Cobalt Oxide Fragments Bring the Unique CO_2 Photoreduction Activity of a Bulk Material into the Flexible Domain of Molecular Science" (https://doi.org/10.1021/jacs.1c08817) and the work about $[Ni_{30}(OH)_{24}(Nb_6O_{19})_{10}]^{44-}$ is in preparation.

4.1 Background

The photoreduction of CO_2 using solar energy into valuable chemicals and especially more energy-dense organic compounds such as CO, HCOOH, CH_3OH, and CH_4 among others is regarded as a promising but challenging strategy to lessen our dependence on fossil fuels and guarantee sustainable energy development.[1] In this respect, chemists have dedicated research for decades to the establishment of synthetic catalytic systems for the CO_2 photochemical reduction, as summarized in a series of recent reviews.[2] As the classical photocatalysts of CO_2 reduction, POMs' photochemical behaviors when serving as a catalyst independently have been extensively studied both experimentally and theoretically. However, the research about the multi-components' catalysts containing POM clusters is insufficient where the roles of the POM, the interactions among multiple components, as well as the complete catalytic mechanism involved multi-electrons transfer are still not clear in many cases. Here, aiming to provide an in-depth understanding on the photocatalytic behaviors of the POM clusters in those complicated systems, we examined the photoreduction processes of CO_2 catalyzed by two types of multi-component systems based on POM clusters by calculations. The first system is a three-component hybrid construct involving a pure POM cluster, while the other two systems are related to coordinated POM clusters formed by combining different kinds of metal-oxide clusters.

According to numerous reviews, transition-metal compounds capable of photochemically catalyzing CO_2 reduction have been actively sought.[1a, 3] Of those compounds that can catalyze the reduction of CO_2 to CO, *fac*-Re(bipy)$(CO)_3$Cl (bipy = 2,2′-bipyridine) and its analogues have been proven to be superior to the majority of others with regard to rates, selectivity, as well as catalyst lifetime.[4] These reduction reactions are usually carried out in organic solvents such as dimethylformamide or acetonitrile with or without an explicit extrinsic proton source. By adjusting the substituents at the 4,4′-positions of the bipy ligand, the reduction potential of the Re(I)-catalysts can be easily manipulated and a variety of substitutents have been shown to modulate activity.[5] Simple experimental operating conditions and easy-to-control reduction potentials make Re(I)-catalysts very promising candidates for industrial CO_2 photoreduction. Compared to those simple systems which only involve one component in the catalytic system, the hybrid construct composed of two parts with different functions: a photosensitizing agent and a catalyst is more implied with

enhanced light absorption and catalytic performance. Recently, a series of hybrid systems consist of rhenium complexes and phosphotungstate, $[PW_{12}O_{40}]^{3-}$ were prepared and corresponding reaction mechanisms were reported for the photochemical reduction of CO_2 to CO incorporating the reduction and protonation of $[PW_{12}O_{40}]^{3-}$.[4a-c, 6] In another instance $[PW_{12}O_{40}]^{3-}$ transfer multiple electrons from the amino ligand of NH_2-MIL-53 to the Pt-catalyst driven by the irradiation and the hybrid material synergistically catalyze the H_2 evolution which proceeds on the platform of Pt nanoparticles.[7] More recently, a Ti-substituted polyoxotungstate embedded into the cavities of HKUST-1 together with Au nanoparticles was reported that it can promote photoreduction of CO_2 to CO and CH_4, acting as an electron/proton pond.[8] All of these hybrid constructs demand photoexcited electron transfer from the photo absorber to the catalyst, which markedly affect the catalytic efficiency. Hence, the majorization of the electron transfer pathway is essential for efficient catalytic photoreduction.

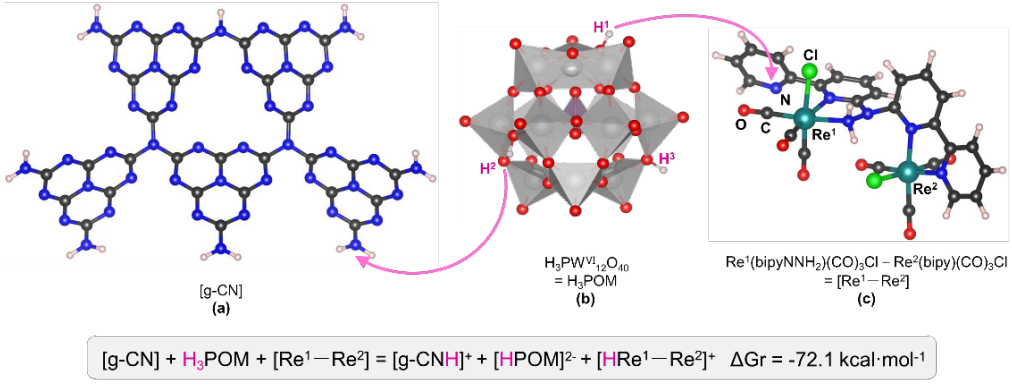

Figure 4.1. The structural representation of the hybrid ([g-CN](a)/H_3POM(b)/[Re^1–Re^2](c)) construct. The three components are attached to each other by acid-base interactions. The transfer of two protons from $H_3[PW_{12}O_{40}]$ to [g-CN] and to the catalyst [Re^1–Re^2] is an exergonic process. Color code: C (dark gray), N (blue), O (red), Cl (green), W (light gray), Re (cyan), H (pink).

Inspired by the above research background and considering that the transformation of CO_2 to CO is a two-electron redox reaction accompanied by the consumption of two protons to form H_2O, Neumann and his coworkers proposed the first example of a CO_2 photochemical reduction reaction in the MeCN solvent coupled to a hydrocarbon dehydrogenation reaction catalyzed by a hybrid construct.[4a] A three-component construct (Figure 4.1) was reported that includes g-CN as a

visible-light photosensitive semiconductor,[9] a phosphotungstate POM, $[PW_{12}O_{40}]^{3-}$, that behaves as an electron relay transferring electrons from the g-CN to a dimeric-rhenium-catalyst ($[Re^1(bipyNNH_2)(CO)_3Cl–Re^2(bipy)(CO)_3Cl]$, bipy = 2,2'-bipyridine) for CO_2 photoreduction. Upon photoactivation of g-CN, a cascade is initiated involving a hydrocarbon dehydrogenation coupled to the polyoxometalate reduction. Visible-light excites the reduced polyoxometalate to transfer electrons to the rhenium-based catalyst, enabling it to selectively reduce CO_2 to CO. Based on this experimental research and previous computational investigation on Re(I)-based organometallic complexes,[4c] we used computational methods to validate the proposed mechanism for the hybrid system. To this end, we first established the two-electron transfer pathway between the three components and the photoreduction mechanism of CO_2 to CO by the bimetallic Re-catalyst. In order to couple CO_2 reduction with hydrocarbon dehydrogenation, a multiple-proton transfer route accompanied by electron transfer is also proposed. We have also analyzed the electronic properties of several Re(I) catalysts to explain why the bimetallic $[Re^1(bipyNNH_2)(CO)_3Cl–Re^2(bipy)(CO)_3Cl]$ is one of the best rhenium-based catalysts for transforming CO_2 to CO, as it combines a low reduction potential with a small energy barrier to reduce CO_2.

Moreover, even though the rational design of the multi-component catalysts has been well explored and made moderate achievements, the various problems during the fabrication process of those systems caused by the traditional impregnation,[10] calcination,[11] or the deposition of preformed nanocrystals[12] bring in new challenges.[13] In this context, molecular science could play a transformative role by using the tractability and versatile solution-state chemistries of well-defined molecular complexes to simplify device fabrication. Ira A. Weinstock and his coworkers pioneered to use a coordination complex of structurally and electronically recognizable fragments of a bulk metal oxide as a versatile molecular "module" for replacing the parent oxide to avoid those fabrication problems. Based on that concept, they synthesized two cooridnated metal-oxo clusters, $[Co_{15}O_8(Nb_6O_{19})_6]^{27-}$ and $[Ni_{30}(OH)_{24}(Nb_6O_{19})_{10}]^{44-}$, which can repalace the parent bulk cobalt oxide or nickel oxide to reduce CO_2 coupled with oxidizeing H_2O by the solar energy. As shown in Figure 4.2, these two anions were obtained by combining two different types of metal-oxide clusters, where the core part is the $[Co_{13}O_8]$ (thus, the $[Co_{15}O_8(Nb_6O_{19})_6]^{27-}$ would be simplied as $[Co_{13}O_8(Nb_6O_{19})_6]^{31-}$), or the $[Ni_{30}O_{24}]$ cluster while the peripheral part is located by several $[Nb_6O_{19}]$ clusters. The two parts are held together

by sharing the common oxygen ligands between them. According to the experiments, the energy levels of HOMO, and LUMO as well as the gap of the coordinated $[Co_{13}O_8(Nb_6O_{19})_6]^{31-}$ structure are similar to the pure Co_3O_4 nanoscrystal, which seems to imply that the enegy levels of the FMOs of the core $[Co_{13}O_8]$ fragment is independent from the periperial $[Nb_6O_{19}]$ cluster and there is no interaction between the $[Co_{13}O_8]$ and $[Nb_6O_{19}]$ parts. However, the clear Co-O-Nb coordination can not be ignored, which could result in significant orbital mixing between Nb-O and Co-O bonds. These controversial points about the interaction between the two reactive fragments are necessary to figure out since it is crucial to the catalytic performance, like the redcution potential or the catalytic center. Compared to the $[Co_{13}O_8(Nb_6O_{19})_6]^{31-}$ anion, the situation of the structure of $[Ni_{30}(OH)_{24}(Nb_6O_{19})_{10}]^{44-}$ with higher negative and charges more appealing to the protons and counter cations in the solution is more complicated. The protonation undoubtedly affects the partial MOs and thereby the interaction between the $[Ni_{30}O_{24}]$ and the $[Nb_6O_{19}]$ clusters. To determine the existence of the interaction as well as to clarify its influence on the FMOs of the cooridnated cluster can be achieved by examing the electronic structure with theoretical calculations.

Hence, we conduct the DFT caluclations on both coordinated clusters, hopefully to shed a light on the interaction between those mixed metal-oxide fragment. No interaction is found between the core $[Co_{13}O_8]$ fragment with the peripherial $[Nb_6O_{19}]$ clusters due to the big enegy difference of the orbitals of Co and Nb, in which the FMOs are only contributed by the core $[Co_{13}O_8]$ clusters. However, for the coordinated cluster of $[Ni_{30}(OH)_{24}(Nb_6O_{19})_{10}]^{44-}$, the HOMO is mainly located at the core $[Ni_{30}O_{24}]$ clusters whereas the LUMO is contribued by the Nb-domianted orbital but the Ni-dominated empty orbital is only 0.60 eV higher. The relatively small energy differences between Nb and Ni empty MOs may suggest that photochemical excitation can induce also some electron transfer from Ni to Nb orbitals. The simulated UV-vis absorption spectrum vadidates the conjecture with the obsrvation that there is only the electronic transtion from the occupied Ni orbitals to the unoccupied Nb orbitals in the first 200 excitations.

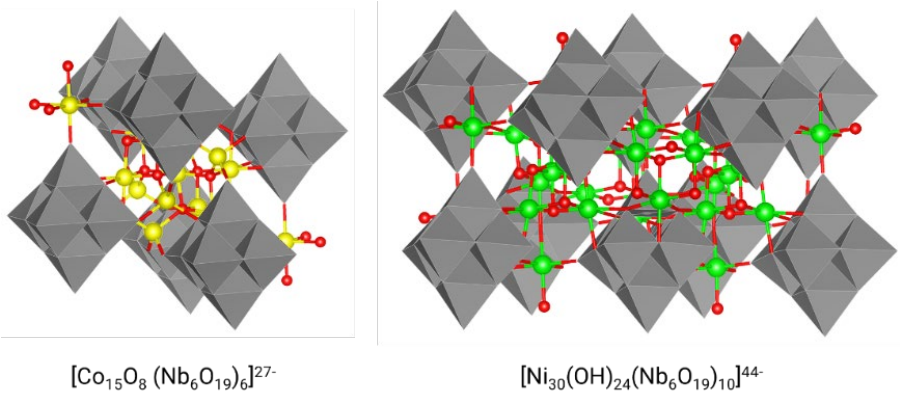

Figure 4.2. Combined balls–and–sticks and polyhedral representation of the two coordinated clusters $[Co_{15}O_8(Nb_6O_{19})_6]^{27-}$ with a $[Co_{13}]$ core, and $[Ni_{30}(OH)_{24}(Nb_6O_{19})_{10}]^{44-}$. Color code: Co (yellow), Ni (green), O (red) and H atom is hidden.

4.2 Computational Details

For the three-component hybrid construct system, all DFT calculations involved were performed by employing the Gaussian 16 A.03 program package.[14] The geometries were optimized by the hybrid B3LYP exchange-correlation functional.[15] The LanL2DZ ECP basis set[16] commonly used for Re complexes[4c, 5a, 17] was applied for Cl, W and Re atoms, while the 6-31G(d,p) basis set[18] was applied for the remaining H, C, O, and N atoms. Vibrational frequency calculations were carried out at 298.15 K and 1 atm using the same level of theory as for the geometry optimizations for all intermediates to confirm that those geometries locate at the lowest point of the potential energy surface. The single imaginary frequency of the transition state structure is related to the normal mode of vibration linking reactants and products. The visible absorption spectra were acquired through TDDFT calculations.[19] The M06,[20] O3LYP,[21] and CAM-B3LYP[22] functionals were applied to calculate the spectra. The solvent MeCN effect (ε = 36.6, refractive index = 1.334) was included adopting the IEF-PCM solvent model.[23] The CASSCF/CASPT2 calculations were done with the OpenMolcas code.[24] Single point calculations were carried out on DFT optimized structures, restricting the Re-CO_2 distance. The basis sets taken from the ANO-RCC internal library, which contains basis sets optimized for scalar relativistic corrections and semi-core valence electron correlation.[25] The following contractions of the primitive set of functions were used: Re(7s,6p,5d,2f,1g); C, N, O (4s,3p,1d) and H (2s,1p). The active space contained 13 electrons distributed in all possible ways over

13 active orbitals (see Figure. S4.8 in the Additional information part). A state-average optimization of the energy over the lowest eight doublets was performed to ensure that the active orbitals keep their character along the whole potential energy surface. In order to compare with other reported compounds, we also calculated the reduction potential of POMs and Re-catalysts involved in the current work by computing the free energy associated with the process. The reduction potentials were obtained using the formula $E = -\frac{\Delta G_{ox|red}}{F}$, where $\Delta G_{ox|red}$ is the free energy change of the reduction process. E_{abs} = -4.24 V was taken as the absolute standard potential of this half reaction, $\frac{1}{2}H_2(g) \rightarrow H^+(aq) + 1e^-$.[26]

For the coordinated POM systems, geometry optimizations including symmetry treatment were carried out in ADF.2019 code[27] using the GGA PBE functional.[28] Single point calculations were performed with the hybrid B3LYP functional with 20% and 15% of HF exchange contribution.[29] Frozen-electron triple-zeta-quality basis sets with single polarization functions (TZP) were used for Co and Nb atoms and double-zeta-quality basis sets (DZP) for O atoms.[30] Relativistic effects were considered via the zeroth-order regular approximation (ZORA).[31] To simulate the aqueous solution, the conductor-like screening model (COSMO)[32] with a dielectric constant (ε) of 78 was used in all calculation. The UV-vis absorption spectrum was simulated by considering excitations as the orbital energy differences which only needs to calculate Kohn-Sham orbital energy instead of the relative expensive TDDFT calculation of excitation energies.[27]

4.3 Results and Discussion for the Pure POM Cluster

4.3.1 Absorption spectra and energy balance

Initially, computations showed that the strong Brønsted acid $H_3PW_{12}O_{40}$ transfers one proton to a basic primary, terminal amine of g-CN and another proton to the Re-catalyst. The MEP map (seen in Figure S4.1) for [Re^1-Re^2] demonstrates that the pyridine nitrogen is the most basic N site for protonation and the structure protonated at the pyridine nitrogen is more stable than the structure protonated at the amino nitrogen by 13.8 kcal mol^{-1}, which provides additional evidence that protonation is most likely to occur in pyridine nitrogen. Thus, another proton of the

POM transfers to the pyridinyl nitrogen atom of the bipy ligand which is not coordinated to the Re(I) center, forming three charged components: $[g\text{-}CNH]^+$ (**1a**), $[HPW_{12}O_{40}]^{2-}$ (**1b**) and $[HRe^1\text{–}Re^2]^+$ (**1c**). These two proton transfer reactions combined are very exergonic, ΔG_r = -72.1 kcal mol^{-1}, as shown in Figure 4.1, enabling the formation of a very stable three-component hybrid construct.

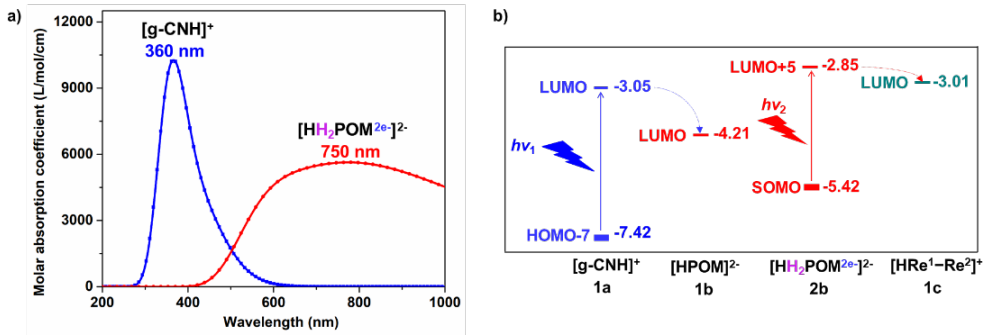

Figure 4.3. a) Simulated UV-vis-NIR spectra of $[g\text{-}CNH]^+$ (**1a**) in blue and reduced $[H_3POM^{2e}]^{2-}$ (**2b**) in red at the B3LYP level; b) Simplified molecular orbital energy diagram. The strongest light absorption corresponds to the transition of **1a** from HOMO-7 to LUMO, and from SOMO to LUMO+5 for reduced **2b**.

The computed absorption spectra and corresponding FMOs at the B3LYP level of the various components are presented in Figure 4.3a and 4.3b. The simulated absorption spectrum of **1a** in blue shows that it mainly absorbs blue visible light with an absorption maximum at 360 nm. This corresponds to an electronic transition from HOMO-7 to LUMO. The energy of the latter is -3.05 eV, while the LUMO level of **1b** is -4.21 eV (Figure 2b). The large energy gap between the LUMO of **1a** and the LUMO of the POM (**1b**) provides a strong driving force for the transfer of an excited electron from **1a** to the LUMO of the POM (**1b**). The simulated absorption spectrum of the reduced POM (**2b**) is depicted by the red line in Figure 4.3a. The peak maximum is at 750 nm, corresponding to the electronic transition from the SOMO to LUMO+5. The LUMO+5 lies at higher energy (-2.85 eV) than the LUMO of **1c** (-3.01 eV), making it possible to transfer electrons from the reduced POM to **1c**. Those spectra calculated by other functionals, M06, O3LYP, and CAM-B3LYP, are presented in Figure S4.2 and S4.3, from which it can be found that the simulated spectra by B3LYP are in good consistency with the experimental spectra.[4a] Overall, the use of g-CN and reduced POM as the photosensitizer enables the excitation energies to envelop a large area of the visible spectrum and thereby allows the absorption of a significant part of the solar spectrum.

4.3.2 Central role of POM as a shuttle for electrons and protons

Figure 4.4 schematizes the overall electron and proton transfer process. Excited by blue light, **1a** generates two higher-energy electrons with co-formation of two-electron oxidized **2a** (blue cycle). The hydrocarbon, for example, cyclohexene (C_6H_{10}) is hole oxidized to yield $[C_6H_{10}]^{2+}$ with the transfer of two electrons to **2a** and recovery of **1a**. **1b** can accept two photoexcited electrons from **1a** and two protons from intermediate $[C_6H_{10}]^{2+}$ generating two-electron reduced **2b**, where the two extra electrons are distributed on the W atoms of the POM (red cycle). After absorbing red light, **2b** acts as multiple electrons and protons donor transferring them to the Re catalyst for CO_2 reduction (green cycle). The two-electron/two-proton transfer process is an exothermic reaction with a substantial negative ΔG_r = -3.86 eV (the computational details are described in Figure S4.6). The transfer of the two protons is considered to be a single-step process, because the hypothetical intermediate involving a loss of a single proton, $[C_6H_9]$, is a highly unstable radical, which requires free energy about +12 eV, obviously unreachable at room temperature. Irradiation by red light excites the reduced-**2b** leading to the transfer of two electrons to **1c**, thereby activating the rhenium-based photoreduction catalyst. In the following subsections, we will add more details to the description of the mechanism.

This discussion of the overall process shows that the POM, acting as the electron/proton switch, promotes hydrocarbon dehydrogenation by boosting the electron/hole separation and facilitates the transfer of electrons and protons to the Re-based catalytic CO_2-reduction system. Other divalent anionic POM systems, such as $[SW_{12}O_{40}]^{2-}$, $[H_2SiW_{12}O_{40}]^{2-}$, $[H_4CoW_{12}O_{40}]^{2-}$, $[H_4P_2W_{18}O_{62}]^{2-}$, $[Mo_6O_{19}]^{2-}$ and $[HPMo_{12}O_{40}]^{2-}$ were studied, and we observed that the Keggin polyoxotungstates exhibit probably the optimal electronic structure to act as electrons and protons shuttle between **1a** and **1c**. While the LUMO levels for the Keggin polyoxotungstate anions depend not too much on the central ion, the Dawson polyoxotungstate, $[H_4P_2W_{18}O_{62}]^{2-}$ and the polyoxomolybdate, $[Mo_6O_{19}]^{2-}$ and $[HPMo_{12}O_{40}]^{2-}$ anions would not be appropriate carriers because their LUMOs would be too low or too high (Figure S4.4).

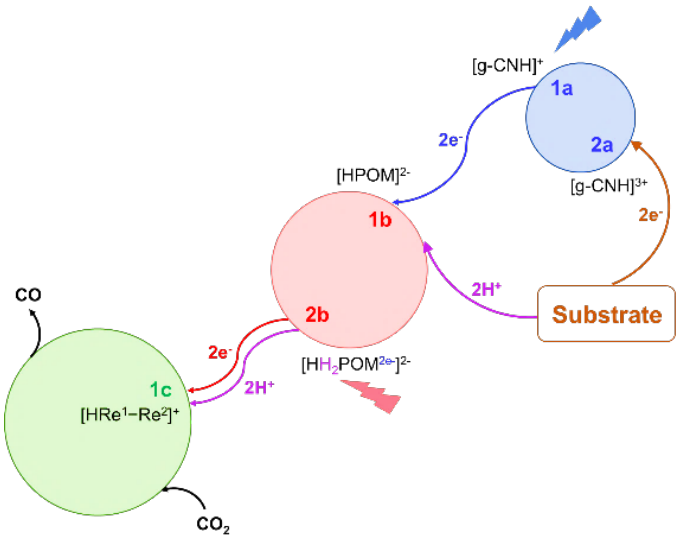

Figure 4.4. Schematic general view of the mechanism for the coupling CO_2 photoreduction and dehydrogenation of the substrate catalyzed by the hybrid $[g\text{-}CNH]^+$(**1a**)/$[HPOM]^{2-}$(**1b**)/$[HRe^1–Re^2]^+$(**1c**) system.

4.3.3 Details of the catalytic cycle

We then carried out a detailed analysis of the CO_2 reduction catalyzed by $[HRe^1Cl–Re^2Cl]^+$, **1c**. According to the known photochemistry of rhenium-based bipyridine complexes, a ligand, typically CO or Cl^-, can be eliminated by UV-blue light irradiation giving a solvent molecule such as MeCN the opportunity to occupy the created vacancy.[33] In this case, the rhenium catalyst is not symmetrical, that is, Re^1 is bound to one pyridinyl moiety and the bridging hydrazinyl group, while Re^2 is bound to two pyridinyl moieties. The peak maximum of the simulated absorption spectrum of $[HRe^1Cl–Re^2Cl]^+$ is located at 300 nm and the corresponding transition is from σ orbitals between Re and Cl to π^* orbitals of the bipy ligands, as shown in Figure S4.5. Hence, blue light irradiation could in principle de-chlorinate both rhenium centers, thereby allowing coordination of CO_2. However, the calculations show that the ΔG_r and $\Delta G_r^{\ddagger}$ (activation barrier) for CO_2 addition to Re^2 are +16.8 kcal mol^{-1} and ~ +20 kcal mol^{-1}, respectively, while for CO_2 addition to Re^1 they are only +0.7 kcal mol^{-1} and +2.4 kcal mol^{-1}, respectively. These values clearly indicate that Re^1 is the preferred catalytic center. Catalysis at the Re^1 site will be the focus of the further study of the CO_2 reduction mechanism. Reasons for the different catalytic reactivity at Re^1 and Re^2 will also be analyzed below.

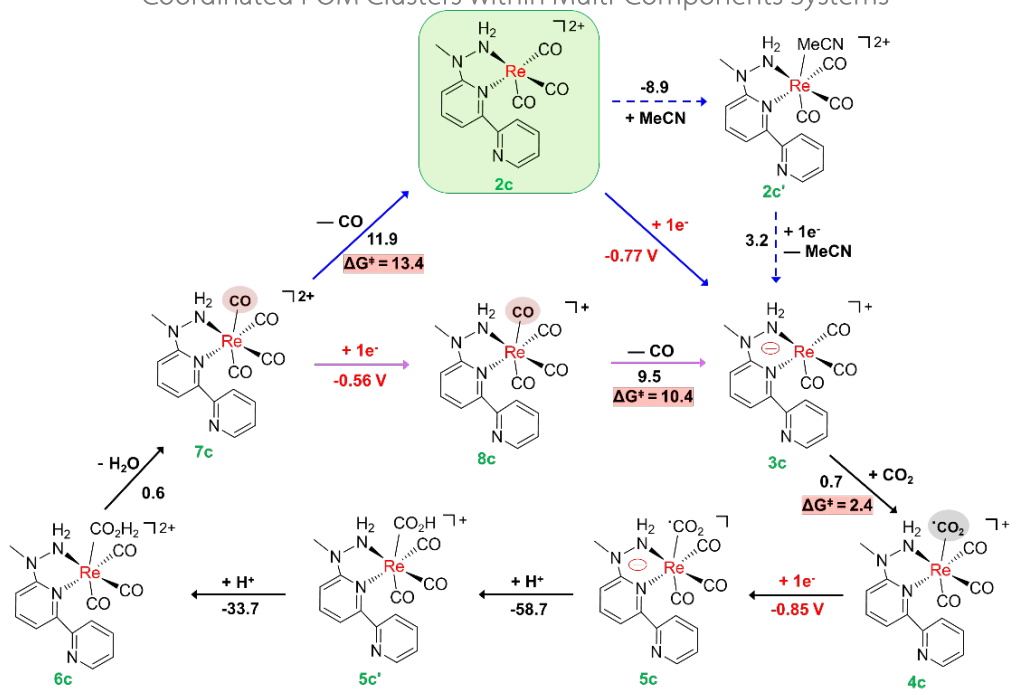

Figure 4.5. Reaction free energies and activation barriers (in kcal mol^{-1}) for the catalytic cycle. Only ligands of the active Re^{I} center are shown for clarity. In all the species represented, the Re center acts as a Re(I) since the 1e-reduction of **2c** and **4c** leads to **3c** and **5c** with the additional electron being delocalized over the bipyNNH$_2$ ligand. The coordination of CO_2 and protonation on the ligand promote the electron transfer to the metal center from the organic ligand (see text). The potential addition and elimination steps of MeCN (**2c** → **2c'**→ **3c**) are shown in dotted arrow lines. Energies associated with **5c** → **5c'**→ **6c** steps are obtained considering that the protons are transferred from H_2POM and HPOM, respectively.

The ΔG_r and $\Delta G_r^{\ddagger}$ of the reaction steps associated with the catalytic cycle are summarized in Figure 4.5. After the elimination of Cl^- to yield **2c**, the solvent molecule MeCN is likely coordinated in an actually photoactivated ligand exchange reaction step giving **2c'**. The binding energy of MeCN to Re^{I} is -19.5 kcal mol-1 and ΔG_r of this reaction is -8.9 kcal mol^{-1}. The elimination of MeCN requires a free energy of +3.2 kcal mol^{-1} with reduction of the Re^{I} center. Although the addition and elimination of MeCN are thermodynamically favorable, as shown by the dotted arrow line (**2c** → **2c'** → **3c**) in Figure 4.5, the reaction is not necessarily faster than the electron transfer from the POMs (**2c** → **3c**). After one-electron transfer to **2c** (or **2c'**), **3c** with a 5-coordinated Re center is generated, in which the spin density is largely localized on the

bipyNNH$_2$ ligand. Only a small fraction of the spin density is found on the coordinatively unsaturated Re center while the three CO ligands have negligible spin populations (Figure 4.6c). Hence, **3c** is considered as a [Re(I)–bipyNNH$_2$(1-)] compound as opposed to a [Re(0)–bipyNNH$_2$(0)] intermediate. This is consistent with previous spectroscopic evidence that demonstrated a shift of about 21 cm^{-1} in the high-energy band that was attributed to the formation of a bipy radical.[34] Whereas the *d*-orbitals of first-row transition metal ions are relatively tightly bound to the nucleii and display a low orbital energy, the 5*d* orbitals of the Re atom are more diffuse and higher in energy. Thus, the bipy π* orbital is predicted to be lower in energy than the Re 5*dz*^{2} orbital. The initial formation of [Re(I)–bipyNNH$_2$(1-)] indeed shows that the first one-electron reduction is at the bipyNNH$_2$ ligand. This is also supported by experimental observations that the reduction potential of the Re(I)-catalyst can be manipulated by adjusting the substituents at the 4,4′-positions of the bipy ligand (see section 4.3.4).

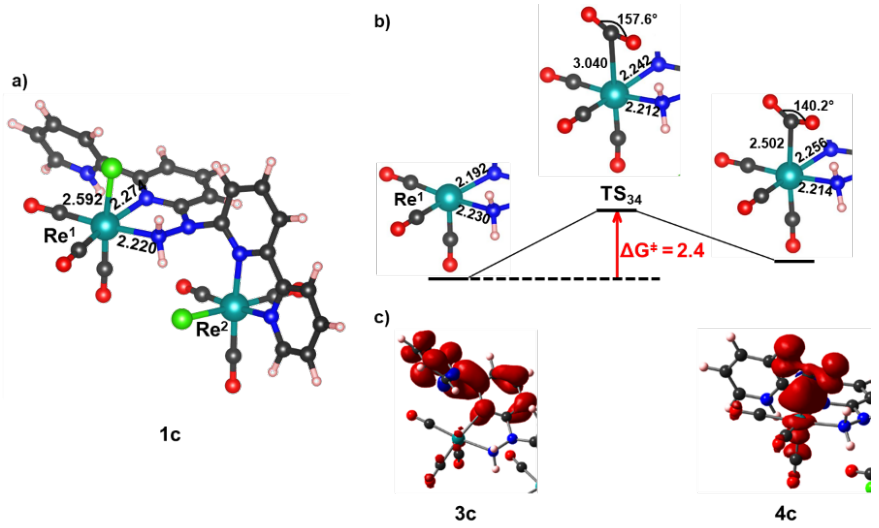

Figure 4.6. Structure of **1c** (**a**), free energy profile (**b**) and spin density distribution (**c**) for the CO_2 ligation steps. Since the single electron is only (de)localized over the ligands of Re^1 center in **2c**, only the atoms around the Re^1 center are shown in **3c**, **TS$_{34}$** and **4c**, where all atoms around of Re^2 are omitted for clarity.

Furthermore, complete active space self-consistent field (CASSCF) calculations were carried out to better understand the electron transfer in the process of CO_2 approaching the Re center. The CASSCF spin populations of the ground and first excited state as function of the distance between Re and CO_2 and corresponding active

orbitals are shown in Figure S4.7-8. The two active orbitals marked as "Re–CO_2 σ/π* bipyNNH_2" are the two orbitals that are singly occupied in the first two roots of the CASSCF calculation. A unitary transformation of these two orbitals leads to localized orbitals, either on the bipyNNH_2 ligand or on Re–CO_2. Because of the multiconfigurational character of the wave function, localized and delocalized descriptions are equivalent and, as can be seen in spin population plots, the lowest root has one unpaired electron on bipyNNH_2 ligand at a large distance, which is transferred to Re–CO_2 at a shorter distance. The low occupation of the 5dz^2 orbital on Re^1 in **3c** facilitates the approach of CO_2 as there is initially no electron-electron repulsion between the ligand and Re. In a later stage, when the CO_2 is closer to the Re^1 center, the unpaired electron is transferred from bipyNNH_2 to the Re-5dz^2 orbital, and the Re–C bond formation is initiated. Therefore, we postulate that the interaction between the bipyNNH_2 π^* orbital and the Re^1 *d* orbitals and their succeeding occupations after reduction has a major impact on the CO_2 ligation, which is confirmed in the next section. The CASSCF calculated energy barrier for CO_2 coordination is much higher than the one predicted with the DFT calculation. This is not unexpected since the CASSCF wave function does not account for the so-called dynamic electron correlation. This effect is commonly included with second-order perturbation theory (CASPT2). Indeed, the corresponding potential energy surface depicted in Figure S4.9 (right) shows a barrier of the same order of magnitude as the DFT barrier. The inversion of the stability of the [Re(I)–bipyNNH_2(1-)] and [Re(0)–bipyNNH_2(0)] electronic states occurs when the distance between Re and CO_2 is around 3.1 Å during the approach of CO_2 to Re.

The ligation of CO_2 to intermediate **3c** by forming a Re–C bond is a little bit endothermal by ~0.7 kcal mol^{-1} to generate **4c**. Figure 4.6 presents the free energy profile and structural changes for the CO_2 ligation, which shows that the activation barrier for the CO_2 coordination is only +2.4 kcal mol^{-1} where the Re–C bond is belike 3.0 Å and the O=C=O angle is about 158° in the transition state structure (**TS_{34}**), while the Re–C bond length is 2.5 Å and the O=C=O angle is 140° in intermediate, **4c**. This indicates that the interaction between Re center and CO_2 is stronger than in the previous studied Re-polyoxometalate hybrid construct, where the Re–C bond length is ~2.9 Å and the O=C=O angle ~165°.[4c]

When a second electron is transferred from the POM to the catalyst, the additional electron is also located on the bipyNNH_2 ligand of Re^1 center generating **5c**

$[Re(I)–bipyNNH_2(1-)]$. Later, it is transferred to the Re^1 center, forming the $[Re(0)–bipyNNH_2(0)]$ electronic state. The potential energy surface and structural changes for the second electron transfer and CO elimination are presented in Figure 4.7. The reduction does not significantly affect the $Re–CO_2$ bond. The O=C=O angle remains 140° and the Re–C distance is still ~2.5 Å. On the basis of previous experimental and computational investigation,[1a, 4d, 10b, 14b, 15] two subsequent protonation steps are demanded to generate CO. As presented in Figure 6c, the electron of the $[Re^1(bipyNNH_2)(CO)_3(CO_2)]$ part in **4c** is largely distributed on the CO_2 ligand, which leads to a fractional negative charge on the CO_2 and promotes the first protonation of the bound CO_2 ligand to form a hydroxycarbonyl complex **5c'**, which is about 59 kcal mol^{-1} lower in energy. Previous computational research on Re-based catalytic systems has demonstrated that these protonation steps are barrier-free.[16] The protonation step weakens one of the C=O bonds and elongates it to 1.37 Å in **5c** from 1.22 Å in **5c'**, while the Re–C(COOH) bond is strengthened with the length decreasing considerably by 0.34 Å. Due to a fractional negative charge still on the COOH ligand in **5c'**, further protonation can occur, which leads to the cleavage of C–OH bond and the generation of H_2O and the cationic tetracarbonyl complex **6c**, releasing CO after photoreduction. This step is exothermal by about -34 kcal mol^{-1}, assuming the reduced POM to be the proton source. The departure of H_2O is a slightly endothermal process by 0.6 kcal mol^{-1} from **6c** to **7c**. At this point, there are two alternatives involving the removal of a CO and 1e-reduction step. As shown the blue path in Figure 4, the free energy barrier for the direct cleavage of the Re–CO bond of **7c** is not very high, +13.4 kcal mol^{-1}. Similar results (~12 kcal mol^{-1}) have been found in studies on related compounds.[16e] However, when CO is released from the previously reduced **7c**, the energy barrier is slightly lower, +10.4 kcal mol^{-1} (the purple path in Figure 4). Although this latter pathway is more favorable from the energy point of view, we can not rule out that both can occur simultaneously.

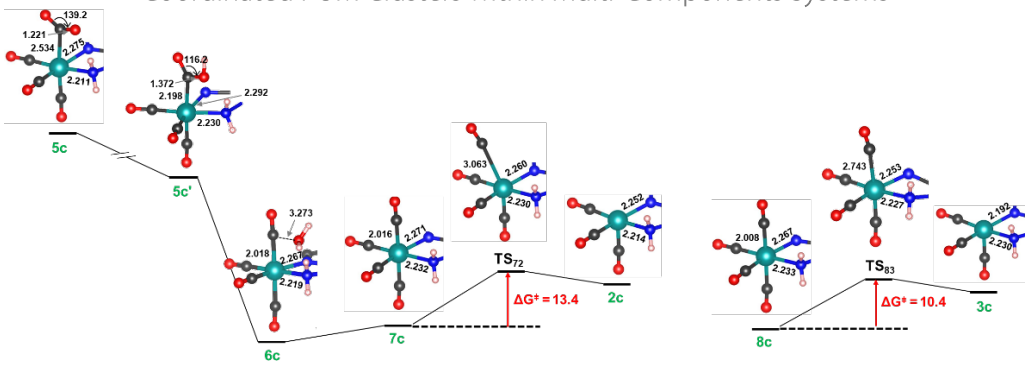

Figure 4.7. The schematic diagram for the potential energy surface of the second electron transfer and CO elimination. All distances are in Å, and angles are in degrees and the free energy barriers are in kcal mol^{-1}. For other numerical values see Figure 4.5.

4.3.4 Influence of substituents on the bipy ligand

The redox potential and the overall catalytic activity are significantly influenced by substituents on the bipy ligand. As shown in Chart 4.1, the experimental reduction potentials of a series of Re(I)-catalysts ranging from -0.73 V to -1.70 V, are nicely reproduced by our present DFT calculations. Unlike the previously studied monometallic-Re(I) catalysts (**1**-**9**), the catalyst analyzed here contains two Re(I) centers, one Re^2 center has the classical $[Re^2(bipy)(CO)_3Cl]$ coordination where both sp^2 N-atoms of the bipy ligand are ligated to the metal while the other Re center, Re^1, $[Re^1(bipyNNH_2)(CO)_3Cl]$, has a less conventional coordination sphere with only one Re–N(bipy) bond and a second Re^1–N bond with the NNH_2 ligand with a sp^3 hybridization (see Chart 4.1 for a schematic view of the structure). The main consequence of this non-symmetric coordination is that the LUMO of the bimetallic catalyst is localized on the $bipyNNH_2$ ligand of the Re^1 center, with a lower energy than most of the other rhenium compounds reported in Chart 4.1. Therefore, the spin density of the bimetallic catalyst after one-electron reduction **3c** is also localized on the $bipyNNH_2$ ligand of Re^1. This confirms again that the CO_2 reduction occurs at the Re^1 center. In fact, if we replace the entire $Re^2bipy(CO)_3Cl$ moiety with a methyl group, the properties of the catalyst (summarized in Table S4.1, $[Re^1–CH_3]$) change only marginally compared to the bimetallic $[Re^1–Re^2]$ catalyst, supporting the conclusion that the Re^2 center does not play a direct role on the CO_2 reduction cycle. Among the compounds examined in Chart 4.1, **6** and **7** were of special note because of their low

reduction potential, -0.88 V and -0.99 V, respectively. Compound **6** has two carboxyl groups at the 4,4 '-positions of the bipy ligand and compound **7** has two alkynyl groups at the 3,3'-positions of the bipy ligand. The difference between the two compounds lies in the $\Delta G_r^{\ddagger}$ for the CO_2 addition, which were computed to be +10.6 kcal mol^{-1} and +22.1 kcal mol^{-1}, respectively. The latter $\Delta G_r^{\ddagger}$ is very similar to the value computed for the parent compound with an unsubstituted bipy ligand, **1**. However, the carboxyl groups in **6** reduces $\Delta G_r^{\ddagger}$ by more than 10 kcal mol^{-1} with respect to **1**. These carboxylate electron-withdrawing groups reduce the energy of the Re-*d* and the bipy-π^* orbitals. The stabilization is larger for the Re-*d* orbitals and the overall effect is a reduction of the gap between the bipy-π^* and the Re-*d* orbitals from 0.85 eV in **1** to 0.46 eV in **6**. The smaller gap favors electron transfer from bipy to the Re atom explaining the lower $\Delta G_r^{\ddagger}$ for the CO_2 addition of **6**.

Compared to the aforementioned compounds, the Re^1 center in $[Re^1–Re^2]$ exhibits both a very low reduction potential (-0.85 V) and a very low $\Delta G_r^{\ddagger}$ (+2.4 kcal mol^{-1}) for the CO_2 addition. Thus, the bimetallic $[Re^1–Re^2]$ compound is expected to be a superior catalyst for the reduction of CO_2 to CO. By exchanging one N (sp^2) coordination site with a sp^3 hybridized N atom, the σ donating character of the coordination sphere is reduced. This significantly lowers the ligand-field exerted on the metal and stabilizes the Re-*d* orbitals in comparison to the classical symmetric bidentate bipy coordination complexes. The *d*-π^* orbital energy gap is further reduced, leading to an extremely low $\Delta G_r^{\ddagger}$ for CO_2 addition. Specifically, the energy gap in **6** of 0.46 eV is reduced to almost 0 eV, allowing a strong interaction between the Re^1 center and the bipyNNH_2 ligand. The FMOs, Figure S4.10, show that the Re-*d* orbitals and the bipy-π^* orbital are completely separated in compounds **1** and **6**, while $[Re^1–Re^2]$ shows nearly degenerate *d*-π^* orbitals of Re and the bipyNNH_2 ligand. Therefore, when CO_2 approaches Re^1, the electrons on the bipyNNH_2 ligand can be easily transferred to Re^1 to interact with CO_2 without any barrier, very significantly reducing the $\Delta G_r^{\ddagger}$ for CO_2 addition. These results confirm our previous hypothesis based on CASSCF calculations that the CO_2 additive affinity is mainly influenced by the energy gap between the bipy π^* orbital and the Re *d* orbitals and the succeeding occupations after reduction.

Chart 4.1. The comparison of the previously reported classical Re(I) catalysts (1-9) and the present work ([Re¹–Re²])

Compound	Structure		DFT			Exp.
			LUMO[a]	$\Delta G^{\ddagger}$[b]	V[c]	V[c]
1	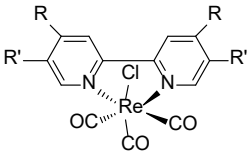	R=H; R'=H	-2.49	+21.2	-1.34	-1.34[5i]
2		R=CH_3; R'=H	-2.39		-1.53	-1.43[5i]
3		R=*tBu*; R'=H	-2.31		-1.56	-1.45[5i]
4		R=OCH_3; R'=H	-2.19		-1.62	-1.49[5i]
5		R=OH; R'=H	-2.26		-1.55	-1.53[5b]
6		R=COOH; R'=H	-3.05	+10.6	-0.88	-0.94[5i]
7		R=H; R'=alkynyl	-2.89	+22.1	-0.99	-1.15[5d]
8	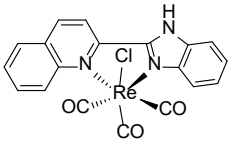		-2.73		-1.16	-1.40[5h]
9	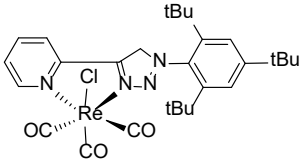		-2.12		-1.73	-1.70[5g]
[Re^1–Re^2]	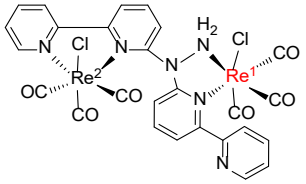		-3.01	+2.4	-0.77	-0.73[4a]

[a]in eV; [b]free energies barriers in kcal·mol^{-1}; [c]the first reduction potential in V (*vs* SHE).

4.4 The electronic structure analysis for the Coordinated POM Systems

4.4.1 Interaction between cobalt-oxide and hexaniobate cluster

According to the experiment, the core part of the cubic-spinel-like hexaniobate-encapsulated cobalt oxide fragment ($[Co_{13}O_8(Nb_6O_{19})_6]^{31-}$) is composed of 13 Co atoms with mixed valent, where the Co^{II}: Co^{III} ratio is 6:7. As shown in Figure 4.8a, all six Co^{II} ions locates at the T_d sites and via μ_2-O and μ_4-O linkages to the $[Co^{III}_7O_8]$ unit. As a starting point of calculations, we analyzed the possible spin multiplicities for those mixed-valent Co centers. As expected from the magnetic results, the lowest energy electronic state corresponds to that in which the tetrahedral Co(II) and octahedral Co(III) have high and low spin configurations, respectively, seen in Figure 4.8b and the Mulliken spin density distribution of that electronic state is also presented in Figure 4.8c.

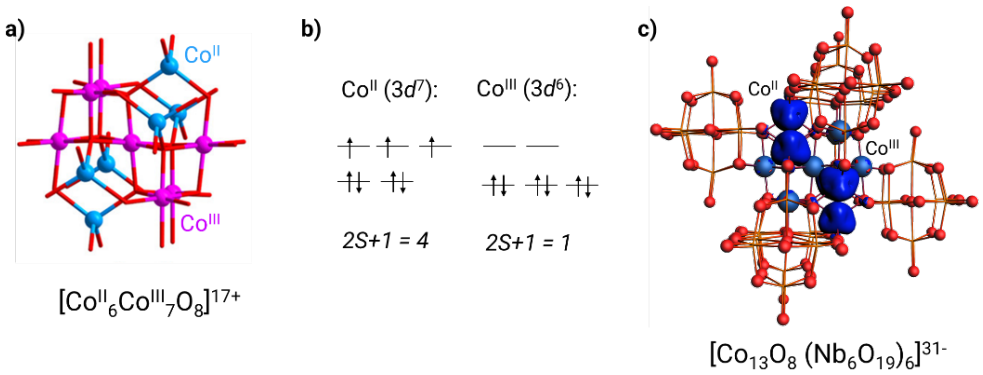

Figure 4.8. a) Balls–and–sticks representation of the core $[Co^{II}_6Co^{III}_7O_8]^{17+}$ part; **b**) the favorable electronic configurations for the tetrahedral Co^{II} and octahedral Co^{III} ions; **c**) the computed Mulliken spin density distribution of the coordinated clusters $[Co_{13}O_8(Nb_6O_{19})_6]^{31-}$.

The DFT calculations performed at the PBE level reproduce the experimental geometry very well (Figure S4.11). To obtain a more localized set of molecular orbitals, we performed a single point calculation with the hybrid B3LYP functional using the PBE optimized structure. Figure 4.9 displays the energy of the pseudo-bands obtained at the B3LYP level near the frontier orbital region. The highest occupied set of MOs are essentially contributed by Co orbitals, the HOMO lying approximately at -4 eV, which is mainly localized on Co^{II} centers. Just below, we find a set of MOs that have

larger contribution of atomic orbitals of oxygen atoms belonging ti to the Co_xO_y cluster. The oxygen atoms have been labeled as O_{Co}, whereas those that are part of the POM are labeled O_{Nb}. It is worth mentioning that the orbitals of Nb_6O_{19} ligand contribute in less than 5 % to the MOs of the so-called Co and O_{Co} bands and we have not observed any significant interaction between orbitals of cobalt and niobium atoms. For the lowest unoccupied orbitals, we find a similar behavior, the lowest set being localized on Co^{III} centers, and again with very low contribution from Nb_6O_{19} ligands. The HOMO-LUMO (H-L) gap was computed to be 3.74 eV, somewhat larger than the experimental value of 2.4 eV. However, it is well-know that the H-L gap is overestimated in hybrid functionals. Hence, for example, when the so-called HF exchange contribution is reduced from 20% in the standard B3LYP to 15%, the H-L gap decreases to 3.0 eV and 2.3 eV if the HF exchange contribution is only 10%. In summary, present DFT calculations clearly shows that the electronic structure of the central cobalt cluster hardly changes by the coordination of the 6 POM ligands. Since both HOMO and LUMO are contributed by the core $[Co_{13}O_8]$ part, the CO_2 reduction, as well as the H_2O oxidisation, are predicted to be catalysed by the core Co centers.

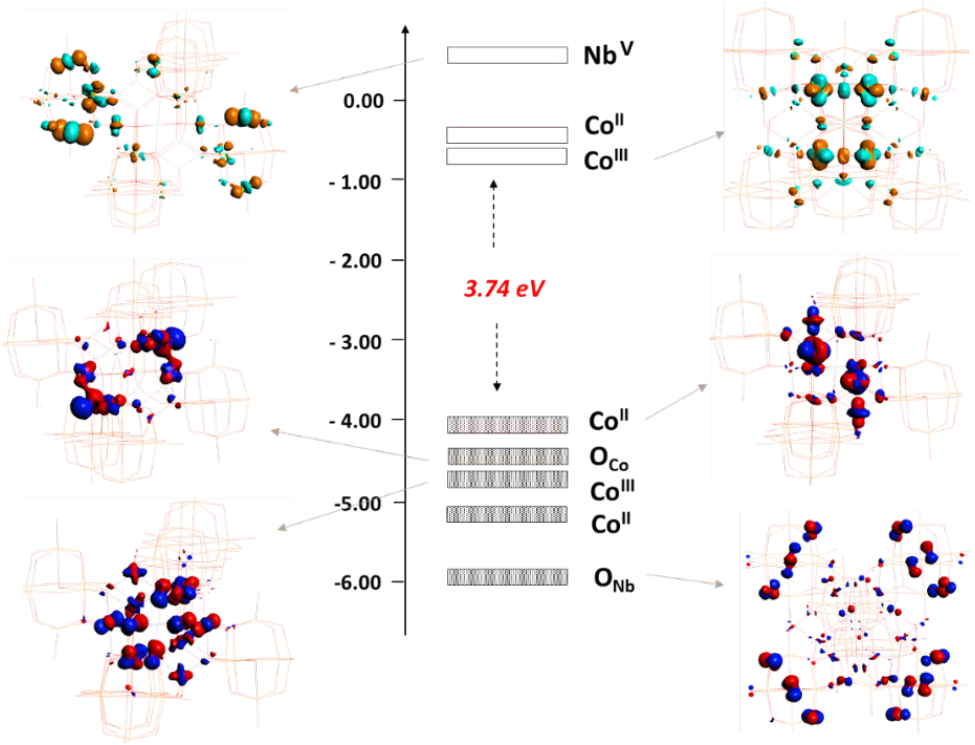

Figure 4.9. MOs diagram for $[Co_{13}O_8(Nb_6O_{19})_6]^{31-}$. The energy (in eV) of pseudobands for the occupied and unoccupied molecular orbitals are represented by filled and empty boxes, respectively. Co, O_{Co}, Nb, and O_{Nb} are used to represent which type of atoms contribute the most to each set of molecular orbitals. Representative molecular orbitals for each band are also shown. The HOMO–LUMO gap computed at B3LYP (20% HF exchange) is in red.

4.4.2 Interaction between nickel-oxide and hexaniobate cluster

Similarly, we conducted calculations on the coordinated cluster of $[Ni_{30}(OH)_{24}(Nb_6O_{19})_{10}]^{44-}$. Due to its big size and all Ni^{II} centers locating at the same crystal field, i.e., the octahedral field composed of six O ligands within the cluster, we applied a simplified model containing only three Ni^{II} centers surrounded by three Nb_6O_{19} anions in the calculations. Concerning that the high negative charges and abundant O atoms may attract protons and counter-cations from the aqueous solution, we optimized this model without any protonation and with protonating each O atoms of the Ni_3O_4 part by the PBE functional, respectively, as shown in Figure 4.10a and b. The structural comparison related to the main distances between the optimized models and the experimental crystal can be found in Figure S4.12. While the unprotonated model causes the overlong Ni-O(Nb) bonds with a distance of 3.240 Å,

the protonated model can reproduce the experimental crystal structure well. Hence, we will carry out more calculations on the protonated model. The influence of the counter-cations is also considered by adding several K^+ cations around the protonated model, seen in Figure 4.10c. Due to the large radii of the K^+ ions, they not only interact with the O(Ni), but also with O(Nb), resulting in the almost same decline of both orbitals of Ni and Nb without changing the distributions of the molecular orbitals (MOs). As a result, we did not include the K^+ cation in the further calculations.

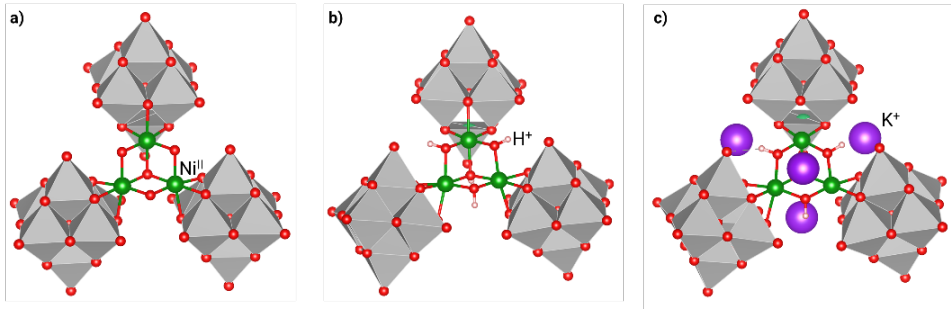

Figure 4.10. The combined ball-and-stick (Ni_3O_4) and polyhedral (Nb_6O_{19}) representation of the three models applied in the calculations, $[Ni_3O_4(Nb_6O_{19})_3]^{26-}$, $[Ni_3(OH)_4(Nb_6O_{19})_3]^{22-}$, and $[K_4Ni_3(OH)_4(Nb_6O_{19})_3]^{18-}$.

Figure 4.11a is the calculated electronic structure of the $[Ni_3(OH)_4(Nb_6O_{19})_3]^{22-}$ anion by the B3LYP functional. The HOMO lying at about -4.0 eV is contributed by the Ni-O mixed orbitals, whereas the LUMO is located at the Nb_6O_{19} cluster. The Ni-dominated empty orbital is only 0.6 eV higher. The relatively small energy differences between Nb and Ni empty orbitals may imply that photochemical excitation can induce also some electron transfer from Ni to Nb orbitals. The gap of HOMO-LUMO is 3.70 eV, which is well consistent with the experimental value (3.60 eV). To check the transition after irradiation, we simulated the UV-vis absorption spectrum of this model, from which we only observed electronic transitions from the occupied Ni to the unoccupied Nb in the first 200 excitations, seen in Figure 4.12a. To validate our conclusion, we enlarged our model from $[Ni_3(OH)_4(Nb_6O_{19})_3]^{22-}$ with three Ni^{II} centers to $[Ni_7(OH)_8(Nb_6O_{19})_6]^{42-}$ with seven Ni^{II} centers. Similar results shown in Figure S4.13 are found for the bigger model for Ni→Nb transitions, whereas the Ni→Ni transitions are predicted to be shifted to higher energies (lower λ). These latter transitions do not appear in the first 200 excitations, either. Therefore, we conclude that the CO_2 is possible to be reduced by receiving excited electrons from the

peripheral Nb cluster. However, the situation where CO_2 is immediately reduced by the Ni center can not be excluded, which has been reproted by many works.[35] The H_2O is predicted to be oxidised by receiving the holes from the core Ni centers.

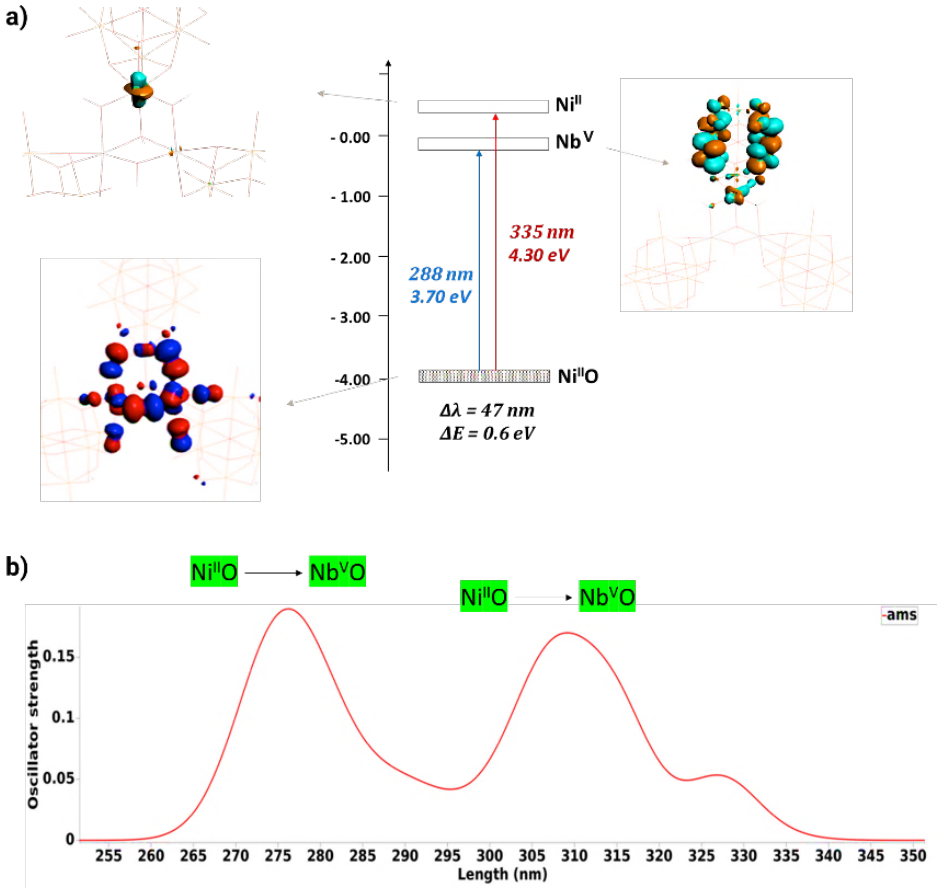

Figure 4.11. a) Molecular orbital diagram for $[Ni_3O_4(Nb_6O_{19})_3]^{26-}$. The energy (in eV) of pseudobands for the occupied and unoccupied molecular orbitals are represented by filled and empty boxes, respectively. Co, Nb, and NbO are used to represent which type of atoms contribute the most to each set of molecular orbitals. **b**) The calculated absorption spectrum for the model of $[Ni_3O_4(Nb_6O_{19})_3]^{26-}$.

4.5 Concluding Remarks

In summary, a detailed computational study has been accomplished for the mechanism of the photochemical reduction of CO_2 to CO coupled to hydrocarbon

dehydrogenation catalyzed by a three components of hybrid construct, ([g-CN]–POM–[Re^1–Re^2]). We first rationalize the electron/proton transfer pathway between the three components. After absorbing blue light, [g-CN] transfers two electrons to the POM, which is driven by a large LUMO energy difference between the two compounds. Then, the hydrocarbon, transfers two electrons to the holes of oxidized g-CN and two (or even more) protons to the reduced POM, leading to the dehydrogenation of the hydrocarbon. The transfer of the two protons is considered as a single-step process with the formation of [C_6H_8], skipping the highly unstable radical [C_6H_9] due to the loss of a single proton. Next, the reduced POM is excited by red light and then transfers two electrons to Re(I) species. Finally, the activated catalyst captures and reduces CO_2 and in the process the hydrogen-rich POM transfers two protons to the CO_2-coordinated Re-species to generate the reduction products, CO and water. Throughout the process, the POM is crucial. On the one hand, it acts as an electron acceptor to facilitate electron-hole separation, and on the other hand, it serves as an electron donor to a Re-based CO_2 catalytic reduction system. By studying the catalytically photochemical reduction cycle of CO_2 to CO by the Re(I)-catalyst, the formation of the species [Re^1(I)–bipyNNH$_2$(1-)] indicates that it is a ligand-based reduction instead of a metal-based reduction and thus the bipyNNH$_2$ ligand is responsible for the first reduction potential. Moreover, the energy gap between the bipyNNH$_2$ π^* orbital and the Re dz^2 orbitals and the succeeding occupations after reduction is predicted to be the main reason of the CO_2 binding affinity. The particular environment of Re^1 in the bimetallic complex, [Re^1–Re^2] makes this catalyst exceptional, with a very low reduction potential and high affinity for CO_2 coordination after its reduction.

Except the role of the pure POM cluster as well as its interaction with other components within a muti-component catalyst system, we also anslyzed the electronic structures of two coordinated clusters, $[(Co_{13}O_8)(Nb_6O_{19})_6]^{31-}$ and $[Ni_{30}(OH)_{24}(Nb_6O_{19})_{10}]^{44-}$. The DFT calculations demonstrate that the core $[Co_{13}O_8]$ fragment of the anion $[(Co_{13}O_8)(Nb_6O_{19})_6]^{31-}$ is relatively independent to the $[Nb_6O_{19}]$ fragment due to the big gap between the MOs contributed by the two metals, respectively. Both HOMO and LUMO are contributed by the core $[Co_{13}O_8]$ fragment and thereby the CO_2 reduction, as well as the H_2O oxidisation, are catalyzed by the core Co centers. On the contrary, the core $[Ni_{30}O_{24}]$ fragment of the anion $[Ni_{30}(OH)_{24}(Nb_6O_{19})_{10}]^{44-}$ has considerable interaction with the $[Nb_6O_{19}]$ cluster, resulting that the HOMO is

mainly contributed by the $[Ni_{30}O_{24}]$ part and the LUMO is located at the orbital of Nb. The Ni empty orbital is slightly higher, resulting in the potential electron transfer from the Ni to the Nb cluster after irradiation. As a result, the CO_2 is possible to be reduced by receiving excited electrons from the peripheral Nb cluster. However, the possiblity where CO_2 is immediately reduced by the Ni centers can not be excluded totally. The H_2O is predicted to be oxidized by receiving the holes from the core Ni centers. Having revealed the interaction between the two reactive fragments provides in-depth understanding on stabilizing coordinated metal-oxide clusters within molecular complexes, which demenstrates that complexation of small metal oxide clusters whose structural motifs closely match those of solid-state crystalline analogues can bring the unique reactivities of the bulk materials into the flexible realm of molecular science.

References

1. (a) Liang, H.-P.; Acharjya, A.; Anito, D. A.; Vogl, S.; Wang, T.-X.; Thomas, A.; Han, B.-H., *ACS Catal.* **2019,** *9* (5), 3959-3968; (b) Sun, Z.; Talreja, N.; Tao, H.; Texter, J.; Muhler, M.; Strunk, J.; Chen, J., *Angew. Chem. Int. Ed.* **2018,** *57* (26), 7610-7627; (c) Khalil, M.; Gunlazuardi, J.; Ivandini, T. A.; Umar, A., *Renew. Sust. Energ. Rev.* **2019,** *113*, 109246; (d) Fu, J.; Liu, K.; Jiang, K.; Li, H.; An, P.; Li, W.; Zhang, N.; Li, H.; Xu, X.; Zhou, H.; Tang, D.; Wang, X.; Qiu, X.; Liu, M., *Adv. Sci.* **2019,** *6* (18), 1900796; (e) Ye, L.; Wang, H.; Jin, X.; Su, Y.; Wang, D.; Xie, H.; Liu, X.; Liu, X., *Sol. Energy Mater. Sol. Cells* **2016,** *144*, 732-739.

2. (a) Thompson, W. A.; Sanchez Fernandez, E.; Maroto-Valer, M. M., *ACS Sustain. Chem. Eng.* **2020,** *8* (12), 4677-4692; (b) Li, X.; Yu, J.; Jaroniec, M.; Chen, X., *Chem. Rev.* **2019,** *119* (6), 3962-4179; (c) Wu, H.-L.; Li, X.-B.; Tung, C.-H.; Wu, L.-Z., *Adv. Mater.* **2019,** *31* (36), 1900709; (d) Li, R.; Zhang, W.; Zhou, K., *Adv. Mater.* **2018,** *30* (35), 1705512.

3. (a) Feng, X.; Pi, Y.; Song, Y.; Brzezinski, C.; Xu, Z.; Li, Z.; Lin, W., *J. Am. Chem. Soc.* **2020,** *142* (2), 690-695; (b) Wang, X.-K.; Liu, J.; Zhang, L.; Dong, L.-Z.; Li, S.-L.; Kan, Y.-H.; Li, D.-S.; Lan, Y.-Q., *ACS Catal.* **2019,** *9* (3), 1726-1732; (c) Todorova, T. K.; Huan, T. N.; Wang, X.; Agarwala, H.; Fontecave, M., *Inorg. Chem.* **2019,** *58* (10), 6893-6903; (d) Meier, A. J.; Garg, A.; Sutter, B.; Kuhn, J. N.; Bhethanabotla, V. R., *ACS Sustain. Chem. Eng.* **2019,** *7* (1), 265-275; (e) Xie, Y.; Fang, Z.; Li, L.; Yang, H.; Liu, T.-F., *ACS Appl. Mater. Interfaces* **2019,** *11* (30), 27017-27023; (f) Chen, E. X.; Qiu, M.; Zhang, Y. F.; Zhu, Y. S.; Liu, L. Y.; Sun, Y. Y.; Bu, X.; Zhang, J.; Lin, Q., *Adv. Mater.* **2018,** *30* (2), 1704388; (g) Yan, Y.; Yu, Y.; Huang, S.; Yang, Y.; Yang, X.; Yin, S.; Cao, Y., *J. Phys. Chem. C.* **2017,** *121* (2), 1089-1098.

4. (a) Yu, H.; Haviv, E.; Neumann, R., *Angew. Chem.* **2020,** *132* (15), 6278-6282; (b) Haviv, E.; Shimon, L. J. W.; Neumann, R., *Chemistry* **2017,** *23* (1), 92-95; (c) Ci, C.; Carbo, J. J.; Neumann, R.; Graaf, C. d.; Poblet, J. M., *ACS Catal.* **2016,** *6* (10), 6422-6428; (d) Khenkin, A. M.; Efremenko, I.; Weiner, L.; Martin, J. M.; Neumann, R., *Chem. Eur. J.* **2010,** *16* (4), 1356-1364.

5. (a) Benson, E. E.; Sampson, M. D.; Grice, K. A.; Smieja, J. M.; Froehlich, J. D.; Friebel, D.; Keith, J. A.; Carter, E. A.; Nilsson, A.; Kubiak, C. P., *Angew. Chem. Int. Ed.* **2013,** *52* (18), 4841-4844; (b) Manbeck, G. F.; Muckerman, J. T.; Szalda, D. J.; Himeda, Y.; Fujita, E., *J. Phys. Chem. B* **2015,** *119* (24), 7457-66; (c) Teesdale, J. J.;

Pistner, A. J.; Yap, G. P.; Ma, Y. Z.; Lutterman, D. A.; Rosenthal, J., *Catal. Today* **2014,** *225*, 149-157; (d) Portenkirchner, E.; Gasiorowski, J.; Oppelt, K.; Schlager, S.; Schwarzinger, C.; Neugebauer, H.; Knör, G.; Sariciftci, N. S., *ChemCatChem* **2013,** *5* (7), 1790-1796; (e) Qiao, X.; Li, Q.; Schaugaard, R. N.; Noffke, B. W.; Liu, Y.; Li, D.; Liu, L.; Raghavachari, K.; Li, L.-s., *J. Am. Chem. Soc.* **2017,** *139* (11), 3934-3937; (f) Andrade, G. A.; Pistner, A. J.; Yap, G. P.; Lutterman, D. A.; Rosenthal, J., *ACS Catal* **2013,** *3* (8), 1685-1692; (g) Ching, H. Y.; Wang, X.; He, M.; Perujo Holland, N.; Guillot, R.; Slim, C.; Griveau, S.; Bertrand, H. C.; Policar, C.; Bedioui, F.; Fontecave, M., *Inorg Chem* **2017,** *56* (5), 2966-2976; (h) Sinha, S.; Berdichevsky, E. K.; Warren, J. J., *Inorg. Chim. Acta* **2017,** *460*, 63-68; (i) Smieja, J. M.; Kubiak, C. P., *Inorg. Chem.* **2010,** *49* (20), 9283-9289.

6. Ettedgui, J.; Diskin-Posner, Y.; Weiner, L.; Neumann, R., *J. Am. Chem. Soc.* **2011,** *133* (2), 188-190.

7. Guo, W.; Lv, H.; Chen, Z.; Sullivan, K. P.; Lauinger, S. M.; Chi, Y.; Sumliner, J. M.; Lian, T.; Hill, C. L., *J. Mater. Chem. A* **2016,** *4* (16), 5952-5957.

8. Liu, S. M.; Zhang, Z.; Li, X.; Jia, H.; Ren, M.; Liu, S., *Adv. Mater. Interfaces* **2018,** *5* (21), 1801062.

9. (a) Kuriki, R.; Sekizawa, K.; Ishitani, O.; Maeda, K., *Angew. Chem. Int. Ed.* **2015,** *54* (8), 2406-2409; (b) Kuriki, R.; Matsunaga, H.; Nakashima, T.; Wada, K.; Yamakata, A.; Ishitani, O.; Maeda, K., *J. Am. Chem. Soc.* **2016,** *138* (15), 5159-5170; (c) Kuriki, R.; Yamamoto, M.; Higuchi, K.; Yamamoto, Y.; Akatsuka, M.; Lu, D.; Yagi, S.; Yoshida, T.; Ishitani, O.; Maeda, K., *Angew. Chem. Int. Ed.* **2017,** *56* (17), 4867-4871.

10. Munnik, P.; de Jongh, P. E.; de Jong, K. P., *Chem. Rev.* **2015,** *115* (14), 6687-6718.

11. (a) Wang, J.; Tang, H.; Zhang, L.; Ren, H.; Yu, R.; Jin, Q.; Qi, J.; Mao, D.; Yang, M.; Wang, Y., *Nature Energy* **2016,** *1* (5), 1-9; (b) Guo, S.; Zhao, S.; Wu, X.; Li, H.; Zhou, Y.; Zhu, C.; Yang, N.; Jiang, X.; Gao, J.; Bai, L., *Nat. Commun.* **2017,** *8* (1), 1-9.

12. (a) Chang, X.; Wang, T.; Zhang, P.; Zhang, J.; Li, A.; Gong, J., *J. Am. Chem. Soc.* **2015,** *137* (26), 8356-8359; (b) Li, T.; Yao, Y.; Huang, Z.; Xie, P.; Liu, Z.; Yang, M.; Gao, J.; Zeng, K.; Brozena, A. H.; Pastel, G., *Nat. Catal.* **2021,** *4* (1), 62-70.

13. (a) Liu, F.; Xu, S.; Cao, L.; Chi, Y.; Zhang, T.; Xue, D., *J. Phys. Chem. C.* **2007,** *111* (20), 7396-7402; (b) Mohapatra, P.; Shaw, S.; Mendivelso-Perez, D.; Bobbitt, J. M.; Silva, T. F.; Naab, F.; Yuan, B.; Tian, X.; Smith, E. A.; Cademartiri, L., *Nat. Commun.* **2017,** *8* (1), 1-7; (c) Boles, M. A.; Engel, M.; Talapin, D. V., *Chem. Rev.* **2016,** *116* (18), 11220-11289.

14. Frisch, M. J.; Trucks, G. W.; Schlegel, H. B.; Scuseria, G. E.; Robb, M. A.; Cheeseman, J. R.; Scalmani, G.; Barone, V.; Petersson, G. A.; Nakatsuji, H.; Li, X.; Caricato, M.; Marenich, A. V.; Bloino, J.; Janesko, B. G.; Gomperts, R.; Mennucci, B.; Hratchian, H. P.; Ortiz, J. V.; Izmaylov, A. F.; Sonnenberg, J. L.; Williams; Ding, F.; Lipparini, F.; Egidi, F.; Goings, J.; Peng, B.; Petrone, A.; Henderson, T.; Ranasinghe, D.; Zakrzewski, V. G.; Gao, J.; Rega, N.; Zheng, G.; Liang, W.; Hada, M.; Ehara, M.; Toyota, K.; Fukuda, R.; Hasegawa, J.; Ishida, M.; Nakajima, T.; Honda, Y.; Kitao, O.; Nakai, H.; Vreven, T.; Throssell, K.; Montgomery Jr., J. A.; Peralta, J. E.; Ogliaro, F.; Bearpark, M. J.; Heyd, J. J.; Brothers, E. N.; Kudin, K. N.; Staroverov, V. N.; Keith, T. A.; Kobayashi, R.; Normand, J.; Raghavachari, K.; Rendell, A. P.; Burant, J. C.; Iyengar, S. S.; Tomasi, J.; Cossi, M.; Millam, J. M.; Klene, M.; Adamo, C.; Cammi, R.; Ochterski, J. W.; Martin, R. L.; Morokuma, K.; Farkas, O.; Foresman, J. B.; Fox, D. J. Wallingford, CT, 2016.

15. (a) Vosko, S. H.; Wilk, L.; Nusair, M., *Can. J. Phys.* **1980,** *58* (8), 1200-1211; (b) Becke, A. D., *Phys. Rev. A* **1988,** *38* (6), 3098-3100; (c) Lee, C.; Yang, W.; Parr, R. G., *Phys. Rev. B* **1988,** *37* (2), 785-789; (d) Becke, A. D., *J. Chem. Phys.* **1993,** *98* (7), 5648-5652; (e) Stephens, P. J. D., F. J.; Chabalowski, C. F.; Frisch, M. J. Ab, *J. Phys. Chem.* **1994,** *98*.

16. (a) Wadt, W. R.; Hay, P. J., *J. Chem. Phys.* **1985,** *82* (1), 284-298; (b) Hay, P. J.; Wadt, W. R., *J. Chem. Phys.* **1985,** *82* (1), 299-310; (c) Hay, P. J.; Wadt, W. R., *J. Chem. Phys.* **1985,** *82* (1), 270-283.

17. (a) Tang, H.; Brothers, E. N.; Grapperhaus, C. A.; Hall, M. B., *ACS Catal.* **2020,** *10* (6), 3778-3789; (b) Argibay-Otero, S.; Graña, A. M.; Carballo, R.; Vázquez-López, E. M., *Inorg. Chem.* **2020,** *59* (19), 14101-14117; (c) Marazzi, M.; Gattuso, H.; Fumanal, M.; Daniel, C.; Monari, A., *Chem. Eur. J.* **2019,** *25* (10), 2519-2526; (d) Popov, D. A.; Luna, J. M.; Orchanian, N. M.; Haiges, R.; Downes, C. A.; Marinescu, S. C., *Dalton Trans* **2018,** *47* (48), 17450-17460.

18. (a) Ditchfield, R.; Hehre, W. J.; Pople, J. A., *J. Chem. Phys.* **1971,** *54* (2), 724-728; (b) Hehre, W. J.; Ditchfield, R.; Pople, J. A., *J. Chem. Phys.* **1972,** *56* (5), 2257-2261; (c) Hehre, W. J.; Pople, J. A., *J. Chem. Phys.* **1972,** *56* (8), 4233-4234; (d) Binkley, J. S.; Pople, J. A., *J. Chem. Phys.* **1977,** *66* (2), 879-880; (e) Francl, M. M.; Pietro, W. J.; Hehre, W. J.; Binkley, J. S.; Gordon, M. S.; DeFrees, D. J.; Pople, J. A., *J. Chem. Phys.* **1982,** *77* (7), 3654-3665.

19. (a) Casida, M. E.; Jamorski, C.; Casida, K. C.; Salahub, D. R., *J. Chem. Phys.* **1998,** *108* (11), 4439-4449; (b) Stratmann, R. E.; Scuseria, G. E.; Frisch, M. J., *J. Chem. Phys.* **1998,** *109* (19), 8218-8224.

20. Zhao, Y.; Truhlar, D. G., *Theor. Chem. Acc.* **2008,** *120* (1-3), 27.

21. Handy, N. C.; Cohen, A. J., *J. Chem. Phys.* **2002,** *116* (13), 5411-5418.

22. Yanai, T.; Tew, D. P.; Handy, N. C., *Chem. Phys. Lett.* **2004,** *393* (1-3).

23. Cancès, E.; Mennucci, B.; Tomasi, J., *J. Chem. Phys.* **1997,** *107* (8), 3032-3041.

24. (a) Aquilante, F.; Autschbach, J.; Baiardi, A.; Battaglia, S.; Borin, V. A.; Chibotaru, L. F.; Conti, I.; Vico, L. D.; Delcey, M.; Galván, I. F.; Ferré, N.; Freitag, L.; Garavelli, M.; Gong, X.; Knecht, S.; Larsson, E. D.; Lindh, R.; Lundberg, M.; Malmqvist, P. Å.; Nenov, A.; Norell, J.; Odelius, M.; Olivucci, M.; Pedersen, T. B.; Pedraza-González, L.; Phung, Q. M.; Pierloot, K.; Reiher, M.; Schapiro, I.; Segarra-Martí, J.; Segatta, F.; Seijo, L.; Sen, S.; Sergentu, D.-C.; Stein, C. J.; Ungur, L.; Vacher, M.; Valentini, A.; Veryazov, V., *J. Chem. Phys.* **2020,** *152* (21), 214117; (b) Fdez. Galván, I.; Vacher, M.; Alavi, A.; Angeli, C.; Aquilante, F.; Autschbach, J.; Bao, J. J.; Bokarev, S. I.; Bogdanov, N. A.; Carlson, R. K.; Chibotaru, L. F.; Creutzberg, J.; Dattani, N.; Delcey, M. G.; Dong, S. S.; Dreuw, A.; Freitag, L.; Frutos, L. M.; Gagliardi, L.; Gendron, F.; Giussani, A.; González, L.; Grell, G.; Guo, M.; Hoyer, C. E.; Johansson, M.; Keller, S.; Knecht, S.; Kovačević, G.; Källman, E.; Li Manni, G.; Lundberg, M.; Ma, Y.; Mai, S.; Malhado, J. P.; Malmqvist, P. Å.; Marquetand, P.; Mewes, S. A.; Norell, J.; Olivucci, M.; Oppel, M.; Phung, Q. M.; Pierloot, K.; Plasser, F.; Reiher, M.; Sand, A. M.; Schapiro, I.; Sharma, P.; Stein, C. J.; Sørensen, L. K.; Truhlar, D. G.; Ugandi, M.; Ungur, L.; Valentini, A.; Vancoillie, S.; Veryazov, V.; Weser, O.; Wesołowski, T. A.; Widmark, P.-O.; Wouters, S.; Zech, A.; Zobel, J. P.; Lindh, R., *J. Chem. Theory Comput.* **2019,** *15* (11), 5925-5964.

25. Roos, B. O.; Veryazov, V.; Widmark, P.-O., *Theor. Chem. Acc.* **2004,** *111* (2), 345-351.

26. Marenich, A. V.; Ho, J.; Coote, M. L.; Cramer, C. J.; Truhlar, D. G., *Phys. Chem. Chem. Phys.* **2014,** *16* (29), 15068-15106.

27. E.J. Baerends, T. Z., A.J. Atkins,; J. Autschbach, O. B., D. Bashford, A. Bérces, F.M. Bickelhaupt, C. Bo, P.M. Boerrigter, L. Cavallo, C.; Daul, D. P. C., D.V. Chulhai, L. Deng, R.M. Dickson, J.M. Dieterich, D.E. Ellis, M. van Faassen, L. Fan,; T.H. Fischer, C. F. G., M. Franchini, A. Ghysels, A. Giammona, S.J.A. van Gisbergen, A. Goez,; A.W. Götz, J. A. G., O.V. Gritsenko, M. Grüning, S. Gusarov, F.E. Harris, P. van den Hoek, Z. Hu, C.R.; Jacob, H. J., L. Jensen, L. Joubert, J.W. Kaminski, G. van Kessel, C. König, F.

Kootstra, A. Kovalenko,; M.V. Krykunov, E. v. L., D.A. McCormack, A. Michalak, M. Mitoraj, S.M. Morton, J. Neugebauer, V.P.; Nicu, L. N., V.P. Osinga, S. Patchkovskii, M. Pavanello, C.A. Peeples, P.H.T. Philipsen, D. Post, C.C.; Pye, H. R., P. Ramos, W. Ravenek, J.I. Rodríguez, P. Ros, R. Rüger, P.R.T. Schipper, D. Schlüns,; H. van Schoot, G. S., J.S. Seldenthuis, M. Seth, J.G. Snijders, M. Solà, M. Stener, M. Swart, D.; Swerhone, V. T., G. te Velde, P. Vernooijs, L. Versluis, L. Visscher, O. Visser, F. Wang, T.A. Wesolowski,; E.M. van Wezenbeek, G. W., S.K. Wolff, T.K. Woo, A.L. Yakovlev, **2019**.

28. (a) Perdew, J. P.; Burke, K.; Ernzerhof, M., *Phys. Rev. Lett.* **1996,** *77* (18), 3865-3868; (b) Swart, M.; Ehlers, A. W.; Lammertsma, K., *Mol. Phys.* **2004,** *102* (23-24), 2467-2474.

29. Stephens, P. J.; Devlin, F. J.; Chabalowski, C. F.; Frisch, M. J., *J. Phys. Chem.* **1994,** *98* (45), 11623-11627.

30. Van Lenthe, E.; Baerends, E. J., *J. Comput. Chem.* **2003,** *24* (9), 1142-1156.

31. (a) van Lenthe, E.; Baerends, E. J.; Snijders, J. G., *J. Chem. Phys.* **1994,** *101* (11), 9783-9792; (b) Klopper, W.; van Lenthe, J. H.; Hennum, A. C., *J. Chem. Phys.* **2000,** *113* (22), 9957-9965.

32. Pye, C. C.; Ziegler, T., *Theor. Chem. Acc.* **1999,** *101* (6), 396-408.

33. Sato, S.; Matubara, Y.; Koike, K.; Falkenström, M.; Katayama, T.; Ishibashi, Y.; Miyasaka, H.; Taniguchi, S.; Chosrowjan, H.; Mataga, N.; Fukazawa, N.; Koshihara, S.; Onda, K.; Ishitani, O., *Chem. Eur. J.* **2012,** *18* (49), 15722-15734.

34. Smieja, J. M.; Kubiak, C. P., *Inorg Chem* **2010,** *49* (20), 9283-9289.

35. (a) Wang, J.-W.; Liu, W.-J.; Zhong, D.-C.; Lu, T.-B., *Coord. Chem. Rev.* **2019,** *378*, 237-261; (b) Chen, Y.; Guo, Z.-W.; Chen, Y.-P.; Zhuang, Z.-Y.; Wang, G.-Q.; Li, X.-X.; Zheng, S.-T.; Yang, G.-Y., *Inorg. Chem. Front* **2021,** *8* (5), 1303-1311.

Chapter 5. Switchable Rashba Anisotropy in Layered Hybrid Organic-Inorganic Perovskite by Hybrid Improper Ferroelectricity

CHAPTER 5

Switchable Rashba Anisotropy in Layered Hybrid Organic-Inorganic Perovskite by Hybrid Improper Ferroelectricity

The coexistence of ferroelectricity and spin-orbit interactions play a key role in optoelectronic properties of HOIP materials. We perform a detailed study on a recently synthesized ferroelectric layered HOIP, (AMP)PbI_4 (AMP = 4-aminomethyl-piperidinium). The calculated polarization and Rashba parameter are in excellent agreement with experimental values. We report a striking effect, i.e., an extraordinarily large Rashba anisotropy that is tunable by ferroelectric polarization: as polarization is reversed, not only the spin texture chirality is inverted, but also the major and minor axes of the Rashba anisotropy ellipse in k-space are interchanged – a pseudo rotation. A $k \cdot p$ model Hamiltonian and symmetry-mode analysis reveal a quadrilinear coupling between the cation-rotation modes responsible for the Rashba ellipse pseudo-rotation, the framework rotation, and the polarization. These findings may provide different avenues for spin-optoelectronic devices such as spin valves or spin FETs. Please find the published version of this work with the same title here (https://doi.org/10.1038/s41524-020-00450-z)

5.1 Background

In recent years, there has been an intense research effort surrounding the conversion of solar energy into electric power through photovoltaic cells.[1] HOIPs with composition ABX_3 (A = organic cation, such as $[CH_3NH_3]^+$; B = divalent metal cation, such as Sn^{2+}, Pb^{2+}; X = halogen anion) are proposed as a next generation of materials for solar cells and light-emitting diodes.[2] The increase in structural degrees of freedom from the inclusion of organic cations into a BX_3 inorganic framework enables structural distortions and columnar shifts which are otherwise forbidden in standard inorganic perovskites. Furthermore, ferroelectricity (FE) originating from structural symmetry breaking is a potentially critical phenomenon in such soft and flexible photovoltaic materials, where the electric field plays an important role in promoting electron-hole pair separation and suppressing charge recombination, inherently breaking the Shockley-Queisser limit.[3] Therefore the FE properties of perovskites have

attracted broad attention, though their presence and influence in perovskite solar cells are still a matter of debate.[4]

A strong spin-orbit coupling (SOC) involving the heavy Pb atom and its surrounding halogens, combined with the absence of an inversion symmetry in the crystal structure, can lead to a Rashba effect which, in turn, can impact photovoltaic performance.[5] Non-centrosymmetry provides a spin-degenerate band with the possibility to split two reversely spin-polarized states, and the equation of

$$E_{\pm}(k) = \frac{\hbar^2 k^2}{2m} \pm \alpha_R |k| \qquad (8.)$$

can be used to clarify the dispersion relation of electrons (or/and holes), in which α_R is the Rashba splitting parameter.[6] The coexistence of ferroelectricity and a Rashba effect is believed to mediate interesting effects, such as the switching of spin-texture chirality with an electric-polarization reversal.[7] These effects are mainly studied in the context of inorganic materials; only a few hybrid-material examples have been explored so far.[6a, 8]

Very recently, Sum *et al.* demonstrated the presence of both ferroelectricity and a Rashba effect in a layered Dion-Jacobson (DJ) phase HOIP with formula (AMP)PbI_4, where AMP is the divalent 4-aminomethyl-piperidinium cation (Figure 5.1, FE state).[9] Its measured value of P_s is 9.8 μC cm^{-2}, which is very high amongst HOIPs,[10] and more comparable to those of conventional inorganic perovskites such as $BaTiO_3$ (15 ~ 26 μC cm^{-2}).[11] A measured Rashba splitting energy (E_R) of 85 meV and Rashba coefficient (α_R) of 2.60 eV·Å suggest real promise for spintronic applications.[8] This exciting experimental evidence now motivates a theoretical investigation into the microscopic mechanism of ferroelectricity and its interplay with spin-orbit coupling in the HOIPs.

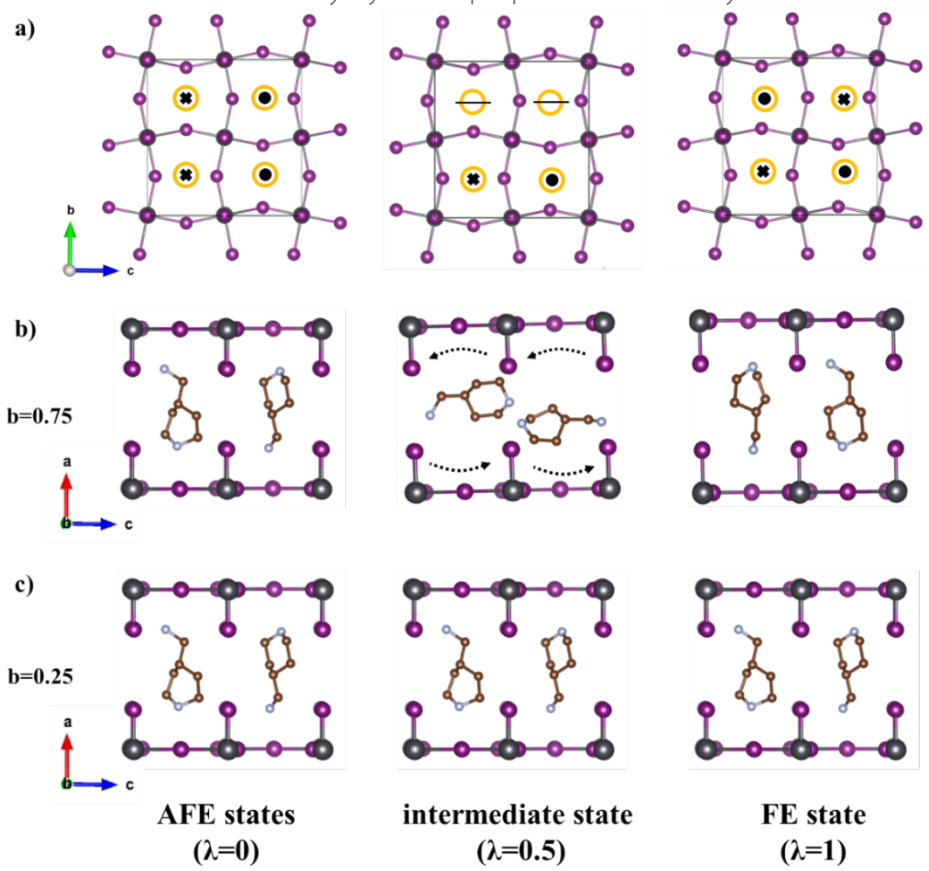

Figure 5.1. The structures of AFE and FE $(+P)$ phases. Top **(a)** and side (**b**, **c**) views with purple Pb, gray I, brown C and blue N. AMP-cation hydrogen atoms are omitted for clarity. The black dot or cross in the yellow circle of **(a)** represent the AMP-cation orientation as having the aminomethyl group of the molecule along the up $(+a)$ or down $(-a)$ axis, respectively.

Starting with this aim in mind, we perform a detailed DFT analysis of $(AMP)PbI_4$, focusing on estimates of the ferroelectric and spin-orbit properties of the band structure. While the estimate of the Rashba splitting is now a routine work, we focus here on the corresponding anisotropy, which is far much less studied. Our estimate of P_S and α_R are 10.72 μC cm^{-2} and 2.39 eV·Å, in excellent agreement with the experimental 9.80 μC cm^{-2} and 2.60 eV·Å. In addition, the E_R of spin-polarized bands is calculated to be 16 meV, which is of the same order of magnitude as the experimental 85 meV value. In addition to a spin-texture that can be switched via

ferroelectric polarization reversal, we further observe a sizeable anisotropy in the Rashba spin splitting. Remarkably, we show that the axis of major anisotropy can be switched between two orthogonal directions by reversing the ferroelectric polarization from $+P$ to $-P$. Reversing the FE polarization induces an apparent 90° 'rotation' of the anisotropy ellipse, *i.e.,* a pseudo-rotation. This effect has never been highlighted in the context of usual spin-texture tunability under polarization reversal and may suggest different avenues for spin-optoelectronic devices based on hybrid organic-inorganic perovskites.

5.2 Computational Details

The starting point for our calculations is the experimental crystallographic data reported in Ref.,[9] where we relax all of the atoms of the ferroelectric structure until the Hellmann-Feynman forces are smaller than 0.001 eV $Å^{-1}$. The projector saugmented wave (PAW)[12] method is used to solve Kohn-Shan equations with the PBE exchange-correlation functional,[13] as implemented in the Vienna *ab initio* simulation package (vasp). The energy cutoff for the plane wave expansion is set to 550 eV, and a 2×2×2 Monkhorst-Pack grid of *k*-point is used after systematic convergence tests. The van der Waals interactions are taken into account in calculations using DFT-D3 method.[14] The Berry phase approach is used to evaluate the ferroelectric polarization through constructing a properly AFE reference state and a suitable path connecting FE with AFE states.[15] Details of the evaluation of the polarization are discussed in the results section. Spin-orbit interaction is self-consistently considered in all band structure calculations, but not in the calculations of polarization. Van Waals interactions are included in all of calculations.[16]

5.3 Results and Discussion

5.3.1 Structural analysis

We start our simulations with the experimental ferroelectric phase of $(AMP)PbI_4$ refined at T = 298 K having space group Pc (#7, C_s^2) with monoclinic b-axis in Ref.[9] Two nearby AMP^{2+} cations located in the space between $[PbI_4]^{2-}$ layers have alternating orientations when they are adjacent along the b or c axes, but common

orientations when adjacent along diagonal $b + c$ or $b - c$ directions, as shown in Figure 5.1 (FE state), so that the structure lacks a center of inversion, thus paving the way for the existence of ferroelectric polarization in the system. It is interesting to note that the cation's center of mass is displaced somewhat from the ideal midpoint between two adjacent $[PbI_4]^{2-}$ layers so as to be slightly closer to one layer or the other. We perform quantum chemical analyses of the isolated AMP^{2+} cation using both the Hirshfield[17] and Natural population methods[18] implemented in the Gaussian16 software.[19] Both methods define an electric dipole moment of the molecule pointing approximately towards the aminomethyl group from the center of the AMP cation, as shown in Figure S5.1 (in the Additional information section). Although the long-range ordering of AMP-cation orientations should be associated with a strong FE polarization along the a axis at the first glance, this alone is not sufficient for understanding the overall polarization of a hybrid system, which typically has several different contributions to the polarization, as explained in details in Ref.[20] According to the modern theory of polarization,[15a, 21] we introduce a centrosymmetric anti-ferroelectric (AFE) phase by enforcing the existence of an inversion point, and define a suitable path connecting the AFE and FE state via atomic rotations or/and displacements in order to estimate the polarization by first principles calculations. The AFE model is built from the FE model by simultaneously rotating two AMP^{2+} cations adjacent along the b-axis by 180° so that the diagonal AMP cations are related by inversion symmetry. The $[PbI_4]^{2-}$ framework is also properly centrosymmetrized to ensure that the AFE structure (both framework and AMP cations) possesses an inversion symmetry point at (0.5, 0.5, 0.5), as shown in Figure 5.1 (AFE state). The resulting space group symmetry is $P2/m$ ($\#10, C_{2h}^1$) with monoclinic b-axis in the same unit cell.

5.3.2 Ferroelectric property

We introduce the normalized variable λ to simultaneously parameterize both the rotations of the AMP cations and the atomic displacements of the $[PbI_4]^{2-}$ framework from AFE ($\lambda = 0$) to FE ($\lambda = 1$) states. Therefore λ represents the amplitude of the combined roto-displacive distortions connecting the prototype AFE-phase structure and the real FE-phase structure. The intermediate structures along the path ($0 \leq \lambda \leq 1$) are only introduced in order to monitor the accidental introduction of a quantum of polarization and to ensure a continuous variation of the polarization along the path

itself. In practice, λ has been varied in finite increments, so that stepwise AMP-cation rotations are approximated by 18 steps of 10° each from 0° (AFE state) to 180° (FE state), together with incremental linear displacements of the $[PbI_4]^{2-}$ framework. In order to understand the origin of the polarization, the separate contributions of the organic AMP^{2+} cations and the inorganic $[PbI_4]^{2-}$ framework to the total polarization are considered in three different ways. Firstly, we rotate AMP cations while keeping the $[PbI_4]^{2-}$ framework centrosymmetric. In this way, we obtain the contribution coming from the organic groups (P_{cation}), *i.e.,* a rotational contribution to the polarization. Secondly, the displacive distortions of $[PbI_4]^{2-}$ framework are considered while fixing AMP cations in a centrosymmetric configuration. In this way, the polarization only originates from the inorganic framework (P_{frame}), *i.e.,* a displacive contribution to the total polarization. Finally, both of AMP-cation rotations and $[PbI_4]^{2-}$ layer displacements are simultaneously activated in order to recover the total polarization (P_{total}), *i.e.,* the full roto-displacive contribution to the polarization. In this way, we are able to disentangle the different contributions to the polarization and to observe the couplings between them. For each case, we consider the contribution from the ionic and electronic subsystems to the resulting polarization.

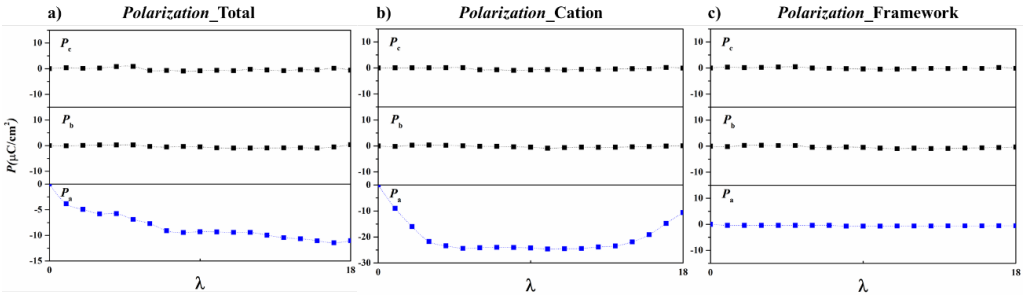

Figure 5.2. The FE polarization along the *a*, *b*, and *c* axes of $(AMP)PbI_4$ as a function of the parameter λ, which represents the normalized AMP^{2+} cation rotations and $[PbI_4]^{2-}$ framework displacements. (**a**) The total FE polarization. (**b**, **c**) The polarization contribution of the cation and framework, respectively.

The results of the polarization calculations are presented in Figure 5.2. In the AFE state, the net polarization is exactly zero, as expected. As λ gradually increases towards 1, the asymmetry with respect to the centric phase and the magnitude of the total polarization both increase steadily along the *a*-axis but remain near zero for the *b* and *c*-axis components. For $(\lambda = 1)$, we extract the estimated value of P_{total}, which is equal to 10.72 $\mu C\ cm^{-2}$, in very good agreement with the experimental value of

9.80 μC cm^{-2}. From our analysis, the contributions from organic cations and inorganic framework are 10.34 μC cm^{-2} and 0.59 μC cm^{-2} respectively. Clearly, the AMP cations dominate the total polarization, so that the framework contribution appears negligible in comparison. An applied electric field then mainly rotates the AMP cations while displacing the $[PbI_4]^{2-}$ framework only a little. Because the switchable FE polarization is primarily due to the long range orientational order of the organic cations, the true AFE state lying between the $+P$ and $-P$ states could be consistent with either ordered or disordered but balanced arrangements of AMP-cation orientations, thus supporting a null electric polarization. Indeed, the AFE ordered state of the crystal represents only a computational reference phase to evaluate the final polarization, and in principle may be not exclusively defined. In the present case, we have fixed a possible AFE ordering, but, according to modern theory of polarization, the final polarization does not depend on the particular path considered for $0 \leq \lambda \leq 1$.[22]

5.3.3 Electronic structure and the Rashba SOC effect

We now examine the electronic structure and Rashba SOC effect of ferroelectric (AMP)PbI_4. The Brillouin Zone (BZ) and corresponding Rashba spin-polarized bands of the FE structure are shown in Figure 5.3a and 5.3b. The valence band maximum (VBM), conduction band minimum (CBM) and related band gap are localized in *k*-space around the high-symmetry B point. The VBM and CBM are strongly spin-split due to the spin-orbit interaction and are also shifted away from the B point in *k*-space. As usual, the "momentum offset" (k_R) corresponds to the distance between the apex of the splitting band and the high-symmetry point in *k*-space, while E_R corresponds to the energy difference between them. In our case, k_R and E_R are estimated as 0.0133 Å^{-1} and 16 meV for the VBM and as 0.0132 Å^{-1} and 12 meV for the CBM, which shows rather fairly good agreement with the respective experimental values of 0.067 Å^{-1} and 85 meV. Indeed, according to the definition

$$\alpha_{\mathrm{R}} = \frac{2E_R}{k_R} \qquad (9.)$$

α_R is calculated to be 2.39 eV·Å for the VBM, which agrees with the experimental 2.60 eV·Å very well. It must be noted that the k_R values for the VBM and CBM are very similar, indicating that they are located essentially at the same point in *k*-space to form a "direct" band gap, which is beneficial for electronic transitions in photovoltaic-cell

applications. We show the band dispersion of the spin-split bands, *i.e.,* a 3D plot of the VBs around the high-symmetry B point, in Figure 5.3c. The corresponding spin-textures of the spin-split bands are projected onto the 2D plane perpendicular to the FE *P* in Figure 5.3d. In the inner and outer bands, the sense of rotation (left-handed or right-handed) of the spin-textures are opposite due to the spin-orbit interaction. As reported in Refs.,[23] the polarization reversal resulting from the application of an external electric field should be able to switch the spin textures. Indeed, we also observe that the spin textures completely switch from left- to right-handed sense of rotation as the polarization goes from $-P$ to $+P$, as shown in Figure 5.3d-e.

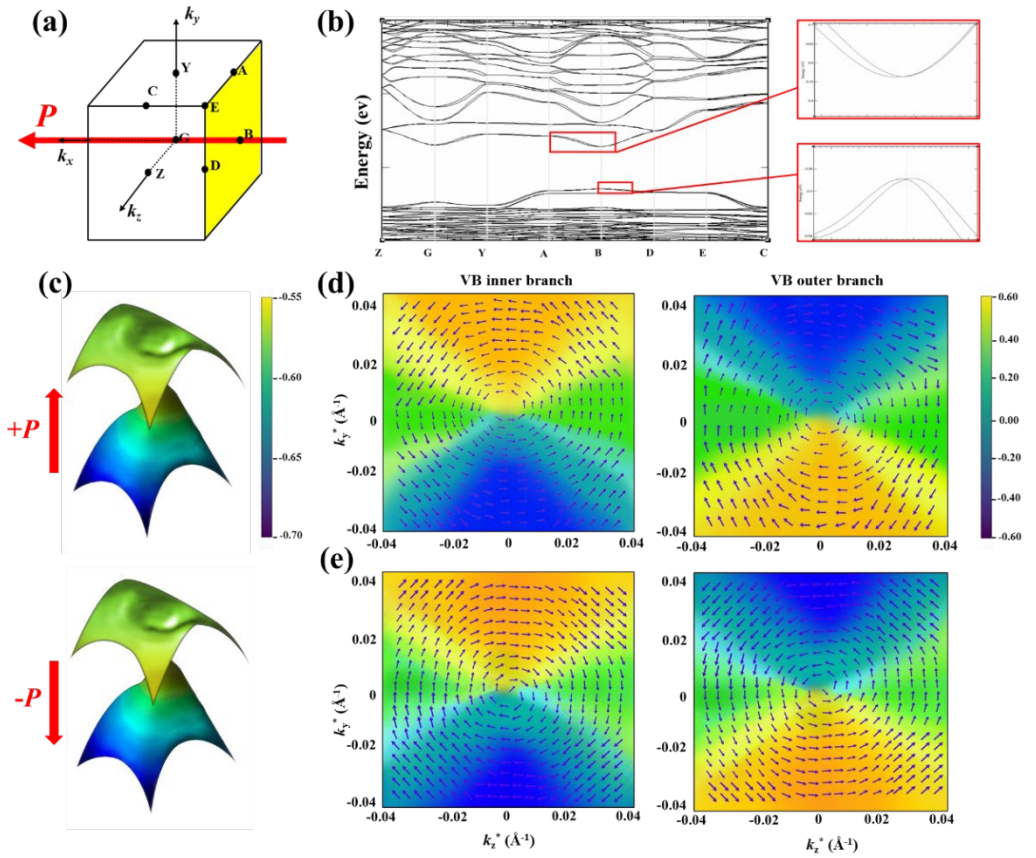

Figure 5.3. The band structure of the FE state. **(a)** The high-symmetry points of BZ. **(b)** Dispersed band structures along the whole BZ; the spin-split bands of the VBM (bottom) and CBM (top) were magnified in the red frames for emphasis. **(c)** 3D plot of band dispersion for valence bands (VBs) around B point. The color evolution from blue to yellow represents the VB eigenvalues. **(d, e)** The spin-textures projected on the 2D plane perpendicular to the FE polarization (*P*). The color code represents the s_x spin component.

Chapter 5: Switchable Rashba Anisotropy in Layered Hybrid Organic-Inorganic Perovskite by Hybrid Improper Ferroelectricity

While most studies on spin-orbit related properties estimate the Rashba parameter for a given direction (in the plane perpendicular to the polarization) and visualize the spin-texture and its switching properties, in addition here we focus on the anisotropy of the Rashba parameter and its relationship to the switching of the ferroelectric polarization. To probe this anisotropy, the band structure was calculated on a fine grid of points in the vicinity of the reciprocal-space B point within the 2D plane perpendicular to the FE polarization (the yellow $k_y k_z$ plane in Figure 5.3a). The calculated α_R parameters are summarized in Figure 5.4a, where we use a polar plot indicating the blue curves corresponding to the a_R obtained from the VBs and the green curves corresponding to those from the CBs. It can be seen that α_R parameters show a marked anisotropy, both at VBs and CBs. The maximum α_R of the VB at the B point (the blue curve in Figure 5.4a) is 2.39 eV·Å, located on the k_z-axis, whereas the minimum is 0.94 eV·Å, located on the k_y-axis, which indicates that α_R is not a constant but rather a function of the angle θ with respect to the negative k_z-axis (in the yellow plane in Figure 5.3a). Remarkably, we find that when the FE polarization is switched from $+P$ to $-P$, the major and minor axis of the Rashba anisotropy are exchanged as shown in Figure 5.4b, so that the maximum α_R value of the VB (2.22 eV·Å) shifts from the k_z-axis (b-axis) to the k_y-axis (c-axis), and the minimum α_R value (0.87 eV·Å) shifts the opposite way In other words, while the polarization switches from $+P$ to $-P$, the major axis α_R value decreases, while the minor axis α_R value increases. If we compare the $+P$ and $-P$ anisotropy ellipses, the net effect is an apparent 90° rotation of the anisotropy ellipse, *i.e.,* a pseudo-rotation. To the best of our knowledge, this is the first time that a polarization-switchable Rashba anisotropy has been observed, which is also connected to a very large anisotropy.

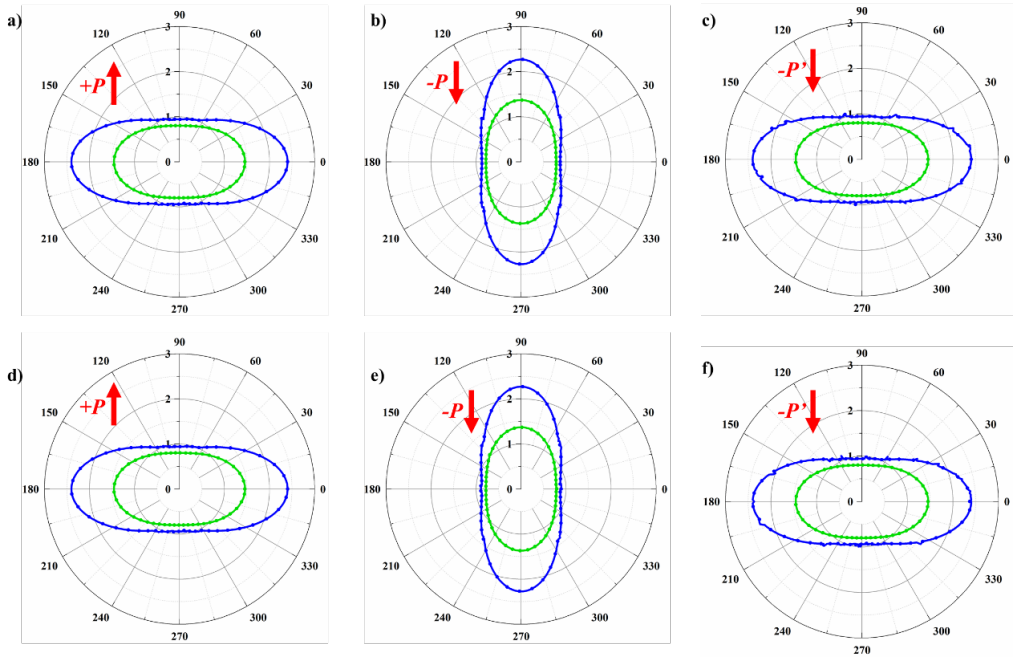

Figure 5.4. Polar plots of variable α_R for Rashba spin-split bands obtained along different directions in the plane perpendicular to the FE polarization. The plots of (**a-c**) are acquired at the B point while those of (**d-e**) are at the G point. The blue curves correspond to the α_R obtained from the VBs while the green curve corresponds to those from the CBs. The red arrows indicate the direction of the polarization, and $-P'$ indicates an alternative $-P$ structure wherein each AMP molecule rotates 180° relative to the $+P$ structure around the axis perpendicular to its maximum-electron-density plane rather than around the b axis. However, this $-P'$ is energetically unfavorable as discussed in text.

We propose a structural mechanism for this highly unusual polarization-switchable pseudo rotation of the Rashba anisotropy. As the AMP-cation orientations evolve between the $+P$ and $-P$ states, the roughly 180° rotation (approximately around the b-axis) of each cation not only switches the aminomethyl group between the $+a$ and $-a$ sides of the cation, but also rotates its maximum-electron-density plane (MEDP) by about 90° in the bc plane, which is dual to the $k_y k_z$ plane of the BZ (can be seen in Figure S5.2). To verify our hypothesis that this polarization-reversal-induced 90° rotation of the AMP cation's MEDP is responsible for the rotation of the Rashba-anisotropy, we construct an alternative $-P'$ structure from the $+P$ structure by rotating each AMP cations by 180° around the axis perpendicular to its MEDP, so that its aminomethyl group is still moved between the $+a$ and $-a$ sides, but without allowing the MEDP to rotate in the bc plane. When the structure is thus evolved, we

see no rotation of the Rashba anisotropy in its band structures (Figure 5.4c and 5.4f). Furthermore, compared to the isoenergetic $+P$ and normal $-P$ structures, the alternative $-P'$ structure has a 0.48 eV higher energy than $-P$ and is separated from $+P$ by an energy barrier of greater than 1.20 eV, demonstrating that the $-P'$ structure would be very difficult to obtain at room temperature.

To understand the Rashba anisotropy and spin texture under polarization switching, we construct the effective $k \cdot p$ model near the B point. The little group of the B point is C_s with only mirror symmetry operator My. Under the mirror transformation My: $(x, y, z) \rightarrow (x, -y, z)$, $(k_x, k_y, k_z) \rightarrow (k_x, -k_y, k_z)$ and $(\sigma_x, \sigma_y, \sigma_z) \rightarrow (-\sigma_x, \sigma_y, -\sigma_z)$. Then the two-band Hamiltonian for the VBM or CBM at $k_x = 0$ near the B point can be written as

$$H(k_y, k_z) = \varepsilon_0 + \frac{\hbar^2 k_y^2}{2m_y} + \frac{\hbar^2 k_z^2}{2m_z} + \alpha_1 k_z \sigma_y + \alpha_2 k_y \sigma_z + \alpha_3 k_y \sigma_x \quad (10.)$$

Here m_y and m_z are the effective masses along the k_y and k_z directions near the B point, and σ_x, σ_y and σ_z are Pauli matrices. α_1, α_2, and α_3 are three Rashba parameters. The last three terms are SOC terms that include the Rashba and Dresselhaus SOC effects, which can be rewritten in the form

$$H_{so} = \lambda_D(k_z \sigma_y + k_y \sigma_z) + \lambda_R(k_z \sigma_y - k_y \sigma_z) + \alpha_3 k_y \sigma_x \quad (11.)$$

where

$$\lambda_D = (\alpha_1 + a_2)/2 \quad (12.)$$

and

$$\lambda_D = (\alpha_1 - a_2)/2 \quad (13.)$$

are the Dresselhaus and Rashba parameters, respectively.[24] The last term $k_y \sigma_x$ leads to the emergence of the s_x spin component on the $k_y k_z$ plane which is consistent with our first principles calculation of the spin textures. The eigenvalues of the two-band Hamiltonian read as

$$E(k_y, k_z) = \varepsilon_0 + \frac{\hbar^2 k_y^2}{2m_y} + \frac{\hbar^2 k_z^2}{2m_z} \pm \sqrt{\alpha_1^2 k_z^2 + \alpha_2^2 k_y^2 + \alpha_3^2 k_y^2} \quad (14.)$$

To understand the Rashba anisotropy under polarization switching, the eigenvalues can be written as

$$E(k_r, \theta) = \varepsilon_0 + \left(\frac{\hbar^2}{2m_y} \sin^2\theta + \frac{\hbar^2}{2m_z} \cos^2\theta\right) k_r^2 \pm \sqrt{\alpha_1^2 \cos^2\theta + (\alpha_2^2 + \alpha_3^2) \sin^2\theta}\, |k_r| \quad (15.)$$

in polar coordinates. Here k_r is defined as the distance of k from the B point in the $k_y k_z$ plane, and θ is the angle between $\vec{k}_r$ and $\vec{k}_z$. One can define the general "Rashba parameter" with different directions on the $k_y k_z$ plane in polar coordinates as:

$$\alpha^{\uparrow}(\theta) = \sqrt{\alpha_1^2 \cos^2\theta + (\alpha_2^2 + \alpha_3^2)\sin^2\theta} \quad (16.)$$

where the arrow ↑ means the polarization along the $+x$ direction corresponding to the $+P$ state. The reorientation of the AMP cation, which involves the combination of a M_x mirror operation and a C_{4x} rotation operation, effects a 90° rotation of the crystal fields at the cation site such that $(x, y, z) \rightarrow (-x, z, y)$ and $(k_x, k_y, k_z) \rightarrow (-k_x, k_z, k_y)$. The eigenvalue of effective Hamiltonian of the $-P$ state should then be

$$E^{\downarrow}(k_r, \theta) = \varepsilon_0 + \left(\frac{\hbar^2}{2m_y}\cos^2\theta + \frac{\hbar^2}{2m_z}\sin^2\theta\right)k_r^2 \pm \sqrt{\alpha_1^2 \sin^2\theta + (\alpha_2^2 + \alpha_3^2)\cos^2\theta}\,|k_r| \quad (17.)$$

in polar coordinates. So the anisotropy of Rashba parameter of the $-P$ state is

$$\alpha^{\downarrow}(\theta) = \sqrt{\alpha_1^2 \sin^2\theta + (\alpha_2^2 + \alpha_3^2)\cos^2\theta} \quad (18.)$$

where the arrow ↓ means the polarization along the $-x$ direction. It is easy to see that

$$\alpha^{\uparrow}(\theta) = \alpha^{\downarrow}\left(\theta + \tfrac{\pi}{2}\right) \quad (19.)$$

which means the anisotropy of the Rashba parameter is rotated by 90° under polarization switching, which is equivalent to a 180° rotation of polarization. The proposed $k \cdot p$ model is thus nicely consistent with our DFT results in terms of a 90° pseudo-rotation. We introduce parameter

$$\mu = \left|\frac{\alpha_R(k_z) - \alpha_R(k_y)}{\alpha_R(k_y)}\right| = \left|\frac{\alpha_R(k_z)}{\alpha_R(k_y)} - 1\right| \quad (20.)$$

to quantify the strength of the anisotropy where $\alpha_R(k_z)$ and $\alpha_R(k_y)$ are the numerical values of the Rashba parameter along the k_z and k_y axes of the BZ, respectively. The larger the value of μ, the more pronounced the anisotropy of α_R is. In the case of the $-P$ and $+P$ polarizations, μ has quite similar values of 1.7 and 1.6, respectively, reflecting the robustness of the Rashba anisotropy in this system.

It is interesting to note that the pseudo-rotation of the Rashba anisotropy induced by polarization reversal occurs not only at a single point in *k*-space, but at several points where the Rashba splitting is effective. Our observations of the Rashba anisotropy in the VB and CB near both the B and G points of the BZ are all

qualitatively consistent with the description and explanation of Figure 5.4d-f above. At both of these points, the pseudo-rotation of the anisotropy ellipse occurs when reversing the polarization perpendicular to the framework layers.

5.3.4 Symmetry mode analysis

The $+P$ and $-P$ FE structures can be viewed as distorted "children" of an idealized "parent" structure, which allows us to characterize their symmetry-breaking structural variables (*i.e.,* symmetry modes) in terms of the irreducible representations (irreps) of the parent space-group symmetry. We construct this idealized parent from the centrosymmetric AFE structure in the left panel of Figure. 5.1a by regularizing the PbI_6 octahedra and zeroing the PbI_6 octahedral rotations in order to straighten out the framework, and by replacing each AMP cation with a polar vector (attached to a dummy atom at the molecular centroid location) that points along the appropriate $\pm a$ direction, resulting in centrosymmetric space group $Pcmm$ (#51, D_{2h}^5) on an orthorhombic $(\boldsymbol{a}, \boldsymbol{b}/2, \boldsymbol{c})$ unit-cell basis with zero origin shift relative to the child. We also idealize the FE children by replacing each AMP cation with an appropriate polar vector in order to apply the symmetry mode analysis consistently.

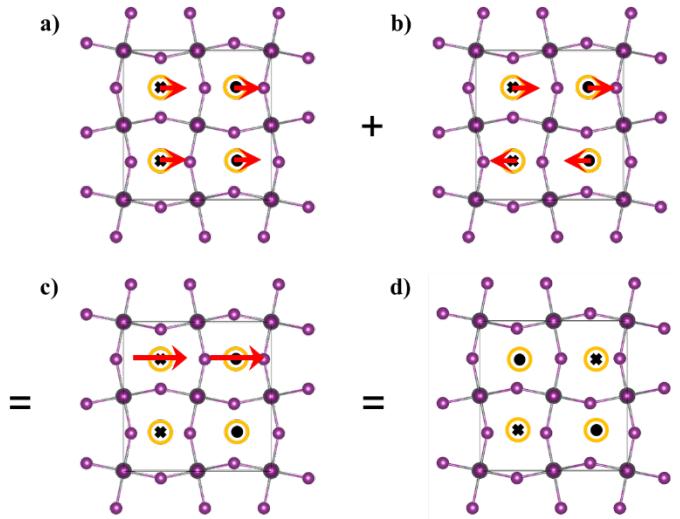

Figure 5.5. Molecular rotation modes. Short (90°) and long (180°) red arrows indicate right-handed molecular rotations relative to the AFE configuration. Summing the ferrorotational (FR) **(a)** and anti-ferrorotational (AFR) **(b)** patterns of 90° rotations causes only two of four molecules to rotate by 180° **(c)**, which is precisely the FE structure **(d)**.

The key order parameters of the idealized parent structure that characterize our FE child structures are (1) the PbI_6 octahedral framework rotation around the a-axis, which belongs to parent irrep Y_3^+, (2) the ferroelectric displacements along the a-axis, which belong to FE parent irrep Γ_2^-, and (3) the large AMP-cation rotations around the b-axis, which are achieved through the cooperative action of two parent irreps, ferrorotational (FR) irrep Γ_4^+ and anti-ferrorotational (AFR) irrep Y_1^-, as shown in Figure 5.5. Using the INVARIANTS software package, we find that these four primary order parameters provide a quadrilinear invariant term in the free energy expansion, so that simultaneously invoking the framework (Y_3^+) and the cation (Γ_4^+, Y_1^-) rotational modes breaks the inversion symmetry of parent, thus allowing them to couple to a secondary (*i.e.,* improper) ferroelectric moment (Γ_2^-).

Because the PbI_4 framework is only slightly disturbed in switching between the $+P$ and $-P$ states, it is convenient to treat the Y_3^+ framework rotation as a large preexisting structural feature in a slightly less-symmetric parent structure with space group $Pnmm$ (#59, D_{2h}^{13}) and unit-cell basis and origin identical to those of the child. For this this less-symmetric parent structure, the FR and AFR cation rotations form a simple trilinear invariant with the ferroelectric moment.

The $+P$ cation arrangement is obtained from the parent via the superposition of a 90° FR motion (Γ_4^+) and a 90° AFR motion (Y_1^-), so that two of the AMP cations are rotated by a full 180° while the other two remain stationary (as shown in Figure. 5.1). The $-P$ cation arrangement is achieved instead by merely reversing the sense of the AFR contribution. Due to the unfavorable energy at the 90° midpoint of rotation, it makes no sense to view the FR and AFR rotations as separate processes; they must occur simultaneously and cooperatively, so that the Γ_4^+ and Y_1^- order parameters are tightly coupled to have equal amplitudes. The product of two such large order parameters facilitate a strong trilinear coupling to the FE polarization. It remarkable that two centric modes, *i.e.,* Γ_4^+ and Y_1^-, combine together to give rise a hybrid mode, which in turn, breaks inversion symmetry and allows the polarization to arise in this system. Moreover, the coherent switching of both of them, *i.e.,* the switching of the hybrid mode, allows to switch the polarization giving rise to a hidden pseudo-rotation in k-space, as highlighted in this work with the switchable Rashba anisotropy ellipse. It is intriguing that the switchable Rashba anisotropy occurs coherently at different relevant point in k-space.

5.4 Concluding Remarks

In summary, HOIPs are emerging as a class of photovoltaic materials. In this work, DFT methods have been used to study the ferroelectric properties and Rashba spin-orbit effect as well as the coupling between the FE P_s and the anisotropy of α_R for a layered HOIP, $(AMP)PbI_4$, where AMP is 4-(aminomethyl)piperidinium. We calculate P_s and α_R to be 10.72 μC cm^{-2} and 2.39 eV·Å, respectively, which are nicely consistent with the experimentally reported values of 9.8 μC cm^{-2} and 2.60 eV·Å. To gain insight into the origin of the polarization, the contributions of the organic AMP^{2+} cations (10.34 μC cm^{-2}) and inorganic $[PbI_4]^{2-}$ framework (0.59 μC cm^{-2}) have been disentangled, demonstrating that the AMP cations contribute almost all of the total polarization.

As previously reported for Rashba ferroelectrics, the spin-texture sense of rotation can be reversed by a switching of the FE polarization direction along the polar axis.[40] However, in $(AMP)PbI_4$, we calculate a large and robust anisotropy in the Rashba parameter. Remarkably, we find that the major and minor axes of the ellipse can be exchanged under reversal of the electric polarization, causing a 90° pseudo-rotation of the Rashba anisotropy, which we have also been confirmed from a theoretical $k \cdot p$ model. The same effect is observed in both the VBs and CBs at multiple points in the Brillouin Zone where the Rashba splitting is significant. A structural mechanism for this effect is presented and explained in terms of a quadrilinear coupling of order parameters involving two large-amplitude AMP-cation rotation modes, a large octahedral framework rotation, and the ferroelectric polarization. To the best of our knowledge, this is the first report of a coupling of ferroelectric polarization and switchable highly-anisotropic Rashba spin-split bands and it may be possible that same property can be found in other layered hybrid perovskites. This deserves further investigations. Spin-optoelectronic devices based on hybrid organic-inorganic trihalide perovskites like spin-LEDs have been recently discussed for the parent compound $MAPbBr_3$,[25] circularly polarized light detections,[26] spin-FETs. This strong coupling may provide a potential probe of the spin degrees of freedom in photovoltaic materials and a different avenue for developing spin-optoelectronic devices based on HOIPs materials.

References

1. (a) Cui, Y.; Yao, H.; Zhang, J.; Zhang, T.; Wang, Y.; Hong, L.; Xian, K.; Xu, B.; Zhang, S.; Peng, J.; Wei, Z.; Gao, F.; Hou, J., *Nat. Commun.* **2019,** *10* (1), 2515; (b) Hong, L.; Yao, H.; Wu, Z.; Cui, Y.; Zhang, T.; Xu, Y.; Yu, R.; Liao, Q.; Gao, B.; Xian, K., *Adv. Mater.* **2019,** *31* (39), 1903441; (c) Aguiar, A.; Farinhas, J.; da Silva, W.; Susano, M.; Silva, M. R.; Alcacer, L.; Kumar, S.; Brett, C. M.; Morgado, J.; Sobral, A. J., *Dyes Pigm.* **2020,** *172*, 107842.

2. (a) Tsai, H.; Nie, W.; Blancon, J.-C.; Stoumpos, C. C.; Asadpour, R.; Harutyunyan, B.; Neukirch, A. J.; Verduzco, R.; Crochet, J. J.; Tretiak, S., *Nature* **2016,** *536* (7616), 312-316; (b) Wu, T.; Wang, J., *Nano Energy* **2019,** *66*, 104070; (c) Ghosh, D.; Aziz, A.; Dawson, J. A.; Walker, A. B.; Islam, M. S., *Chem. Mater.* **2019,** *31* (11), 4063-4071; (d) Ferdani, D. W.; Pering, S. R.; Ghosh, D.; Kubiak, P.; Walker, A. B.; Lewis, S. E.; Johnson, A. L.; Baker, P. J.; Islam, M. S.; Cameron, P. J., *Energy Environ. Sci.* **2019,** *12* (7), 2264-2272; (e) Brenes, R.; Eames, C.; Bulović, V.; Islam, M. S.; Stranks, S. D., *Adv. Mater.* **2018,** *30* (15), 1706208.

3. (a) Kahmann, S.; Loi, M. A., *J. Mater. Chem. C* **2019,** *7* (9), 2471-2486; (b) Wang, Z.; Song, Z.; Yan, Y.; Liu, S.; Yang, D., *Adv. Sci.* **2019,** *6* (7), 1801704; (c) Fang, H.-H.; Adjokatse, S.; Shao, S.; Even, J.; Loi, M. A., *Nat. Commun.* **2018,** *9* (1), 243; (d) Polman, A.; Knight, M.; Garnett, E. C.; Ehrler, B.; Sinke, W. C., *Science* **2016,** *352* (6283), aad4424; (e) Tayebjee, M. J.; McCamey, D. R.; Schmidt, T. W., *J. Phys. Chem. Lett.* **2015,** *6* (12), 2367-2378.

4. (a) Shi, C.; Ye, L.; Gong, Z.-X.; Ma, J.-J.; Wang, Q.-W.; Jiang, J.-Y.; Hua, M.-M.; Wang, C.-F.; Yu, H.; Zhang, Y., *J. Am. Chem. Soc.* **2019,** *142* (1), 545-551; (b) Pandey, R.; Vats, G.; Yun, J.; Bowen, C. R.; Ho-Baillie, A. W. Y.; Seidel, J.; Butler, K. T.; Seok, S. I., *Adv. Mater.* **2019,** *31* (43), e1807376; (c) Balachandran, P. V.; Kowalski, B.; Sehirlioglu, A.; Lookman, T., *Nat. Commun.* **2018,** *9* (1), 1668; (d) Hua, X.-N.; Liao, W.-Q.; Tang, Y.-Y.; Li, P.-F.; Shi, P.-P.; Zhao, D.; Xiong, R.-G., *J. Am. Chem. Soc.* **2018,** *140* (38), 12296-12302; (e) Pan, Q.; Liu, Z.-B.; Tang, Y.-Y.; Li, P.-F.; Ma, R.-W.; Wei, R.-Y.; Zhang, Y.; You, Y.-M.; Ye, H.-Y.; Xiong, R.-G., *J. Am. Chem. Soc.* **2017,** *139* (11), 3954-3957; (f) Xu, W.-J.; Li, P.-F.; Tang, Y.-Y.; Zhang, W.-X.; Xiong, R.-G.; Chen, X.-M., *J. Am. Chem. Soc.* **2017,** *139* (18), 6369-6375.

5. (a) Lee, H.; Im, J.; Jin, H., *Appl. Phys. Lett.* **2020,** *116* (2), 022411; (b) Lin, Z.; Si, C.; Duan, S.; Wang, C.; Duan, W., *Phys. Rev. B* **2019,** *100* (15), 155408; (c) He, J.; Di

Sante, D.; Li, R.; Chen, X.-Q.; Rondinelli, J. M.; Franchini, C., *Nat. Commun.* **2018,** *9* (1), 492; (d) Djani, H.; Garcia-Castro, A. C.; Tong, W.-Y.; Barone, P.; Bousquet, E.; Picozzi, S.; Ghosez, P., *npj Quantum Mater.* **2019,** *4* (1), 51; (e) Kepenekian, M.; Robles, R.; Katan, C.; Sapori, D.; Pedesseau, L.; Even, J., *ACS Nano* **2015,** *9* (12), 11557-11567.

6. (a) Zhai, Y.; Baniya, S.; Zhang, C.; Li, J.; Haney, P.; Sheng, C.-X.; Ehrenfreund, E.; Vardeny, Z. V., *Sci. Adv.* **2017,** *3* (7), e1700704; (b) Picozzi, S., *Front. Phys.* **2014,** *2* (10); (c) Vajna, S.; Simon, E.; Szilva, A.; Palotas, K.; Ujfalussy, B.; Szunyogh, L., *Phys. Rev. B* **2012,** *85* (7), 075404.

7. (a) Maaß, H.; Bentmann, H.; Seibel, C.; Tusche, C.; Eremeev, S. V.; Peixoto, T. R. F.; Tereshchenko, O. E.; Kokh, K. A.; Chulkov, E. V.; Kirschner, J.; Reinert, F., *Nat. Commun.* **2016,** *7* (1), 11621; (b) Kim, M.; Im, J.; Freeman, A. J.; Ihm, J.; Jin, H., *Proc. Natl. Acad. Sci. U.S.A.* **2014,** *111* (19), 6900-6904.

8. (a) Rinaldi, C.; Varotto, S.; Asa, M.; Sławińska, J.; Fujii, J.; Vinai, G.; Cecchi, S.; Di Sante, D.; Calarco, R.; Vobornik, I.; Panaccione, G.; Picozzi, S.; Bertacco, R., *Nano Lett.* **2018,** *18* (5), 2751-2758; (b) Krempaský, J.; Muff, S.; Bisti, F.; Fanciulli, M.; Volfová, H.; Weber, A. P.; Pilet, N.; Warnicke, P.; Ebert, H.; Braun, J.; Bertran, F.; Volobuev, V. V.; Minár, J.; Springholz, G.; Dil, J. H.; Strocov, V. N., *Nat. Commun.* **2016,** *7* (1), 13071.

9. Park, I.-H.; Zhang, Q.; Kwon, K. C.; Zhu, Z.; Yu, W.; Leng, K.; Giovanni, D.; Choi, H. S.; Abdelwahab, I.; Xu, Q.-H., *J. Am. Chem. Soc.* **2019,** *141* (40), 15972-15976.

10. (a) Zheng, F.; Takenaka, H.; Wang, F.; Koocher, N. Z.; Rappe, A. M., *J. Phys. Chem. Lett.* **2015,** *6* (1), 31-37; (b) Li, L.; Liu, X.; Li, Y.; Xu, Z.; Wu, Z.; Han, S.; Tao, K.; Hong, M.; Luo, J.; Sun, Z., *J. Am. Chem. Soc.* **2019,** *141* (6), 2623-2629.

11. (a) von Hippel, A., *Rev. Mod. Phys.* **1950,** *22* (3), 221-237; (b) Shieh, J.; Yeh, J. H.; Shu, Y. C.; Yen, J. H., *Materials Science and Engineering: B* **2009,** *161* (1), 50-54.

12. Blöchl, P. E., *Phys. Rev. B* **1994,** *50* (24), 17953-17979.

13. Perdew, J. P.; Ruzsinszky, A.; Csonka, G. I.; Vydrov, O. A.; Scuseria, G. E.; Constantin, L. A.; Zhou, X.; Burke, K., *Phys. Rev. Lett.* **2008,** *100* (13), 136406.

14. Grimme, S.; Antony, J.; Ehrlich, S.; Krieg, H., *J. Chem. Phys.* **2010,** *132* (15), 154104.

15. (a) Spaldin, N. A., *J. Solid State Chem.* **2012,** *195*, 2-10; (b) Resta, R., *Rev. Mod. Phys.* **1994,** *66* (3), 899-915; (c) King-Smith, R. D. V., V, *Phys. Rev. B* **1993,** *47* (3), 4.

16. Grimme, S., *J. Comput. Chem.* **2004,** *25* (12), 1463-1473.

17. Fonseca Guerra, C.; Handgraaf, J.-W.; Baerends, E. J.; Bickelhaupt, F. M., *J. Comput. Chem.* **2004,** *25* (2), 189-210.

18. Reed, A. E.; Weinstock, R. B.; Weinhold, F., *J. Chem. Phys.* **1985,** *83* (2), 735-746.

19. Frisch, M. J.; Trucks, G. W.; Schlegel, H. B.; Scuseria, G. E.; Robb, M. A.; Cheeseman, J. R.; Scalmani, G.; Barone, V.; Petersson, G. A.; Nakatsuji, H.; Li, X.; Caricato, M.; Marenich, A. V.; Bloino, J.; Janesko, B. G.; Gomperts, R.; Mennucci, B.; Hratchian, H. P.; Ortiz, J. V.; Izmaylov, A. F.; Sonnenberg, J. L.; Williams; Ding, F.; Lipparini, F.; Egidi, F.; Goings, J.; Peng, B.; Petrone, A.; Henderson, T.; Ranasinghe, D.; Zakrzewski, V. G.; Gao, J.; Rega, N.; Zheng, G.; Liang, W.; Hada, M.; Ehara, M.; Toyota, K.; Fukuda, R.; Hasegawa, J.; Ishida, M.; Nakajima, T.; Honda, Y.; Kitao, O.; Nakai, H.; Vreven, T.; Throssell, K.; Montgomery Jr., J. A.; Peralta, J. E.; Ogliaro, F.; Bearpark, M. J.; Heyd, J. J.; Brothers, E. N.; Kudin, K. N.; Staroverov, V. N.; Keith, T. A.; Kobayashi, R.; Normand, J.; Raghavachari, K.; Rendell, A. P.; Burant, J. C.; Iyengar, S. S.; Tomasi, J.; Cossi, M.; Millam, J. M.; Klene, M.; Adamo, C.; Cammi, R.; Ochterski, J. W.; Martin, R. L.; Morokuma, K.; Farkas, O.; Foresman, J. B.; Fox, D. J. Wallingford, CT, 2016.

20. Park, I. H.; Zhang, Q.; Kwon, K. C.; Zhu, Z.; Yu, W.; Leng, K.; Giovanni, D.; Choi, H. S.; Abdelwahab, I.; Xu, Q.-H.; Sum, T. C.; Loh, K. P., *J. Am. Chem. Soc.* **2019,** *141* (40), 15972-15976.

21. Resta, R.; Vanderbilt, D., *Theory of polarization: a modern approach*. Springer Berlin Heidelberg: Berlin, Heidelberg, 2007; pp 31-68.

22. Karin M. Rabe; Charles H. Ahn; Triscone, J.-M., *Physics of Ferroelectrics: A Modern Perspective*. Springer, Berlin, Heidelberg: 2007; p XII, 388.

23. (a) Di Sante, D.; Barone, P.; Bertacco, R.; Picozzi, S., *Adv. Mater.* **2013,** *25* (4), 509-513; (b) Stroppa, A.; Di Sante, D.; Barone, P.; Bokdam, M.; Kresse, G.; Franchini, C.; Whangbo, M.-H.; Picozzi, S., *Nat. Commun.* **2014,** *5* (1), 1-8.

24. (a) Tao, L. L.; Paudel, T. R.; Kovalev, A. A.; Tsymbal, E. Y., *Phys. Rev. B* **2017,** *95* (24), 245141; (b) Tao, L. L.; Tsymbal, E. Y., *Nat. Commun.* **2018,** *9* (1), 2763.

25. Wang, J.; Zhang, C.; Liu, H.; McLaughlin, R.; Zhai, Y.; Vardeny, S. R.; Liu, X.; McGill, S.; Semenov, D.; Guo, H.; Tsuchikawa, R.; Deshpande, V. V.; Sun, D.; Vardeny, Z. V., *Nat. Commun.* **2019,** *10* (1), 129.

26. Chen, C.; Gao, L.; Gao, W.; Ge, C.; Du, X.; Li, Z.; Yang, Y.; Niu, G.; Tang, J., *Nat. Commun.* **2019,** *10* (1), 1-7.

Chapter 6. Density Functional Theory Analysis of Single-molecule Ferroelectricity in Preyssler-type Polyoxometalates

CHAPTER 6

Density Functional Theory Analysis of Single-molecule Ferroelectricity in Preyssler-type Polyoxometalates

A detailed study on the single-molecule ferroelectric property of Preyssler-type POMs, $[M^{3+}P_5W_{30}O_{110}]^{12-}$ (M = La, Gd and Lu), is performed by DFT calculations. Linked to one H_2O molecule, the cation (M^{3+}) encapsulated in the cavity of the Preyssler framework is off-centered and it generates a permanent dipole, which is essential for a ferroelectric ground state. Accompanied with a 180° rotation of H_2O, the switching of M^{3+} between two isoenergetic sites on both sides of the cavity results in a calculated barrier of 1.15 eV for Gd^{3+}, leading to the inversion of the electric polarization. The height of the barrier is in good agreement with the experimentally measured barrier for the Tb^{3+} ion, whose ionic radius is similar to Gd^{3+}. The total polarization value of the crystal is simulated to be 4.7 $\mu C/cm^2$ as calculated by the modern theory of polarization, which is quite close to the experimental value. Considering that the order of contributions to the polarization is M^{3+}-H_2O > counter cations (K^+) > $[P_5W_{30}O_{110}]^{15-}$, the interconversion of M^{3+}-H_2O between the two isoenergetic sites is predicted to be the main origin of the ferroelectricity with a polarization contribution of 3.4 $\mu C/cm^2$; the K^+ counter-cations contribute by 1.2 $\mu C/cm^2$ and it cannot be disregarded, while the framework appears to contribute negligibly to the total polarization. Our study suggests that a suitable choice of the M^{3+}-H_2O could be used to tune the single-molecule ferroelectricity in Preyssler-type polyoxometalates. Please find the published version of this work with the same title here (https://doi.org/10.1063/5.0035778).

6.1 Background

In the vast family of POMs, the doughnut-shaped molecule constituted of five PO_4 tetrahedra surrounded by 30 WO_6 octahedra is termed as Preyssler-type POMs ($[M^{n+}P_5W_{30}O_{110}]^{(15-n)-}$, abbreviated as $[M^{n+}@P_5W_{30}]^{(15-n)-}$), and shown in Figure 6.1.[1] Compared to the classical Keggin- and Dawson-type POMs, Preyssler anions display distinctive properties, among which most notably are their (1) high negative charges (-12 ~ -15); (2) large oxidation potential, and (3) reversible transformation. The diameter of the internal cavity of Preyssler clusters approaches 5 Å, large enough to

accommodate at least one metal cation (M^{n+}).[2] So far, most studies addressed the (electro)catalytic activities and extending frameworks for functionalization of Preyssler clusters,[3] but very recently, Nishihara and co-workers reported a Preyssler cluster, $[Tb^{3+}@P_5W_{30}]^{12-}$, showing switchable electric polarization with high spontaneous polarization (6 μC/cm²) and coercive electric fields, which is the first discovery of FE in the family of POMs.[4] It was assumed that a Tb^{3+} cation encapsulated in the Preyssler cluster could be interconverted by thermal energy and electric field between two isoenergetic sites (Site-A and Site-A' in Figure 6.1), leading to the inversion of polarization. Although the bi-stability of the two isoenergetic sites provides the basic ingredients to explain FE, there are still some points that need further clarification for a complete description of the origin of FE in the Preyssler clusters. In the first place, it is not clear whether there is a water molecule bound to the Tb^{3+} cation inside the cavity of the POM, which would certainly influence the interconversion of the cation between the two isoenergetic sites. X-ray and EXAFS studies of $[M^{n+}@P_5W_{30}]^{(15-n)-}$ (M = Na, Ca, Y, Ag and Bi) have typically indicated the presence of a water molecule inside the cavity linked to the M^{n+} ion.[3b, 5] Moreover, due to the relatively high charge of the Preyssler anion, quite a few counter-cations are present in the crystal, which is closely associated with the redistribution of charges and may play a role in the polarization switching. While experimental studies have been addressed for Preyssler systems, a detailed analysis based on DFT for the microscopic mechanism at the origin of this "single-molecule" ferroelectricity is still lacking due to the complexity of the system. This motivated us to close this gap.

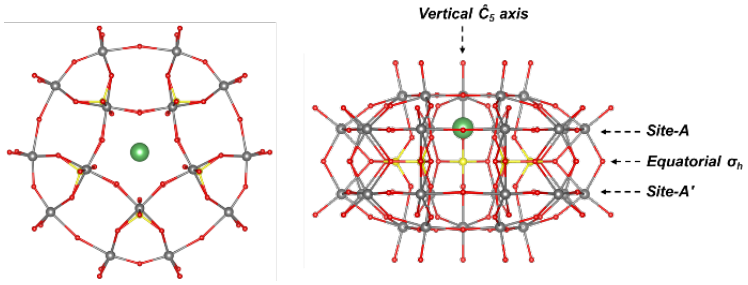

Figure 6.1. The top (left) and side (right) views of the ball-and-stick model of $[M^{n+}@P_5W_{30}]^{(15-n)-}$ cluster. Color code: gray (W), red (O), yellow (P) and green (M). The two isoenergetic sites of an encapsulated M^{n+} cation are Site-A and Site-A', the population of which is assumed to be interconverted by thermal energy and electric field.

Here we report DFT calculations carried out to explore the effect of a water molecule inside the cavity and the origin and main contributions to the ferroelectric

property experimentally observed in the $[M^{3+}@P_5W_{30}]^{12-}$ system, with M = La, Gd and Lu. Gd^{3+} has a similar ionic radius as Tb^{3+} but is computationally much simpler because of the half-filled 4f shell. DFT has in general important problems in treating ions with partially filled f-shells other than $4f^7$. La^{3+} ($4f^0$) and Lu^{3+} ($4f^{14}$) are studied for comparison, being the largest and smallest ions of the lanthanide series, respectively. Our results are arranged as follows. We first systematically examine the structures of the Preyssler anions $[M^{3+}@P_5W_{30}]^{12-}$, combined with the energy comparison between ferroelectric and anti-ferroelectric phase. We find that one water molecule linked to the internal cation is necessary for a ferroelectric ground state. Without an extra water molecule in the cavity, there is no indication that the metal will leave the center of the cavity and break the structural symmetry. Then we explore the switching path connecting Site-A and Site-A' of the encapsulated cation-water unit (M^{3+}-H_2O). Combining the displacement of M^{3+} between the two isoenergetic sites with a 180° rotation of H_2O results in a barrier of 1.15 eV for Gd^{3+}, in good agreement with the experimental barrier of 0.96 eV for Tb^{3+}.[4] Finally, we calculate the polarization value to be 4.7 μC/cm^2 of the Preyssler crystal using the Berry phase method,[6] which is in fairly good agreement with the experimental value of about 6 μC/cm^2.[4] We also observe that the interconversion of M^{3+}-H_2O between two isoenergetic sites induces a polarization of 3.4 μC/cm^2, and it can be considered as the main origin of the FE. The polarization contribution of K^+ counterions is about 1.2 μC/cm^2. It is certainly non-negligible while the contribution of the $[P_5W_{30}]^{15-}$ framework is much smaller and can safely be ignored.

6.2 Computational Details

Geometry optimizations for the isolated molecule were performed with the ADF 2016 package[7] using the OPBE functional.[8] All-electron triple-ζ-quality basis sets with single polarization functions (TZP) were used for all atoms.[9] Relativistic effects were included via the zeroth-order regular approximation (ZORA).[10] The solvent effects were treated by the conductor-like screening model (COSMO) with a dielectric constant (ε) of 78 to simulate the aqueous environment, as implemented in ADF 2016.[11] Different point-group symmetries were applied considering the complexity of the Preyssler cluster. Open-shell electronic configurations were considered with the spin-unrestricted formalism in the Gd^{3+} case.[12] For the crystal structure, we started our calculations from the experimental crystallographic data of the Preyssler system with

M^{3+} = Bi^{3+}.[66] The structure is orthorhombic, space group Pnma with a = 28.6997 Å; b = 21.5091 Å; c = 20.8737 Å and has 114 symmetry unique centres. It is optimized until Hellmann-Feynman forces were smaller than 0.05 eV/Å. Kohn-Shan equations were solved using the projector-augmented-wave (PAW) method,[13] as implemented in VASP.[14] The standard corresponding pseudopotentials represent the La [Kr-4d]; Gd, Lu, W [Xe]; K (1s2-3s2); P (1s2-2p6); O (1s2) core electrons. We have used the PBE functional for exchange-correlation functional.[15] The energy cutoff for the plane wave expansion was set to 400 eV in concordance with cutoffs used in other studies.[16] Geometry optimizations at the Gamma point and a 2×2×2 grid was used for the calculation of electronic polarization. By establishing a suitable antiferroelectric phase, the Berry phase approach is used to evaluate the ferroelectric polarization.

6.3 Results and Discussion

6.3.1 Structural analysis

The first issue that needs to be clarified is the possible presence of water molecules inside the cavity. In the experimental study, the crystals were dried before the polarization measurements.[4] This could imply that in addition to the interstitial water molecules, also the water molecule(s) on the inside of the Preyssler cage (if present at all) were removed from the sample. Experimental studies showed that in some $[M@P_5W_{30}]$ systems the encapsulated ion is bound to a water molecule[5a] and located off-centre, while in others no sign of water was found.[16a] In previous studies in our group of a series of $[M@P_5W_{30}]^{q-}$ structures, it was established that only the inclusion of a water molecule inside the cavity leads to an optimized structure with the Na^+ ion at the position measured in experiment.[2a] Due to computational limitations, other systems (among which also the here studied compound with La^{3+}) were optimized without water on the inside of the cage. Now that the computational limitations are no longer pressing, we have studied the geometry of $[M@P_5W_{30}]^{12-}$ and $[M\text{-}H_2O@P_5W_{30}]^{12-}$ (M= La^{3+}, Gd^{3+} and Lu^{3+}) only imposing the symmetry restrictions of C_s spatial group. This ensures that all structural relaxations (off-site movement of the encapsulated cation, W-O-W bond length alternation, *etc.*) can take place when energetically favourable.

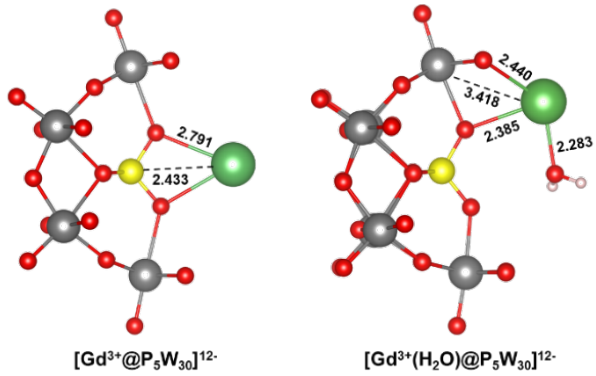

Figure 6.2. Optimized ball-and-stick representation of one-fifth of $[Gd^{3+}@P_5W_{30}]^{12-}$ and $[Gd^{3+}(H_2O)@P_5W_{30}]^{12-}$. Main distances in Å. Color code: gray (W), red (O), yellow (P) and green (Gd^{3+}).

Table 6.1. The computed alternating long and short W-O bond lengths ($d_{(W\text{-}O)}$, Å) of the $[M^{3+}@P_5W_{30}]^{12-}$ clusters (without H_2O bound to the M^{3+} cation inside the cavity), the equatorial distance of the M^{3+} cation from the vertical [circ]-$\hat{C}_5$ axis ($d_{M\text{-}\hat{C}5}$, Å), the vertical distance of the M^{3+} cation from the center of the cavity ($d_{M\text{-center}}$, Å), and energy differences (ΔE, kcal/mol) in different symmetry.

	La^{3+}		Gd^{3+}		Lu^{3+}	
	C_1	D_{5h}	C_1	D_{5h}	C_1	D_{5h}
$d_{(W\text{-}O)\text{-long}}$	2.12	1.94	2.12	1.94	2.12	1.94
$d_{(W\text{-}O)\text{-short}}$	1.82	1.94	1.82	1.94	1.82	1.94
$d_{M\text{-}\hat{C}5}$	0.48	0	0.70	0	0.84	0
$d_{M\text{-center}}$	0.00	0.00	0.01	0.00	0.01	0.00
ΔE	0	+15.90	0	+25.41	0	+36.94

Without water molecule, all three systems converge to a geometry with the cation at the centre of the cavity, while the incorporation of a water molecule pushes the cations away from it. The bond lengths are 2.381 Å for La^{3+}-H_2O, 2.283 Å for Gd^{3+}-H_2O and 2.203 Å for Lu^{3+}-H_2O, as depicted in Figure 6.2 (right). More structural details including long and short W-O bond lengths, the equatorial distance of the M^{3+} cation from the vertical [circ]-$\hat{C}_5$ axis, and the vertical distance of the M^{3+} cation from

the center of the cavity, can be found in Table 6.1. Two isoenergetic positions are also discovered; Site-A in the upper half of the cavity and Site-A' in the lower half. The position of Site-A (A') is not exactly the same for the three ions, and depending on the radius of the lanthanide, i.e. 1.798 Å for La^{3+}, 1.743 Å for Gd^{3+} and 1.723 Å for Lu^{3+} above (or below) the center of the cavity. We roughly estimate the binding energy ($\Delta E_{binding\_H2O}$, kcal/mol) between the internal M^{3+} cation and a H_2O molecule and compare the modulus with the case where the internal cation is Na^+. The calculation model of the binding energy can be seen in Figure 6.3. The structure of $[Na^+@P_5W_{30}]^{14-}$ has been experimentally confirmed that Na^+ is combined with a H_2O molecule encapsulated in the cavity. The results are summarized in Figure 6.4, in which the cases of M^{q+} = Ca^{2+} and Bi^{3+} are also listed for comparison. The observation that the binding energy of the three lanthanide ions is larger than in the case of Na^+ indicates that the water molecule can indeed reside inside the cavity.

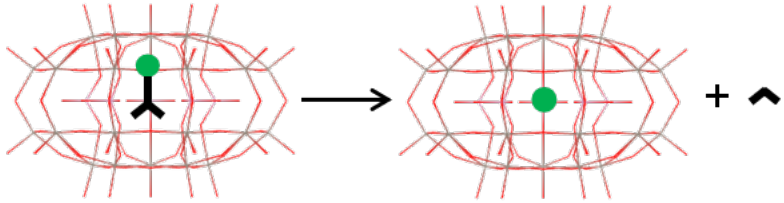

Figure 6.3. The calculation model of the binding energy between an internal cation and an H_2O molecule. Color code: red Preyssler framework, green internal M^{q+} cation, and black two black sticks signify the H_2O molecule.

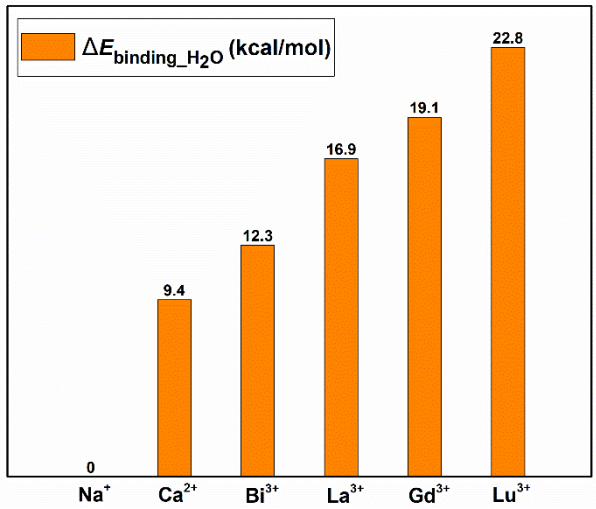

Figure 6.4. Calculated binding energy ($\Delta E_{binding\_H2O}$, kcal/mol) relative to $[Na^+(H_2O)@P_5W_{30}]^{14-}$ of different internal cations (M^{q+}) with a H_2O molecule.

6.3.2 The interconversion of M^{3+}(-H_2O)

Following the assumption that the ferroelectric property of the Preyssler cluster originates from the interconversion of the cation trapped in the cavity between the two isoenergetic sites (Figure 6.1), the energies related to the process of M^{3+} moving from Site-A to Site-A' along the vertical $\hat{C}_5$ axis are calculated. The study is carried out as a series of restricted geometry optimizations fixing the M^{3+} ion at different positions on the $\hat{C}_5$ axis with steps of 0.5 Å. Every structure is re-optimized, keeping the position of M^{3+} frozen, under the C_{5v} symmetry without H_2O and under the C_s symmetry with one H_2O molecule bound to the cation. Figure 6.5 displays the schematic energy profiles associated with the interconversion process of the M^{3+}, where the solid curve on the top panel corresponds to the presence of H_2O inside the cavity while the dashed curve on the bottom corresponds to the absence of H_2O. While the relative energies are different for the three ions, the shape is strictly the same in all cases. When M^{3+} is not connected to H_2O, the energy decreases by 0.28 eV for La^{3+}, 0.34 eV for Gd^{3+} and 1.38 eV for Lu^{3+} as the cation moves from Site-A to the center position and then increases again by the same amount moving on to Site-A'. If the cation moves further outward beyond Site-A', the energy of the system continues to rise, and it will reach a maximum when the ion passes through the window of the framework. Therefore, the energy

profile of the whole process is a simple parabola with a single minimum representing as the M^{3+} displaces along the $\hat{C}_5$ axis.

However, the situation changes dramatically when a H_2O molecule is linked to M^{3+}. The energy increases by 0.57 eV for La^{3+}, 0.24 eV for Gd^{3+} and 0.032 eV for Lu^{3+} from A to the center, reaching a maximum at the center of the cavity, and then decreases again when M^{3+} moves to Site-A'. We have also verified that the M^{3+} ion located at Site-A shifts to the center of the molecule when the structure is fully relaxed without symmetry constraints. This is important since POM frameworks present what is known as alternating bond distortions that are hampered with the presence of symmetry constraints.[16b] The two completely different profiles suggest that the presence of water is necessary for having the cation off-centered giving rise to two isoenergetic sites of the cation, a necessary condition for (anti-)ferroelectric properties. So far, we have only studied the displacement of the M^{3+}-H_2O unit from the center of the cavity to the Site-A or A' but as can be seen in the broken solid curve (the half green part and half blue part) of Figure 6.5, the two potential energy surfaces cannot be connected as the orientation of the water molecule is opposite for the two cases.

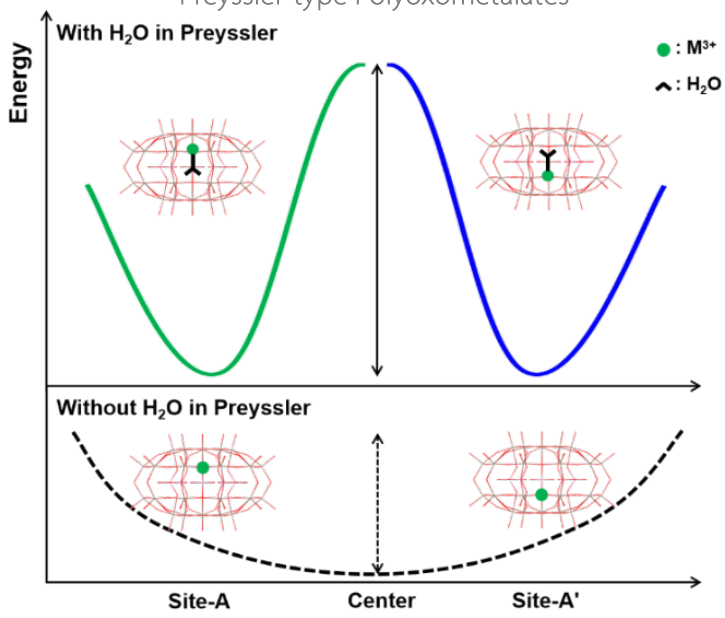

Figure 6.5. Schematic energy profiles for M^{3+} displacement with H_2O (the "broken" solid curve) or without H_2O (the full dashed curve) from Site-A to Site-A' along the vertical $\hat{C}_5$ axis of the Preyssler cluster. The "broken" solid line includes green and blue parts, where green represents the movement from A to the centre of the cavity while blue represents from A' to the centre. The green and blue curves cannot be connected because of the different orientation of the water molecule. Color code: Preyssler framework (red), M^{3+} cation (green) and H_2O (Λ-shaped black sticks).

Therefore, we explore the potential energy profiles for the displacement of the internal M^{3+}-H_2O unit in more detail, especially the way the unit passes through the centre. We study three possibilities for the unit to switch between the two isoenergetic points. In the first one the orientation of M^{3+} and H_2O (M^{3+} is up and H_2O is down) is assumed to remain constant during the interconversion, as depicted by the blue curve in Figure 6.6. Starting from the minimum A, the energy first rises and then falls until reaching the second minimum when M^{3+} is located near the center of the cavity, which is 0.72 eV (in the Gd^{3+} case) higher than A. As M^{3+}-H_2O continues to move down, the energy increases again and reaches a maximum when M^{3+} is about 1 Å below the center and H_2O is exactly located at the window, the narrowest part of Preyssler, suggesting a strong interaction between H_2O and the framework here. If the metal is pushed further downwards to Site-A', the M-H_2O bond breaks and water leaves the cavity. As explained above, the bare metal ion tends to occupy the center of the cavity.

Considering the experimental observation that the ferroelectric polarization has the same numerical value with the opposite direction at two isoenergetic points, we expect that the structures at these points should have a symmetry operation relating to each other. Hence, this path is not consistent with the experimental fact, although the relatively low barrier makes it possible for Gd^{3+} and Lu^{3+} to move from the upper part of the cavity to the lower one at room temperature.

The second hypothesis assumes that the displacement of M^{3+}-H_2O is accompanied by the gradual rotation of H_2O and their relative orientation is reversed from up-down at A to down-up at A', described by the red curve in Figure 6.6. In this way, one can guarantee that the two structures at the isoenergetic sites are symmetrical to each other. The intermediate situation with the M^{3+}-H_2O lying in the σ_h plane (the center of the cavity, $\theta = 90°$) turns out to be a (meta-)stable intermediate connected to the initial position (Site-A) by a transition state ($\theta = 39°$), 0.6 Å from the σ_h plane, at slightly higher energy (0.19 eV for Gd^{3+}). The overall energy barriers to go from Site-A to A' are 1.61, 1.15 and 0.52 eV for La^{3+}, Gd^{3+} and $Lu^{3+,}$ respectively. Among them, the barrier of 1.15 eV for Gd^{3+} matches the experimental 0.96 eV for Tb^{3+} quite well, in line with the similar radii of both ions. The final possibility that we explored is that a second H_2O enters the Preyssler framework from the outside, pushes the M^{3+}-H_2O unit down until the original H_2O leaves the Preyssler framework (the far right panel of Figure. 6.6). However, the calculations show that inserting a water molecule consumes more than 2.0 eV of energy. Therefore, we also have to overthrow the third hypothesis and mark the second scenario as the most probable mechanism for inverting the dipole moment of the POM.

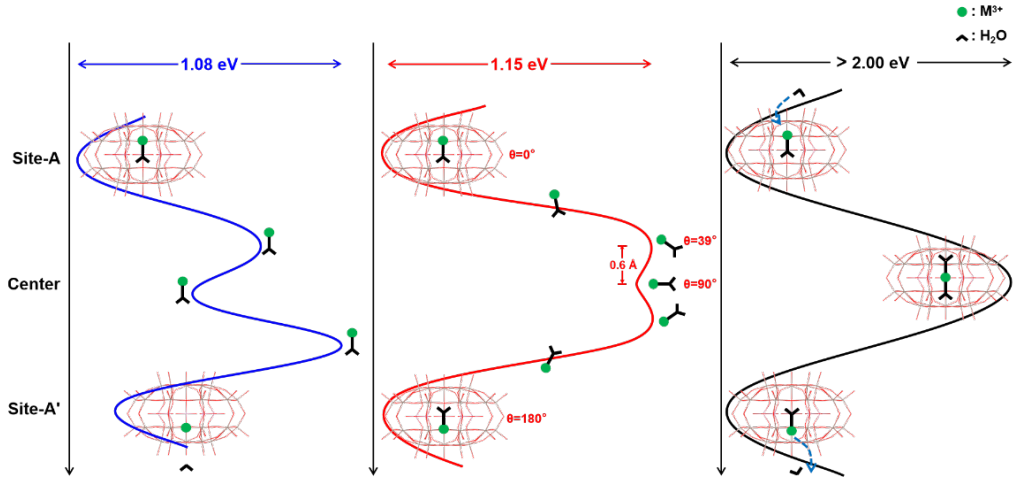

Figure 6.6. Three possible pathways for the Gd^{3+}-H_2O unit to switch between Site-A and Site-A'. The blue curve represents that the relative orientation of Gd^{3+} and H_2O remains unchanged. The red curve describes that the displacement of Gd^{3+}-H_2O is accompanied by the rotation of H_2O and their relative orientation is finally reversed at A', where θ is the angle formed by the oxygen atom of H_2O, M^{3+} and the $\hat{C}_5$ axis of the Preyssler cluster. The black curve shows that a second H_2O enters the framework and participate in the displacement of the Gd^{3+}-H_2O unit. Color code: Preyssler framework (red), internal cation (green) and H_2O (Λ-shaped black sticks).

6.3.3 Ferroelectric property

For a more detailed analysis of the ferroelectric properties, we need to go beyond the molecular approach that we have adopted so far. Therefore, we now turn our attention to the crystal structure and analyse the differences between the ferroelectric phase (FP) and antiferroelectric phase (AFP) as shown in Figure. 6.7. The full relaxation of the ferroelectric phase (FP) (the left panel) maintains the orthorhombic nature with four Preyssler molecules per unit cell and reproduces quite accurately the lattice vectors of the x-ray structure of the Preyssler system with Bi ion inside the cavity.[5b] It also predicts the four cations (La^{3+} or Gd^{3+}) to be off-center and arranged in the same direction (all Site-A or all Site-A') when linked to a water molecule. The displacement of the metal ion from the center is similar to the one found in the molecular calculations. In order to estimate the polarization and to avoid the inclusion of quantum of polarization,[6] it is necessary to build a centrosymmetric antiferroelectric phase (AFP) with inversion symmetry as well as a way to connect FP with AFP

structure through atomic displacements. The AFP is constructed by moving the M^{3+}-H_2O unit from Site-A to A' along the $\hat{C}_5$ axis in the two of Preyssler anions, accompanied with the rotation of 180° of the H_2O molecule so that the four encapsulated M^{3+}-H_2O unit are in a head-to-tail arrangement (head-to-head arrangements are expected to be higher in energy) with two units in Site-A and the other two in A', as shown in Figure 6.7 (right, AFP). In order to ensure the inversion symmetry of the AFP structure, the two Preyssler frameworks and the surrounding 24 K^+ counter-cations outside the frameworks have also been properly displaced. For both structures we have performed a full geometry relaxation (cell parameters and atomic positions) and the energy difference between the two is 1.67 eV per unit cell in favor of the FP structure. In line with the experimental conditions, we have removed the 96 water molecules from the unit cell outside the POM, only leaving the four that are inside the cavity bonded to the metal ion.

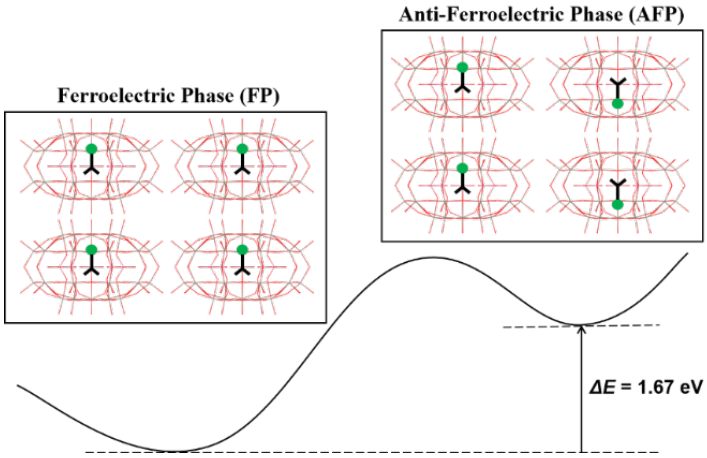

Figure 6.7. Energy comparison between ferroelectric phase (FP) with anti-ferroelectric phase (AFP). Color code: Preyssler framework (red), internal cation (green) and H_2O (Λ-shaped black sticks).

To connect the FP and AFP, we have followed the interconversion path that is studied in the molecular calculations in which the metal displacement is accompanied by a gradual rotation of the H_2O molecule bonded to it. The parameter λ collects all the geometrical changes along this path and interpolates between the AFP ($\lambda = 0$) and the FP ($\lambda = 1$) increasing the angle of the M-H_2O bond and the $\hat{C}_5$ rotation axis of the Preyssler anion in steps of 10 degrees. The total polarization of the system can be split into two parts, one that arises from the Preyssler molecule with the M-H_2O unit on the inside and a second part that is caused by changes in the positions of the K^+ counter-

cations. The polarization value of the AFP structure is 0 due to the presence of an inversion point at the center of the unit cell by construction. Figure 6.8 shows that the polarization increases along the b-axis, which coincides with the direction of the $\hat{C}_5$ axis of the isolated Preyssler cluster, resulting from the increase of asymmetry relative to the non-polar reference structure. The polarization along the a and c directions remain very close to zero for all λ values. The calculated polarization value at FP is 4.7 $\mu C/cm^2$, only 1.3 $\mu C/cm^2$ different from the experimental value.

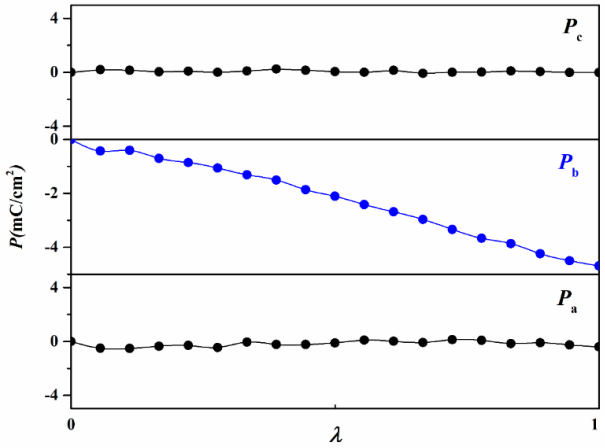

Figure 6.8. The FE polarization along the a, b, c axes of the Preyssler crystal as a function of the parameter λ, which represents the normalized distortions of two Preyssler molecules from AFP to FP. Hence, $\lambda = 0$ corresponds to the AFP while $\lambda = 1$ corresponds to the FP.

To trace the origin of the polarization and clarify the role of K^+ counterions, we consider the individual contribution of the Gd^{3+}-H_2O unit, $[P_5W_{30}]^{15-}$ and K^+ cations to the total polarization by displacing only appropriate functional units while keeping the other units at the centrosymmetric atomic position. For instance, to calculate the contribution of the Gd^{3+}-H_2O unit, only Gd^{3+}-H_2O units are displaced from AFP to FP structure while $[P_5W_{30}]^{15-}$ and K^+ cations are kept in the non-polar structure. The contributions of $[P_5W_{30}]^{15-}$ and K^+ cations are obtained in the same way. The contributions of the Gd^{3+}-H_2O unit, $[P_5W_{30}]^{15-}$ and K^+ cations are 3.4 $\mu C/cm^2$ and 0.5 $\mu C/cm^2$ and 1.2 $\mu C/cm^2$, respectively. The sum of the three individual polarization is 5.1 $\mu C/cm^2$, approximately the same as the calculated total polarization of 4.7 $\mu C/cm^2$, proving the rationality and consistency of decomposition of the polarization into three separate contributions. According to the order of the polarizations of 3.4 $\mu C/cm^2$ > 1.2 $\mu C/cm^2$ > 0.5 $\mu C/cm^2$, the interconversion of the Gd^{3+}-H_2O unit along the $\hat{C}_5$ axis

between two isoenergetic sites dominates the generation of overall polarization, and hence, can be considered to be the main origin of the FE in the Preyssler cluster. The redistribution of overall charge caused by the movement of Gd^{3+} relocates the K^+ counterions, resulting in an additional contribution that cannot be ignored while the contribution of $[P_5W_{30}]^{15-}$ is quite small.

6.4 Concluding Remarks

In summary, the single-molecule ferroelectric property of the Preyssler cluster, $[M^{3+}@P_5W_{30}]^{12-}$ (M = La, Gd and Lu) is studied by DFT calculations. By examining the structure of the single anion, we find that the cation enclosed in the Preyssler framework needs to bind one water molecule to go off-center and create the possibility of a polar structure. When the metal cation occupies one of the Site-A or A', the inversion of the cluster is broken and a permanent dipole moment is created, which is the basis of ferroelectric properties. Combining the interconversion of M^{3+} between the Site-A and Site-A' with a 180° rotation of H_2O results in a barrier of 1.15 eV for Gd^{3+}, in good agreement with the experimental barrier for Tb^{3+}, leading to the switching of the polarization. Moreover, we simulated the polarization of the Preyssler crystal using the Berry phase method to be 4.7 $\mu C/cm^2$, close to the experimentally measured value. The interconversion M^{3+}-H_2O contributes more than 66%, while the relocation of K^+ counter cations contributes less than 10% to the total polarization. Clearly the interconversion of M^{3+}-H_2O is the main reason for the generation of the ferroelectric polarization, which agrees with the hypothesis proposed by Nishihara and coworkers[41] that the ferroelectricity of the Preyssler POMs origins from the bi-stability of the two isoenergetic sites of the M^{3+}.

References

1. (a) Mohammed H. Alizadeh, S. P. H., Yves Jeannin, Jeanne Martin-FrBre and Michael T. Pope, *J. Am. Chem. Soc* **1985,** *107* (9), 8; (b) Qin, C.; Song, X. Z.; Su, S. Q.; Dang, S.; Feng, J.; Song, S. Y.; Hao, Z. M.; Zhang, H. J., *Dalton Trans* **2012,** *41* (8), 2399-407.

2. (a) Fernández, J. A.; López, X.; Bo, C.; de Graaf, C.; Baerends, E. J.; Poblet, J. M., *J. Am. Chem. Soc.* **2007,** *129* (40), 12244-12253; (b) Hayashi, A.; Wihadi, M. N. K.; Ota, H.; López, X.; Ichihashi, K.; Nishihara, S.; Inoue, K.; Tsunoji, N.; Sano, T.; Sadakane, M., *ACS omega* **2018,** *3* (2), 2363-2373.

3. (a) Hu, T. P.; Zhao, Y. Q.; Jaglicic, Z.; Yu, K.; Wang, X. P.; Sun, D., *Inorg. Chem.* **2015,** *54* (15), 7415-7523; (b) Du, J.; Cao, M. D.; Feng, S. L.; Su, F.; Sang, X. J.; Zhang, L. C.; You, W. S.; Yang, M.; Zhu, Z. M., *Chem. Eur. J.* **2017,** *23* (58), 14614-14622; (c) Turo, M. J.; Chen, L.; Moore, C. E.; Schimpf, A. M., *J. Am. Chem. Soc.* **2019,** *141* (11), 4553-4557.

4. Kato, C.; Machida, R.; Maruyama, R.; Tsunashima, R.; Ren, X. M.; Kurmoo, M.; Inoue, K.; Nishihara, S., *Angew. Chem.* **2018,** *130* (41), 13617-13620.

5. (a) Kim, K. C.; Pope, M. T.; Gama, G. J.; Dickman, M. H., *J. Am. Chem. Soc.* **1999,** *121* (48), 11164-11171; (b) Hayashi, A.; Haioka, T.; Takahashi, K.; Bassil, B. S.; Kortz, U.; Sano, T.; Sadakane, M., *Z. Anorg. Allg. Chem.* **2015,** *641* (15), 2670-2676.

6. Spaldin, N. A., *J. Solid State Chem.* **2012,** *195*, 2-10.

7. te Velde, G.; Bickelhaupt, F. M.; Baerends, E. J.; Fonseca Guerra, C.; van Gisbergen, S. J. A.; Snijders, J. G.; Ziegler, T., *J. Comput. Chem.* **2001,** *22* (9), 931-968.

8. (a) Swart, M.; Ehlers, A. W.; Lammertsma, K., *Mol. Phys.* **2004,** *102* (23-24), 2467-2474; (b) Zhang, Y.; Wu, A.; Xu, X.; Yan, Y., *Chem. Phys. Lett.* **2006,** *421* (4-6), 383-388.

9. (a) Barbieri, P. L.; Fantin, P. A.; Jorge, F. E., *Mol. Phys.* **2006,** *104* (18), 2945-2954; (b) Jensen, F., *Wiley Interdiscip. Rev. Comput. Mol. Sci.* **2013,** *3* (3), 273-295.

10. (a) van Lenthe, E.; Baerends, E. J.; Snijders, J. G., *J. Chem. Phys.* **1994,** *101* (11), 9783-9792; (b) Klopper, W.; van Lenthe, J. H.; Hennum, A. C., *J. Chem. Phys.* **2000,** *113* (22), 9957-9965.

11. (a) Klamt, A., *J. Phys. Chem.* **1995,** *99* (7), 2224-2236; (b) Pye, C. C.; Ziegler, T., *Theor. Chem. Acc.* **1999,** *101* (6), 396-408.

12. Xu, S.; Jia, F.; Yang, Y.; Qiao, L.; Hu, S.; Singh, D. J.; Ren, W., *Phys. Rev. B* **2019,** *100* (10), 104408.

13. (a) Blöchl, P. E., *Phys. Rev. B* **1994,** *50* (24), 17953-17979; (b) Kresse, G.; Joubert, D., *Phys. Rev. B* **1999,** *59* (3), 1758.

14. (a) Kresse, G.; Furthmüller, J., *Computational Materials Science* **1996,** *6* (1), 15-50; (b) Kresse, G.; Furthmüller, J., *Phys. Rev. B* **1996,** *54* (16), 11169-11186.

15. (a) Perdew, J. P.; Burke, K.; Ernzerhof, M., *Phys. Rev. Lett.* **1996,** *77* (18), 3865-3868; (b) Perdew, J. P.; Ruzsinszky, A.; Csonka, G. I.; Vydrov, O. A.; Scuseria, G. E.; Constantin, L. A.; Zhou, X.; Burke, K., *Phys. Rev. Lett.* **2008,** *100* (13), 136406.

16. (a) Hao, Z.; Zeng, R.; Yuan, L.; Bing, Q.; Liu, J.; Xiang, J.; Huang, Y., *Nano Energy* **2017,** *40*, 360-368; (b) Lucignano, P.; Alfè, D.; Cataudella, V.; Ninno, D.; Cantele, G., *Phys. Rev. B* **2019,** *99* (19); (c) Rang, M.; Kresse, G., *Phys. Rev. B* **2019,** *99* (18).

CHAPTER 7

General Conclusion

This last chapter summarizes the main achievements and conclusions of Chapters 3 to 6 of this doctoral thesis.

Chapter 3: Electrochemical Catalysis of the CO Oxidation and CO_2 Reduction Using Trimetallo-oxo POMs as Alternatives for Rare-metal Based Catalysts

- The triprotonated, 2-electron reduced species were those active in CO_2 and CO binding and activation.
- For $H_3[SiFe^{II}Ni^{II}Ni^{I}W_9]$, the binding of CO_2 and CO occurs at the Ni^{I} center with true bonding interactions.
- The $H_3[SiCu^{II}{}_2Cu^{I}W_9]$ anion shows no 1-electron binding interaction with CO_2 until 2-electrons are injected. The two Cu^{I} centers indicate a synergy effect by transferring an electron from one Cu^{I} to the other Cu^{I} and therefore forming a polyanion with an $H_3[SiCu^{II}{}_2Cu^{0}W_9]$ electronic configuration where CO_2 is bound to the Cu^{0} atom.
- Since the Lewis acid center Ga^{III} brings one more site to coordinate CO_2, the GaCuFe-POM can easily fix CO_2 by a usual double-bonding mode, Ga-O-C-O(Cu). Notably, this coordination process occurs before any reduction step, leading to a lower potential.

Chapter 4: The Photocatalytic Behaviors of the Pure and Coordinated POM Clusters within the Multi-components Systems Reducing CO_2 to CO

For the three-components hybrid construct system:

- The protons-coupled multiple electrons transfer mechanism is summarized as follows: after absorbing blue light, [g-CN] transfers two electrons to the POM, driven by a large LUMO energy difference. Then, the hydrocarbon, transfers two electrons to the holes of the oxidized g-CN and two (or even more) protons to the reduced POM, leading to the dehydrogenation of the hydrocarbon. Next, the reduced POM is excited by red light and then transfers two electrons to Re(I)

species. Finally, the activated catalyst captures and reduces CO_2 and in the process the hydrogen-rich POM transfers two protons to the CO_2-coordinated Re-species to generate the reduction products, CO and water.

- The roles of the POM are crucial by acting as an electron acceptor to facilitate electron-hole separation and an electron donor to a Re-based CO_2 catalytic reduction system.
- The reduction of the Re(I)-catalyst is a ligand-based reduction. The energy gap between the bipyNNH$_2$ π^* orbital and the Re dz^2 orbitals, and the succeeding occupation after reduction is the main reason of the CO_2 binding affinity.

For the two coordinated clusters:

- The core $[Co_{13}O_8]$ fragment is relatively independent to the $[Nb_6O_{19}]$ fragment due to the big gap between the MOs contributed by the two metals, respectively. Both HOMO and LUMO are contributed by the core $[Co_{13}O_8]$ fragment.
- The core $[Ni_{30}O_{24}]$ fragment has considerable interaction with the $[Nb_6O_{19}]$ cluster, resulting in that the HOMO is mainly contributed by the $[Ni_{30}O_{24}]$ part and the LUMO is located at the orbital of Nb. The Ni empty orbital is slightly higher, resulting in the potential electron transfer from the Ni to the Nb cluster after irradiation.

Chapter 5: Switchable Rashba Anisotropy in Layered Hybrid Organic-Inorganic Perovskite by Hybrid Improper Ferroelectricity

- The computational results of P_s and α_R are nicely consistent with the experimentally reported values where the AMP cations contribute almost all of the total polarization. The spin-texture sense of rotation can be reversed by a switching of the FE polarization direction along the polar axis.
- A large and robust anisotropy in the Rashba parameter is firstly found where the major and minor axes of the ellipse can be exchanged under reversal of the electric polarization, causing a 90° pseudo-rotation of the Rashba anisotropy, which we have also confirmed from a theoretical $k \cdot p$ model. The same effect is observed in both the VBs and CBs at multiple points in the Brillouin Zone where the Rashba splitting is significant.

- A structural mechanism is presented and explained in terms of a quadrilinear coupling of order parameters involving two large-amplitude AMP-cation rotation modes, a large octahedral framework rotation, and the ferroelectric polarization.

Chapter 6: Density Functional Theory Analysis of Single-molecule Ferroelectricity in Preyssler-type Polyoxometalates

- Linking one water molecule is necessary for the M^{3+} to go off-center and create the possibility of a polar structure. When the metal cation occupies one of the Site-A or A', the inversion of the cluster is broken and a permanent dipole moment is created, which is the basis of ferroelectric properties.
- Combining the interconversion of M^{3+} between the Site-A and Site-A' with a 180° rotation of H_2O results in the switching of the polarization.
- The polarization of the Preyssler crystal using the Berry phase method to be 4.7 $\mu C/cm^2$, close to the experimentally measured value.
- While the relocation of K^+ counter cations contributes less than 10% to the total polarization, the interconversion of M^{3+}-H_2O with a contribution of 66% is the main reason for the generation of the ferroelectric polarization, which agrees with the hypothesis proposed by Nishihara and coworkers that the ferroelectricity of the Preyssler POMs origins from the bi-stability of the two isoenergetic sites of the M^{3+}.

Acknowledgments

The Ph.D. life at URV is one of the most unforgettable experiences for me, through which I have learned and improved a lot. There are so many people for who I want to gratitude for the huge help they provided to me.

First of all, I want to give my special thanks to my two supervisors, Prof. Josep Maria Poblet and Prof. Coen de Graaf. They gave me so much support and help on my Ph.D. projects and this thesis.

Josep M. (I usually call you Poblet), the most thanks to you. I am deeply impressed by your rigorous research attitude and rich chemical knowledge! You have given me great freedom and patience at work. Notably, you not only guide me with the scientific work but also support me in daily life. You are not just my supervisor, more like my family in Spain looking after me. You are like a big tree standing there and let me believe that no matter when I am in need, I can rely on you! A big "ABRAZO" to you!!

Coen, many thanks to you. It is a great pleasure for me to have a supervisor like you who is knowledgeable, responsive, and serious about work! Your influence on me permeates many aspects, especially the huge passion for scientific research. Your guidance and opinions always inspire me and keep me going! In the future, I will continue my scientific work by bearing your teaching and help in mind. Muchas gracias!!

Here I also want to thank the other senior numbers of the academic group. Rosa, many thanks to you for helping me to solve all kinds of enrollment issues. Toni and Maria, thank you a lot for the supporting you gave me on my teaching task. Also thanks to Xavi for those tips on the Preyssler project. Thanks Jose, Elisenda, and Moisés for technical help.

Here, I would like to many thank the guest supervisor in Italy, Dr. Alessandro Stroppa (CNR-SPIN L'Aquila) for the warm hospitality and guidance when I was learning there! Thanks to other international collaboration groups, Prof. Ronny (Weizmann Institute of Science, Israel), Prof. Weinstock (Ben Gurion University, Israel), and Prof. Kortz (Jacobs University, Germany) groups, our collaboration is very pleasant and beneficial!

I also want to show my thanks to the students of the academic group, my lovely friends. We work together and also have fun together, which gave me so many wonderful moments. Albert (Masip) and Gonzalo, we have shared the office for a long time. Many thanks to you for those times when you were working as my "Spanish translator"

and more importantly, for that funny talking and jokes! Yannick, whenever I need help, you always lend me a helping hand at the first time. I really appreciate your enthusiastic help. I hope that one day you can find an opportunity to visit China and enjoy life there. By then, please contact me without any hesitation! Toni and Albert (Sole), thanks a lot for your help in the office as well as those fun times we spent together. I sincerely wish you a bright and beautiful future! Alumudena, many thanks for the help you gave me when we shared a flat. Your optimism and enthusiasm have given me a lot of warmth! Thanks also to other students, including Marc, Antonio, Aitor, Jordi, Ricardo, Evgenii, Yeamin, Roser, et al., although it is a pity that we only spent a short time.

Now, I switch to Chinese to gratitude my family, those professors in China as well as my Chinese friends.

首先感谢我的父母对我出国读博的理解和支持。他们对我无限的爱和包容是我一路走来最强大的动力和后盾。在这里，我还要感谢我的姐姐，在我出国期间替我照顾父母，免除了我的后顾之忧。之后，我要特别感谢延边大学的孙光延教授，她曾是我硕士导师，但她对我的帮助和支持从未停止过。在我博士期间，她也一如既往得关心我的学业和生活，使在异国他乡的我倍感温暖！此外我还要感谢东北师范大学的颜力楷教授和郎中玲副教授在我博士之初，由于签证原因不能出国时为我提供学习和生活居所的支持，东师的学习生活让我受益匪浅！最后，我要感谢我的挚友，王甜、李明阳和周杰，那年夏天，海绵宝宝和派大星成为了永远的好朋友，谢谢你们最暖心的陪伴，未来我们还要一起走下去。此处绝对不能省略的当然还有陪我一起长大的发小们啊（脱亚琦，王婧和王培娜），每次回国回家，都给我最热烈温暖的欢迎。最后还有我在 Tarragona 的好朋友们（王珺璟，李善明，何巧玲和潘杰），谢谢你们一起陪我走过的漫长的留学路程，我将永远铭记那些我们共同经历过的美好的回忆。

Additional information

Chapter 4

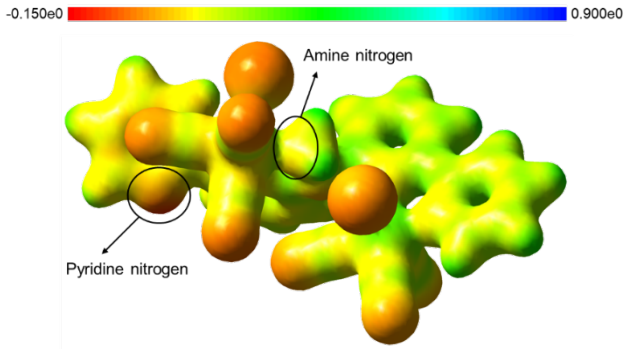

Figure S4.1. Molecular electrostatic potential (MEP) map projected on a density isosurface (ρ = 0.04) for [Re^1-Re^2]. The MEP map evolves from blue to red, indicating more negative electrostatic potentials (more proton-attractive and dipole-orienting) at the surface.

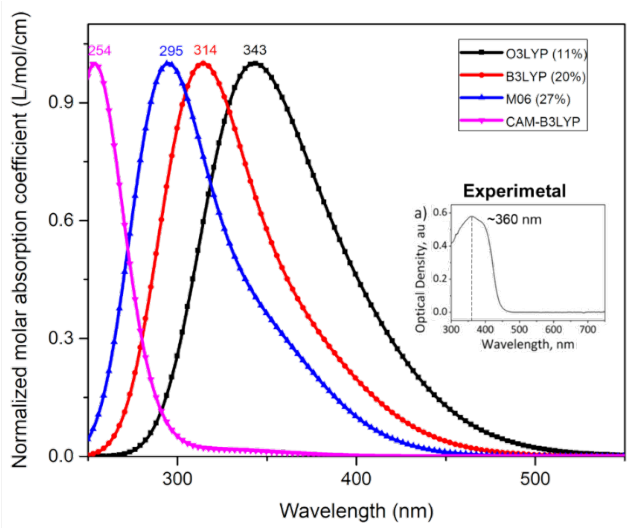

Figure S4.2. Simulated absorption spectra of [g-CN] (**a**) with different functionals (O3LYP, B3LYP, M06, and CAM-B3LYP). The experimental absorption spectrum is inserted for comparison.

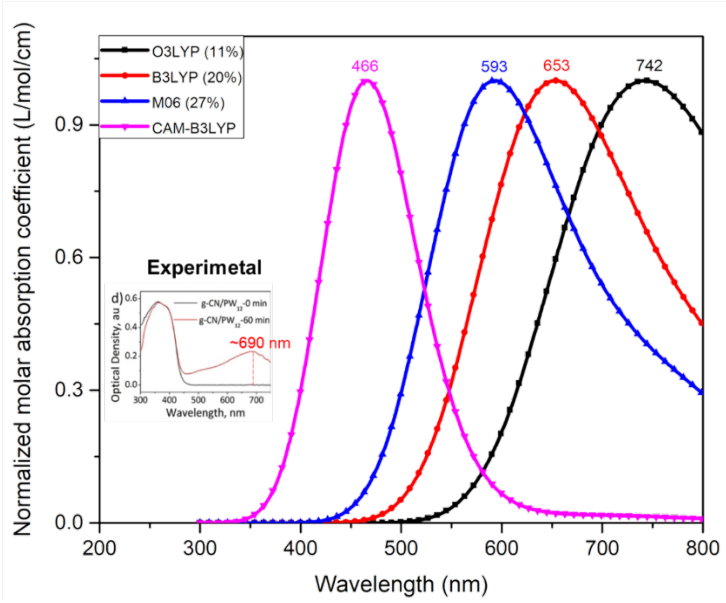

Figure S4.3. Simulated absorption spectra of reduced POM (reduced-**b**) with different functionals (O3LYP, B3LYP, M06, and CAM-B3LYP). The experimental absorption spectrum is inserted for comparison.

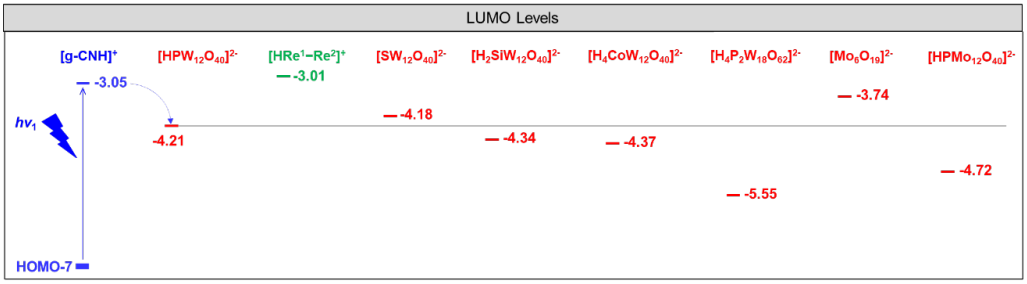

Figure S4.4. Comparison of orbital energy levels for electron transfer from [g-CNH]$^{+}$(**1a**) to [HRe^{1}–Re^{2}]$^{+}$(**1c**) taking different POMs as shuttle.

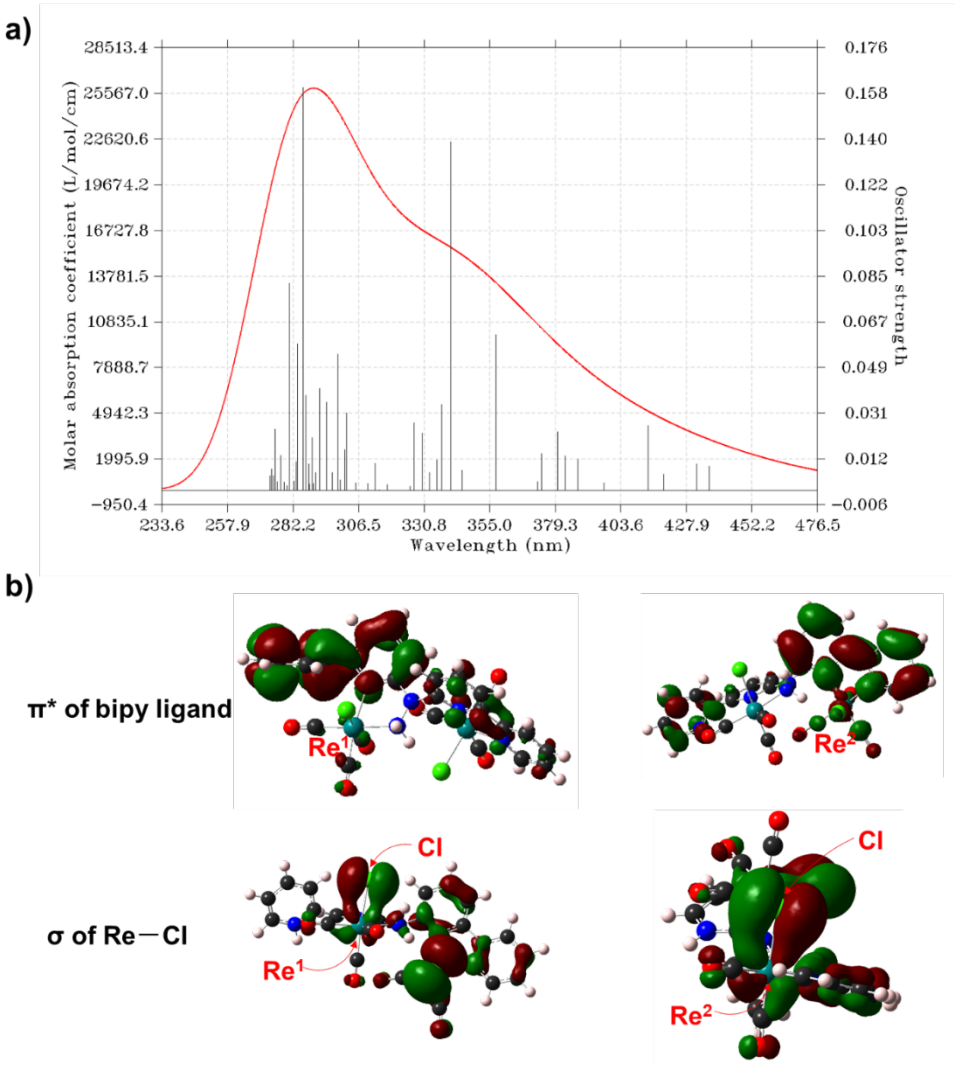

Figure S4.5. a) Simulated absorption spectrum of $[HRe^1–Re^2]^+$ by TD-B3LYP and **b**) the strongest transition corresponding molecular orbitals.

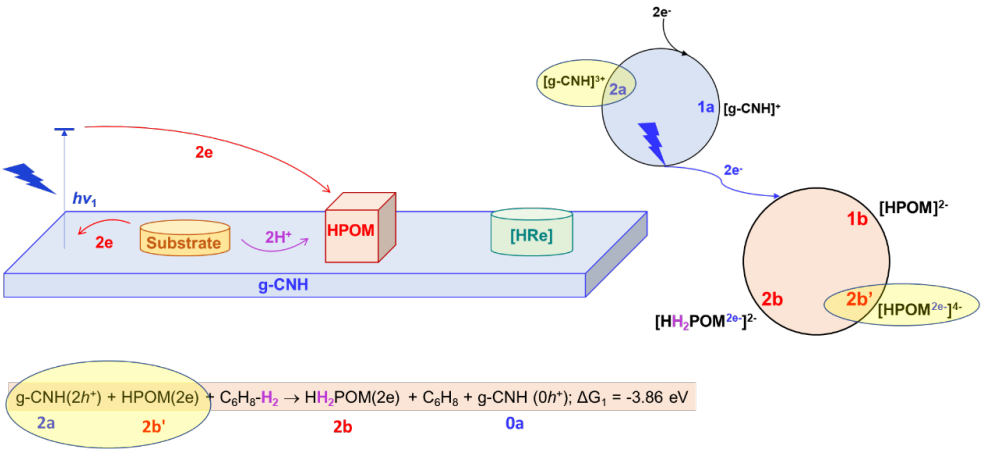

Figure S4.6. The schematic diagram for energy balance and the computational details of the ΔG associated with the protons transfer from the substrate to the red cycle.

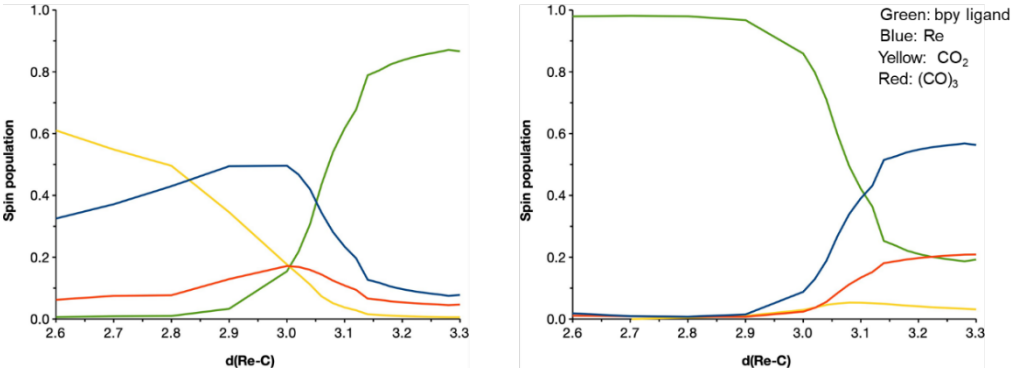

Figure S4.7. The CASSCF spin populations of the ground (left) and first excited state (right) as a function of the distance between Re and CO_2.

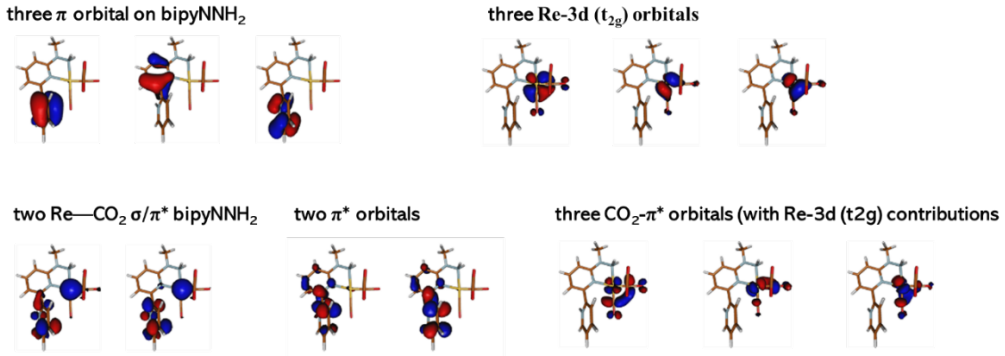

Figure S4.8. The active orbitals of CASSCF(13,13) calculation.

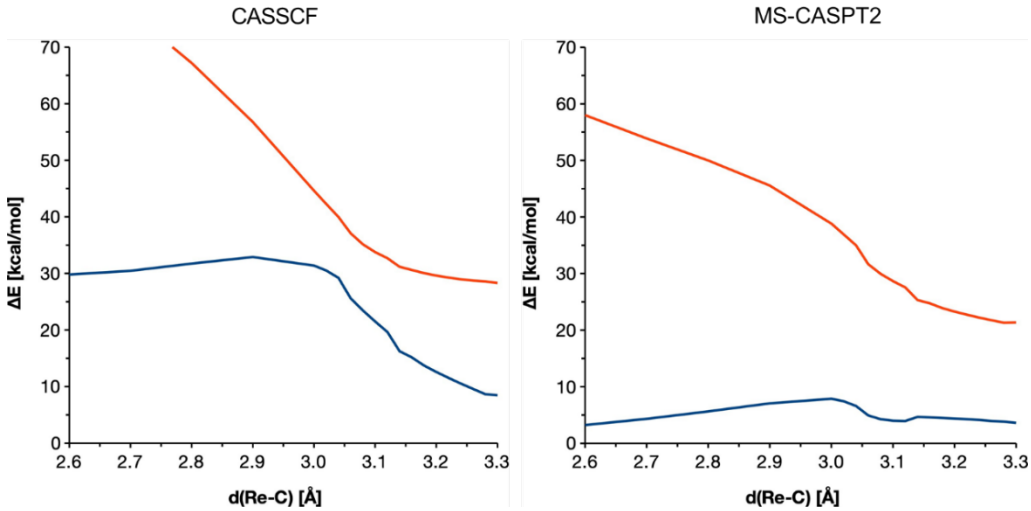

Figure S4.9. CASSCF curves and relative MS-CASPT2 energies of the ground and first excited state as a function of the distance between Re and CO_2.

Table S4.1. The comparison of the reduction potential (V, vs SHE, in green) and reaction free energy (ΔG, kcal/mol) of the bimetallic [$\mathbf{Re^1–Re^2}$] and monometallic [$\mathbf{Re^1–CH_3}$].

	[$Re^1–Re^2$]	[$Re^1–CH_3$]
2-3	**-0.77**	**-0.89**
3-4	0.7	0.6
T_{34}	2.4	3.2
4-5	**-0.85**	**-0.92**
5-6	-57.5	-59.5
6-7	0.6	-1.3
7-2	-28.5	-26.8
TS_{72}	13.4	10.4

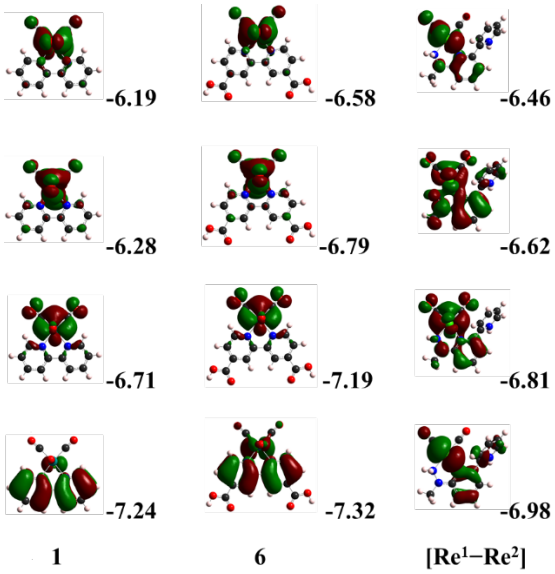

Figure S4.10. Frontier molecular orbitals and corresponding energies (in eV) of compounds **1** and **6** as well as [**Re¹–Re²**]

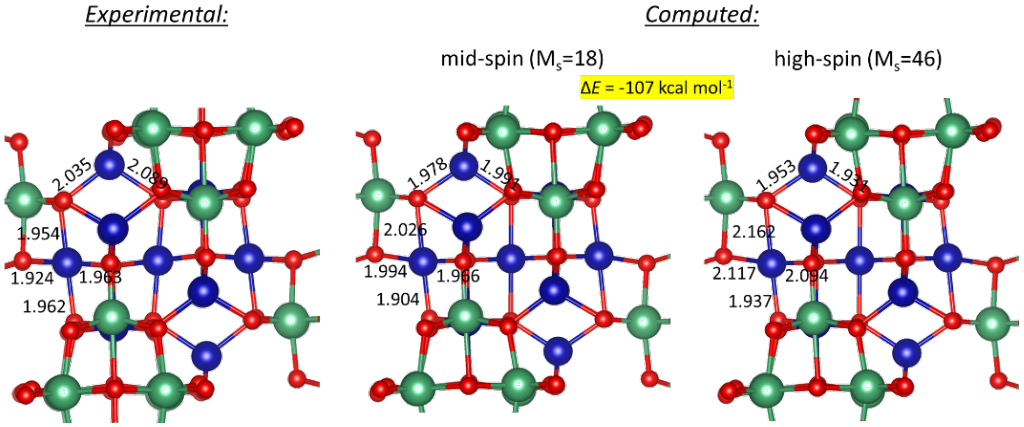

Figure S4.11. The comparison between experimental and computed structures with different spin multiplicities. The computed energy difference (ΔE) of the optimized structures in different spin states is also given. Color code: Co (blue), O (red) and Nb (green). The Nb6O19 clusters are partly hidden for clarification.

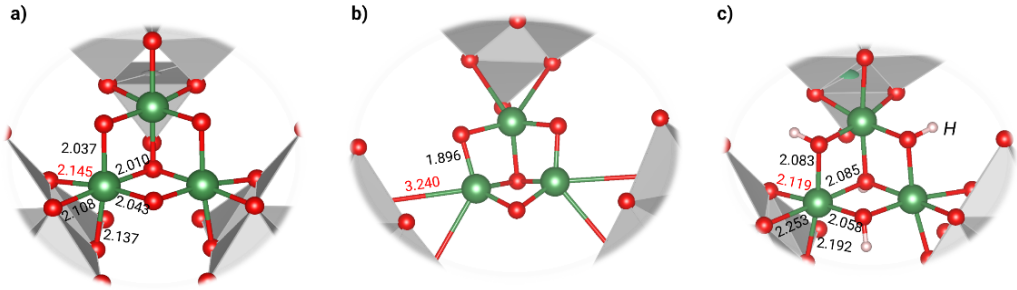

Figure. S4.12. a) The representation of the experimental crystal where the main bond lengths are listed in Å; **b**) and **c**) the optimized structures by using the simplified model, $[Ni_3O_4(Nb_6O_{19})_3]^{26-}$ with and without bonding protons to the O atoms of the core Ni_3O_4 part.

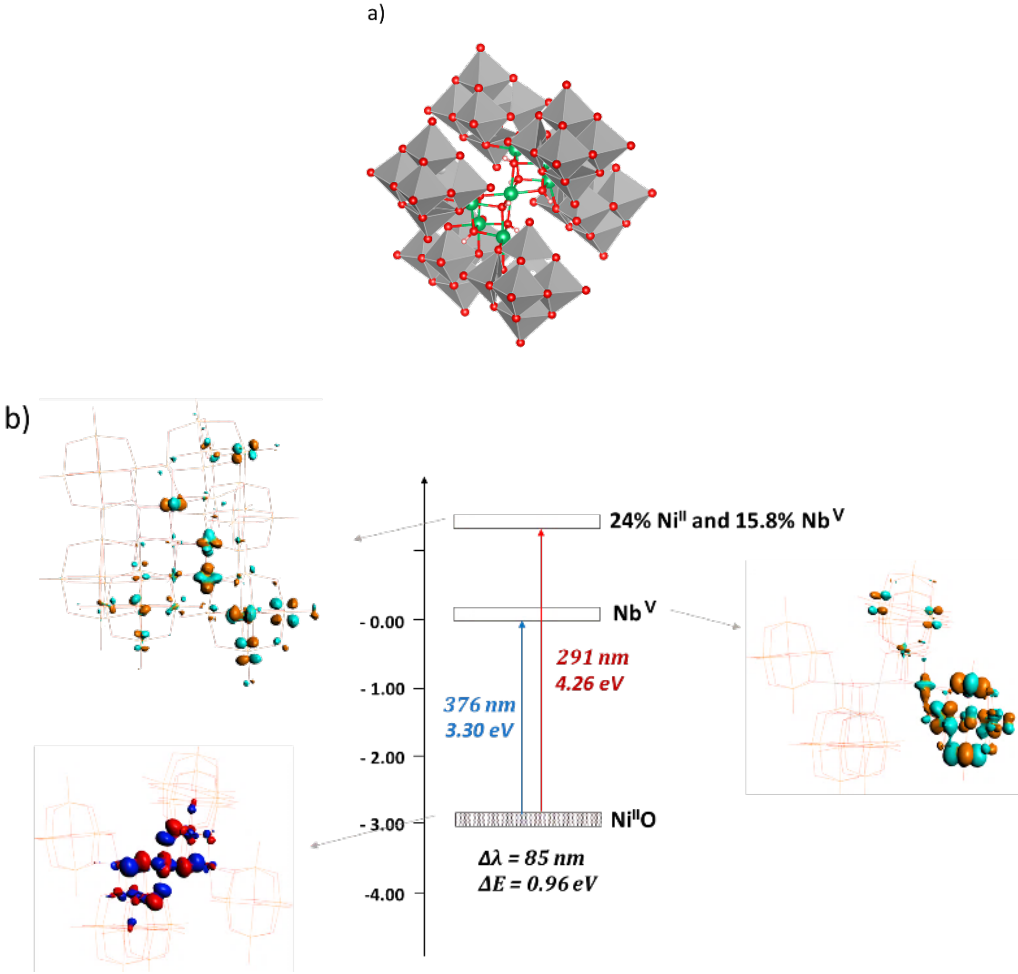

Figure S4.13. The structural representation (**a**) and corresponding MO diagrams (**b**) of the bigger model, $[Ni_7(OH)_8(Nb_6O_{19})_6]^{42-}$.

Chapter 5

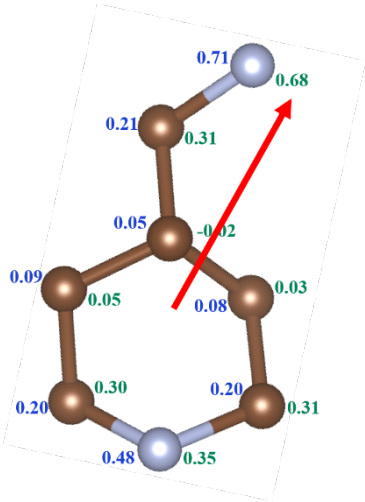

Figure S5.1. The Hirshfield (blue values) and Natural (green values) population analysis on the isolated AMP cation, with purple Pb, gray I, brown C, and blue N. The charges of hydrogen atoms (omitted) are summed into the heavy atoms. The red arrow indicates the direction of the dipole moment.

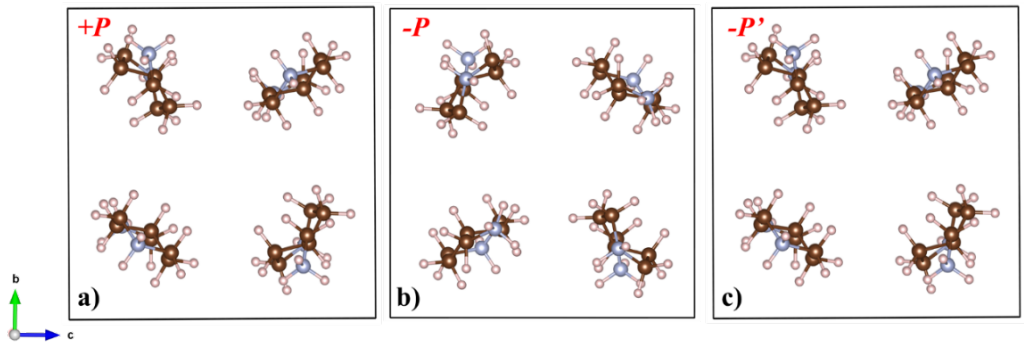

Figure S5.2. The orientations of four AMP molecules on the *bc* plane of ***+P*** (**a**), ***-P*** (**b**), and ***-P'*** (**c**), in which the PbI_4^{2-} the inorganic framework is ignored for clarity. Color code: brown C, blue N, and pink H.